Humboldt-Universität zu Berlin

DISSERTATION

Elementary solute-solvent interactions and the photophysical properties of photoacids

zur Erlangung des akademischen Grades doctor rerum naturalium (Dr. rer. nat.)

Mathematisch-Naturwissenschaftlichen Fakultät I

M.Sc-Chem Mirabelle Prémont-Schwarz

Dekan: Prof. Stefan Hecht

Gutachter/in: 1. Prof. Dr. Thomas Elsässer

2. Prof. Dr. Peter Vöhringer

3. Prof. Dr. Beate Röde

Datum der Einreichung: 07.02.2013

Datum der Promotion: 12.07.2013

Zusammenfassung

Photosäuren sind aromatische Alkohole, sogenannt aufgrund der Erhöhung ihrer Azidität, die aus der elektronischen Anregung folgt. Allerdings muss ein plausibles Verständnis der Prozesse, die zu der Erhöhung der Azidität führen noch etabliert werden. Zu diesem Zweck wird die Photophysik zweier Photosäuren, 1-Naphthol (1N) und 2-Naphthol (2N), untersucht.

Mit Hilfe der Femtosekunden-UV-Anrege/IR-Abtast-Spektroskopie wird die OH-Streckschwingung sowohl im Grundzustand als auch im angeregten Zustand gemessen. Die intrinsische elektronische Ladungsverteilung, die aufgrund der Anregung in der Säure auftritt, in apolaren Lösungsmitteln untersucht. Der Vergleich mit Resultaten eines theoretischen Modells stellte einwandfrei fest, dass eine geringe Ladungsverteilung in der Photosäure auftritt. Die OH-Streckschwingung von wasserstoffverbrückten Komplexen zwischen 2N und Acetonitril wird gemessen. Obwohl experimentell gefunden wurde, dass der angeregte Zustand verglichen mit dem Grundzustand eine nahezu doppelt so große solvatochromatische Verschiebung zeigt, scheitern theoretische Modelle daran, diese Ergebnisse wiederzugeben.

Die Ladungstransferreaktion im angeregten Zustand von 1N und 2N zu halogenierten Lösungsmitteln wird zur Abfrage der elektronischen Dichte am aromatischen Ring nach Anregung verwendet. Wurde ermittelt, dass verglichen mit dem unkomplexierten Molekül die Elektrontransferrate in einem wasserstoffverbrückten Komplex mit Acetonitril 10 mal höher ist. Auf diese Weise hat sich der Einfluss der Wasserstoffbrückenbindung auf das Ausmaß der Ladungsverteilung gezeigt.

Mittels zeitaufgelöster Anisotropie, Fluoreszenz und IR-Messungen war es möglich festzustellen, dass die ultraschnelle (<60fs) Zustandskreuzung hin zu einem polareren Zustand tatsächlich in 1N, aber nicht in 2N stattfindet. Sind diese Zustandsdynamiken folgen wahrscheinlich aus Umlagerungen der Wasserstoffbrücke, zwischen 1N und dem Lösungsmittel.

Schlagwörter: Femtosekunden-UV-Anrege/IR-Abtast-Spektroskopie, Photosäure, Zustandskreuzung, OH-Streckschwingung.

Abstract

Photoacids are aromatic alcohols, characterized by a dramatic increase in acidity upon electronic excitation. A coherent view of the processes giving rise to this increase in acidity has yet to be established. To this effect, the photophysics of photoacids 1-naphthol (1N) and 2-naphthol (2N) are investigated.

Using femtosecond UV pump-IR probe spectroscopy, the OH stretch vibration in both the ground and excited-state is measured. The intrinsic electronic charge redistribution in the acid upon excitation is investigated in non-polar solvents where specific interactions are absent. Comparison with results from a theoretical model based on the Pullin-van der Zwan-Hynes perturbative approach established that little charge redistribution occurs in the photoacid. The OH stretch vibration of hydrogen-bonded complexes of 2N with acetonitrile is measured. While it was found experimentally that the excited-state is characterized by a solvatochromic response that is almost twice as large as in the ground-state, the theoretical model failed to reproduce these results. Instead, the calculations predict no significant differences between the behaviour of the two states.

The excited-state charge transfer reaction of 1N and 2N to halogenated solvents is used as a probe for the electronic density on the aromatic ring upon excitation. The charge transfer rate for the hydrogen-bonded complex with acetonitrile is found to be ten times higher than for the uncomplexed molecule. In this way, the influence of a hydrogen-bond on the extent of charge redistribution was evinced.

Using time resolved anisotropy, fluorescence and IR measurements, it was determined that ultrafast (<60fs) level crossing to a more polar state occurs in 1N and not in 2N, where the level dynamics are likely due to rearrangements of the hydrogen-bond donated from 1N to the solvent after excitation. Also, significant level mixing is inferred.

Keywords: Femtosecond UV pump-IR probe spectroscopy, photoacids, level crossing, OH stretch vibration.

Contents

List of abbreviations

APTS	8-Aminopyrene-1,3,6-trisulfonic acid trisodium salt
B3LYP	Becke three parameter Lee-Young-Parr
BBO	beta barium borate
5C2N	5-cyano-2-naphthol
1,2-DCE	1,2-dichloroethane
DCM	dichloromethane
DFM	difference frequency mixing
N,N-DMF	N,N-dimethylformamide
DMSO	dimethylsulfoxide
DFT	density functional theory
EA	electron affinity
ET	electron transfer
ESPT	excited-state proton transfer
EtOH	ethanol
GVD	group velocity dispersion
HB	hydrogen bond/ hydrogen bonding
HFIP	hexafluoroisopropanol
1HP	1-hydroxypyrene
HPTA	8-Hydroxy-N,N,N′,N′,N″,N″-hexamethylpyrene-1,3,6 trisulfonamide

HPTS	8-Hydroxypyrene-1,3,6-trisulfonic acid trisodium salt
IP	ionozation potential
IR	infrared
KT	Kamlet-Taft
LC	level crossing
MeCN	acetonitrile
MIR	mid infrared
N	naphthalene
1N	1-naphthol
2N	2-naphthol
1Nate	1-naphtholate
2Nate	2-naphtholate
NOPA	non-collinear optical parametric amplifier
SFM	sum frequency mixing
TD-DFT	time dependent density functional theory
TDM	transition dipole moment
THF	tetrahydrofuran
TrIR	transient infrared
TST	transition state theory

1. Introduction

Photoacidity is a term that was coined in order to highlight the increased excited state acidity of aromatic alcohols and protonated aromatic amines [1]. This property was first discovered and investigated by Weber [2], Förster [3, 4], and Weller [5, 6], more than half a century ago while looking at the fluorescence spectra of these compounds in water. Indeed, excited state proton transfer (ESPT) was first revealed through the presence of a significantly red-shifted emission band arising from the conjugate base, easily assigned by comparison with the directly excited anion. An illustrative example is that of 2-Naphthol (2N) in water shown in figure 1.1. As a comparatively weak photoacid, 2N undergoes only partial deprotonation leading to dual emission from both the acid and the conjugate base.

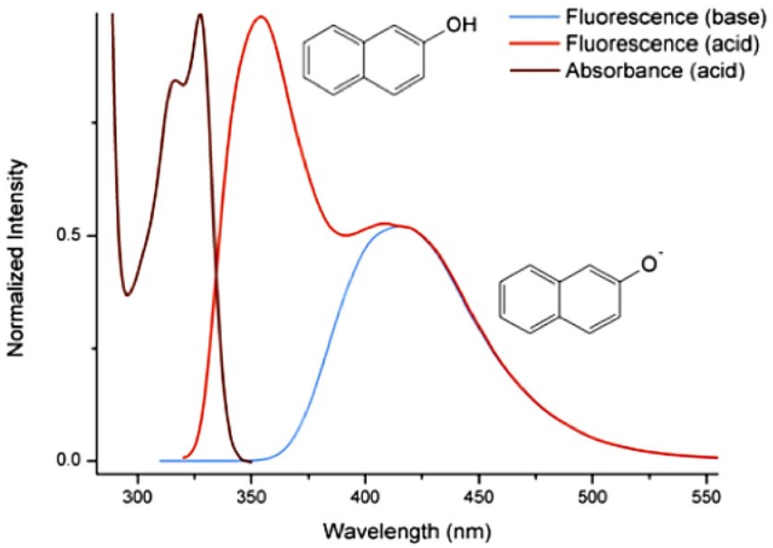

Figure 1.1: Absorbance and fluorescence spectra of 2-Naphthol in neutral H_2O as well as the fluorescence spectra in H_2O at pH 12 corresponding to the direct excitation of the anion.

1.1 Excited-state proton transfer reactions and the nature of photoacidity

Most research has focused on using the unique properties of photoacids to enable dynamical studies of acid base reactions [7, 8, 9]. While proton transfer is a fundamental reaction central to acid base chemistry, biological energy transduction or enzyme catalysis, before the advent of ultrafast techniques, studies were limited to equilibrium properties as an investigation of the microscopic events at play was impossible due to the fast picosecond timescales of typical

proton transfer reactions. The advent of short pulsed lasers made it possible to resolve events happening on femtosecond timescales, but a trigger for the proton transfer reaction was needed. Photoacids can provide such a trigger as they are activated by ultrashort ultraviolet or visible pulses, thereby generating protons at a specified instant in time. Through their use, it has been possible to separate on-contact rates of neutralization from diffusion controlled dynamics, allowing for a better understanding of the molecular details of proton transfer reactions [10, 11, 12, 13]. The microscopic proton transport properties as well as geminate recombination processes have been investigated [14, 15, 16, 17]. Photoacids have also been applied in pH jump experiments [18, 19, 20], as probes of the environment around proteins [21, 22, 23, 24], as initiators of catalytic reactions [25] or polymerizations [26], or in photo-deprotection systems [27].

Recently, there has been renewed interest in answering the more fundamental question as to which are the processes at the origin of this increased acidity. Indeed, despite the fact that almost a century has passed since its discovery, a coherent view of photoacidity and the molecular mechanism behind ESPT has yet to emerge.

The main debate in the recent literature concerns the driving force for the increase in acidity. The traditional view of photoacidity first put forward by Weller ascribes the increase in acidity to larger charge redistribution from the oxygen into the aromatic ring in the excited-state of the acid [5]. However, due to computational calculations which evidence no charge transfer upon excitation of gas-phase photoacids, it has now been proposed that it is instead electronic redistribution occurring in the conjugate photobase which is at the source of the increase in excited-state acidity [28, 29].

The role of excited state level crossing is another aspect which requires further characterization. There is substantial experimental evidence that solvent driven level crossing from the ^1L_b to the ^1L_a state occurs in photoacids like 1N [30, 31, 32, 33, 34, 35]. However, claims of a special “photoacid” state from whence ESPT would be triggered have been dashed as no indication of such behavior has been found for 1N’s geometrical isomer, 2N, nor for numerous other common photoacids. While it is generally thought that level crossing in 1N is responsible for the thousand times stronger photoacidity it exhibits compared to 2N, the characteristics of this level crossing as well as its role in the marked photoacidity increase remains unknown. However, this excited-state level crossing highlights the fact that treating excited state acidity solely within the ground-state paradigm might not be wholly adequate. Another example of the limitation of the ground-state description is that for certain weaker photoacids like 1-hydroxypyrene, no equilibrium is attained within their finite excited state

lifetimes, thereby rendering thermodynamic descriptions of equilibrium properties unsuitable [36].

An issue which has largely been ignored in conjunction with descriptions of photoacidity, are the numerous photochemical reactions known to occur in aromatic compounds besides ESPT. The reactivity of phenol is best exemplified by its efficient anti-oxidant properties due to its ability to scavenge radicals by rapid hydrogen or electron transfer [37]. The fluorescence of aromatic molecules has been found to be quenched by halogen containing solvents, likely through a charge-transfer complex [38, 39, 40, 41, 42, 43, 44, 45, 46]. In addition, excited-state intramolecular proton transfer from the hydroxyl group to the ring has been found to occur in 1N and 1-hydroxypyrene with high quantum yields [36, 47, 48, 49, 50]. Also, phenols, naphthols and to a greater extent their respective anions, have been shown to yield solvated electrons following single photon excitation [51, 52, 53, 54, 55, 56, 57, 58, 59, 60, 61]. A recent femtosecond transient absorption study of the photoionization of phenolate has revealed that the electrons are generated via two channels: the first being the locally excited state and the second the relaxed S_1 state, where this last slower ejection channel accounts for 64% of the electrons [62]. While the quantum yields of photoionization are understandably much less in the neutral molecules, given the delayed nature of the ionization process in the anion, this mechanism could be operative upon indirect generation of the anion through ESPT. In this sense, the proton coupled electron transfer reaction found for gas-phase photoacids is revealing and the importance of these reactions in solution should not be discounted without further investigation. A critical re-examination of the current data in conjunction with experiments carefully designed to address various questions of interest are essential in order to better characterize photoacidity, and more fundamentally still, understand the photochemistry of aromatic alcohols.

1.2 Thesis outline

First, the electronic and IR spectroscopy of photoacids, and more specifically, 1N and 2N, will be presented in Chapter 2. The theory of electron transfer reactions and models for calculating solvent induced vibrational frequency shifts will be presented in Chapter 3. Chapter 4 will then provide the nonlinear optical theory necessary to understand the ultrafast experiments and the particulars of the various experimental methods utilized in this thesis such as UV pump-IR probe spectroscopy and fluorescence up-conversion. In Chapter 5, the complex ESPT reaction of photoacids is first reduced to its first step: the intrinsic changes

occurring in the photoacid upon excitation and the solute-solvent couplings. For this we look at the transient OH stretch vibration of 1N and 2N in a series of solvents where no specific interactions are understood to occur. However, proton transfer reactions proceed along a hydrogen bonded coordinate. Thus, formation of a specific hydrogen bonded complex is of central importance to the ESPT event. For this reason, the hydrogen bonded complex of 2N in acetonitrile in various non-polar solvents is also investigated. In Chapter 6, the electronic density of the aromatic ring after electronic excitation is probed by utilizing the established quenching properties of aromatic systems by halocarbon solvents. In Chapter 7, the occurrence and importance of excited state level crossing in ESPT reactions and for photoacidity in general will be investigated by combining fluorescence up-conversion and transient IR measurements of the two prototype photoacids: 1N and 2N. Finally, the main conclusions derived from this work will be summarized and an outlook to further work provided in Chapter 8.

2. Photoacidity, electronic and infrared spectroscopy of 1- and 2-naphthol

2.1 Photoacidity

Photoacids are Brønstead acids and are typically described using the formalism developed for the ground state, whereby an acid is a molecular entity or chemical species capable of donating a proton (Bronsted [63]. The proton transfer reaction involves the transfer of a proton from the acid to an accepting base forming the respective conjugate acid and conjugate base.

$$AH(acid)+B(base)\leftrightharpoons A^{-}(conjugate\ base)+BH^{+}(conjugate\ acid) \quad (2.1)$$

The dissociation reaction is characterized by an equilibrium constant defined as:

$$K_a = \frac{A^-\ \ BH^+}{HA} \quad (2.2)$$

Given the large range spanned by acidity constants, a logarithmic scale is defined for better convenience, where:

$$pK_a=-\log_{10}K_a \quad (2.3)$$

Thus, the lower the pK_a value, the stronger the acid, or alternatively, the more the equilibrium will lie on the dissociated product side.

For the excited state, Förster realized that the observed increase in acidity in aromatic alcohols and protonated aromatic amines can be estimated by way of a thermodynamic cycle determined from the fluorescence and absorbance spectra, now called Förster cycle [4]. Indeed, if one looks at a schematic representation of the energy levels for an acid and its conjugate base in both the ground and excited state such as presented in figure 2.1, one clearly sees that there are two pathways for the generation of the excited state photobase.

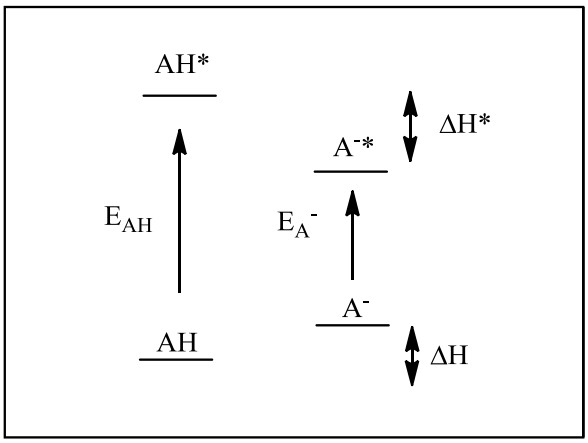

Figure 2.1: Schematic four level representation of the Förster cycle for a photoacid AH and its conjugate base A^-

As both pathways are thermodynamically equivalent this requires that:

$$E_{AH} + \Delta H^* = E_{A^-} + \Delta H \tag{2.4}$$

where E_{AH} and E_{A^-} are the vertical transition energies of the acid and the conjugate base and ΔH is the dissociation enthalpy (which can be either endothermic or exothermic) with the * representing the excited state. Assuming that the entropies of the proton transfer reaction are the same in the ground and excited state then since $E_i = Nhv_i$,

$$\Delta G - \Delta G^* = Nh(v_{AH} - v_{A^-}) \tag{2.5}$$

The Gibbs free energy can be related to the pKa with the following expression:

$$pKa = \frac{\Delta G}{\log(RT)} \tag{2.6}$$

which gives:

$$pKa - pKa^* = \frac{(v_{AH} - v_{A^-})}{2.303k_BT} \tag{2.7}$$

where k_B is the Boltzmann constant and T is the absolute temperature.

It is worth mentioning that v_{AH} and v_{A^-} in equation 2.7 represent the frequencies for the pure electronic transition, ie the 0-0 transition. For most compounds, an accurate determination of these parameters is not straightforward in room temperature solutions. However, when a mirror image relation exists between the absorbance and fluorescence spectra, after correcting for the dispersion of the detecting system, this entails that the band maxima are equally displaced in energy. Averaging the energies of the fluorescence and absorbance transitions therefore provides a good approximation of the 0-0 transition energy.

In this way, it is possible to obtain a good estimate of the strength of a photoacid knowing solely the ground state pK_a and the transition energies of the acid and its conjugate base. As these are all properties which are generally well known, the Förster cycle is an easily applicable and convenient tool. In aromatic alcohols, the change in pK_a is from 5 for weaker photoacids like phenol to 12 pK_a units for stronger photoacids like cyano-naphthols [64, 65]. The structure, pK_a and pK_a* of some common photoacids are presented in table 2.1.

Table 2.1: Chemical structures, pK_a and pK_a* of some common photoacids.

Photoacid	Structure	pK_a	pK_a*	ΔpK_a
phenol	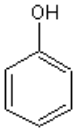	9.82	4	5.82
1-naphthol	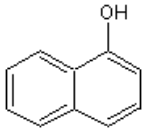	9.4	-0.2	9.6
2-naphthol	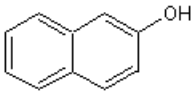	9.6	2.8	6.8
5-cyano-1-naphthol	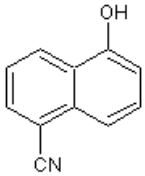	8.5	-2.8	11.3
5-cyano-2-naphthol	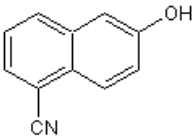	8.75	-0.3	9.05
2-napthol-6,8-disulfonate	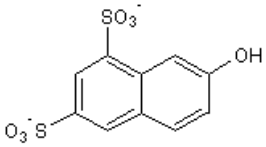	8.99	0.7	8.29
1-Hydroxypyrene	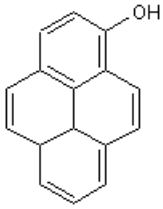	8.7	3.6	5.1
HPTS (8-hydroxypyrene-1,3,6-trisulfonate)	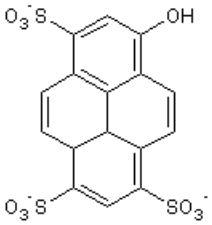	8.0	1.4	6.6
HPTA (8-hydroxypyrene-N,N,N',N',N'',N''-hexamethylpyrene-1,3,6-trisulfonamide)	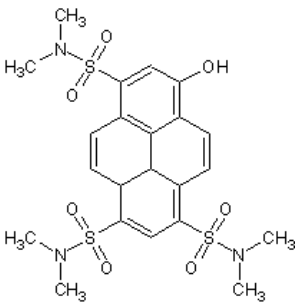	5.6	-0.8	6.4

2.1.1 Molecular mechanism behind photoacidity

Hydroxyarenes, the homologous family containing a hydroxyl group directly bound to an aromatic ring, can be considered the enol form of their respective cyclodiones. This is shown for phenol as the simplest hydroxyarene in figure 2.2.

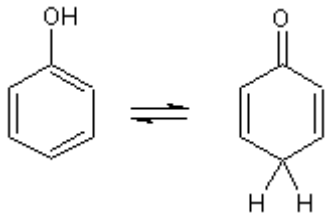

Figure 2.2: Keto-enol tautomerization of phenol.

While the tautomeric keto-enol equilibrium lies far to the ketone side in the case of aliphatic ketones, for hydroxyarenes it is shifted almost completely to the enol side by the high resonance stabilization of the *ortho*- and *para*-quinoid resonance structures as shown in figure 2.3.

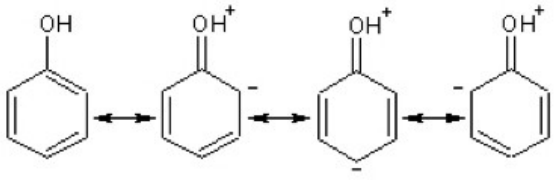

Figure 2.3: Resonance structures of phenol.

The explanation for photoacidity proposed by Weller [5] is that the excited state is characterized by a greater electronic redistribution from the non-bonding electrons of the oxygen into the π system of the aromatic ring effectively weakening the O-H bond and ultimately leading to proton transfer to either an accepting base or water. However, while it is universally conceded that electron density is transferred from the oxygen to the aromatic ring at some point in the ESPT reaction, renewed debate concerning when the charge transfer process occurs relative to the proton transfer reaction has arisen. Indeed, while for ground state acidity the importance of the stabilization of the conjugate base has long been acknowledged, this aspect has typically been neglected in descriptions of excited-state acidity

which have predominantly focused on the properties of the acid. This matter was first raised by Schulman [31], but it did not receive much attention until it was highlighted again by Hynes [29, 66] and later Agmon [67]. This re-evaluation was prompted by their theoretical calculations where very little electronic redistribution was found to occur in the excited acid molecule compared to the significant changes occurring in the excited base. They further support their findings by the thermodynamical consideration whereby lowering the S_1 state of the acid should make dissociation to the S_1 state of the base more uphill, thereby leading instead to a net *decrease* in photoacidity.

As an equilibrium property, an increase in acidity can be achieved either by making the acid more acidic or alternatively by making its conjugate base less basic. Since this last effectively reduces the energy separation between the acid and the base, it has led some to postulate that, contrarily to what was first proposed by Weller, photoacidity is instead driven by changes occurring in the conjugate base. While this re-evaluation of the commonly held description of photoacidity was apposite, and in many ways brings the excited-state description closer to that of the ground-state, in order to justify a product-side driven reaction, one must show that both the internal and solvation energies of the excited photobase are larger than in the ground state and are consequently driving the proton transfer reaction. Furthermore, an important consideration is the fact that these calculations were performed for gas-phase photoacids. It has recently been shown that the operating mechanism for some gas-phase photoacid:base clusters such as phenol:ammonia, is actually hydrogen transfer due to a level crossing between the initially excited $^1\pi\pi^*$ state and a higher excited singlet $^1\pi\sigma^*$ Rydberg state which is dissociative along the OH coordinate [68, 69, 70, 71]. The non-adiabatic hydrogen transfer from the hydroxyl group to the ammonia cluster results in a concerted electron and proton transfer mechanism instead of the initially postulated ESPT. This marked different behavior in the gas-phase clearly highlights the important role of the solvent in the ESPT mechanism. This is further exemplified by what has been termed the “anomalous solvent effect” [72]. Indeed, ESPT occurs predominantly in water, only for very strong photoacids like cyanonaphthols is the reaction possible in solvents like alcohols or DMSO. The anomaly is then that these last solvents are actually more basic than water.

It is possible that solvation driven changes in the photoacids can explain why, while gas-phase calculations do not reveal any charge distribution, several experimental results point to the fact that the acid is indeed undergoing significant changes upon excitation in solution. Notably, it has been found that proton dissociation rates become much faster while proton

recombination rates only decrease slightly. In the case of HPTS for example, proton dissociation rates to water rise from about $10^5 s^{-1}$ in the ground state to $10^{10} s^{-1}$ in the excited-state representing an increase of five orders of magnitude. In the meantime, the proton recombination rates only decrease by about two orders of magnitude from $3x10^9 s^{-1}$ to $10^{12} s^{-1}$ in the excited-state [37]. Furthermore, solvatochromic studies invariably find that the hydrogen bond donating capabilities of the photoacid become stronger in the excited-state. This finding has been substantiated by measurements on gas-phase clusters of 1N and 2N with water and ammonia, where the OH stretch frequency was found to be red-shifted by about 100-250cm^{-1} compared to the ground-state complex frequency [73, 74, 75, 76]. On the other hand, the solvatochromic studies also reveal that the base is a less effective hydrogen-bond acceptor in the excited-state compared to its ground-state. This is schematized in figure 2.4 where the two types of hydrogen bonds of photoacids with the solvent are shown: hydrogen bonds donated from the photoacid to the solvent (α) and hydrogen bonds accepted by the photoacid (β). One could thus very well imagine that changes in *both* the photoacid and its conjugate base are important in explaining the substantial increase in acidity. However, the nature of the molecular mechanism is as of yet unclear: what is the role of the solvent, which side is providing the driving force and does this hold for all hydroxyarene photoacids?

It must be noted that while protonated aromatic amines are also very good photoacids with the NH_3^+ group acting as proton donor and the neutral NH_2 the conjugate base, the ESPT reaction is characterized by a constant-charge dissociation making this mechanism less sensitive to solvent polarity. This is in marked contrast to ESPT from hydroxyarenes where an ion pair is generated from a neutral molecule. Also, as a positively charged species, it is expected that no electronic charge redistribution is occurring in the acid as the lone electron pair on the nitrogen is no longer available. Most changes are therefore understood to occur in the conjugate photobase. Given the very different behavior of these two classes of photoacids, this thesis focuses solely on the case of hydroxyarene photoacids.

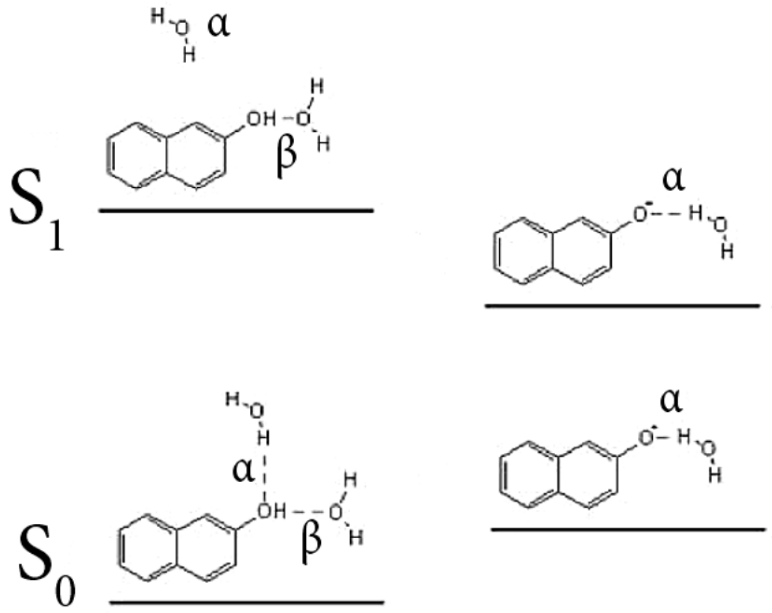

Figure 2.4: Schematic representation of the HB interactions derived from solvatochromic studies of the acid and its conjugate base in both the ground and excited state.

2.2 Electronic spectroscopy of naphthalene, 1- and 2-naphthol

Prior to delving into the electronic spectroscopy of 1-naphthol (1N) and 2-naphthol (2N), it is instructive to consider that of the parent molecule, naphthalene (N). As determined by Platt [77, 78], the two lowest electronic transitions are designated ^1L_b ($^1B_{1u}\leftarrow{}^1A_{1g}$) and ^1L_a ($^1B_{2u}\leftarrow{}^1A_{1g}$) and have dipole moments polarized perpendicular to each other (figure 2.1a). The ^1L_a transition at around 35000cm^{-1} (285nm) has a dipole moment oriented through the short-axis along the central C-C bond connecting the two aromatic rings, and the ^1L_b transition at around 32000cm^{-1} (312.5nm) has a dipole moment along the through-bond axis (figure 2.1) [79, 80, 81]. While the $^1L_a\leftarrow S_0$ transition has substantial oscillator strength, the $^1L_b\leftarrow S_0$ transition is formally forbidden but obtains some oscillator strength through vibronic coupling with the ^1L_a state via b_{1g} modes [82]. Upon substitution with a hydroxyl group in either the 1- or 2- position to give 1N and 2N respectively, the D_{2h} symmetry of naphthalene is broken. This mixes the two electronic states with a concomitant change in relative energy spacing and in relative magnitudes of transition dipole moments. Furthermore, the hydroxyl group is a well-known auxochrome, that is, an auxiliary group which interacts with the chromophore

through the delocalization of its lone pair of electrons thereby extending the conjugation resulting in a bathochromic (red) shift of the electronic spectra [83].

The absorbance spectra for N, 1N and 2N in n-hexane are given in figure 2.5b. It is immediately apparent that the position of the hydroxyl group on the aromatic ring leads to very different couplings between the two electronic states of naphthalene. This can easily be rationalized given the direction of the two transition dipole moments: it is expected that the ring polarization resulting from substituents in positions 1, 4, 5 and 8 (marked in blue in figure 2.5a) will have a large effect on the ^1L_a transition which is parallel to the direction of charge transfer from the hydroxyl group and, concomitantly, little effect on the ^1L_b transition. On the other hand, substituents in positions 2, 3, 6 and 7 (marked in red) will result in a polarization with vectorial components pertaining to both ^1L_a and ^1L_b thereby likely resulting in further mixing of the two states [84, 85]. Furthermore, the greater oscillator strength of the ^1L_a transition is expected to introduce significant short-axis polarization in the ^1L_b transition.

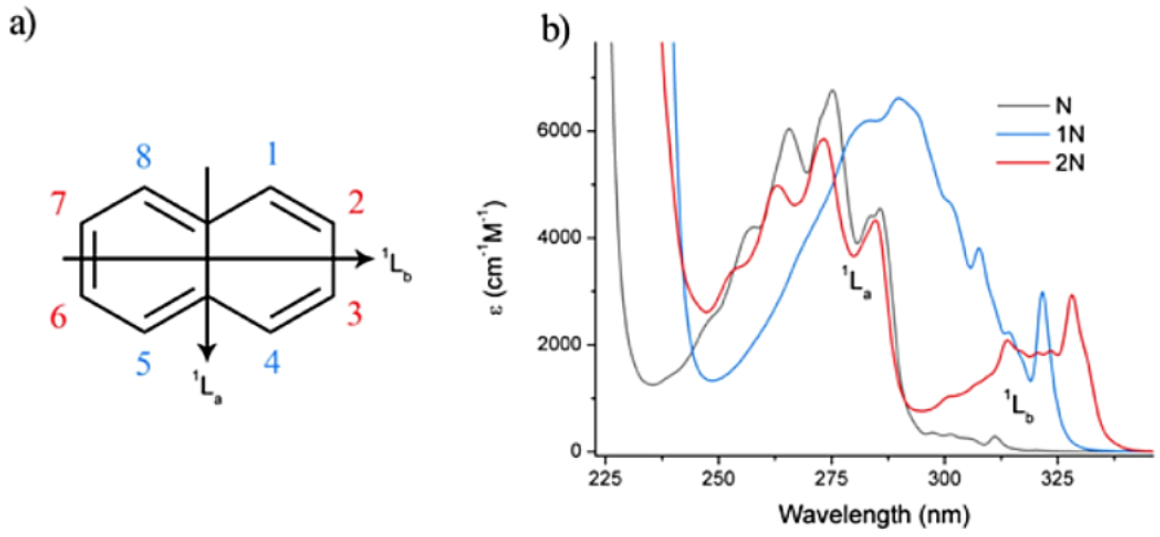

Figure 2.5: a) Structure of the naphthalene molecule with the direction of the first two transition dipole moments: ^1L_a and ^1L_b. The carbon atom numbering is shown with the numbers in blue corresponding to positions where the ^1L_a band is expected to be affected by substituents and the numbers in red corresponding to positions where effects on both the ^1L_a and ^1L_b are awaited. b) Absorbance spectra of N, 1N and 2N in n-hexane.

This simple model correctly predicts the general effects of substitutions: the ^1L_a band of 1N is substantially red-shifted leading to overlap with the ^1L_b band which shows only a small red-shift, whereas for 2N, the energy splitting between the two bands is increased by the small blue-shift of the ^1L_a band and the significant red-shift of the ^1L_b band. Numerical studies reported in the literature based on calculations at various levels of theory all confirm that that

the ^1L_a and ^1L_b state are more heavily mixed in 2N than in the parent N molecule and in 1N [86, 87, 88, 89, 90, 91, 92, 93, 94]. Furthermore, magnetic circular dichroism [95, 96], polarization [97] and the rotational contour analysis of the electronic-origin of high resolution molecular vapour absorption spectra [98, 99, 100] found that in 2N the ^1L_b transition is rotated close to the short axis of the molecule making it almost parallel with the ^1L_a transition which is marginally affected. In comparison, 1-substitution was found to have little effect on the transition dipole moment vector and therefore the direction of polarization compared to the parent N molecule. Quantification of these effects was provided by time-dependent density functional theory (TD-DFT) quantum calculations at the B3LYP/TZVP level (Becke, three-parameter, Lee-Yang-Parr/triple zeta valence plus polarization) on the ground and excited states of 1N and 2N. The resulting oscillator strengths and direction of the transition dipole moments are collated in table 2.2 where one must distinguish between two possible rotamers which differ by the orientation of the O-H bond vector relative to the aromatic ring, labelled *cis* and *trans* [101, 102].

Table 2.2: Transition dipole moments of 1N and 2N represented by blue arrows, and their respective oscillator strength *f,* calculated by TD-DFT at the B3LYP/TZVP level.

	$S_0 \rightarrow {}^1L_a$	$S_0 \rightarrow {}^1L_b$
***cis*-1N**	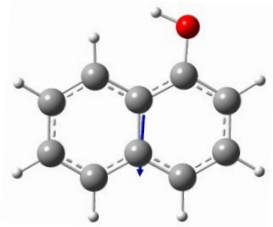 f=0.0666	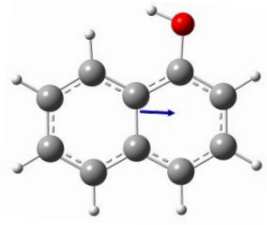 f=0.0236
***trans*-1N**	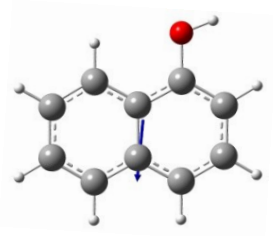 f=0.0738	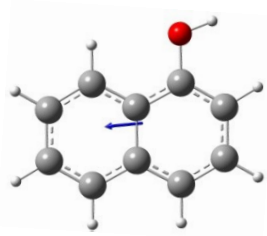 f=0.0271
***cis*-2N**	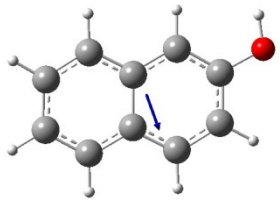 f=0.0520	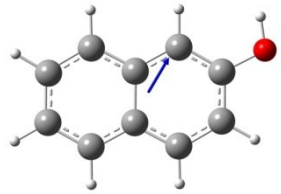 f=0.0150
***trans*-2N**	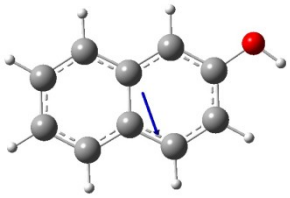 f=0.0644	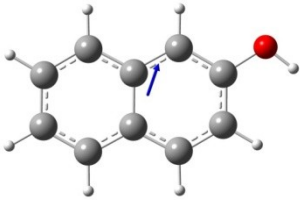 f=0.0099

As discussed, both the ${}^1L_b \leftarrow S_0$ and ${}^1L_a \leftarrow S_0$ transition dipole moments of *cis*- and *trans*-1N are polarized in a manner very close to the parent N molecule whereas for 2N the ${}^1L_b$ transition has been rotated by about 70° and lies close to the short axis of the naphthalene ring (table 2.3). Also, while the ${}^1L_b$ transition has gained in oscillator strength at the expense of the ${}^1L_a$ transition, this last remains the transition with the largest oscillator strength for both 1N and 2N.

Table 2.3: Calculated angles (absolute values, with a range of 0-90°) of transition dipole (TDM) and electrical dipole (EDM) moments relative to the x-axis (along the long axis).

	Calcd angle of TDM (°)	Exptl angle of TDM (°) [a]	Calcd angle of EDM (°)		Exptl angle of EDM (°) [b]	
			S_0	^1L_b	S_0	^1L_b
***cis*-1N**	11	6	9	32		
***trans*-1N**	18	33	7	3		
***cis*-2N**	49	66	75	83	70	82
***trans*-2N**	61	74	70	59		

[a] from reference [103]

[b] from reference [104]

2.2.1 Solvent effects on the absorbance and emission spectra

The effect of specific hydrogen bonding interactions on the electronic absorption spectra of 1N and 2N was first investigated by Baba and Suzuki [105] and Nagakura and Gouterman [106]. By measuring spectra in a non-polar alcane solvent, to which an increasing amount of a HB accepting molecule was added, they were able to isolate the HB contribution from general solvation effects. Hydrogen bonding was found to bring about noticeable changes in both the frequencies and intensities of the transitions, while, apart from some broadening, the shape of the electronic band is mostly preserved. This last is attributed to the fact that all the vibrational components of a given transition are shifted uniformly and thus additionally allows for the identification of spectrally overlapping transitions. Their methodology was applied here to 1N in n-hexane to which dimethylsulfoxide (DMSO) or hexaisofluoropropanol (HFIP) were added (figure 2.6). This last is a good HB donor molecule but very poor acceptor due to the effect of the electron withdrawing fluorines. In contrast, the lone pair on the oxygen of DMSO makes it a very good HB acceptor.

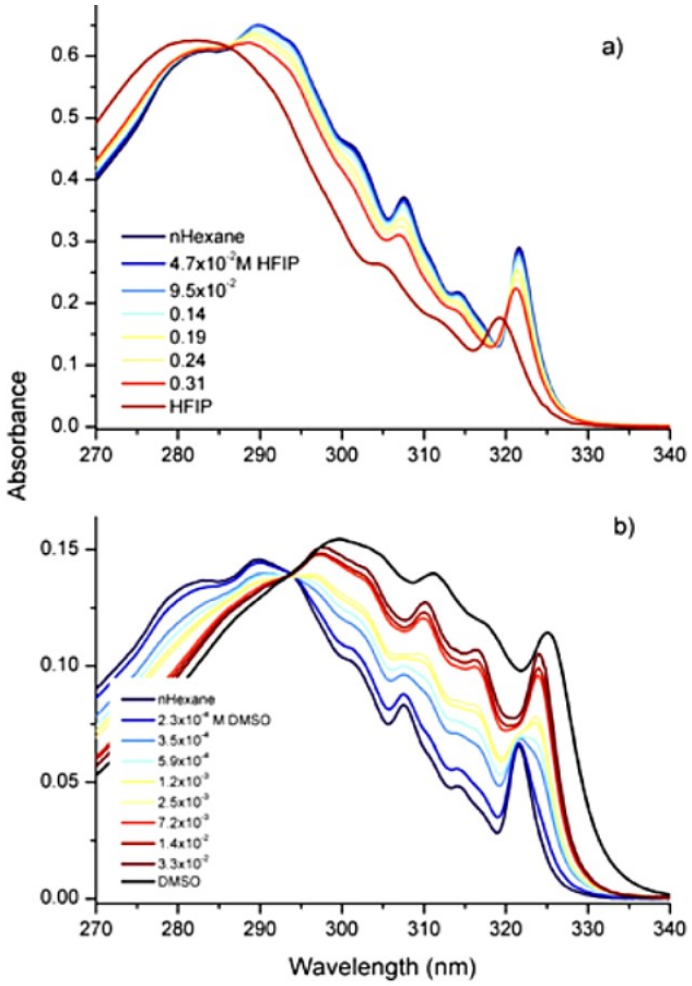

Figure 2.6: a) Absorbance spectra of $1.5x10^{-4}$M 1N in n-hexane with increasing concentration of HFIP and b) absorbance spectra of $3.5x10^{-5}$M 1N in n-hexane with an increasing concentration of DMSO.

It is immediately apparent that HB donation to the naphthols leads to a blue-shift which can readily be understood by the diminution of the oxygen's capacity to delocalize electronic density to the aromatic ring. In contrast, HB donation to the solvent leads to a frequency red-shift.

Confirmation that the effects observed in the absorption spectra are indeed due to complexation through a HB is obtained by measuring the electronic absorption spectra and IR spectra under the same conditions. This is shown in figure 2.7 for 2N in dichloromethane (DCM) to which an increasing concentration of DMSO is added. The disappearance of the free OH stretch in the IR spectra and rise of the hydrogen-bonded OH vibration (the IR spectra of naphthols is discussed in more detail in section 2.3) is found to be correlated with the red-shift of the electronic spectra.

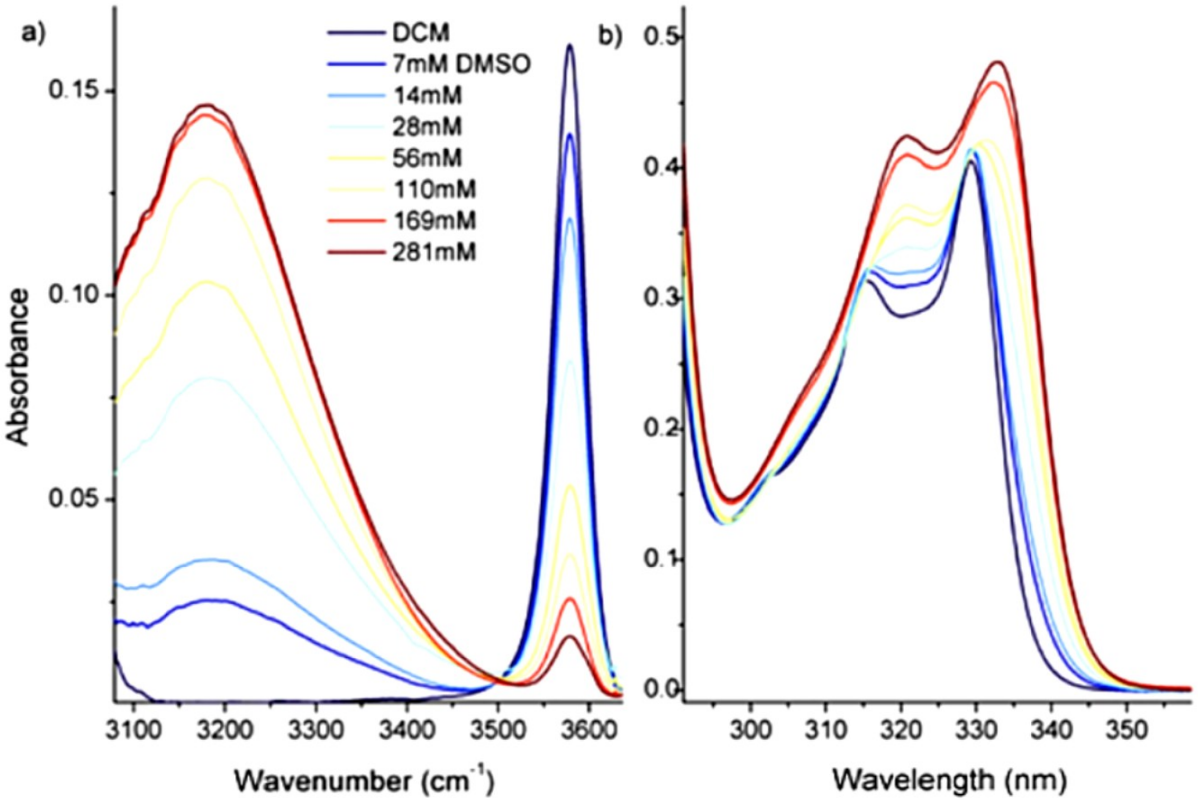

Figure 2.7: a) IR spectra and b) electronic absorbance spectra of 20mM 2N in DCM with increasing concentration of DMSO.

The formation constant of the hydrogen-bonded complex, K_f is given by:

$$K_f = \frac{C}{A \quad B_0 - C} \tag{2.8}$$

$$= \frac{A_0 - A}{A \quad B_0 - A_0 + A} \tag{2.9}$$

where C is the concentration of the HB complex, A_0 is the initial concentration of the proton donor (2N), A is the equilibrium concentration of the free donor and B_0 is the initial concentration of the proton acceptor (DMSO). For both IR and electronic spectra one finds a formation constant of 165±5M^{-1} which is similar to the values of 209.7M^{-1} [107] and 183M^{-1} [108] found for complexes of phenol with DMSO in carbon tertrachloride. The higher polarity of dichloromethane compared to carbon tetrachloride explains the lower formation constant obtained in this study.

A parallel between the effect of hydroxyl substitution on the parent N molecule and the effect of hydrogen bonding was drawn by Baba and Suzuki, as bands which showed the largest red-shifts upon substitution with the hydroxyl group also show the largest red-shifts upon formation of a HB with an acceptor molecule [105].

Disambiguation between the overlapping ^1L_a and ^1L_b transitions in 1N is further confirmed by the marked differences in shifts produced by hydrogen bond interactions: the bands at 31094, 31827 and 32510cm^{-1} attributed to the ^1L_b transition show shifts of only 230cm^{-1} upon complexation with DMSO compared to 1175cm^{-1} for the ^1L_a band. This is also in agreement with the magnetic circular dichroic measurement of 1N (figure 2.8).

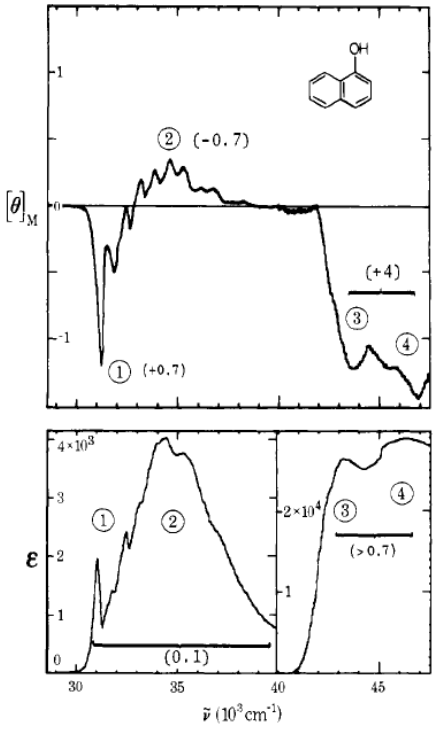

Figure 2.8: Magnetic circular dichroic measurement of 1N from reference [95].

Ternary systems such as those described here are of use in isolating and characterizing the effect of different solvent contributions, however, other methods are required in order to quantify their relative magnitudes. Indeed, while it was seen that the HB accepting capabilities of DMSO gave rise to larger shifts than the HB donating capabilities of HFIP, this is also a reflection on the respective HB strengths of the solvents and not solely a property of the solute in question. A systematic characterization allowing for the simultaneous quantification of the various solvation effects on the optical transition frequencies of a

chromophore is afforded by solvatochromic studies such as described by Kamlet and Taft [109, 110, 111].

2.2.1.1 Kamlet-Taft analysis

The Kamlet-Taft (KT) empirical solvent scale uses a multiparameter fit in order to correlate solvent induced properties of a chromophore:

$$P_{s\text{-}s}=P_{s\text{-}s}^{0}+s\pi^{*}+a\alpha+b\beta \qquad (2.10)$$

where $P_{s\text{-}s}$ is the measured solvent-induced property of the solute such as the frequency position in an absorption, emission or IR spectra; $P_{s\text{-}s}^{0}$ is the value of the chosen property in the reference cyclohexane solvent; π^{*} is the normalized solvent polarity scale; α is a measure of the solvent's hydrogen bonding donating capabilities otherwise known as the solvent acidity scale; and finally, β is the solvent basicity scale, ie, a measure of its HB accepting capabilities. These parameters are assumed to be independent of each other and additive. The initial table of these parameters derived by Kamlet and Taft can be found in reference [111] with an updated list for various solvents in reference [112]. The resulting a, b and s values are characteristic of a particular solute with their sign and magnitude allowing for the quantification of the effect of the various solvent characteristics.

2.2.2 Absorbance and emission spectra of 2-naphthol

Changes in electron density may be probed by comparison of the solvatochromic shifts experienced in absorption and emission. According to the model established by Pimentel, for any proton containing molecule and its conjugate base, the excited state is a stronger acid than the ground state if the absorbance or emission spectrum of the conjugate base is characterized by a bathochromic shift relative to that of the acid [113].

The KT analysis found in the literature for the absorption and emission spectra of several photoacids have been collected in table 2.4. In accordance with the results found in the previous section where HB donation from the solvent was found to lead to blue-shifts while HB accepting solvents were instead found to produce red-shifts in the electronic absorption spectra, one finds a positive value of 270cm^{-1} for a and a negative b value of 510cm^{-1}. General non-specific solvation leads to a further red-shift which is of much smaller magnitude than specific interactions: the p value of 70cm^{-1} is only one seventh of specific HB donating

effects. Thus the main effect of the solvent on the absorption spectra is due to specific interactions, primarily through HB donation to the solvent.

Comparison of the a, b and p values for the emission spectra with those found for the absorption spectra (table 2.4) reveals an increase in the sensitivity of 2N to the solvent polarity commensurate with a higher excited state dipole moment (p parameter). The 1.6 times increase in b denotes a much stronger donation of the hydrogen bond to the solvent which is in line with the traditional view of photoacidity, whereby electronic density at the oxygen is transferred to the aromatic ring. This also serves to explain the negligible dependence on the HB donating properties of the solvent in the excited-state as the lone pair on the oxygen is no longer as available to accept such a HB.

The behavior observed in 2N where the dependence on π* and β increases in the excited-state, while the dependence on α is significantly reduced seems to be a generalized behavior for photoacids. This has led to the stipulation that while ground state photoacids accept hydrogen bonds from solvents such as water or alcohols, these bonds are broken upon electronic excitation due to a decrease in the charge density on the oxygen atom. The dependence on α in the emission spectra of 8-hydroxypyrene-1,3,6-trisulfonate (HPTS) has been explained by hydrogen bonds being donated to the three sulfonate groups established by comparison with the behavior of pyrenetrisulfonate [114].

Table 2.4: KT coefficients in wavenumbers for various photoacids in both the ground and excited-states. 2Nate: 2-naphtholate; 5CN2N: 5-cyano-2-naphthol; HPTS: 8-hydroxypyrene-1,3,6-trisulfonate.

photoacid		**S_0**			**S_1**		**reference**
	p	b	a	p	b	a	
2N	-70	-510	270	-450	-800	0	[115]
				-475	-657	0	[116]
2Nate		0	3100		0	1770	[117]
5CN2N	-150	-650	170	-1600	-1950	0	[118]
5CN2N anion				0	0	940	[119]
HPTS	-380	-290	-270	-1300	-1820	-1890	[66]

The absorption and fluorescence spectra of 2-naphtholate (2Nate) in water is shown in figure 2.9. Concomitant with the formal negative charge available in 2Nate, the absorption bands are further red-shifted and broadened: the ^1L_a by 1100cm^{-1} and the ^1L_b by 2135cm^{-1}. The dependence on the HB accepting capabilities of the solvent is evidently absent, while the dependence on its HB donating capabilities is twelve times higher than for the acid.

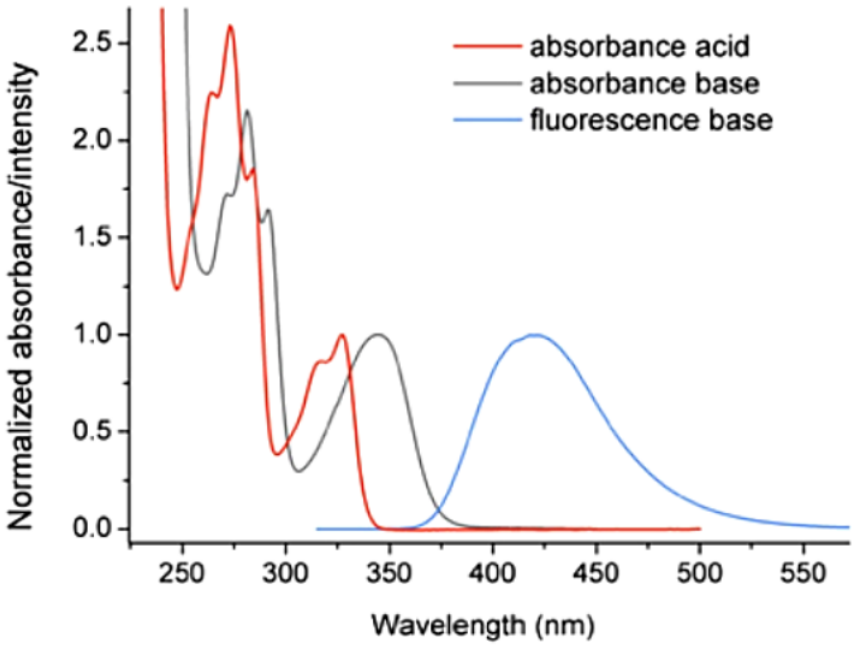

Figure 2.9: Absorption and fluorescence spectra of 2Nate in water.

Comparison of the Kamlet-Taft analysis for the absorbance and fluorescence spectra of 2Nate in table 2.3 reveals that the dependence on the α parameter *decreases* upon excitation. This corresponds to a situation where the effective charge on the oxygen in partially depleted compared to the ground-state by an increase in electronic redistribution to the aromatic ring.

The main trends obtained by this solvatochromic analysis are that: the ground-state acid takes part in two types of HBs with the solvent, one donated to the hydroxyl oxygen and another given to the solvent. Upon excitation, the HB from the solvent is broken while the one donated to the solvent is strengthened. On the other hand, the HB the conjugate base accepts from the solvent is weakened upon electronic excitation (this is schematized in figure 2.4).

2.2.3 Absorbance and emission spectra of 1-naphthol: excited state level crossing

For 2N and 2Nate, intramolecular charge transfer from the oxygen leads to a greater red-shift of the ^1L_b transition compared to the ^1L_a transition. As this effectively results in an increased energy separation between the two, the transition with the lowest energy in both the acid and the anion remains the ^1L_b under all conditions. In contrast, for 1N and 1Nate, it is the ^1L_a transition which experiences the greatest red-shift with increasing intramolecular charge redistribution from the hydroxyl or the anion. Thus the two lowest transitions find themselves increasingly closer in energy. For the acid, the red-edge of the absorption still arises from the ^1L_b transition as assigned by comparison with the naphthalene spectrum, magnetic circular dichroism and polarization studies (see section 2.2). However, the fluorescence spectra in various solvents show a significant solvent dependent Stokes shift (figure 2.10). This has been attributed to excited-state level crossing whereby the more charge-transferred ^1L_a state is better stabilized by polar solvents leading to a reversal of the relative energy of the ^1L_a and ^1L_b states. Thus, emission of 1N in sufficiently polar solvents arises from the ^1L_a state and not the initially excited ^1L_b state. This level crossing is similar to what has been reported for other aromatic compounds such as substituted benzenes [120, 121, 122] or tryptophan/indole [123].

The level crossing hypothesis in 1N is supported by temperature dependent emission studies where, upon lowering the temperature and thus inhibiting solvent relaxation, the broad fluorescence seen at room temperature becomes structured and significantly blue-shifted [30, 32, 33] attributed to ^1L_b emission as confirmed by the polarization spectra [34]. In addition, Knochenmuss and co-workers have found evidence of strong vibrational mixing of the ^1L_a and ^1L_b states in the absorption and fluorescence spectra of jet-cooled 1N [124, 125, 126, 127, 128]. This electronic state mixing induced by a ring deformation mode at 414cm^{-1} is further evidenced by the rotationally resolved fluorescence excitation spectra taken by Humphrey and Pratt where this mode is shown to possess a transition moment rotated away from the long axis polarization characteristic to ^1L_b bands. Vibrational mixing is then thought to aid in the solute-solvent coupling that leads to $^1L_b/^1L_a$ inversion after ^1L_b excitation [129]. Lastly, a solvatochromic study comparing 1N, 2N and their respective methoxy derivatives, found that while the behavior of 2N and 2-methoxynaphthalene could be well described using the KT analysis, this was not the case for either 1N or 1-methoxnaphthalene. Analysis of their fluorescence spectra with Pekarian functions led to the conclusion that there are two emitting states: ^1L_a and ^1L_b with an increasing population occurring from the ^1L_a state with increasing solvent polarity. The solvents HB donating capability was also found to augment ^1L_a

emission. Good KT fits were obtained by fitting the emission spectra of 1N with the two Pekarian functions instead of one band maxima, where the red-edge Pekarian function was found to depend over two times more on the solvent polarity factor π*, three times more on the HB accepting capabilities of the solvent and ten times more on its HB donating capabilities [35].

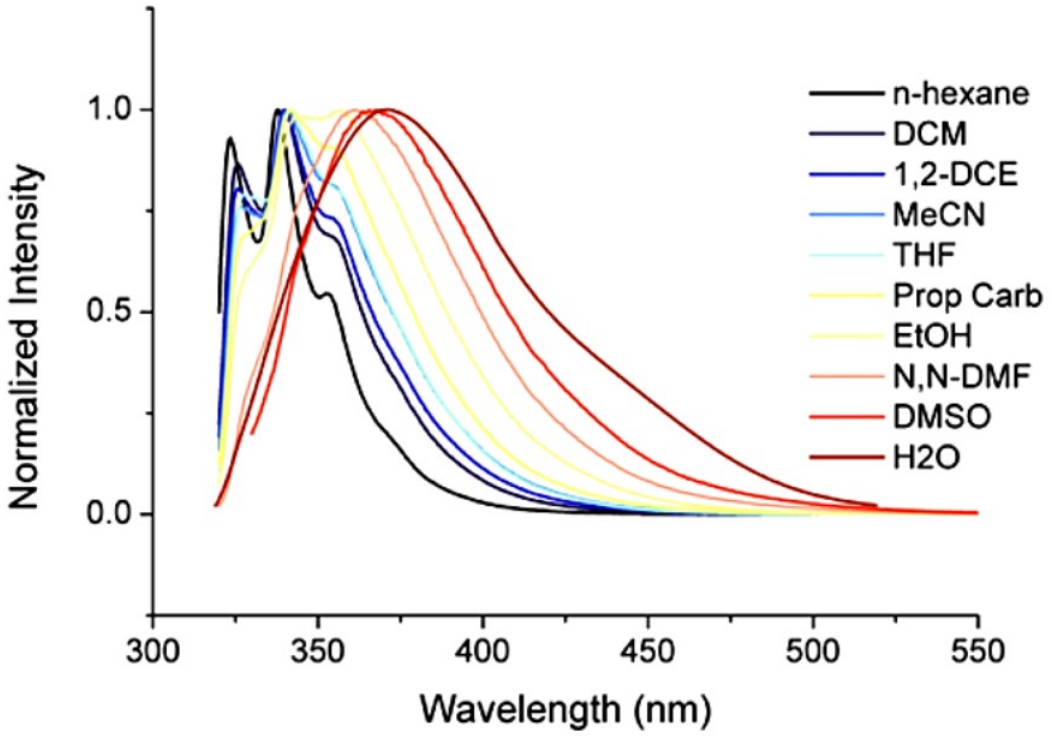

Figure 2.10: Fluorescence spectra of 1N in various solvents: 1,2-DCE: 1,2-dichloroethane, MeCN: acetonitrile, THF: tetrahydrofuran, Prop Carb: propylene carbonate, EtOH: ethanol, and N, N-DMF: N, N-dimethylformamide. The spectrum in water was obtained at pH 2 after subtraction of the anion emission.

2.3 Infrared spectroscopy of 1- and 2-naphthol

Absorption bands due to molecular vibrations are found in the mid-infrared (MIR) spectral region which spans from 4000-200cm^{-1} or alternatively, 2.5-50 μm [130]. One usually distinguishes between the fingerprint region and group frequencies. The first characterizes the region found below 1600cm^{-1} comprised of a multitude of bands due to various stretch, deformation, bending, combination, breathing etc vibrations. The high number of modes located in this region, as well as the complicated coupling between them, usually makes it arduous to assign specific vibrations. However, the correlated advantage is that the resulting

band pattern is highly specific and can thus be used for identification purposes. For example, the characterization of the mode pattern particular to the photoacid and the photobase has enabled the dynamics of proton transfer reactions to be followed by infrared (IR) spectroscopy [12, 131, 132]. In contrast, group frequencies characteristic of a given functional group are found in highly specific regions. Mainly, one distinguishes stretch vibrations such as that of the carbonyl, cyano, C-H, N-H, or O-H groups. These vibrations are to a large extent local vibrations making them both easy to identify, and highly characteristic.

The IR spectra of N, 1N and 2N in c-hexane-d_{12} are given in figure 2.8. Absent in N, but present in 1N and 2N is the free O-H stretch located at 3608cm^{-1} for 1N and 3614cm^{-1} for 2N. The C-H vibrations are found around 3050cm^{-1}. As is usual for aromatic C-H stretches, they are relatively weak vibrations given both their low molecular extinction coefficient and the smaller C-H to carbon ratio compared to aliphatic systems. In N, the C-H stretch bands are quite sharp due to the lack of rotational isomerism or coupling to other modes, while in 1N and 2N they are noticeably broadened.

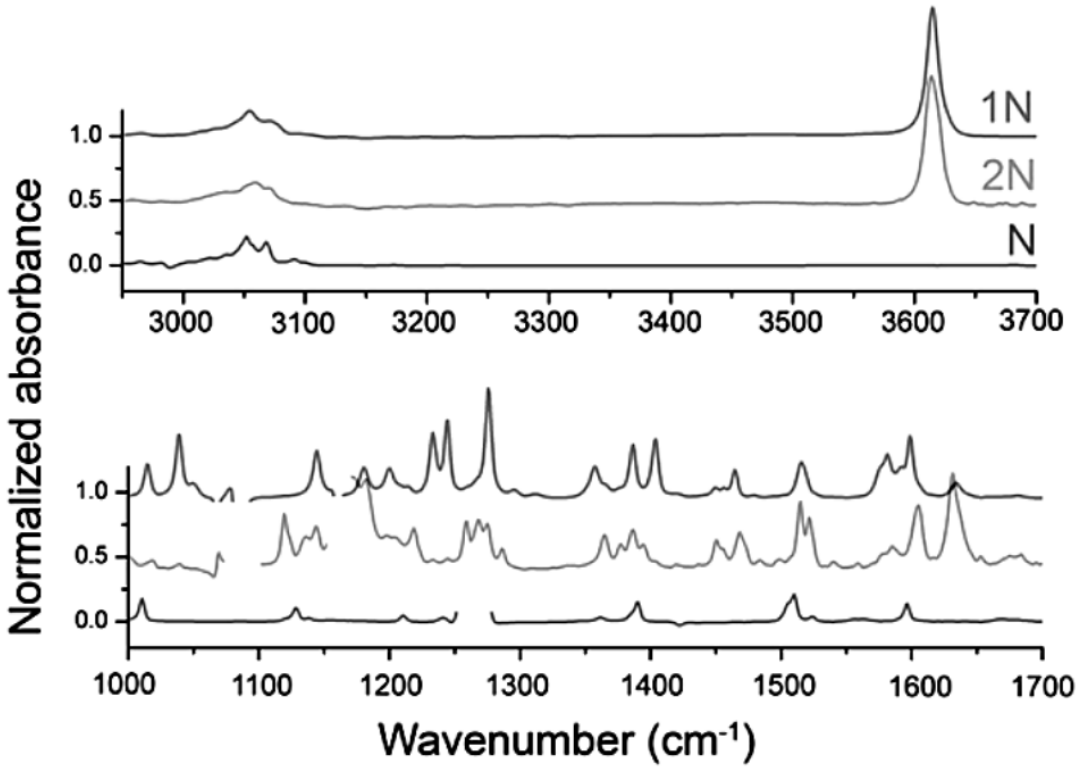

Figure 2.11: a) 2950-3700cm^{-1} and b)1000-1700cm^{-1} region of the IR spectra of N, 1N and 2N in c-hexane-d_{12}. The spectra have been normalized to the OH stretch vibration and displaced by 0.5OD for better visualization.

As expected from their marked electronic differences, substitution at the 1- or 2- position evidently gives rise to significantly different mode patterns in the fingerprint region. For N, 1N and 2N, this region contains several bands characteristic of the aromatic moiety such as the ring C-C stretch bands around 1600-1500cm^{-1} [133]. In addition, for 1N and 2N the C-O-H bend vibration should occur around 1410-1310cm^{-1} and the out-of-phase C-C-O stretch from 1260-1180cm^{-1}. In the well characterized phenol molecule, solvent and isotope effects have enabled the assignation of the band at 1368.3cm^{-1} to the C-O-H bend and the band at 1274.9cm^{-1} to the C-C-O stretch [134]. This is supported by various computational calculations which find that the band assigned to the C-O-H bend has a potential energy distribution containing 18% bend character, the remainder being due to various aromatic in-plane bend modes. Meanwhile, the band assigned to the C-C-O stretch is found to contain 52% from this vibration and 12% from a ring deformation mode [135, 136]. Solvent effects on the spectra of 1N have enabled the identification of its C-O-H bend at 1358cm^{-1} and the C-C-O stretch at 1276cm^{-1}. Quantum chemical calculations using DFT confirm this assignment Comparison of the experimental and calculated IR spectra of 1N in c-hexane is given in table 2.5 showing the very good reproduction of the experimental results obtained by the calculation. The better correspondence with the calculated *trans*-1N spectra reflects the higher relative population of the rotamer [137].

Table 2.5: Comparison between the calculated and measured IR spectra of 1N in c-hexane-d_{12}. The calculated spectrum was scaled by a factor of 0.97 determined from the best correspondence with the experimental frequencies. The (s) indicates a shoulder.

Experimental (cm^{-1})	**Trans 1N (cm^{-1})**	**Cis 1N (cm^{-1})**
1014.8	1016	1017.5
1038.6	1035.4	
1049.1 (s)		
		1062.1
1078.0	1075.5	1077.7
1144.5	1139.8	1143.6
	1157.3	1157.3
1180.2		1172.8

1200	1201.9	1200
1233.2	1233.9	1231
1244.8	1248.5	
1275.6	1275.7	1262&1285
1357.6		
1386.6	1396.1	1384.4
1403.9	1403.9	1396.1
1421.4	1429.1	1433
1450.2	1452.4	1448.5
1464.7	1460.2	1460.2
1515.8	1520.4	1516.5
1581.3	1576.8	1574.7
1591.9	1590.3	1594.1
1598.7		
1634.4	1634.9	1634.9

In the case of 2N, it was not possible to identify these two vibrations involving the C-O bond through solvent effects. Quantum calculations also find this normal mode to be heavily mixed with other vibrations.

2.3.1 Solvent effects on the IR spectra of 1- and 2-naphthol

2.3.1.1 General solvent effects

The solvent effect on the spectra may be classified in two categories: general solvation arising from classical van der Waals interactions such as orientational, induction, or dispersion interactions or specific interactions characterized by their directionality such as complex formation or hydrogen bonding. Inasmuch as general solvation effects are always present, distinguishing their contribution from that of specific effects is necessary. The collective

effect of the solvent molecules has been described by macroscopic characteristics of the solvent such as the dielectric constant or the refractive index. The first model along these lines is attributed to Kirkwood [138] who used Onsager's concept of the reactive field exerted on a molecule by the surrounding solvent molecules [139] to relate the band shift of the solute, approximated by a point dipole at the center of a spherical cavity, to the dielectric constant of the medium. Bauer and Magat expanded this theory by taking into account the anharmonicity of the oscillations [140]. This was found to be essential as the anharmonicity introduces a supplementary contribution to the frequency shift: changes in the equilibrium geometry of the solute in solution translate to changes in the curvature of the potential given the anharmonicity of the vibration. The resulting Kirkwood-Bauer-Magat formula is:

$$\frac{\Delta v}{v} = \frac{v - v_0}{v_0} = -C\frac{\varepsilon - 1}{2\varepsilon + 1} \tag{2.11}$$

where C is a constant that depends solely on the properties of the solute, ε is the dielectric constant of the solvent, v_0 is the gas-phase frequency of the oscillator and v is the frequency in solution. However, this expression had only a limited success and furthermore, cannot be applied to vibrations where $v > v_o$ which is often the case of deformation modes.

Buckingham used a quantum-mechanical model to treat the influence of the solvent on a dielectric solute molecule [141, 142, 143]. The gas-phase Hamiltonian is given by:

$$H = H_0 + H_1 \tag{2.12}$$

where H_0 is the operator for a harmonic oscillator and H_1 is a perturbative correction taking into account the anharmonicity of the vibration. In solution, the interaction energy depends on the configuration of the surrounding solvent molecules. It is thus represented by a power series in the displacement of the nuclei from their equilibrium positions. Averaging over all solvent configurations gives:

$$U = U\ \xi\ = U_0 + U'\xi + \frac{1}{2}U''\xi^2 + \cdots \tag{2.13}$$

where $\xi = \frac{r - r_0}{r_0}$

The Hamiltonian in solution is thus given by:

$$H = H_0 + H_1 + U \tag{2.14}$$

As the last two terms can be treated as perturbations to the gas-phase harmonic oscillator, applying second-order perturbation theory gives the following equation describing the frequency shift between quantum levels m and n:

$$\frac{\Delta\omega_{m,n}}{\omega_{m,n}} = \frac{B_e}{hc\omega_e^2}\ U'' - 3\frac{A}{\omega_e}U' \tag{2.15}$$

where B_e is the rotational constant, $\frac{A}{\omega_e}$ is the anharmonicity, and U' and U'' are the first and second derivatives of the interaction energy of the solute with the solvent. Interpretation of U' and U'' in terms of molecular properties necessitates the introduction of a model. Applying Onsager's reactive field theory for non-polar solvents gives:

$$\frac{\Delta v}{v} = C_1 + \frac{1}{2}C_2\frac{\varepsilon_0 - 1}{2\varepsilon_0 + 1} + \frac{1}{2}C_3\frac{\varepsilon_\infty - 1}{2\varepsilon_\infty + 1} \tag{2.16}$$

While the various C_i constants in the preceeding equation have direct physical meaning in terms of the microscopic properties of the solute and solvent such as the polarizability or the dipole moment, when applying the model to polyatomic molecule, all such meaning is lost [144]. All solvation models incorporate both the static dielectric constant (ε_0) as well as the refractive index ($n^2 = \varepsilon_\infty$) in order to account for the instantaneous and non instantaneous solvent response. The instantaneous solvent response is described by the refractive index and corresponds to the motion of electrons within the solvent molecule. It serves to stabilize both the ground and excited state and explains why the absorption spectrum of most chromophores is at a lower energy in solution compared to the gas phase. In contrast, the non instantaneous response is described by the static dielectric constant (ε_0) which depends on both electronic and molecular motions. The reorientation of the solvent dipoles around the excited state molecule necessitates movement of the entire solvent molecule and is as such time dependent with rates depending on the temperature and the viscosity of the solvent.

Pullin generalized the perturbative approach to polyatomic polarizable molecules. In his treatment, the solvent was considered to lead to the following effects [145, 146, 147]:

1. The distortion effect: the solute experiences a static change in configuration due to the action of the solvent field. This effect depends on the dielectric constant of the solvent and can result in either blue or red-shifts [148].
2. The intensity effect: this is what is commonly referred to as the general red-shift. Upon illumination, the medium is polarized by the dipole moment of the transition. This effect is thus proportional to the intensity of the transition and depends on n^2 [149].
3. The overtone effect: this is a consequence of the anharmonicity of the vibration and is thus generally small, leading to either blue or red-shifts.

Application of both Buckingham and Pullin's theories was long hampered by the fact that several variables needed for a complete analysis are not experimentally accessible. This is currently set to change with the growing advances in computational methods which now enable for an accurate determination of previously inaccessible parameters. Molecular dynamics simulations are also increasingly utilized in order to understand solvation processes [150]. Indeed, by using computer simulations to determine the motion of atoms allowed to interact for a certain period of time, it has been possible to obtain a better insight into the molecular mechanism of solvation. Notably, the importance of the inertial solvation component was first established through molecular dynamics simulations [151].

2.3.1.2 Solvent induced vibrational frequency shifts: Pullin/van der Zwan/Hynes perturbative approach

First, the gas-phase Morse potential of the molecular system $V_i\ Q\ = D_i(1 - e^{-\alpha_i Q})^2$, where D_i is the dissociation energy of the ith electronic state, Q is the vibrational coordinate, $\alpha_i = (V_i''/2D_i)^{1/2}$ and V_i'' is the quadratic force constant, is expanded as a Taylor series:

$$V_i\ Q\ = \frac{1}{2!}V_i''Q^2 + \frac{1}{3!}V_i'''Q^3 + \cdots \tag{2.17}$$

where $V_i''' = -6D_i\alpha_i^2$ is the cubic force constant.

The solvation energy $V_s(Q)$ is then described using the Onsager reaction field approximation:

$$V_s\ Q\ = -\frac{1}{2}\boldsymbol{\mu}_i\ Q\ \boldsymbol{R}(Q) \tag{2.18}$$

$$= V_s^0 + V_s' Q + \frac{1}{2!} V_s'' Q^2 + \cdots \tag{2.19}$$

with $\boldsymbol{\mu}_i\ Q$ the molecular dipole moment. Using a Taylor expansion along the normal coordinate Q, the dipole moment is:

$$\boldsymbol{\mu}_i\ Q\ = \boldsymbol{\mu}_i^0 + \boldsymbol{\mu}_i' Q + \boldsymbol{\mu}_i'' Q^2 + \cdots \tag{2.20}$$

and $\boldsymbol{\mu}_i^0$ is the permanent dipole moment of the solute. The preceding reaction field is given by:

$$\boldsymbol{R}_i\ Q\ = f_0 \boldsymbol{\mu}_i^0 + f_\infty \boldsymbol{\mu}_i' Q + f_\infty \boldsymbol{\mu}_i'' Q^2 + \cdots \tag{2.21}$$

where f_0 and f_∞ are respectively functions of the static (ϵ_0) and optical (ϵ_∞) dielectric constants with:

$$f_0 = \frac{1}{a_i^3}\ \frac{2\varepsilon_0 - 2}{2\varepsilon_0 + 1}\ = \frac{1}{a_i^3} F_0 \tag{2.22}$$

$$f_\infty = \frac{2}{a_i^3}\ \frac{\varepsilon_\infty - 1}{\varepsilon_\infty + 1}\ = \frac{1}{a_i^3} F_\infty \tag{2.23}$$

where a_i is the Onsager cavity radius which can be derived from the Onsager solvation energy V_S^i:

$$V_S^i = -\frac{\mu_i^2}{a_i^3} \frac{F_0}{2} \tag{2.24}$$

The optical dielectric function is related to the static dielectric function by the following equation:

$$f_\infty = f_0 + f'(Q - Q^*) \tag{2.25}$$

where Q^* is the new equilibrium bond length of the Morse potential in solution.

The solvation energy becomes:

$$V_s\ Q\ = -\frac{1}{2}\ \boldsymbol{\mu}_i^0 + \boldsymbol{\mu}_i' Q + \boldsymbol{\mu}_i'' Q^2 + \cdots\ \cdot\ f_0 \boldsymbol{\mu}_i^0 + f_\infty \boldsymbol{\mu}_i' Q + f_\infty \boldsymbol{\mu}_i'' Q^2 + \cdots \tag{2.26}$$

with $V_s' = -\frac{1}{2}(f_0 + f_\infty)\ \boldsymbol{\mu}_i^0 \cdot \boldsymbol{\mu}_i'$.

The resulting solvated Morse potential is given by:

$$V_{sol}\ Q\ = V_i\ Q\ + V_s(Q) \tag{2.27}$$

$$= \frac{1}{2!}V_i'' Q^2 + \frac{1}{3!}V_i''' Q^3 + V_s^0 + V_s' Q + \frac{1}{2!}V_s'' Q^2 + \cdots \tag{2.28}$$

The first derivative is then:

$$V_{sol}' = V_i'' Q\ \ + \frac{1}{2}V_i''' Q^2 + V_s' + V_s'' Q\ \ + \cdots \tag{2.29}$$

While the second derivative is given by:

$$V_{sol}'' = V_i'' + V_i''' Q\ \ + V_s'' + \cdots \tag{2.30}$$

$$= V_i''\ \ 1 - \frac{1}{V_i''}\ f_0\ \ \boldsymbol{\mu}_i'' \cdot \boldsymbol{\mu}_i^0 - \frac{V_i'''}{V_i''}\boldsymbol{\mu}_i' \cdot \boldsymbol{\mu}_i^0\ \ + f_\infty(\boldsymbol{\mu}_i'' \cdot \boldsymbol{\mu}_i^0 + \boldsymbol{\mu}_i' \cdot \boldsymbol{\mu}_i') \tag{2.31}$$

For convenience in the following treatment, Δ is defined as:

$$\Delta = \frac{1}{V_i''}\ f_0\ \ \boldsymbol{\mu}_i'' \cdot \boldsymbol{\mu}_i^0 - \frac{V_i'''}{V_i''}\boldsymbol{\mu}_i' \cdot \boldsymbol{\mu}_i^0\ \ + f_\infty(\boldsymbol{\mu}_i'' \cdot \boldsymbol{\mu}_i^0 + \boldsymbol{\mu}_i' \cdot \boldsymbol{\mu}_i') \tag{2.32}$$

Since, $v = \frac{1}{2\pi}\ \ \overline{\frac{k}{m}}$ where $k = 4\pi^2 mv$ is the oscillator force constant, and m is the reduced mass which is constant, the resulting solvent induced vibrational frequency shift is given by:

$$\frac{\Delta v_i}{v_o^i} = \frac{v_o^i - v_s^i}{v_o^i} = \frac{\overline{V_i''} - \ \overline{V_i''\ 1 - \Delta}}{\overline{V_i''}} \tag{2.33}$$

$$= 1 - \ \ \overline{(1 - \Delta)} \tag{2.34}$$

Using a Taylor expansion which is truncated after the first two terms gives:

$$\frac{\Delta v_i}{v_o^i} \cong \frac{\Delta}{2} \tag{2.35}$$

$$= \frac{1}{2V_i''} \; f_0 \;\; \boldsymbol{\mu}_i'' \cdot \boldsymbol{\mu}_i^0 - \frac{V_i'''}{V_i''} \boldsymbol{\mu}_i' \cdot \boldsymbol{\mu}_i^0 \;\; + f_\infty \; \boldsymbol{\mu}_i'' \cdot \boldsymbol{\mu}_i^0 + \boldsymbol{\mu}_i' \cdot \boldsymbol{\mu}_i' \tag{2.36}$$

Using the relations for the dielectric functions and $V_i'' = k = 4\pi^2 m v_0^2$, the preceding equation becomes:

$$\frac{\Delta v_i}{v_o^i} = \frac{F_0}{8\pi^2 m v_0^i a_i^3} \;\; \boldsymbol{\mu}_i'' \cdot \boldsymbol{\mu}_i^0 - \frac{V_i'''}{V_i''} \boldsymbol{\mu}_i' \cdot \boldsymbol{\mu}_i^0 \;\; + \frac{F_\infty}{8\pi^2 m v_0^i a_i^3} (\boldsymbol{\mu}_i'' \cdot \boldsymbol{\mu}_i^0 + \boldsymbol{\mu}_i' \cdot \boldsymbol{\mu}_i') \tag{2.37}$$

It is thus found that the change in frequency shows a linear dependence on F_0 with slope:

$$S_i = \frac{1}{8\pi^2 m v_0^i a_i^3} \;\; \boldsymbol{\mu}_i'' \cdot \boldsymbol{\mu}_i^0 - \frac{V_i'''}{V_i''} \boldsymbol{\mu}_i' \cdot \boldsymbol{\mu}_i^0 \tag{2.38}$$

and intercept:

$$B_i = \frac{F_\infty}{8\pi^2 m v_0^i a_i^3} (\boldsymbol{\mu}_i'' \cdot \boldsymbol{\mu}_i^0 + \boldsymbol{\mu}_i' \cdot \boldsymbol{\mu}_i') \tag{2.39}$$

Besides the obvious approximation inherent to the model of the point dipole in a solvent with no specific interactions, some other approximations have been made in this derivation. First, due to the fact that the observed frequency shifts are quite moderate and do not imply any strong specific interactions, it was assumed based on numerous ultrafast studies in solution, that the anharmonic coupling between the OH stretch and other normal modes can be neglected [152, 153, 154, 155, 156, 157]. Next, the refractive index is taken to be constant since the reported values are all within 1.4378±0.0655 (see table 2.6). As the refractive index for most liquids in the MIR is a complex function of wavelength due to resonances with IR absorption bands, verifying that this approximation is also valid at 3μm was imperative. In order to achieve this, the group delay of 3μm femtosecond pulses after passing through a 1mm cuvette filled with the solvents of interest was measured and compared to air in order to calculate their refractive indexes. The uncertainty was evaluated by repeating each measurement three times. It was found that all refractive indexes are quite similar to that reported for visible wavelengths with a slightly smaller solvent dependence of 1.379±0.039.

Table 2.6: Dielectric constants and refractive indices for the solvents used in this study.

solvents	ε_0 (lit) [a]	n (lit) [a]	n (3337 cm^{-1})± 0.015	ε_∞ (3337 cm^{-1})
n-hexane	1.8799	1.3723	1.418	2.011
c-hexane	2.0243	1.4235	1.455	2.117
C_2Cl_4	2.28	1.5032	1.457	2.123
$CHCl_3$	4.806	1.4429	1.408	1.982
CH_2Cl_2	8.93	1.4212	1.379	2.020
1,2-DCE	10.0	1.4138	1.408	1.982

[a]: Values taken from reference [158]

2.3.2 Vibrational frequency shifts due to electronic excitation

Solvent relaxation occurs on two timescales: an instantaneous response due to electronic motion occurring during light absorption, as well as a non-instantaneous response due to the orientational solvent reorganization around the excited-state solute. Therefore, following excitation, the solvent is in a non-equilibrium configuration. This is schematized in figure 2.12.

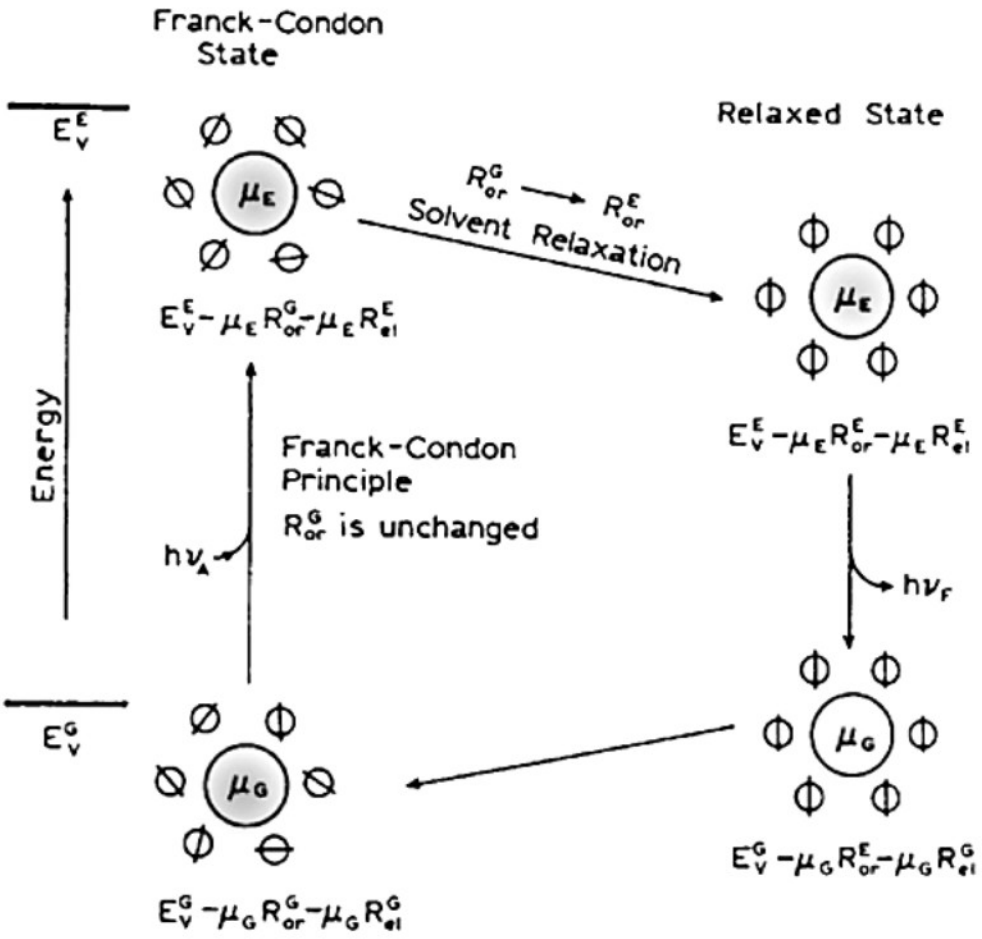

Figure 2.12: Effects of the electronic and orientation reaction fields on a dipole in a dielectric medium where the excited-state is characterized by a higher dipole moment. The smaller circles represent the solvent molecules and the lines their respective dipole moments. Figure adapted from reference [159].

The time dependence of the solvent response was treated by van der Zwan and Hynes [160] who described the resulting time-dependent reaction field $\boldsymbol{R}_i(t)$ by a fictitious time-dependent dipole moment, $\boldsymbol{\mu}\ t\ $:

$$\boldsymbol{R}_i\ t\ = f_\infty \boldsymbol{\mu}_e\ Q\ + f_{or}\boldsymbol{\mu}(t) \tag{2.40}$$

$$\boldsymbol{\mu}\ t\ = \boldsymbol{\mu}_g^0\ 1 - z\ t\ \ + \boldsymbol{\mu}_e^0 z(t) \tag{2.41}$$

where $\boldsymbol{\mu}_g^0$ and $\boldsymbol{\mu}_e^0$ are the permanent dipole moments in the ground and excited-state, and $z(t)$ is the solvation coordinate which varies from $z\ t = 0\ \ = 0$ at the initial solvent configuration to $z\ t = \infty\ \ = 1$ at equilibrium.

Using a treatment similar to what was used for the ground state, one obtains the following time-dependent and solvent-dependent vibrational frequency shift:

$$\frac{\Delta v(t)}{v_0^e} = \frac{f_\infty}{2V_e''} \quad \boldsymbol{g}_e + \boldsymbol{\mu}_e'' \; \boldsymbol{\mu}_e^0 + \boldsymbol{\mu}_e' \cdot \boldsymbol{\mu}_e' \; + \frac{f_{or}}{2V_e''} \boldsymbol{g}_e \boldsymbol{\mu}(t) \tag{2.42}$$

Once the solvent shell has attained an equilibrium distribution at longer times, $\boldsymbol{\mu}\ t\ = \boldsymbol{\mu}_e^0$, and the preceding equation reduces to equation 2.30.

2.3.2.1 Hydrogen bonding

The most dramatic solvent effect on the IR spectra of 1N and 2N is undeniably that involving specific hydrogen bond interactions with the solvent. Indeed, it is because of the high sensitivity of the O-H stretch to such interactions that IR spectroscopy has historically been the method of choice used to characterize and identify HB interactions. Upon formation of a HB, the narrow free O-H stretch around 3600cm^{-1} is red-shifted and broadened with a concomitant increase in intensity. The red-shift can be understood by the decreased effective force constant of the O-H oscillator as well as an increase in anharmonicity along the stretching coordinate. The broadening is attributed to anharmonic coupling of the O-H stretch to low frequency hydrogen bond modes as well as Fermi resonance with overtone or combination bands. These result in a vibrational multilevel system which is broadened by interaction with the fluctuating forces exerted by the solvent through spectral diffusion and broadening of individual vibrational lines [152]. Bratos has classified the behaviour of the O-H stretch frequency into four cases with characteristic spectral properties according to the OH···O distance [161, 162, 163]:

1. Free O-H: OH···O distance of over 3Å characterized by a narrow band around 3620-3590cm^{-1} for aromatic alcohols with a full-width half maximum (FWHM) of about 20cm^{-1}. An example of this is the OH stretch of 1N in CCl_4 shown in figure 2.13a.

2. Weak HB: OH···O distance between 2.8 and 3.0Å presenting a 100-300cm^{-1} red-shift and a 5 to 10 times increase in integrated intensity compared to the respective free O-H band. The FWHM is on the order of 100-300cm^{-1} and the isotope effect is $\overline{2}$ which is characteristic of a harmonic oscillator. An example of such a system is the hydrogen-bonded complex of 1N in acetonitrile shown in figure 2.13b which presents a red-shift of 225cm^{-1}, a FWHM of 145cm^{-1} and an isotope effect of 1.38.

3. Medium-strong HB: OH···O distance between 2.6 and 2.8Å with a 300-1000cm^{-1} red-shift and a 10 to 15 times increase in integrated intensity compared to the respective free O-H band. The FWHM is on the order of 500cm^{-1} but the band is highly asymmetric with a sub-structure that has been assigned as the result of coupling with various overtone and combination bands. The isotope effect on the band maxima is on the order of 1.3 and 2 for the band intensities. The O-H stretch of 1N in DMSO presented in figure 2.13c with a 500cm^{-1} frequency shift corresponds to such a system.

4. Strong HB: OH···O distance under 2.6Å with an IR band which can present several different spectral characteristics. In the case of asymmetric HBs which are more common for molecular species, one usually observes an "ABC" type band profile located in the 1500-2500cm^{-1} region extending over 1000cm^{-1} with a highly anomalous isotope effect.

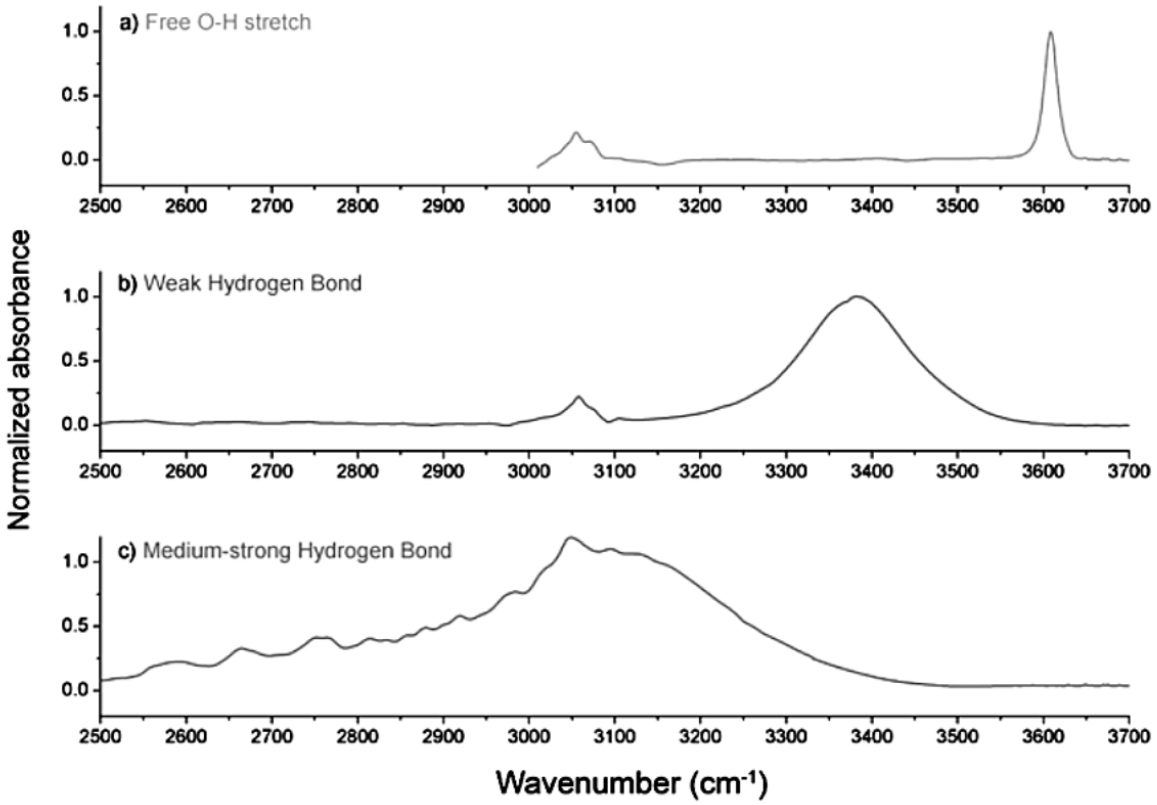

Figure 2.13: MIR O-H stretch band profile for a) 1N in CCl_4 b) 1N in MeCN-d_3 and c) 1N in DMSO-d_6. The band at around 3050cm^{-1} is due to the C-H stretch vibration.

3. Electron transfer theory

Electron transfer (ET) an elementary process involving no breaking or formation of bonds, only bond adjustments and solvent repolarizations. ET is central to many biological reactions such as: metabolic processes, industrial proceedings, or photosynthesis and other solar energy conversion schemes [164, 165]. ET reactions can be electrochemically, thermally or photoinduced. In photoinduced ET reactions, the photon energy is used to transfer an electron between a donor (D) and an acceptor (A) leading to the formation of a pair of high energy intermediates. Photoinduced ET is facilitated either due to the decrease in ionization potential in the excited state of the donor (it requires much less energy to remove an electron from the higher energy S_1 state than the ground S_0 state), or alternatively, the increase in the electron affinity in the excited-state of the acceptor. This is better visualized by considering a typical free energy level diagram for photoinduced ET reaction such as shown in figure 3.1.

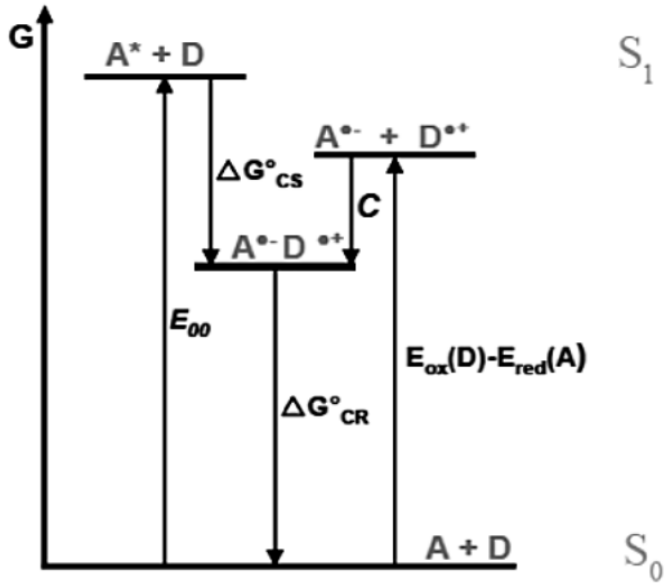

Figure 3.1: Typical Gibbs free energy (G) level diagram for photoinduced electron transfer where CS represents charge separation, CR charge recombination. E_{ox} is the oxidation potential of the donor (D) and E_{red} is the reduction potential of the acceptor (A).

Photoinduced ET reactions usually proceed by an initial charge separation between neutral molecules leading to the formation of radical ions:

$$A^* + D \rightarrow A^{\cdot -} + D^{\cdot +} \quad (3.1)$$

$$A + D^* \rightarrow A^{\cdot -} + D^{\cdot +} \quad (3.2)$$

Following charge separation, charge recombination commonly acts as an excited-state quencher restoring the ground-state of the reactants by thermal charge recombination. However, charge recombination to excited neutral species is also possible. Charge recombination occurring within a geminate ion pair is termed geminate recombination while recombination between well-separated ions is termed homogeneous recombination.

$$A^{\cdot -} + D^{\cdot +} \rightarrow A + D \quad (3.3)$$

$$A^{\cdot -} + D^{\cdot +} \rightarrow A^* + D \quad (3.4)$$

$$A^{\cdot -} + D^{\cdot +} \rightarrow A^* + D \quad (3.5)$$

$$A^{\cdot -} + D^{\cdot +} \rightarrow A + D^* \quad (3.6)$$

One distinguishes between intramolecular ET where the acceptor and the donor are covalently linked, and intermolecular (also called bimolecular) ET where A and D are two separate molecules.

3.1 Classical Marcus-Hush theory

The theory developed by Marcus and Hush [166, 167, 168, 169, 170] provides a framework to describe the rate of ET reactions according to its thermodynamics. The main postulates of the theory are that both precursor and successor states can be described by quadratic functions of the reaction coordinate with equal force constants, nuclear reorganization proceeds classically through low frequency vibrational and rotational modes, and that nuclear reorganization is kinetically symmetrical with $k_n = k_{-n}$, where k_n represents the rate of nuclear reorganization. The theory uses transition state theory (TST) where one generalized nuclear coordinate Q, is introduced in order to simplify the complex potential energy surface of each molecule within the system (including the surrounding solvent) by a one-dimensional profile. The reaction coordinate Q represents the average configuration of all molecules of the system.

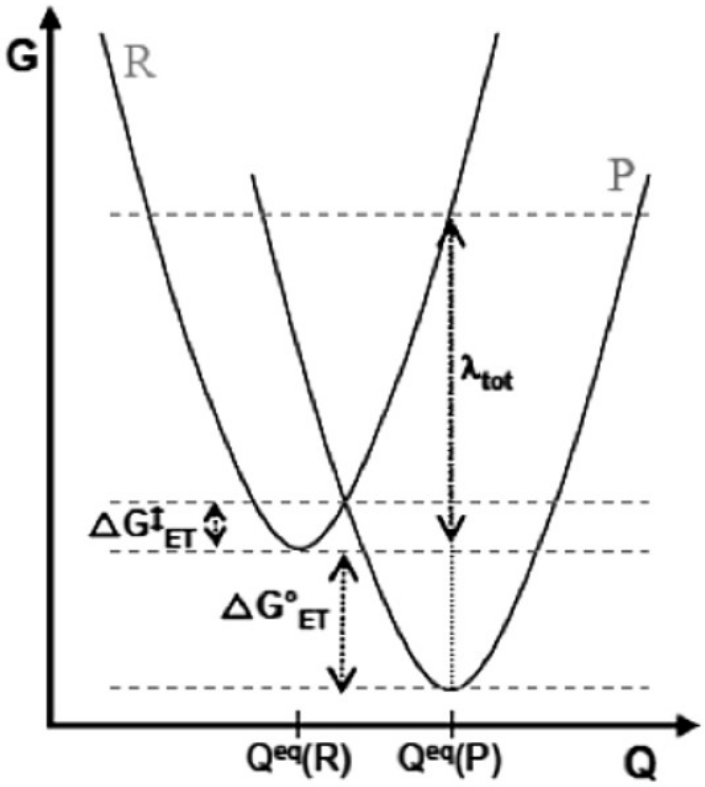

Figure 3.2: Parabolic Gibbs free energy (G) surfaces of the reactants (R) and products (P) according to the classical Marcus-Hush theory.

Figure 3.2 gives a representation of the parabolic free energy surfaces of the reactants and products. The system of equations describing the free energy surfaces can be solved at the point of intersection of the two parabolas enabling the activation energy $\Delta G_{ET}^{\ddagger}$ to be expressed in terms of the free energy of the reaction ΔG_{ET}° and the total reorganization energy, λ_{tot}:

$$\Delta G_{ET}^{\ddagger} = \frac{\Delta G_{ET}^{\circ} + \lambda_{tot}}{4\lambda_{tot}}^{2} \tag{3.7}$$

The total reorganization energy is comprised of both the solvent reorganization energy λ_s and the intramolecular reorganization energy, λ_i:

$$\lambda_{tot} = \lambda_i + \lambda_s \tag{3.8}$$

More specifically, the solvent reorganization energy represents the energy needed by the solvent molecules in order to reach an equilibrium orientation with the products, while the intramolecular reorganization energy represents the change in free energy required to deform

the reactant from the reactant equilibrium position to the product equilibrium position without transferring an electron.

Within the TST, the overall rate of ET, k_{ET} depends on the probability of reaching the transition state, the time required to cross the transition state and the probability of the electronic transition. It is given by the Arrhenius equation:

$$k_{ET} = Aexp \quad \frac{-\Delta G_{ET}^{\ddagger}}{k_B T} \tag{3.9}$$

where A is the pre-exponential factor, T is the temperature and k_B is the Boltzmann constant. The pre-exponential factor gives the probability for a system in the transition state region to cross over to the reactant free energy surface and is thus highly dependent on the electronic coupling V_{RP} between the two states. One distinguishes between non-adiabatic coupling where V_{RP} is small and adiabatic coupling where V_{RP} is large. In the first instance, R and P can be represented by unperturbed potential energy surfaces, while in the second case the large coupling implies an avoided crossing between the potential energy surfaces with an energy splitting of 2 V_{RP} . These two cases are schematized in figure 3.3.

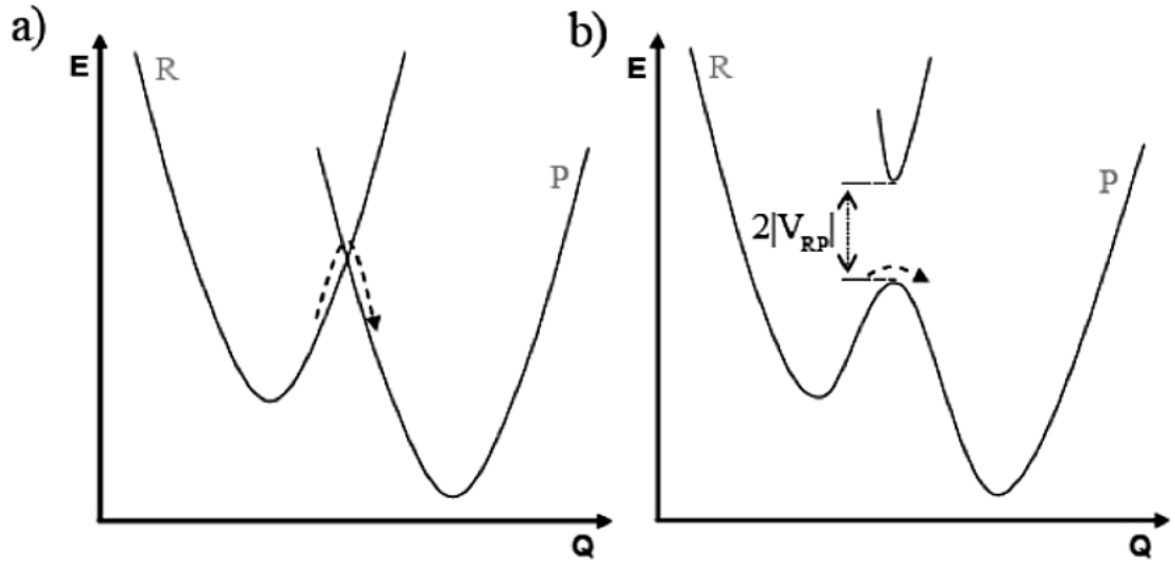

Figure 3.3: Schematic representation of the free energy surfaces for a) non-adiabatic and b) adiabatic ET where P represents the product surface and R the reactant surface.

In the case of non-adiabatic coupling the pre-exponential factor is given by:

$$A = P \ \frac{\omega_0}{2\pi} \tag{3.10}$$

where P is the probability and ω_0 is the oscillation frequency of the system in the reactant well. In the case of adiabatic coupling, using either time-dependent perturbation theory or the classical Landau-Zener theory, Levich and Dogonadze [171] have shown that the pre-exponential factor is proportional to V_{RP}^2:

$$A = \frac{2\pi}{\hbar} \ \frac{V_{RP}^2}{\sqrt{4\pi\lambda_s k_B T}} \tag{3.11}$$

Using equation 3.7 and replacing equation 3.11 into equation 3.9, it is possible to express the rate k_{ET} as a function of the free energy of the reaction $\Delta G^\circ{}_{ET}$:

$$k_{ET} = \frac{2\pi}{\hbar} \ \frac{V_{RP}^2}{\sqrt{4\pi\lambda_s k_B T}} \ exp \ -\frac{\Delta G_{ET}^\circ + \lambda_{tot}}{4\lambda_{tot} k_B T}^2 \tag{3.12}$$

The plot of $\log(k_{ET})$ as a function of ΔG_{ET}° shown in figure 3.4 has a bell-shape where one distinguishes three regions characterized by their exergonicity:

1. Normal regime: $-\Delta G_{ET}^\circ < \lambda_{tot}$
   The rate of electron transfer increases with increasing exergonicity
2. Barrierless regime: $-\Delta G_{ET}^\circ = \lambda_{tot}$
   There is no activation energy for the ET reaction and the ET rate is minimal
3. Inverted regime: $-\Delta G_{ET}^\circ > \lambda_{tot}$
   The rate of electron transfer decreases with increasing exergonicity.

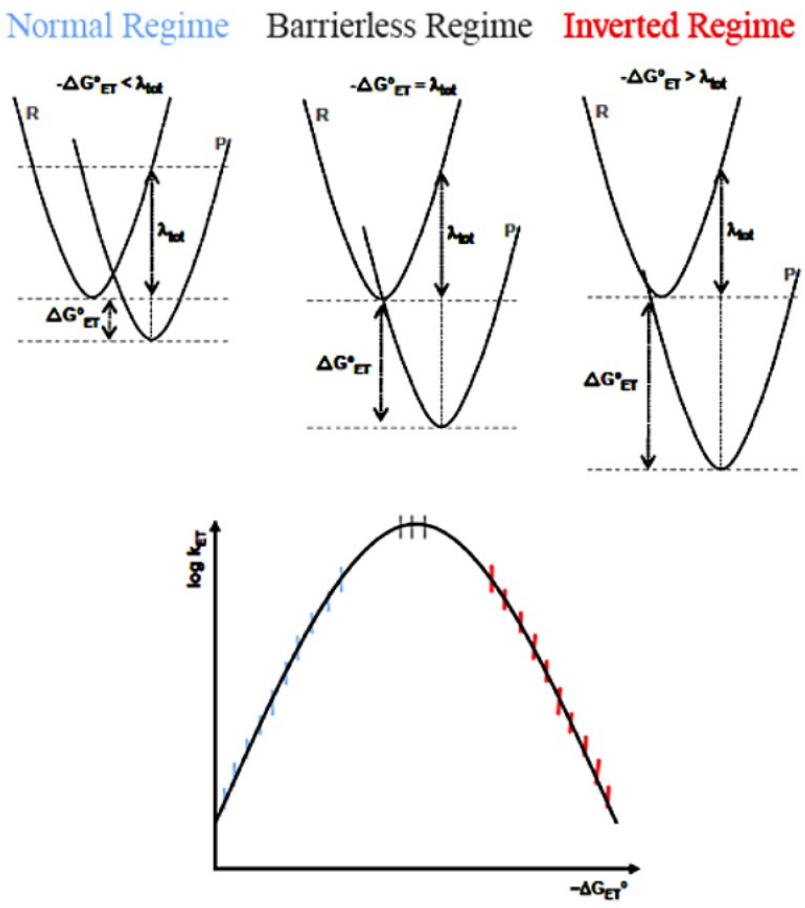

Figure 3.4: Schematic representation of the normal, barrierless and inverted Marcus regimes.

Unlike other excited-state processes like electron exchange or intersystem crossing, electron transfer can be predicted using the redox potentials of the donor and acceptor. Indeed, the thermodynamic efficiency of photoinduced ET can be determined using the equation proposed by Rehm-Weller [172, 173, 174] which gives the free energy of the reaction, ΔG°_{ET} in terms of the oxidation and reduction potential of the acceptor (A) and donor (D):

$$\Delta G^{\circ}_{ET} = e\ E_{ox}(D) - E_{red}(A)\ - E_{00} + C + S \tag{3.13}$$

where C is a coulomb term representing the electrostatic interaction between the ions which accounts for the fact that ions are formed at close distance and not infinite separation, S represents a corrective factor for the solvent when a solvent other than acetonitrile is used, E_{00} is the energy of the 0-0 transition of either A^{*}or D^{*}, the reduction potential $E_{ox}(D)$ represents the following reaction:

$$D^{+} + e^{-} \rightarrow D \tag{3.14}$$

and the oxidation potential $E_{ox}(D)$ describes the following reaction:

$$A + e^- \rightarrow A^- \tag{3.15}$$

The coulomb term C can be estimated based on a point charge model in which the charges are separated by a solvent which is treated as a dielectric continuum:

$$C = \frac{1}{4\pi\varepsilon_0}\frac{-e^2}{\varepsilon_s d} \tag{3.16}$$

where ε_s is the static dielectric constant of the solvent and d is the interionic centre-to-centre distance.

3.2 Semi-classical Marcus-Hush theory

In order to account for experimental data evidencing no temperature dependence for the ET rate constant in the inverted regime and the fact that this last was never measured to be as pronounced as predicted by equation 3.12 [175], the Marcus-Hush theory was generalized in order to include quantum effects [176, 177, 178, 179, 180, 181]. Indeed, for highly exergonic reactions, there is an increasing overlap between the vibrational wavefunctions of the reactant and product states (figure 3.5) leading to important nuclear tunneling effects.

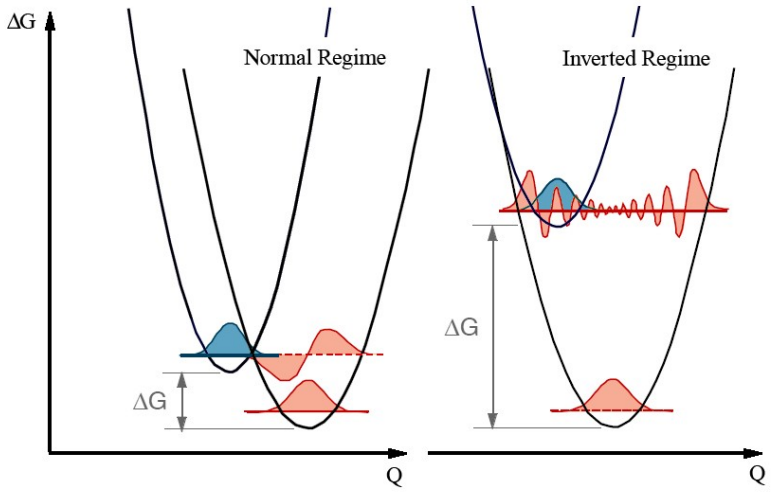

Figure 3.5: Schematic representation of the vibrational overlap between the reactant (R) and product (P) wavefunctions in a) the normal regime and b) the highly exergonic inverted regime.

The overlap between the vibrational wavefunctions means that the coupling matrix element V_{RP} is no longer purely electronic but also vibrational. The coupling is given in the harmonic approximation by the Franck-Condon factor, FC:

$$FC = \quad 0\ n\ \ ^2 = e^{-S}\frac{S^n}{n!} \tag{3.17}$$

with n the number of vibrational quanta excited in the product state and $S = \frac{\lambda_i}{h\nu}$ is the Huang-Rhys factor which is the electron-vibration coupling constant. If the energy of the low frequency modes of the solvent is smaller than the thermal energy, k_BT, the intramolecular reorganization energy may be treated in a quantum-mechanical way while the solvent reorganization energy consisting of low frequency modes is treated classically. Using the dielectric approach and considering the approximation of the single-phonon model, ie, it is considered that a single vibrational frequency is involved in the readjustment of the nuclear coordinates associated with electron transfer, one obtains the following equation:

$$k_{ET} = \frac{2\pi}{\hbar}\ \frac{V_{RP}^2}{\sqrt{4\pi\lambda_s k_B T}}\ \sum_{n=0}^{\infty} e^{-S}\frac{S^n}{n!} exp\ \ -\frac{\Delta G_{ET}^{\circ} + nh\nu + \lambda_s\ ^2}{4\lambda_s k_B T} \tag{3.18}$$

A more detailed derivation of this equation can be found in [182].

3.3 Static and dynamic electron transfer reactions

Neither the classical nor the semi-classical Marcus-Hush theory can adequately describe bimolecular ET reactions. As electron clouds are strongly localized, the electron density falls off very rapidly with distance from the surface of the molecules, and ET necessitates molecular contact at the van der Waals radii. Therefore, when using low concentrations, this necessitates the diffusion of the reactive partners towards each other. Because of this, the fast electron transfer rates are convoluted by the slow diffusive rates and hard to interpret. Indeed, in a seminal experiment, Rehm and Weller showed that the rate constant for bimolecular ET is convoluted with the diffusion rate of the two reactive partners [173]. In the inverted Marcus region where ET rates are faster than diffusion, a diffusion limited plateau was thus observed. In order to account for diffusion, models such as the Smoluchowski-Collins-Kimball are used [183, 184]. However, it was shown that this last does not accurately describe bimolecular ET

reactions as it does not take into account the so-called “static quenching” [185, 186]. The term quenching is commonly used as ET rates have typically been measured using fluorescence techniques where ET quenches the emission from the S_1 state of the fluorophore. One distinguishes between static and dynamic quenching. Static quenching designates ET where a complex exists already in the ground-state between the donor and acceptor. This ground-state complex frequently results in identifiable changes in the absorption spectra of the fluorophore. An example of this is the ET between anthracene and carbon tetrachloride where the different absorption spectra of the complex compared to uncomplexed anthracene results in a wavelength dependent ET reaction due to photoselection [41, 42]. Dynamic quenching on the other hand is the result of collisions between the freely diffusing donor and acceptor molecules. In addition, recent ultrafast experiments on ET reactions have revealed that the situation is even more complex as there is a distribution of distances between the donor and acceptor over which ET takes place [187, 188, 189, 190].

In order to avoid the complicated dynamics associated with diffusion controlled reactions, the ET experiments described in chapter 6, where 1-naphthol and 2-naphthol act as electron donors to halocarbon acceptors, were conducted using the quencher as the solvent.

4. Nonlinear optics and experimental procedures

Stimulated emission, the process at the source of laser radiation, was first formulated by Einstein in 1917 [191]. The titanium doped aluminium oxide (Ti:sapphire) laser was introduced in the mid-eighties and has to some extent replaced dye lasers as the source for tuneable laser output [192]. Its gain medium possesses several highly desirable characteristics such as a relatively large gain cross section, high thermal conductivity, chemical inertness, mechanical rigidity, and hardness. Most notably, the presence of a Kerr lens effect allows for the generation of highly intense femtosecond pulses through the modelocking of a broad gain profile. Even though it is classified as a tunable laser with an output ranging from 600nm to 1000nm, the Ti:sapphire laser would not be so versatile and enjoy such widespread use today, were it not for the field of nonlinear optics [193, 194]. This field developed in parallel to that of lasers which provided the high intensities necessary for nonlinear effects. Through the use of nonlinear phenomena, it is possible to extend the range of the Ti:sapphire laser by using it as a pump for sources from the microwave [195] all the way to the x-ray regime [196] allowing for limitless possibilities in terms of spectroscopic methods and probes. Furthermore, as the basis for describing any nonlinear interaction of light with matter, the field of nonlinear optics also includes light-induced changes to the optical properties of a medium, such as those induced in a pump-probe experiment. The use of multiple light-matter interactions allows information about how quantum states evolve in time as well as their couplings to other states to be accessed. One distinguishes between resonant and non resonant interactions. In the latter case, interaction with the radiation results in a polarization but does not correspond to a real energy transition in the molecule. This is the case with frequency conversion schemes using the properties of non linear crystals. For resonant interactions on the other hand, such as in the UV pump-IR probe experiments conducted in this thesis, the interaction with the radiation corresponds to a real transition of the molecule under investigation.

4.1 Pump-probe spectroscopy

The field of nonlinear spectroscopy features a large number of experimental techniques which make use of multiple light-matter interactions in order to access information which is inaccessible through the use of traditional linear techniques. The second order nonlinear susceptibility of centrosymmetric materials is zero due to their inversion centre. This is also

true of isotropic materials such as liquids or gases given the random orientation of molecules found in such systems. For this reason, second order nonlinear techniques have a very limited scope, primarily being used to investigate interfaces [197]. Most nonlinear techniques, such as pump-probe spectroscopy, transient grating, photo echo or time resolved CARS (Coherent Anti-Stokes Raman Scattering), rely instead on the generation of a third order polarization $P^{(3)}$. The various techniques differ by such variables as the pulse sequence, the detection mode, the phase matching conditions, the wavelength of the involved pulses etc. In a pump-probe experiment, the three interactions are given by: two interactions with the pump pulse, once to create a coherent state and once to create an excited state population, and then one interaction with a weaker probe pulse that stimulates a transient oscillating dipole moment [198, 199]. The wavevector of this signal field is given by the sum of the wavectors of the generating fields:

$$\boldsymbol{k}_{signal} = \pm\boldsymbol{k}_{pump} \pm \boldsymbol{k}_{pump} \pm \boldsymbol{k}_{probe} \tag{4.4}$$

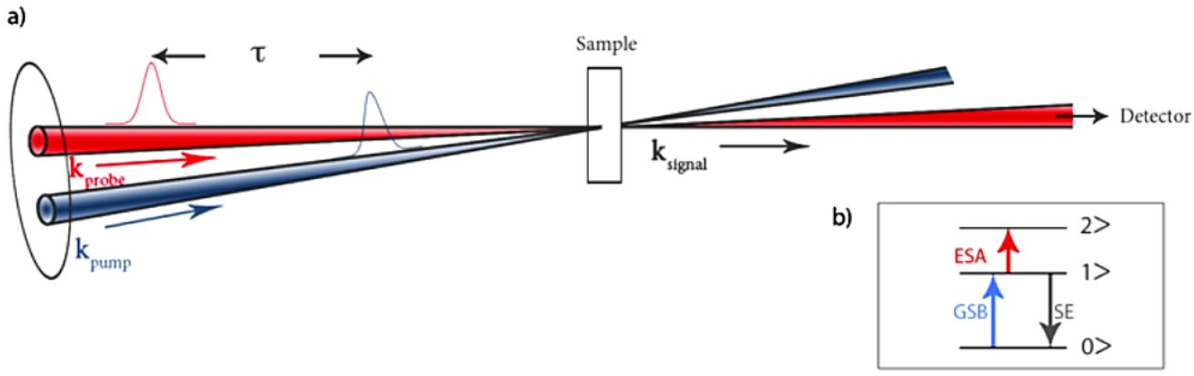

Figure 4.1: a) schematic representation of the various pulses and their respective wavevectors in a pump-probe experiment. b) level diagram, GSB: ground state bleach, ESA: excited state absorption, SE: stimulated emission.

A schematic representation of the pump-probe pulses and the relevant wavevectors is given in figure 4.1b. Effectively, this means that the signal is radiated collinearly with the transmitted probe pulse. For more complicated pulse interactions, such as those found in photon-echo experiments, Feynman diagrams are of use [200, 201]. Since the output field has the same frequency as the probe field, this leads to interference. The spectrally integrated time dependent transmission of the probe field is given by [202]:

$$\Delta T\ \tau,\omega\ = \frac{I\ \tau,\omega}{I_0(\omega)} = \frac{\int_0^\infty dt|E_{probe}\ \omega\ + E_{signal}(\tau,\omega)|^2}{\int_0^\infty dt|E_{probe}(\omega)\ |^2} \tag{4.2}$$

As the laser pulses are short compared to the system response but long compared to the oscillation period of the light, one is in the semi-impulsive limit where the third order polarization $P^{\ 3}\ (t)$ is equal to the third-order response function $S^{\ 3}\ (t)$. For a homogeneously broadened oscillator with linewidth Γ, the third-order response function is given by:

$$S^{\ 3}\ \ t\ = P^{\ 3}\ \ t\ = (4\frac{i}{\hbar^3}\mu_{10}^4 e^{-i\ \varepsilon_1-\varepsilon_0\ t} - 2\frac{i}{\hbar^6}\mu_{10}^2\mu_{21}^2 e^{-i\ \varepsilon_2-\varepsilon_1\ t})e^{-\Gamma t} \tag{4.3}$$

where μ_{10} and $\mu_{21}$are the transition dipole moments and t is the time between the pump and the probe pulse. The third order polarization as a function of time t is measured by a heterodyne detection with the probe pulse:

$$E_{probe}\ t\ + iP^{\ 3}\ \ t\ ^2 - \ E_{probe}\ t\ ^2 = 2Im\ \ E_{probe}\ t\ \cdot P^{\ 3}\ \ t \tag{4.4}$$

A spectrometer performs the Fourier transform with respect to time t, with the resulting probe difference absorption $\Delta A\ \ t,\omega\ $ given by:

$$\Delta A\ \ t,\omega\ \propto \frac{4\mu_{01}^2\mu_{21}^2\Gamma}{(\omega_{21}-\omega)^2+\Gamma^2} - \frac{8\mu_{01}^4\Gamma}{(\omega_{10}-\omega)^2+\Gamma^2} \tag{4.5}$$

In this way, the transmitted intensity of the probe field can either increase when the pump induces stimulated emission or ground state bleaching or it can decrease if the pump creates an excited state population. Pump-probe spectroscopy can thus measure population differences and their respective relaxations. In the case that the pump and probe have very different energies such as in UV pump-IR probe experiments, stimulated emission is not observed.

4.2 Principles of polarization sensitive spectroscopy

Laser radiation is polarized and will thus preferentially excite those molecules whose electronic dipole moments are aligned parallel to its electric field. The measure of this selective photoexcitation from the disordered ensemble of transition dipoles is the anisotropy r, which is the difference between light emitted with the same polarization as the incident light and that emitted in a perpendicular direction:

$$r = \frac{I_{\parallel} - I_{\perp}}{I_{\parallel} + 2I_{\perp}} \tag{4.6}$$

where I is the intensity, with $\parallel$ and $\perp$ representing their alignment. The denominator in equation 4.9 is a normalization over the total intensity.

The time-dependent rotational anisotropy is thus given by:

$$r\ t = \frac{\Delta A(t,\omega)_{\parallel} - \Delta A(t,\omega)_{\perp}}{\Delta A(t,\omega)_{\parallel} + 2\Delta A(t,\omega)_{\perp}} \tag{4.7}$$

where, $\Delta A(t,\omega)_{\parallel} = -log_{10}\ \frac{I(t,\omega)}{I_0(\omega)}_{\parallel}$ and $\Delta A(t,\omega)_{\perp} = -log_{10}\ \frac{I(t,\omega)}{I_0(\omega)}_{\perp}$.

The relationship between the anisotropy and the angle θ between the absorption and emission dipole moments is derived using geometrical considerations. The average angular displacement undergone by the transition dipoles of an isotropic ensemble is found to be:

$$r\ \theta = \frac{1}{5}\ 3cos^2\theta - 1 \tag{4.8}$$

In liquid media, the rotational diffusion of the molecules randomizes this photoselection on timescales of a couple of picoseconds to hundreds of picoseconds depending on the solvent viscosity, size of the probe molecules etc. For a list of timescales for some representative molecules, see table 6.3 in reference [203]. The subsequent anisotropy decay leads to dynamics which can complicate the interpretation. As these decays are on the order of the timescales probed in the typical experiments reported on in this thesis, measurements are performed at the magical angle ($\theta_{magic} = 54.74°$) in order to eliminate contributions from

rotational dynamics. Indeed, under these conditions the second Legendre polynomial in equation 4.8 is zero.

It must be noted that several other mechanisms besides rotational diffusion can lead to an anisotropy decay. Indeed, any process which serves to change the orientation of the dipole orientation will effectively lead to anisotropy changes. An example of this is resonant energy transfer or excited state level dynamics. This last process is investigated in the case of 1N in polar solvents in chapter 7.

4.3 Experimental procedures

4.3.1 Femtosecond UV pump-IR probe spectroscopy

In this technique, the output of the laser is split into two distinct beams: an intense UV pump and a less energetic IR probe. Excitation of the sample is carried out by the pump, and the probe then monitors the time evolution of the changes induced in the sample.

4.3.1.1 The laser system

The UV pump/IR probe experiments were made possible using a commercial Ti:Sapphire chirped pulse amplified system with two home built parametric devices as shown in figure 4.2. The Ti:sapphire oscillator (Spectra Physics, Tsunami) is pumped with an intracavity doubled Nd3+:YVO4 laser (Spectra Physics, Millennia Vs) providing continuous wave output at 532nm. Mode-locking is achieved with an acousto-optic modulator within the cavity generating a periodic loss. The 80fs pulses centred at 800nm with a repetition rate of 80MHz generated by the oscillator are then passed through a Faraday isolator in order to prevent the absorption of reflected pulses.

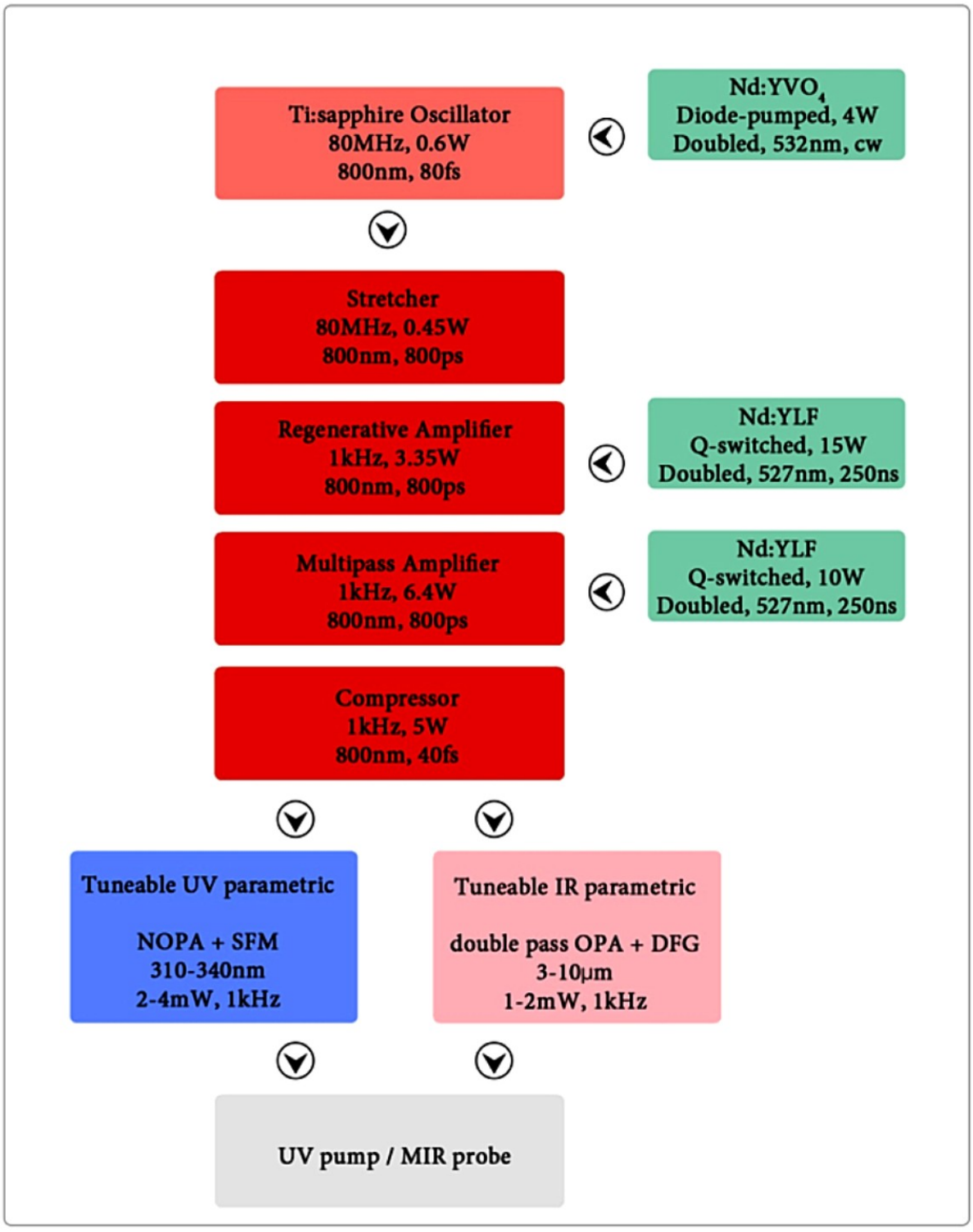

Figure 4.2: Schematic flow diagram of the optical components used in the UV-pump-IR-probe experiment.

Sufficiently high laser output is required in order to pump the two parametrics. However, as the titanium sapphire laser operates with very short, and therefore, intense pulses, amplification of these pulses would give rise to unwanted nonlinear effects as well as possible damage to the optical components. Chirped pulse amplification circumvents these problems

by “stretching” the pulses temporally through use of a grating pair prior to their amplification in order to reduce the peak power. The stretched pulses are then amplified and recompressed.

Amplification of the pulse is achieved in another optical resonator. For titanium sapphire lasers, the gain medium employed is also a Ti:Sapphire rod that is pumped by an intracavity frequency doubled Q-switched neodymium-doped yttrium lithium fluoride (Nd3+:YLF) laser operating at 1kHz providing 250ns pulses of 527nm light with a pump power of 14W. Use of the frequency doubled output of neodymium lasers is mandated by the 3.8μs excited state lifetime of the Ti:Sapphire laser which makes flashlight pumping inefficient seeing as how spontaneous decay out of the excited state would be possible during the long flash pump. The gain material is seeded with the stretched output of the oscillator by using a Pockels cell that injects an oscillator pulse every millisecond thereby reducing the repetition rate to 1kHz. The pulse subsequently undergoes around 25 roundtrips, permitting high gains. A second electro-optic switch then serves to eject the pulse from the resonator when maximum pulse energy, around 3.35mJ, is obtained. Further amplification to 6.4mJ is obtained in a second pass Ti:sapphire stage pumped with 10W of a second Nd3+:YLF laser.

The phase distortion of the various frequencies present in a pulse gives a measure of the dispersive effects. By expressing the phase distortion as a power series around the central frequency it is possible to specify the effect of material dispersion. The quadratic phase derivative is what is generally referred to as group velocity dispersion (GVD). For most of the electromagnetic spectrum, the effect of GVD is that the lower frequencies travel faster than the higher frequencies resulting in pulse broadening. Pulse compression is achieved by inducing negative dispersion through the use of prisms or gratings. The basic idea is to have the lowest frequencies travel a longer path than the higher frequencies. In this way light with higher frequencies takes less time to travel through the compressor than light with lower frequencies and so all the frequencies can effectively “catch up”. The resulting compressed pulses of 40fs with 5mJ output energy are spilt using a beam splitter into a 4mJ and 1mJ pulse. The latter is then split again into a 350μJ pulse that serves to pump the mid-infrared parametric and a second 650μJ pulse to pump the UV parametric.

4.3.1.2 Mid infrared parametric source

Highly stable femtosecond mid-infrared light pulses tunable from 3-10µm are generated as shown in figure 4.3 using a double pass BBO parametric followed by DFM of the signal and idler in a gallium selenide (GaSe) or silver gallium sulfide ($AgGaS_2$) crystal.

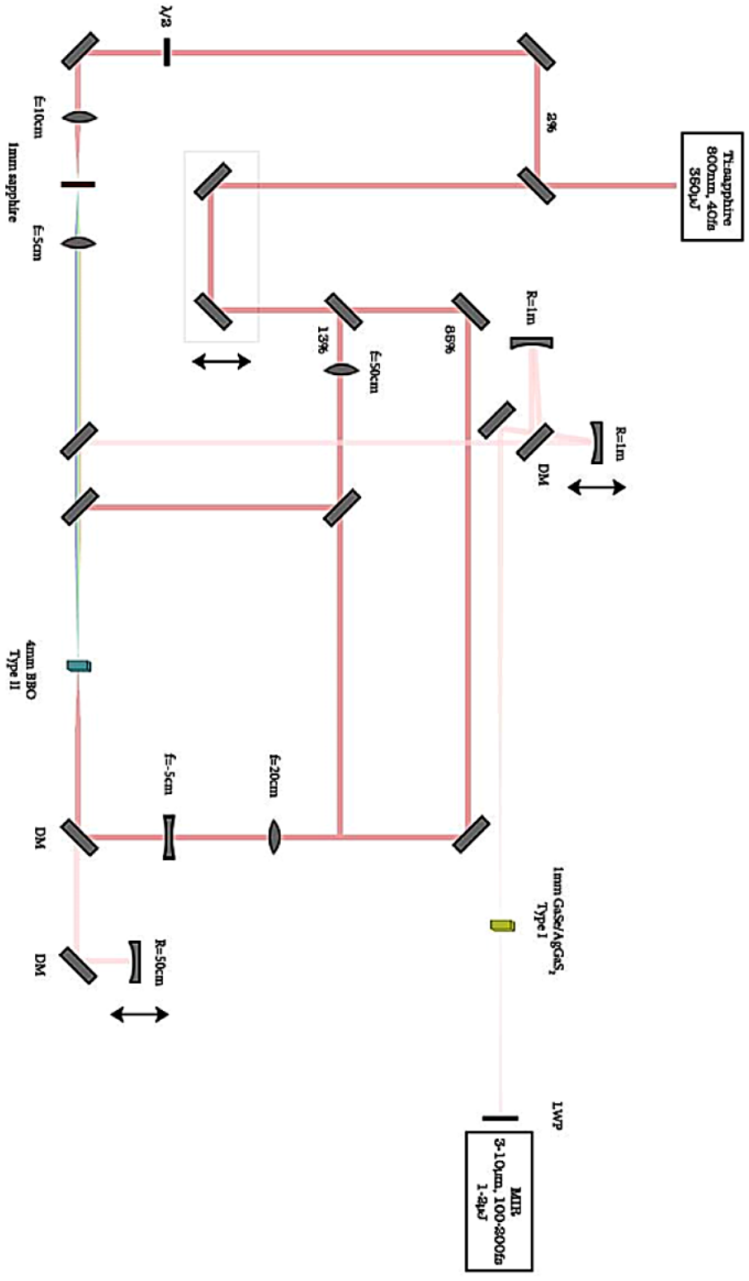

Figure 4.3: Optical design of the IR OPA and subsequent difference frequency mixing step producing tunable MIR pulses. The fundamental and signal of the first and second pass in the amplification stage generating signal and idler are displaced vertically. LWP: long wave pass filter, λ/2: half-wave plate, f: focal length and DM: dichroic mirror.

More specifically, the incoming horizontally polarized 800nm pulse from the Ti:sapphire laser is split up into three beams. The first beam consisting of approximately 2% of the initial 350μm is focused with a lens (f=10cm) onto a 1mm sapphire plate in order to generate a white light continuum extending to the near infrared through self-phase modulation. These wavelengths are amplified through judicious phase matching in a 4mm type II BBO crystal using the second 800nm beam (46μJ) focused with a f=50mm lens as pump. Separation of the generated signal from the residual 800nm beam and horizontally polarized idler is achieved using a dichroic mirror for the former and a polarizing beam splitter for the latter. The signal is then collimated with a concave mirror of radius R=50cm and focused back onto the BBO in a laterally displaced position with the third 800nm beam (298μJ) whose beam diameter has been reduced by means of a 4:1 telescope. For both amplification stages, temporal overlap is ensured by providing the 800nm beam paths with adjustable delay stages. Also, operating the amplifier in the saturation limit ensures small pulse-to-pulse fluctuations [204]. Since the signal beam is tunable from 1.2 to 1.6μm and the idler beam from 2.4 to 1.6μm this allows for MIR pulses from 3 to 10μm through difference frequency generation. Furthermore, using a type II BBO for the OPA has the advantage that the signal and idler have the correct polarization for the DFM step.

4.3.1.3 UV parametric source

The scheme for the generation of tunable ultraviolet light is given in figure 4.4. Specifically, the horizontally polarized 800nm beam is split in three: first, second harmonic generation in a type I 0.5mm BBO crystal provides 150μJ pump photons at 400nm which are then stretched with a 1cm quartz plate, second, a white light continuum is generated by focusing (f=50cm) 65μJ of the fundamental in a 2mm sapphire plate, and third, 60μJ of the fundamental is kept for the sum frequency mixing (SFM) step. A stable white light continuum of good optical quality is obtained by attenuating the pump pulses with a combination of a half-wave plate and polarizer to just above the continuum threshold. Amplification of these seed pulses in the NOPA crystal (BBO, type I, 2mm) typically results in 10μJ pulses which are tuneable from 490 to 660nm. Wavelength tuning is achieved by temporally overlapping selected frequencies of the white light continuum with the pump photons. This is done with a variable delay that modifies the optical path, changing the time at which the different components of the chirped white light reach the crystal.

For the SFM step, the 800nm pump is collimated with a f=4m lens and focused together with the visible NOPA output with a concave mirror (f=15cm) into a 100μm type I BBO crystal. The intersection angle between the two beams is 1.3°. This gives vertically polarized UV pulses between 315-345nm with energies of 2-4μJ.

Table 4.1: Pulse parameters for the UV and IR parametric devices.

	UV parametric	**IR parametric**
Tunning range	315-345nm	3-10μm
Pulse energy	2-4μJ	1-2μJ
Pulse duration	40fs	100-200fs

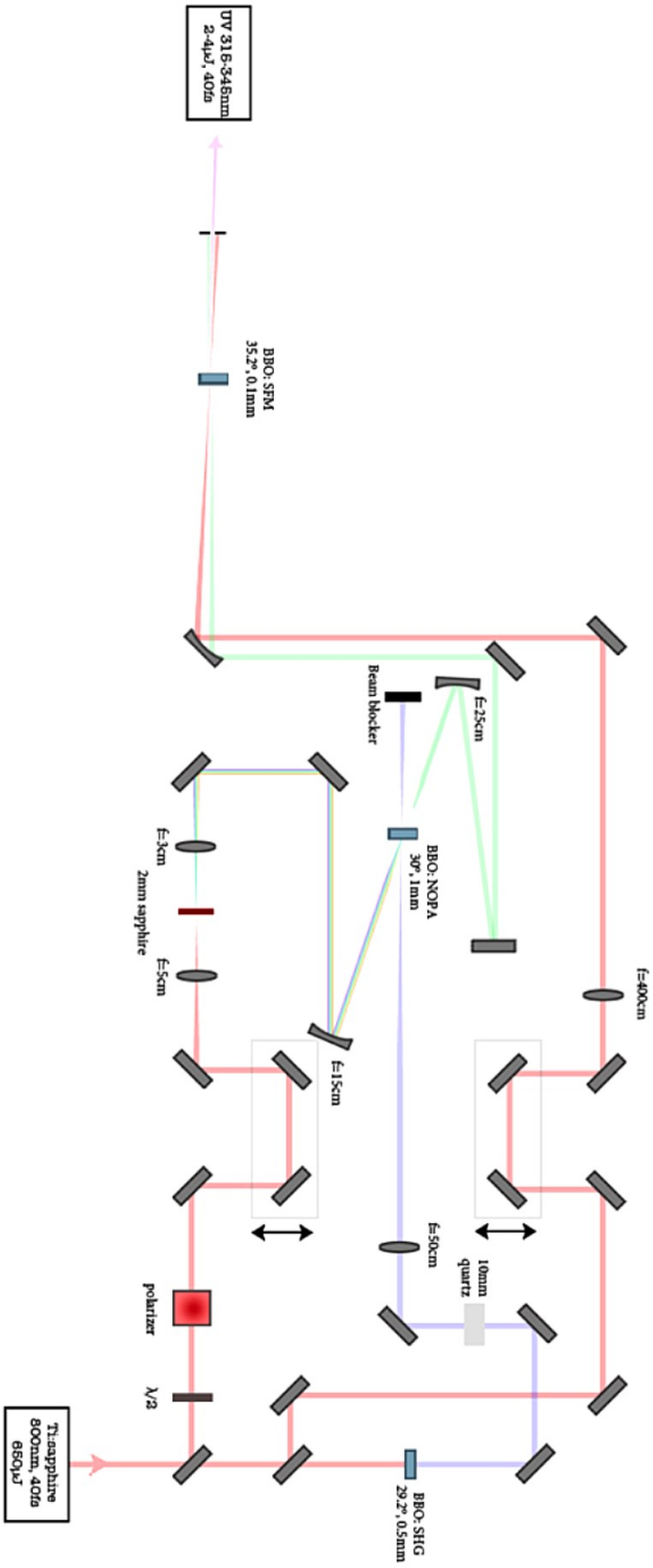

Figure 4.4: Optical design of the noncollinear optical parametric amplifier and sum frequency stage producing tunable UV light. The beam splitters have 10% reflection. λ/2: half-wave plate, f: focal length.

4.3.1.4 Pump-probe experiment

The setup for the pump-probe experiment is shown schematically in figure 4.5. The UV pulses generated by the NOPA followed by SFM with 800nm light is first passed through an optical delay line (Physik Instrumente, M-531.DG) allowing for the time delay between the pump and probe to be varied up to 1ns. A zero-order half-wave plate then serves to modify the polarization of the pump pulses to provide for magic angle detection (54.74°). Monitoring the sample transmission with and without UV excitation is achieved with an optical chopper synchronized to the Q-switch of the Ti:sapphire laser running at half its repetition rate (500Hz), thereby effectively blocking every second pulse. The pump beam is focused with a lens (f=20cm) in such a way as to have the sample before the focal plane to minimize non-resonant signal contributions arising from the solvent and the cell windows. This provides a 200-250μm beam diameter. The mid-infrared light generated in the double pass OPA followed by DFG is first split into two beams by using the front and back reflections (approximately 10% each) off a zinc selenide wedge while the main transmitted beam is blocked. The two beams thus generated for the probe and reference beams, are enlarged by a 2:3 reflection telescope in order to afford a reduction in the focused spot size at the sample position. The probe and reference are focused onto the sample by a 30° off-axis parabolic mirror to a spot size of 100-150μm. The smaller probe size compared to that of the pump ensures that all probed sample has been pumped and that a homogeneous sample volume is probed. The pump and probe are spatially overlapped onto the sample while the reference propagates through a nearby volume not perturbed by the pump pulse. After passing through the sample, the pump pulses are blocked with a beam blocker and the probe and reference signals are re-collimated with a second 30° off-axis parabolic mirror. Focusing unto the entrance slit of a monochromator is achieved with a third off-axis parabolic mirror with a 14cm focal length. Spectral dispersion of the pulses is obtained by use of gratings chosen depending on the central wavelength of the MIR pulse: from 3-5μm a 300 l/mm grating is used, from 5-7μm a 150 l/mm grating is used and finally from 7-10μm either a 100 l/mm or 60 l/mm grating is used depending on the desired resolution.

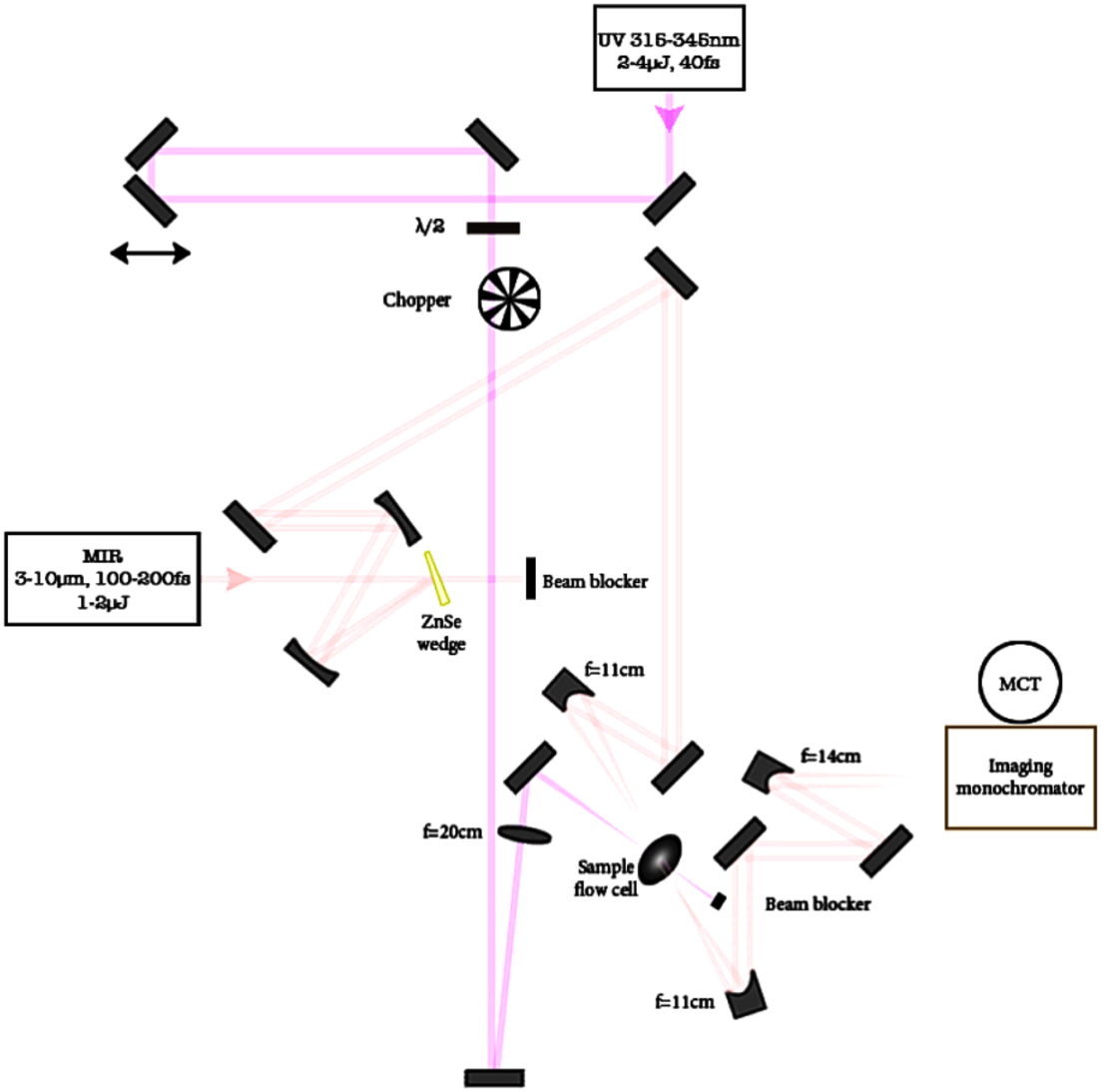

Figure 4.5: Optical design of the pump-probe detection set-up. The reference pulse propagates through a sample volume which is not excited while the generated third-order signal is collinear to the probe pulses. λ/2: half-wave plate, LWP: long wave pass filter, f: focal length. MCT: mercury cadmium telluride detector.

The intensity of each spectral component of both probe and reference pulses is recorded with a liquid nitrogen cooled double array (one for the probe and one for the reference) of 32 infrared sensitive mercury cadmium telluride (MCT) detector elements. These MCTs act as photoresistors, their resistance decreasing with increasing incident MIR light intensity. The change of the bias current is integrated with gated electronics synchronized to the laser repetition rate. A fast 16-bit Analogue-to-Digital converter (Keithley Instruments, DAS-1801-HC) for multi-channel single shot data acquisition is used to convert the input analogue voltage into a digital signal. Use of a reference pulse serves to correct for the intensity

fluctuations of the MIR signal resulting in an improved signal-to-noise ratio, indeed, absorbance changes as small as 10^{-4} can be detected using 400 shots per delay step.

The wavelength and delay times between the pump and the probe pulses are given by matrixes of intensity values. For each data point this corresponds to a normalization of the reference with the transmitted reference pulses and comparison of the pumped and umpumped signals:

$$\Delta A\ t,\omega\ = -log_{10}\ \ \frac{I(t,\omega)}{I_0(\omega)}\ \ probe \cdot\ \frac{I_0(\omega)}{I(\omega)}\ \ reference \tag{4.9}$$

Care was taken to use reflective optics (with the exception of the ZnSe wedge and the bandpass filter) in order to avoid distorting the beam profiles through dispersion or nonlinear effects.

In the MIR, another significant source of spectral and temporal distortion of pulses is due to absorption by water vapour and carbon dioxide (figure 4.6) leading to undesirable resonant interactions. In order to minimize this effect, the pump-probe setup is enclosed in a box purged with nitrogen.

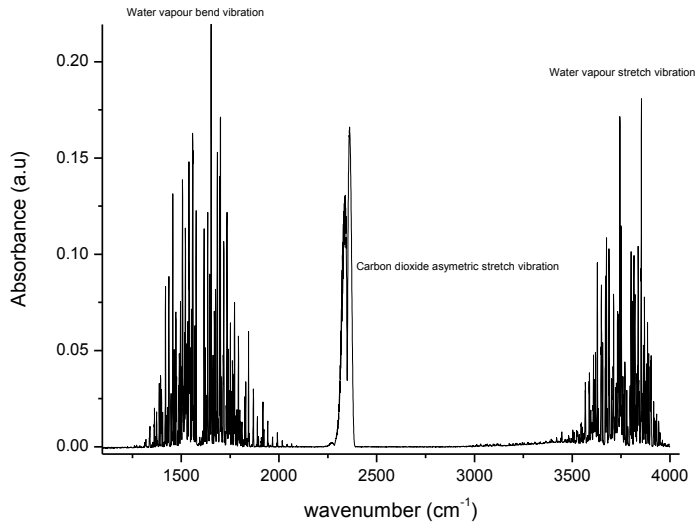

Figure 4.6: Mid Infrared spectral absorbance of atmospheric air at room temperature showing characteristic absorbance from water vapour and carbon dioxide. Around 3700cm^{-1} is the rovibrational fine structure of the symmetric and asymmetric OH stretch vibration of water vapour while the corresponding bending mode can be found at 1600cm^{-1}. The 2300cm^{-1} doublet is due to the asymmetric stretch vibration of gaseous carbon dioxide.

Time zero delay (corresponding to temporal overlap of probe and pump pulses in the sample) as well as the time resolution of the experiment is determined with a spectrally resolved cross-correlation experiment. To this end, a 1mm ZnSe semiconductor is placed in the sample position. Interaction with the UV pulse generates an instantaneous electron-hole plasma which is probed by the MIR pulse. The delay time τ dependant observed signal $S\ \tau$ is given by the temporal convolution of the response function of ZnSe, $R(t)$, with the second order intensity cross-correlation function $G(t)$ between the pump and the probe pulse:

$$S\ \tau\ = \int_{-\infty}^{\infty} R\ t-\tau\ G\ t\ dt \tag{4.10}$$

The response function can be described using the Heavside step function $\xi(t)$, where $R\ t\ = \xi(t)$, and $\xi(t)$=0 for $t < 0$ and $\xi(t)$=1 for $t \geq 0$. An example of this is shown in figure 4.7

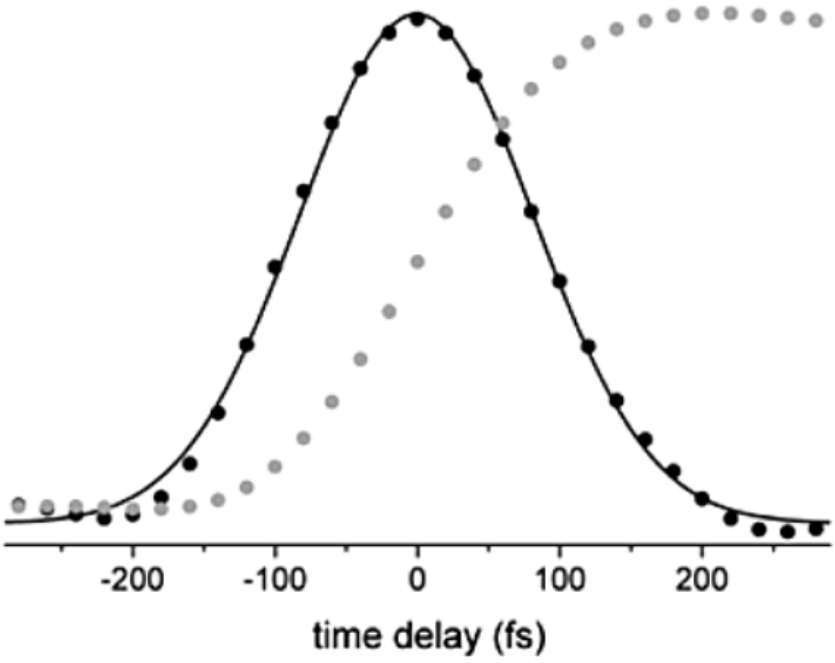

Figure 4.7: Pump-probe signal of a cross-correlation measurement in a ZnSe window for MIR pulses centered at 3µm (grey dots) with corresponding time derivative in black dots and Gaussian fit as a straight line giving a time resolution of 150fs.

In order to avoid possible accumulation of photoproducts and bleached molecules, the sample is continuously circulated through a flow cell consisting of CaF_2 windows separated by a Teflon spacer (25-300μm) by means of a peristaltic pump (Model xx). The small cycle volume insures that each measurement occurs on a fresh sample. The sample holder is further translated in both the vertical and horizontal directions. Viton tubing was used for nonpolar solvents like hexane and dichloromethane while neoprene tubing was used for polar solvents like dimethylsulfoxide and acetonitrile. All measurements were performed at room temperature, T=22.5±0.5°C.

4.3.2 Fluorescence up-conversion spectroscopy

Unlike coherent absorption processes, temporal resolution of spontaneous fluorescence emission cannot be achieved using pump-probe methods. Instead, a technique called fluorescence up-conversion spectroscopy is used whereby the induced emission from the sample is mixed with a gated pulse. More specifically, a first pulse serves to impulsively excite the sample molecules whose subsequent emission is then focused onto a nonlinear crystal where it is mixed with a third pulse thereby generating a nonlinear sum frequency signal when the two pulses overlap in time that is proportional to the emission intensity. By varying the time at which the gate pulse reaches the nonlinear crystal through the use of an optical delay line, one effectively recovers time slices of the temporal evolution of the emission.

The fluorescence up-conversion measurements were performed thanks to the collaboration of Dr. Messina and Dr. Braem in the laboratory of Professor Chergui at the EPFL.

4.3.2.1 The laser system

A chirped pulse amplified Ti:sapphire laser similar to that described in section 3.1.1 was used. The oscillator (Coherent, Mira-SEED) is pumped at 532nm with a 3W Nd:YVO_4 laser (Coherent, Verdi), producing 80nm 3nJ pulses at a repetition rate of 82MHz and with a 40fs pulse duration. This serves as the seed for the amplifier system (RegA) pumped with a 10W Nd:YVO_4 laser which outputs 800nm 50fs pulses at a repetition rate of 150kHz and with around 4μJ pulse energy. A 10/90 pellicle beamsplitter is used to generate the gate beam and the pump power for a UV parametric, respectively.

4.3.2.2 UV parametric source

A commercial OPA system delivers 400nJ pulses tunable from 500-600nm with a 15nm bandwidth. A prism compressor serves to reduce the pulse duration down to 50fs. The pulses are then focused with a lens (f=10cm) onto a 150µm BBO crystal (θ=43.3°) in order to generate the second harmonic with a 10% efficiency. The beam is collimated with a 45° off-axis parabolic mirror (f=5cm) and the remaining fundamental light is filtered out by the use of dielectric mirrors for the UV.

4.3.2.3 Fluorescence up-conversion experiment

A schematic representation of the time-gated up-conversion set-up is given in figure 4.8. The generated UV excitation beam is focused onto the sample with a 90° off-axis parabolic mirror (f=5cm) yielding a spot size at the focal point of 30-40µm. A long wave pass filter serves to remove the remaining pump beam after which the emission is collected with a large solid angle 45° off-axis parabolic mirror (f=5cm), and focused onto a 250µm BBO crystal. A SFM signal is generated with the 800nm, 40mW gate beam which traverses an optical delay stage consisting of a cubic retrorefector mounted on a motorized translation stage before being focused with a 30° off-axis parabolic mirror (f=30cm). In order to acquire spectrally resolved spectra, the SFM BBO crystal is mounted on a motorized rotational stage allowing for a rotation angle of 40° thereby phase-matching an extended wavelength range for every delay.

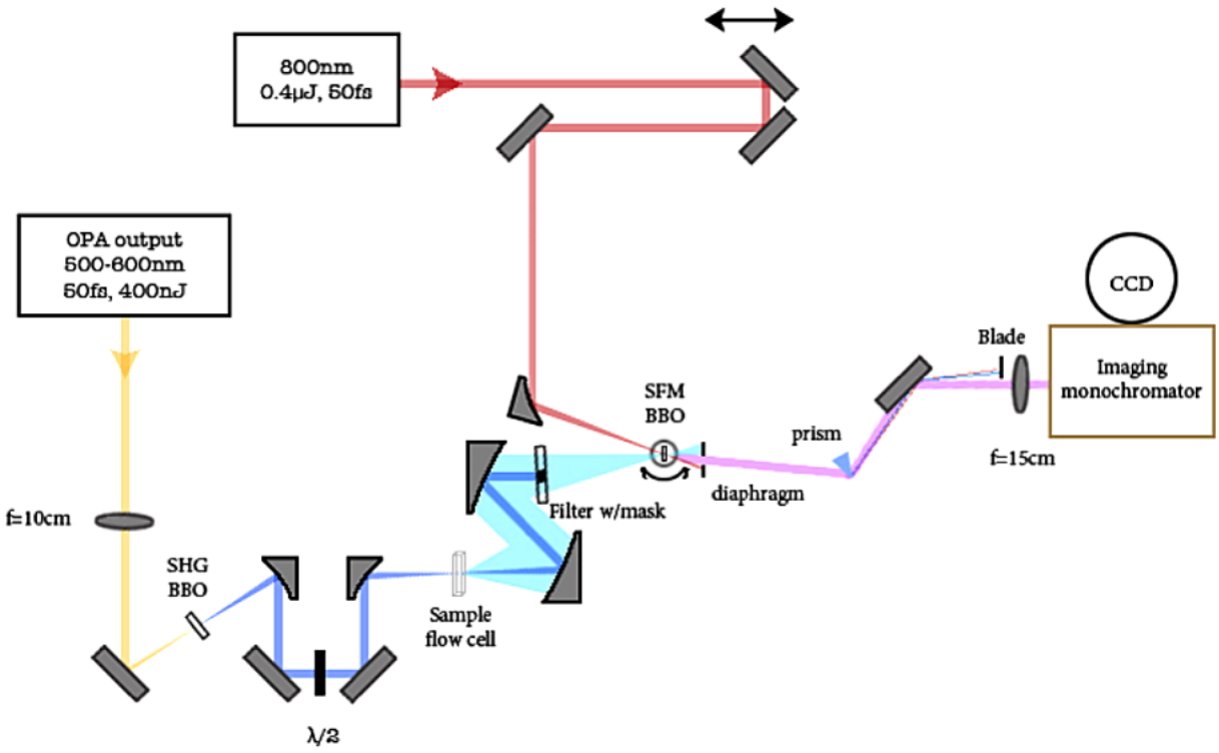

Figure 4.8: Optical design of the UV fluorescence up-conversion set-up. λ/2: half-wave plate, f: focal length, CCD: charge-coupled device detector.

The SFM setup has a noncolinear geometry permitting an efficient spatial filtering of the main part of the emission from the gate and the residual excitation beams through the careful positioning and aperture size of a diaphragm placed after the crystal. Further filtering is achieved by vertically dispersing the signal with a quartz prism and placing a blade in order to block all other wavelengths. The up-converted beam is then focused onto the entrance slit (between 0.25-1mm for a compromise between signal intensity, background noise and spectral resolution) of the monochromator (Acton Research, SpectraPro 500i) with a UV coated lens (f=15cm). A 600 grooves/mm grating blazed for 300nm is used to spectrally resolve the signal and is detected with a liquid nitrogen cooled CCD (charge-coupled device) camera (Photometrics, SDS 9000, 256 pixels with 4x4 binning). As the area of the CCD is much larger than that of the imaged signal, spatial selection of only the relevant area determined horizontally by the dispersion due to the monochromator and vertically by the prism is necessary.

A 0.2mm (check) quartz flow cell (Starna, 48/Q) connected to a peristaltic pump is used for the measurements. Furthermore, problems due to photo-aggregation on the inner flow cell

windows were avoided by mounting the sample holder on horizontally and vertically motorized translation stages effectively changing the sample spot for every laser pulse.

4.3.2.4 Fluorescence anisotropy measurements

Ultrafast fluorescence anisotropy measurements were carried out under 266 nm excitation (60 nJ/pulse) produced by tripling a portion (1/3) of the fundamental. This wavelength selectively excites the ^1L_a electronic state of both 1N and 2N with >95% selectivity, as estimated by decomposing the overall absorption spectrum in ^1L_a and ^1L_b contribution. The remaining 2/3 of the fundamental beam was used as a gate beam to up-convert the emission inside a BBO. Anisotropy measurements were carried out in single-wavelength detection mode. This choice allowed the use of a 0.1-mm thick BBO for the upconversion, which in turn provides a substantially better IRF (140 fs) as compared to polychromatic fluorescence measurements (250 fs), where a thicker (0.25 mm) crystal was necessary to detect the signal spreading over the whole wavelength detection range. A waveplate was used to set the polarization of the excitation beam to be parallel or perpendicular to that of the gate. The anisotropy is obtained by measuring independently the emission in parallel (I_{par}) and perpendicular (I_{perp}) polarization, at the spectral position where the fluorescence band was found to peak at short delay times. The anisotropy was then calculated using equation (4.6).

All anisotropy measurements were carefully corrected for the depolarization effects induced by the parabolic mirrors collecting the fluorescence, and for the finite contrast of the wave plate. To this aim we used as benchmarks the anisotropy of a known dye and that of the Raman signal of water excited at 400 nm or at 266 nm**.** In all time-resolved fluorescence measurements, the concentration of the molecule in solution was chosen to absorb approximately 0.3 OD through the 0.2 mm flow cell at the excitation wavelength.

4.3.2.5 Spectral correction

Artifacts arising from cosmic ray are removed by replacing the affected pixel with the average value of the neighboring pixels. Residual scattered light leads to a wavelength dependent signal which is corrected for by subtracting a background signal taken at negative delays. A low pressure mercury lamp (Oriel) serves to calibrate the detector wavelengths which are subsequently down-converted with the fundamental frequency in order to extract the emission wavelengths.

Although reflective optics are used as much as possible in the detection scheme in order to minimize dispersion effects, use of an excitation cut-off filter, the SFM crystal and the cell windows are unavoidable. These lead to group velocity dispersion (GVD) which induces a wavelength dependent time delay in the emission. As measurements are done over an extended wavelength range, this can lead to a significant distortion of the final data matrix where the time-zero can vary by as much as 1.5 ps between the blue most and red most spectral components. This is rectified by measuring the 2D spectra of a UV dye with well characterized dynamics under the same experimental conditions and applying the necessary correction so that the normalized kinetic traces all start to rise at the same time.

A wavelength dependent spectral response is unfortunately introduced as a consequence of various effects. Mainly; the chromatic aberration of the lens which collects the up-converted signal, the prism which leads to a vertical broadening of the signal beam size and reduced efficiencies of the SFM at angles far from the central phasematching angle due to the increase reflectivity of the incident beams. Correction for this effect is performed by normalizing the spectra of a dye which has no slow dynamics taken at long delays with its steady-state fluorescence spectra. In addition, where applicable, this is compared to the normalization of the probe molecule with its steady-state spectra.

4.3.3 Time correlated single photon counting

Time correlated single photon counting (TCSPC) is a method by which fluorescence lifetimes can easily be measured [205]. This method is based on using low power pulsed lasers with low repetition rates to stimulate emission from the absorbing probe molecule. The low repetition rates ensure that all the molecules are back in the ground state by the time the next pulse arrives, i.e., there is no photobleaching. The low power is important so that at most one fluorescence photon is detected per excitation pulse. Indeed, unlike the fluorescence up-conversion and pump-probe methods described previously, the detection in TCSPC relies on electronics and not nonlinear optical phenomena. Here, a small portion of each excitation pulse is picked off and sent to a photodiode. This serves as the time zero reference for the emitted photon arriving at the microchannel plate photomultiplier. Averaging over many excitation/detection cycles, gives the fluorescence kinetics at one particular wavelength and for one particular excitation frequency. The electronic synchronization means that the time resolution of a TCSPC is generally on the order of tens to hundreds of picoseconds and is thus

not an appropriate method to investigate ultrafast events. However, it is a simple and useful technique to obtain fluorescence lifetimes in the 100ps-ns range.

The TCSPC measurements were performed by Professor Pines and Professor Huppert at the Tel-Aviv University.

4.3.3.1 Experimental setup

Excitation was provided by the third harmonic of a cavity dumped Ti:sapphire femtosecond laser (Coherent, Mira) providing 80fs pulses at a repetition rate of 500kHz and 293nm. The pulse intensity was reduced to 10pJ by the addition of the appropriate neutral density filters. The detection system consists of a photomultiplier (Hamamatsu, 3809U) and an Edinburgh Instruments TCC 900 computer module. The measured instrument response function was 50ps.

4.4 Experimental conditions

1-Naphthol (99%), 2-Naphthol (99%), n-Hexane, cyclohexane, C_2Cl_4, $CHCl_3$, CH_2Cl_2 and 1,2-dichloroethane (Reagent Plus ≥99%) were all purchased from Aldrich. The solvents were then dried over molecular sieves and the naphthols purified by recrystalization. Deuterated acetonitrile (MeCN-d_3) and dimethylsulfoxide (DMSO-d_6) were purchased from Deutero.

In the transient IR measurements, the excitation energy was tuned to the lowest energy peak of the ^1L_b transition for each solvent, thereby ensuring minimal excess energy. As self-association was found to occur in the very non-polar solvents such as n-hexane or cyclohexane, low concentrations of 8-20mM for which no significant self-association occurs were used and path lengths of 300μM were employed in order to have sufficiently high transient signals. In more polar solvents like acetonitrile, concentrations of 50mM and path lengths of 50 μM were used. In the fluorescence up-conversion measurements, solutions of 0.2OD at the excitation frequency of 280-290nm were used in 200 μM cuvettes. Solutions were circulated through a flow cell by means of a peristaltic pump in order to ensure no photobleaching occurs.

Although none of the solvents used in this study showed any characteristic water bands in their respective IR spectra, a measurement was performed in order to verify that possible

minute amounts of water contamination had no bearing on our experiments. For this, the FTIR spectra of 1N in DCM to which known quantities of water were added was measured. No change in either frequency or bandwidth of the band corresponding to the free OH stretch of 1N was observed. This is expected given that the addition of a base to a non-polar solvent is known to deplete the free OH band without modifying its properties and results in the appearance of a new red-shifted and broadened band attributable to the hydrogen bonded complex with the base [206]. However, unlike for other bases like dimethylsulfoxide or acetonitrile, the addition of water did not immediately give rise to a pronounced band but instead a very slow diminution of the free OH stretch was observed with a concomitant slow rise of a broad red-shifted band. Unfortunately, at high water concentrations such as those needed to observe this red-shifted band, disambiguation with water dimers for a proper characterisation becomes problematic. Given the much higher cross-section of hydrogen bonded OH stretch bands, it thus appears that the complexation constant between water and naphthols is very low and as such, possible water contamination will not affect the measurements.

5. The O-H stretching vibration of complexed and uncomplexed naphthols in low dielectric media in the S_0 and S_1 states

The excited state proton transfer (ESPT) reaction which occurs in photoacids is incredibly complex involving namely: the charge redistribution of the photoacid, subsequent solvation and rearrangement of the hydrogen bond network, possible excited state level crossings, the dynamics of the proton transfer to the solvent or an accepting base through diffusion controlled reactions, electronic redistribution in the base, solvation of the base, dynamics of geminate recombination with the proton, possible quenching routes, and finite excited state lifetimes [28]. Untangling all of these processes in order to achieve a microscopic insight into the different steps involved is a momentous task. For this reason, we begin by simplifying the problem as much as possible by looking at the behavior of the OH stretch in low dielectric media where specific interactions are absent and proton transfer does not take place. In this way, we first hope to understand the intrinsic electronic charge redistribution occurring upon excitation and the nature and magnitude of solute-solvent couplings. The OH bond is the ideal mode to observe the charge redistribution event since it is a highly sensitive local probe of the bond involved in the proton transfer reaction. Also, while time resolved fluorescence studies are predominantly used to study solvation [207, 208, 209], given that solute-solvent couplings also affect the frequency position of the vibration of a solute, the field of time resolved IR spectroscopy is poised as an interesting alternative to these methods [210, 211, 212].

Once the behavior of uncomplexed naphthols is understood, 2-naphthol (2N) complexed with acetonitrile (MeCN) will be investigated. Looking at hydrogen bonded photoacids is essential in order to achieve a better understanding of photoacidity as ESPT reactions proceed along the HB formed between the photoacid and the solvent or an accepting base.

Spectroscopic methods are indirect in that they look at changes induced in a light beam as a result of its interaction with matter instead of direct observation of said matter. Extracting microscopic information from the resulting spectra thus requires the use of models. While the possibility of finding simple correlations between the OH stretch frequency and other molecular parameters is quite attractive, such correlations have invariably been found to be of limited applicability. Most correlations have been derived empirically such as Novak's correlation between the bond length and the OH stretch frequency [213]. Indeed, as the

minimum energy position of the nuclei and the vibrational levels are both determined by the potential energy surface, a direct relationship between them is expected. Derived for solids using diffraction methods, it is unfortunately of limited applicability in solution where the fluctuating solvent environment precludes the formation of a single well-defined linear HB geometry [152, 214]. Another notable empirical correlation is that derived by Badger and Bauer between the observed wavenumber shift and the enthalpy ΔH^0, taken as a measure of the bond energy [215]. While for idealized HBs with the same type of donor and acceptor, a simple relationship between the depth of the potential curve and the vibrational levels exists, this is not the case when HBs of differing chemical type are compared. There, numerous other complicating factors arise such as differences in solvation and geometries which severely limit the applicability of the Badger-Bauer relationship [216, 217]. The preponderant use of empirical correlations over the use of models is attributed to the fact that the calculation of frequency shifts requires parameters which cannot be accessed through experimental methods [109, 144]. However, this is slowly changing with the increasing sophistication of computational methods capable of accurately calculating the needed parameters such as the vectorial dipole moment of the solute and its derivatives.

As we are interested in treating a polyatomic molecule in solvents where no specific interactions occur, an approach such as described by Pullin where the solute-solvent interaction is treated as a perturbation to the vibrational Hamiltonian of the gas phase molecule is used [145, 146, 147]. In order to account for the non-equilibrium distribution generated in the excited state, the model is refined with the time-dependent theory by van der-Zwan and Hynes [160] that was described in Chapter 2.

5.1 Uncomplexed 1- and 2-naphthol

5.1.1 Transient IR experimental results

5.1.1.1 Ground-state vibrational spectra of 1- and 2-naphthol

The IR spectra of 1N and 2N in various non-polar solvents are shown in figures 5.1 and 5.2. As expected, the increase in the magnitude of the solute-solvent interactions upon increasing solvent polarity gives rise to a red-shift of the OH stretch frequency and line broadening. While it is well established that several mechanisms such as the solute vibrational population lifetime or the solute vibrational mode anharmonicity contribute to line broadening [152, 214,

218, 219], a simple linear correlation between the OH stretch frequency and the FWHM of the band is found here (figures 5.1b and 5.2b). This is similar to what has previously been reported for complexes with phenol [220, 221]. Furthermore, it is possible to extrapolate this correlation to the gas-phase values reported in the literature for 1N [222] and 2N [73, 75, 76, 223].

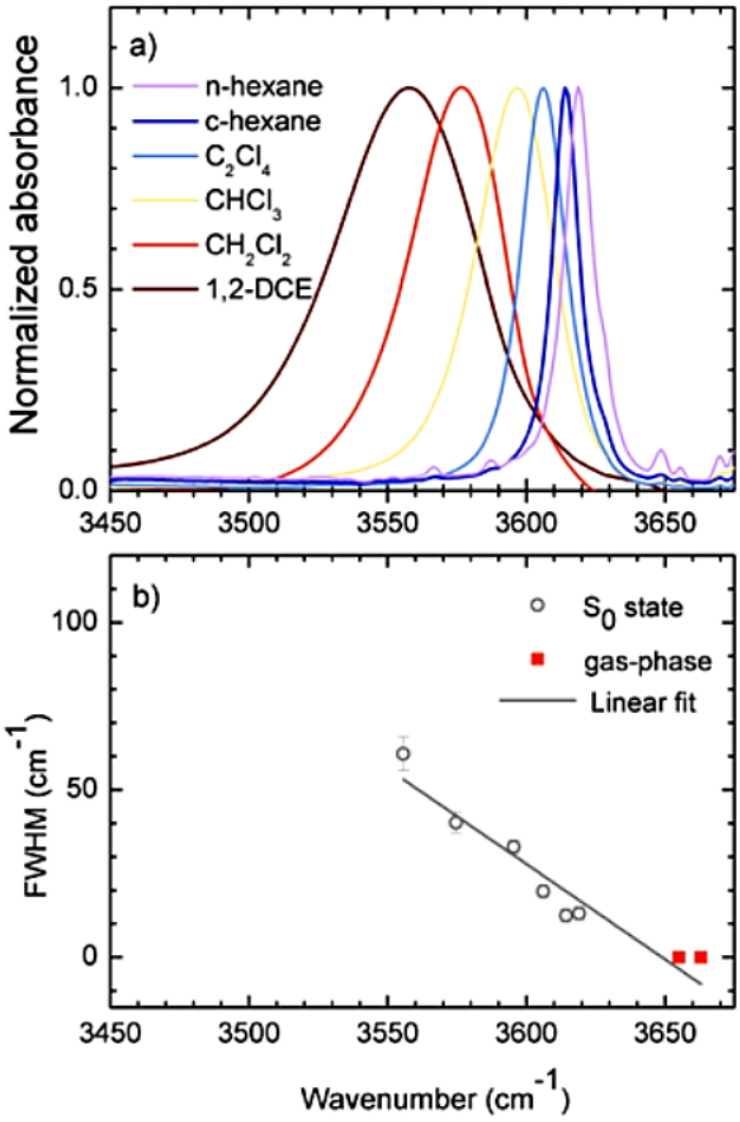

Figure 5.1: a) Steady-state IR spectra of 1N. b) Correlation between the solvent-dependent frequency shift and the bandwidth where the two red-squares represent the gas-phase values of the cis and trans rotamers from reference [222].

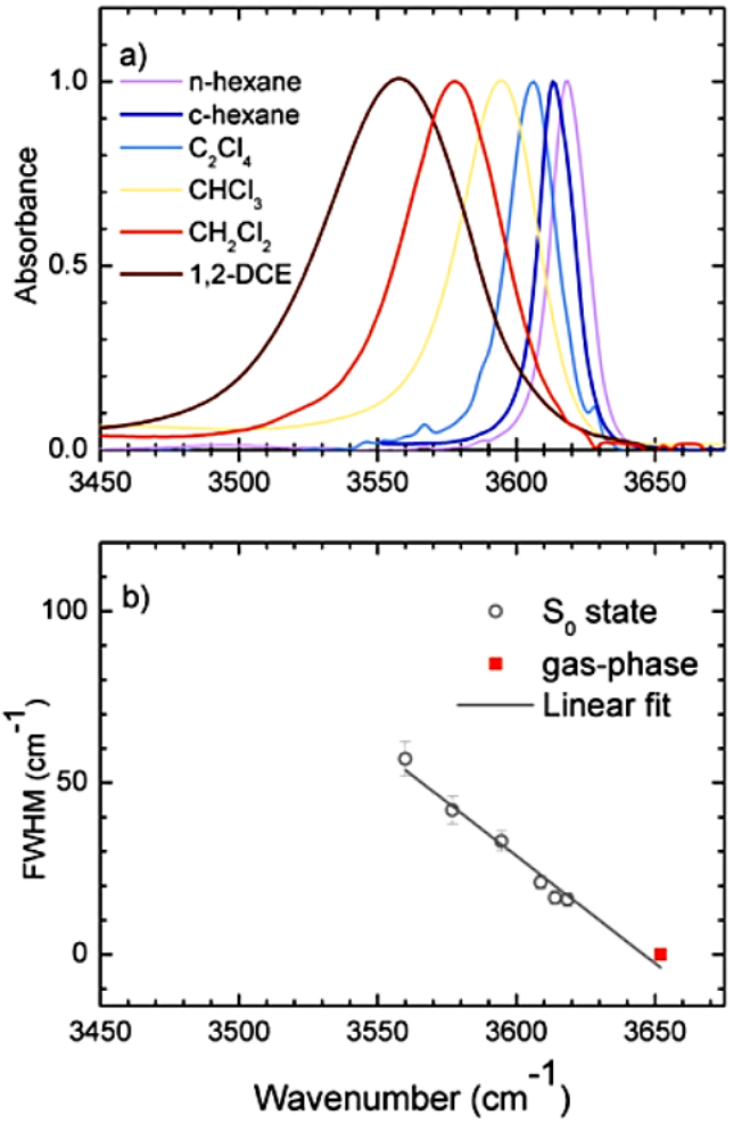

Figure 5.2: a) Steady-state IR spectra of 2N. b) Correlation between the solvent-dependent frequency shift and the bandwidth with the gas-phase value represented as a red square.

The selection rule for vibrational transitions is formally that only transitions between energy levels differing by one vibrational quantum number are allowed: $\Delta v = \pm 1$. This is relaxed by the effect of both the electrical and mechanical anharmonicity giving rise to overtones, where $\Delta v = \pm 2, \pm 3$ .... Electrical anaharmonicity describes the effect of the higher order terms in the expression for the dipole moment, while mechanical anharmonicity characterizes the effect of higher order terms in the potential energy function. The mechanical anharmonicity is defined as: $\omega_e x_e = \frac{v_{0,1} - v_{0,2}}{2}$ and results in diminishing energy spacing between vibrational levels. Mechanical anharmonicities are generally much larger than electrical anharmonicities. For this reason, what is commonly referred to as anharmonicity is the mechanical

anharmonicity. The anharmonicity of a non-hydrogen bonded OH stretch is usually about 100cm^{-1}, while hydrogen-bonded OH vibrations can have anharmonicities of several hundred wavenumbers [152]. The near IR spectra of 1N and 2N were measured from which the anharmonicites were calculated. These are given in table 5.2 in addition to literature values for phenol. Evidently, the anharmonicity does not vary much and actually shows a slight decrease with increasing solvent polarity as has been found by several researchers for phenol [224, 225, 226].

Table 5.1: Frequency of the ν_{02}OH vibration and the resulting calculated anharmonicity for 1N and 2N in various solvents compared to literature values for phenol from reference [226].

	1N		2N		Phenol	
Solvent	ν_{02}(cm^{-1})	$\omega_e x_e$	ν_{02}(cm^{-1})	$\omega_e x_e$	ν_{02}(cm^{-1})	$\omega_e x_e$
Gas-phase	-	-	-	-	7141	84
C_2Cl_4	7048	82	7045	86	-	-
$CDCl_3$	7037	77	7027	81	7032	83
CD_2Cl_2	7013	68	7003	76	7010	78
1,2-DCE	6983	64	6934	73	-	-

5.1.1.2 Excited-state vibrational spectra of 1- and 2-naphthol

The transient IR spectra of 1N and 2N in various non-polar solvents are given in figure 5.3. The spectra are characterized by a negative bleach signal corresponding to the S_0 $\nu_{OH}(\nu_0 \rightarrow \nu_1)$ vibration and a positive red-shifted and broadened signal corresponding to the S_1 $\nu_{OH}(\nu_0 \rightarrow \nu_1)$ vibration. This interpretation is consistent with the high frequency of the OH stretch vibration and excitation conditions at lowest energy maximum of the absorption spectrum resulting in little excess energy. As with the ground-state vibrations, a linear relationship between the frequency and the bandwidth is found (figure 5.3b and 5.3d). The bandwidth were determined through a fitting procedure using Voigt lineshapes in order to deconvolute the excited state peaks from the ground state bleach signals.

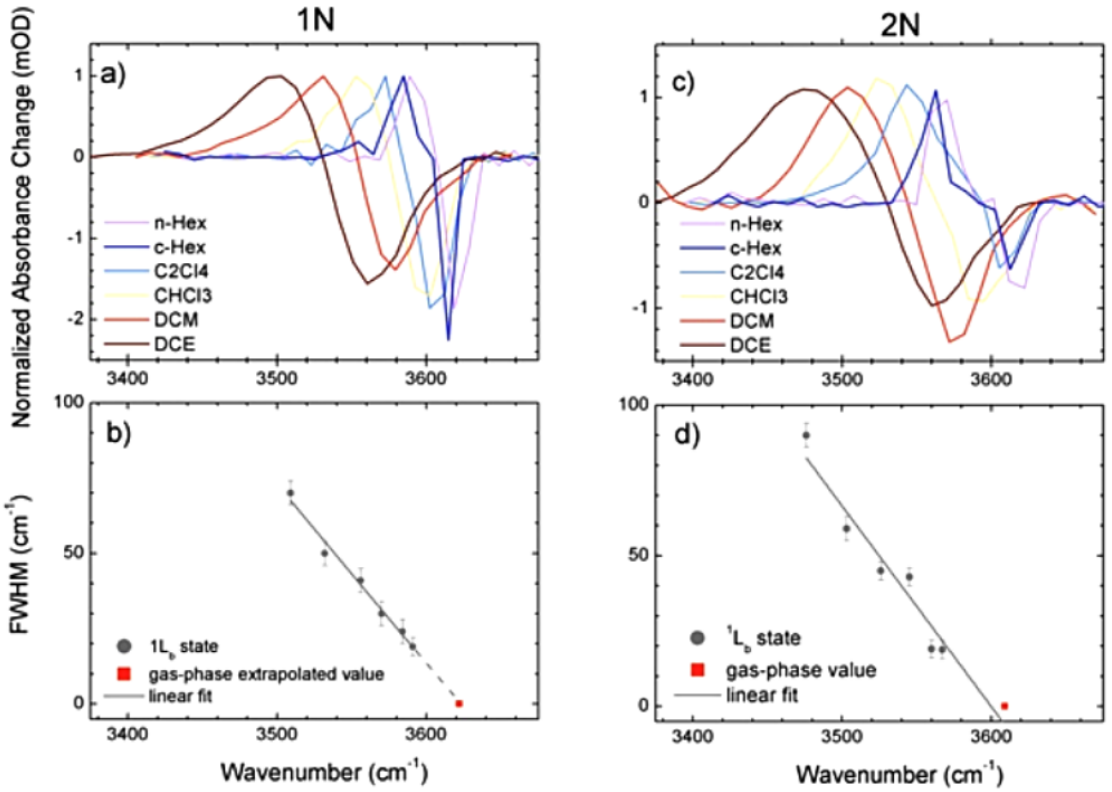

Figure 5.3: Transient IR spectra of a) 1N and c) 2N in various solvents. Correlation between the solvent-dependent frequency shift and the bandwidth for b) 1N and d) 2N. The gas-phase value from reference [73] is given as a red-square for 2N. The transient spectra are given at a time delay of 10ps.

The transient spectra are given at 10ps as no significant dynamics were measured. Only for 2N in the most polar 1,2-DCE solvent is a slight time-dependent frequency shift observed (figure 5.5).

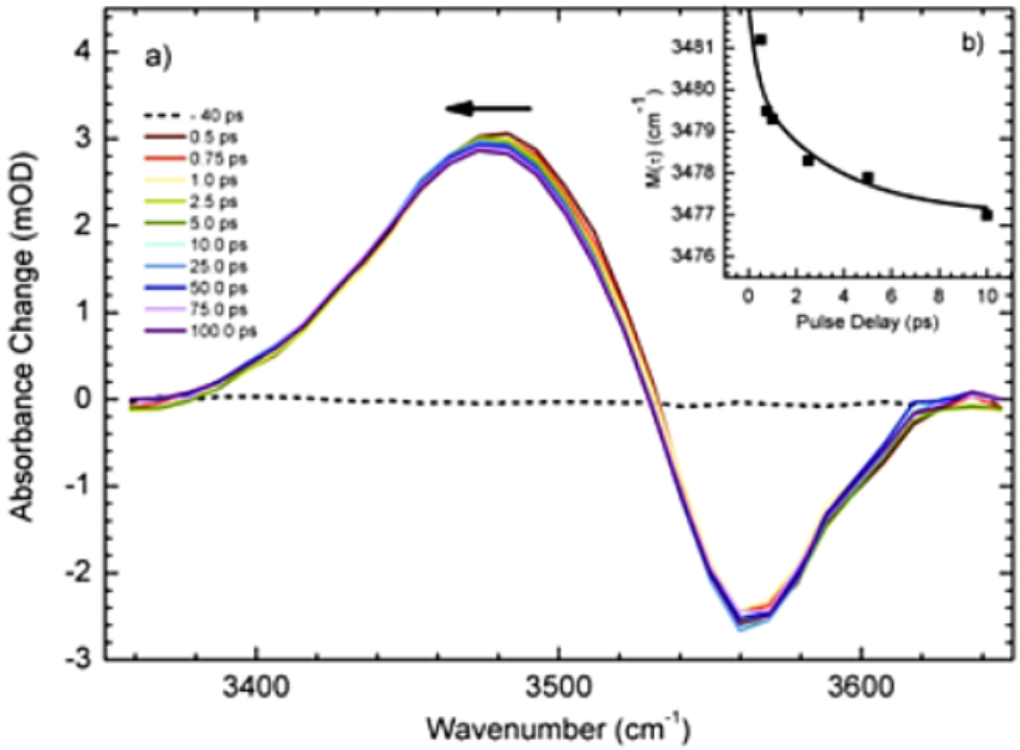

Figure 5.4: a) Transient IR spectra of the OH stretching mode of 2N in 1,2-dichloroethane b) time-dependent frequency shift showing a small red-shift at early delays. The bi-exponential fitting parameters are the same as those used in reference [227]: A_1=0.34, A_2=0.26, τ_1=0.26ps and τ_2=3.5ps.

5.1.2 Quantum chemical results

The quantum calculations were performed by Dr. Xiao in the group of Professor Batista at Yale University.

5.1.2.1 Computational methods

Geometry optimization and calculations of ground state molecular properties, including electronic energies, vibrational normal modes, transition dipole moments, electrostatic potential (ESP) atomic charges, dipole moments, dipole derivatives with respect to normal modes, and solvation energies were obtained at the DFT (B3LYP/TZVP) level of theory, as implemented in *Gaussian 09* [228]. Analogous excited state calculations were performed at the TD-DFT (B3LYP/TZVP) level. The polarizable continuum model (PCM) was used for computations of solvation energies and for geometry optimization in dielectric continuum

media. The order of the excited states ^1L_a and ^1L_b in the energy ladder of both the *cis*- and *trans*- rotamers of 1N or 2N was found to be inverted with respect to the energetic order probed by experiments [78, 229]. This behavior was studied previously and attributed to an underestimation of the interaction between ionic components in the ^1L_a-state due to the improper asymptotic form of standard functionals [230]. However, the distinct electronic symmetry of these states enabled us to identify the ^1L_b state and compute its molecular parameters at the TD-DFT level, including the dipole moment as well as its first and second derivatives.

The anharmonic force constant and the harmonic constant were calculated by the anharmonic vibrational analysis implemented in the *Gaussian 09* program. For the anharmonic vibrational analysis, the HF/6-31g method was used for the ground state, and the CIS/6-31g method was used for the excited state. Once the first derivatives of the dipole moment with respect to the *k*-th normal mode ($\mu_k^{'} = \frac{\partial \mu}{\partial Q}$) were calculated, the second dipole moment derivatives were computed as follows:

$$\mu_k^{''} = \frac{\partial\left(\mu_k^{'}\right)}{\partial Q} = \sum_i \frac{\partial\left(\mu_k^{'}\right)}{\partial x_i} l_{ik} \tag{5.1}$$

where l_{ik} is the transformation matrix from the Cartesian coordinate to the normal mode coordinate and the derivative in the Cartesian coordinate $\frac{\partial\left(\mu_k^{'}\right)}{\partial x_i}$ was calculated numerically by finite differences:

$$\frac{\partial\left(\mu_k^{'}\right)}{\partial x_i} = \frac{\mu_k^{'}\left(x_i + \delta x_i\right) - \mu_k^{'}\left(x_i - \delta x_i\right)}{2\delta x_i} \tag{5.2}$$

5.1.2.2 Calculated molecular parameters

Within the Pullin-van der Zwan-Hynes model, the solvent-dependent vibrational frequency shift is governed by the following parameters: the solute vibrational potentials V_i'' and V_i''',

the solute dipole moment as well as its first and second derivative, and the Onsager cavity size a_i. The last can be estimated within Onsager's reaction field theory [139], while the other parameters can be calculated with *ab initio* quantum chemical methods. Table 5.2 summarizes all the calculated parameters necessary to derive the solvent-induced vibrational frequency shifts according to equation 2.37 described in chapter 2.

Table 5.2: Calculated parameter values for 1N and 2N governing the solvent-induced vibrational frequency shifts.

Term	*cis*-1N		*trans*-1N		*cis*-2N		*trans*-2N	
	^1L_b	S_0	^1L_b	S_0	^1L_b	S_0	^1L_b	S_0
$\mu_i'' \cdot \mu_i^0$ (D^2 A^{-2} amu^{-1})	0.2493	0.5892	3.2824	-2.3544	1.2257	-0.8876	2.0618	-1.5944
$\mu_i' \cdot \mu_i^0$ (D^2 A^{-1} amu$^{-1/2}$)	0.3085	-0.8621	2.8132	1.4500	1.0651	0.6820	1.5468	1.4097
$\frac{V_i'''}{V_i''}$(A^{-1} amu$^{-1/2}$)	7.1204	-7.1510	7.0932	-7.0928	7.1234	-7.1660	7.1295	-7.1714
$\mu_i'' \cdot \mu_i^0 - \frac{V_i'''}{V_i''}\mu_i' \cdot \mu_i^0$	2.4471	-5.9156	23.2370	7.9302	6.3614	3.9996	8.9661	8.5151
$(\mu_e'' - \frac{V_e'''}{V_e''}\ \mu_e') \cdot\ \mu_g^0 \cdot \mu_e^0$	0.5798		4.8622		2.7099		1.9909	
a_i(Å)	0.7611	1.4195	1.5524	1.2667	1.1762	1.1260	1.3071	1.4374
ν_0^i (cm^{-1})	3620	3661	3620	3655	3609	3653	3609	3661
S_i(cm^{-1})	129.96	-47.883	145.43	90.48	91.82	65.00	94.29	66.38
$\mu_i' \cdot \mu_i'$ [D^2 A^{-2} amu^{-1}]	0.9188	1.0201	2.8860	1.6117	1.9995	1.4872	2.3046	1.9135
$\mu_i' \cdot \mu_i' + \mu_i^0 \cdot \mu_i''$	0.6695	1.6093	6.1684	-0.7427	0.7738	0.5996	0.2428	0.3191
B_i [cm^{-1}]	14.2223	5.2105	15.4421	-0.3896	4.4674	3.8981	1.0214	0.9951
$\frac{S_e}{S_g}$	2.71		1.61		1.41		1.42	

In order to calculate the preceding parameters, it was essential to consider the vectorial properties of the dipole moments. The detailed calculated values and orientations of the dipole moments used to calculate the parameters in table 5.2 are given in table 5.3.

Table 5.3: Orientation and calculated values of $\boldsymbol{\mu_0}$, $\boldsymbol{\mu'}$ and $\boldsymbol{\mu''}$ for both cis and trans rotamers of 1N and 2N.

	***cis*-1N**	***trans*-1N**	***cis*-2N**	***trans*-2N**
S_0, μ	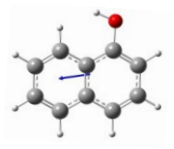	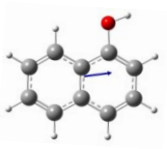	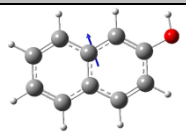	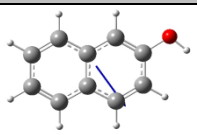
(D)	(1.4425, 0.1685, 0.1648)	(-1.2633, -0.1657, 0.0000)	(0.2822, -1.0500, 0.0000)	(-0.5493, 1.5094, 0.0000)
S_0, μ′	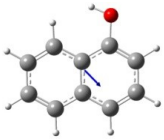	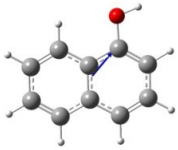	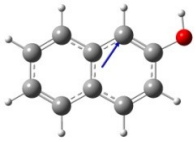	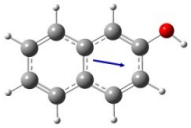
($D \cdot A^{-1} \cdot amu^{-1/2}$)	(-0.4823, -0.8807, -0.1090)	(-1.0552, -0.7059, 0.0000)	(-0.8472, -0.8772, 0.0000)	(-1.3049, 0.4591, 0.0000)
S_0, μ′′	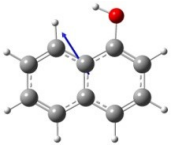	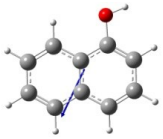	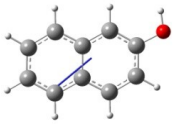	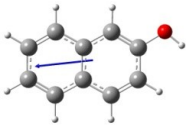
($D \cdot A^{-2} \cdot amu^{-1}$)	(0.6569, 2.0075, -0.1223)	(1.6293, 1.7867, 0.0000)	(2.2077, 1.4387, 0.0000)	(2.5638, -0.1233, 0.0000)
^1L_b, μ	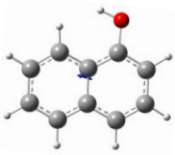	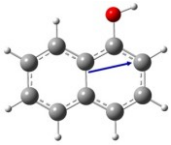	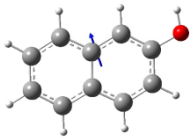	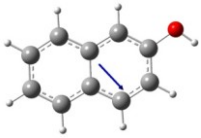
(D)	(0.5274, 0.2977, 0.1415)	(-1.9069, 0.1051, -0.0015)	(0.1445, -1.2190, -0.0016)	(-0.7536, 1.2544, -0.0013)
^1L_b, μ′	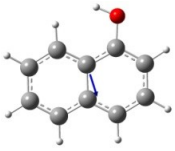	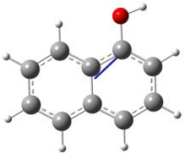	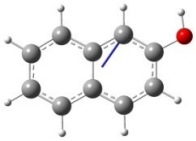	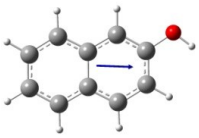
($D \cdot A^{-1} \cdot amu^{-1/2}$)	(-0.0187, -0.9523, -0.1074)	(-1.5174, -0.7693, 0.0000)	(-1.0066, -0.9931, 0.0000)	(-1.4784, 0.3449, 0.0002)
^1L_b, μ′′	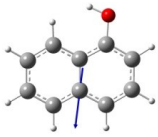	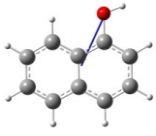	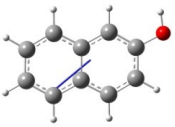	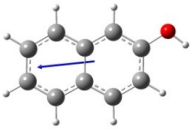
($D \cdot A^{-2} \cdot amu^{-1}$)	(1.0807, -2.5928, -0.3349)	(-1.8408, -2.1678, -0.0043)	(2.2640, 1.2739, 0.0000)	(2.4719, -0.1586, -0.0074)

As is evident from tables 5.2 and 5.3, the *cis* and *trans* isomers have significantly different properties. Comparison with the experiment thus necessitates a precise evaluation of the relative ratio of *cis* and *trans* isomers present for each solvent. In order to do this, the energy difference between the two forms was calculated for both the gas-phase as well as the solvents used in the experiment. Figure 5.5 gives the resulting energy difference between the two rotamers for 1N and 2N in both the electronic ground-state as well as the first excited state.

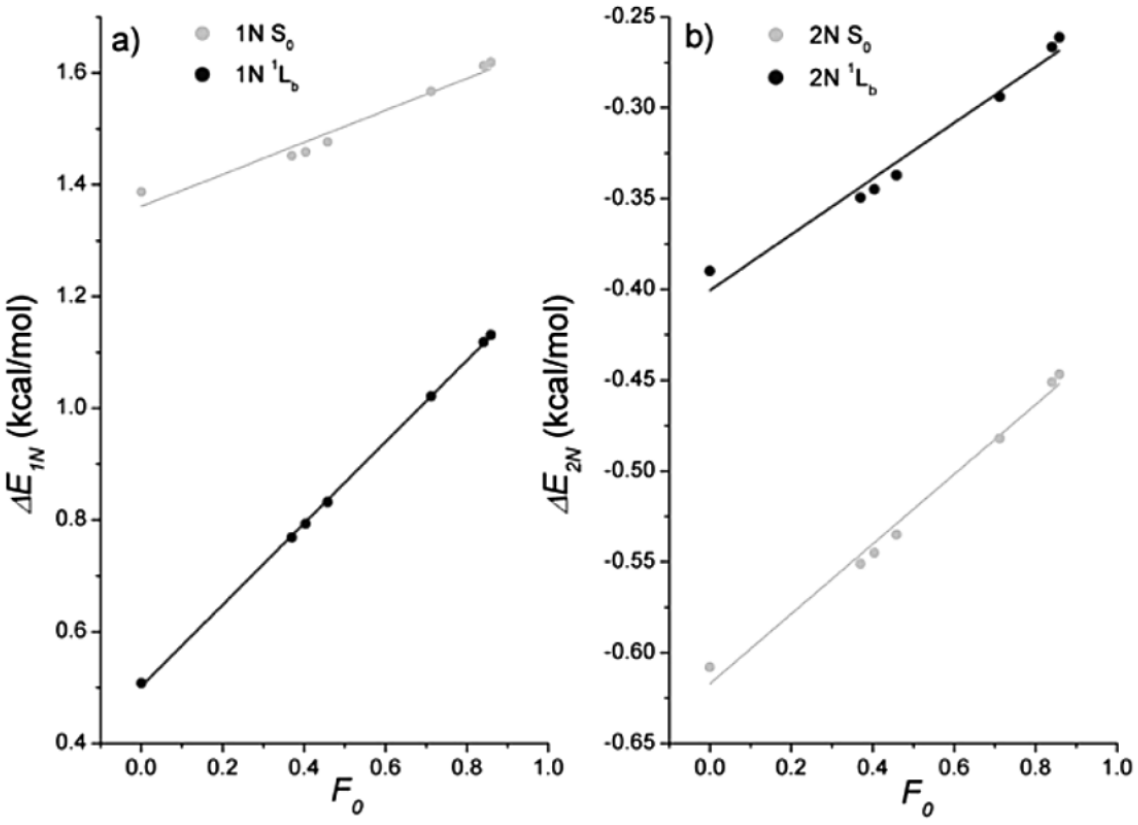

Figure 5.5: Energy difference, $\Delta \boldsymbol{E} = \boldsymbol{E_{cis}} - \boldsymbol{E_{trans}}$, in the ground and first excited state as a function of the solvent function $\boldsymbol{F_0} = \frac{2\varepsilon_0 - 2}{2\varepsilon_0 + 1}$ for a) 1N and b) 2N.

The positive $\Delta E = E_{cis} - E_{trans}$ found for 1N signifies that the *trans* rotamer is the more stable form, with the dielectric medium serving to further increase the energy separation between the rotamers to values much larger than kT (1kT=0.593 kcal/mol at 295K). An average energy separation in solution of 0.82kcal/mol for the ^1L_b-state and 1.5kcal/mol for the S_0-state is found. Assuming a Boltzmann distribution, $\exp(-\frac{\Delta E}{kT})$, the population ratio of *cis*-1N:*trans*-1N in the ground-state is 0.07:0.93, while in the first excited-state it is 0.2:0.8. This last value assumes that equilibration is possible on sub-picosecond timescales. The calculated values for the ground-state are in good agreement with values obtained in an NMR study in

CCl_4 [137]. For 2N, the negative ΔE_{2N} is representative of a lower energy *cis* rotamer, in contrast to 1N. Also, the effect of the dielectric media serves to decrease the energy separation leading to a population ratio of 0.71:0.29 for the ground-state and 0.63:0.47 for the first excited-state. These values are summarized in table 5.4.

Table 5.4: Energy difference and population ratios for 1N and 2N in the ground and first excited-state.

Average ΔE_{1N} (kcal)		***cis*-1N/*trans*-1N**		Average ΔE_{2N} (kcal)		***cis*-2N/*trans*-2N**	
S_0	^1L_b	S_0	^1L_b	S_0	^1L_b	S_0	^1L_b
1.5	0.82	0.07:0.93	0.2:0.8	-0.53	-0.31	0.71:0.29	0.63:0.47

5.1.3 Discussion

5.1.3.1 Excited-state dynamics

As is evident from figure 5.4, even in the most polar solvent used in this study (1,2-DCE), the time-dependent solvation shifts are minimal. The shift upon excitation of 2N in 1,2-DCE is of 79cm^{-1}, of which it is determined that 36cm^{-1} corresponds to a solvation induced component by comparison with the gas-phase values [73, 75]. In contrast, the non-instantaneous solvent-shell rearrangement is only 4cm^{-1}. It is possible to estimate the relative importance of instantaneous versus non-instantaneous contributions to the excited-state time-dependent vibrational frequency shift from the frequency shift ratio. This is the ratio of the early time-dependent shift ($t = 0$) versus the long time shift ($t = \infty$):

$$\sigma \equiv \frac{\Delta v_s^e \ t = 0 \ - \Delta v_s^e \ t = \infty}{\Delta v_s^e \ t = \infty} \tag{5.4}$$

$$= \frac{F_0 - F_\infty \quad \boldsymbol{\mu}_e'' - {}^{V_e'''}_{V_e'} \cdot \boldsymbol{\mu}_g^0 - \boldsymbol{\mu}_e^0}{F_0 \ \boldsymbol{\mu}_e'' - {}^{V_e'''}_{V_e'} \cdot \boldsymbol{\mu}_e^0 + F_\infty \ \boldsymbol{\mu}_e'' \cdot \boldsymbol{\mu}_e^0 + \boldsymbol{\mu}_e' \cdot \boldsymbol{\mu}_e'} \tag{5.5}$$

Figure 5.6a gives the values of F_0 and F_{or} as a function of the static dielectric constant. It is evident that for non-polar solvents like n-hexane, where $F_0 \approx F_\infty$, equation 5.5 will be close to zero explaining why no time-dependent frequency shifts were observed: they are effectively much smaller than our experimental resolution. This is illustrated in figure 5.6b where the

calculated frequency shift ratios are given. For 2N in 1,2-DCE, the model predicts a maximum value of 15% attributable to the non-instantaneous response. The experimental value for the non-instantaneous component of the solvation driven shift is of 10%. The slightly lower value is likely due to the limited temporal resolution where the early components are not properly resolved. Additionally, the temporal behavior of the OH stretch frequency downshift observed here corresponds exactly with the transient shift of the electronic bands of hydroxypyrene trisulfonamide (HPTA) in the same solvent, even though both the ground and excited-state dipole moments are much greater for HPTA than 2N (figure 5.4b) [227].

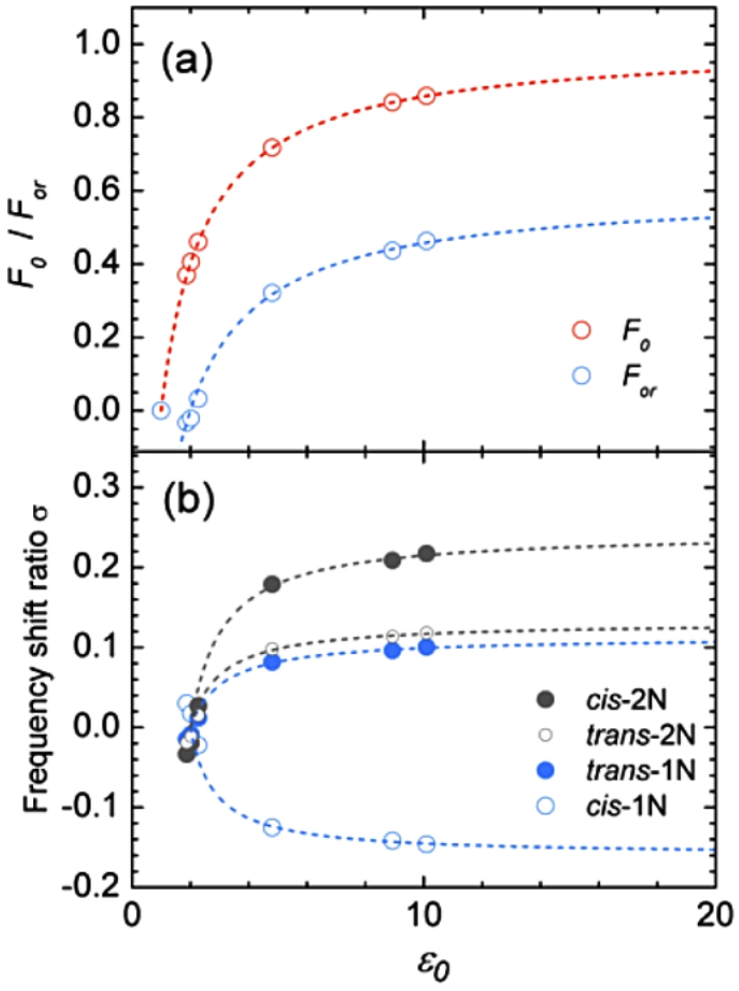

Figure 5.6: Dependence of a) $\boldsymbol{F_0 = \frac{2\varepsilon_0 - 2}{2\varepsilon_0 + 1}}$ and $\boldsymbol{F_{or} = F_0 - F_\infty}$ and b) the frequency shift ratio σ (equation 5.4), on the static dielectric constant. The values of $\boldsymbol{\varepsilon_0}$ taken from the literature and $\boldsymbol{\varepsilon_\infty}$ measured at 3μm are given in table 2.4.

As can be seen in figure 5.6b, the average non-instantaneous response of 1N is about 2-3 times smaller than for 2N. This readily explains why it was not possible to resolve any shifts with our experimental resolution.

It must be noted that while vibrational cooling also gives rise to time-dependent band shifts, it leads to a frequency upshift and not a frequency downshift as was observed here [13, 231]. Also, care was taken to excite the molecules around the electronic origin in order to insure minimal excess energy, thus making vibrational cooling processes for these high frequency bands in non-polar solvents unlikely. One can therefore conclude that the observed shifts are indeed due to solvent-shell rearrangements and that most of the process occurs instantaneously upon excitation.

The frequency shift which has been attributed to the instantaneous solvation response could also be due to changes in the anharmonicity of the OH stretching potential. In order to discount such an effect, the NIR spectra of 1N and 2N were measured from which the anharmonicity was calculated (table 5.1). It can be seen that increasing solvent polarity has very little effect and actually serves to slightly decrease the anharmonicity. Quantum chemical calculations of the gas-phase molecules further shows that the anharmonicity is basically unaffected by electronic excitation. It is thus possible to conclude that the observed shifts are indeed due to solvation response and not changes in anharmonicity.

5.1.3.2 Comparison between experiment and theory

The experimentally measured OH-stretch frequency shifts as a function of F_0 for 1N and 2N, in the S_0 and ^1L_b states are given as points in figure 5.7, with the straight slopes representing the Pullin model in figure 5.7b and 5.7d compared to a TD-DFT calculation with a PCM solvent in figure 5.7a and 5.7c. A much better agreement between the experimental frequency shifts and the corresponding shifts computed with the Pullin's model is achieved compared to predictions based on the standard PCM techniques as implemented in Gaussian 09 at the same level of TD-DFT theory (DFT for the ground-state). This is likely due to the fact that, unlike the standard PCM models which solely include the static response of the solvent, in Pullin's model the reaction field includes both static and optical response functions induced by

changes in the molecular point dipole moment associated with vibrations and/or electronic excitation. Pullin's model has the disadvantage of simplifying the electrostatic description of the molecule to a point dipole, but given the good correspondence between experiment and theory it seems that this is a reasonable approximation for this system.

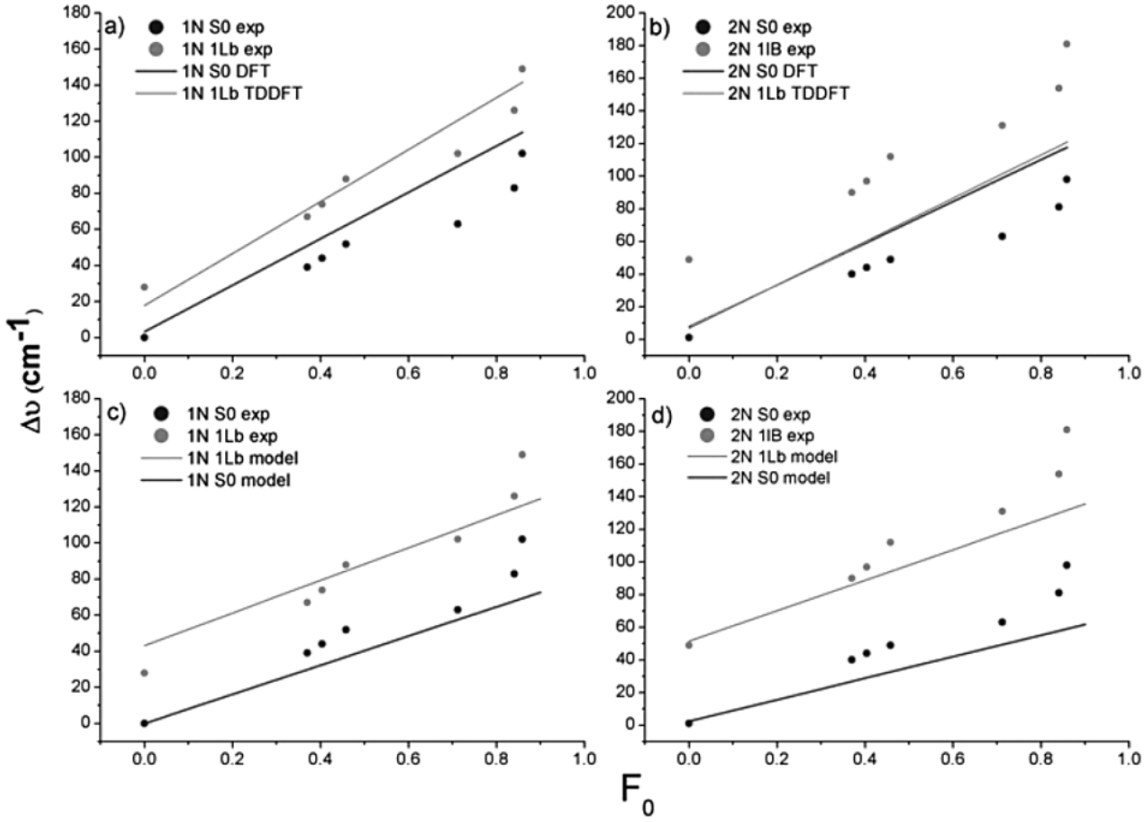

Figure 5.7: Experimental frequency shifts (dots) as a function of F_0 in the S_0 and ^1L_b states with straight lines calculated with the PCM model for a) 1N and b) 2N, and Pullin's model c) 1N and d) 2N.

In order to quantitatively compare the experimental results with Pullin's model, it is useful to define a slope ratio, $S_e \quad S_g$:

$$\frac{S_e}{S_g} = \frac{\boldsymbol{\mu}_e'' \cdot \boldsymbol{\mu}_e^0 - \frac{V_e'''}{V_e''}\boldsymbol{\mu}_e' \cdot \boldsymbol{\mu}_e^0}{\boldsymbol{\mu}_g'' \cdot \boldsymbol{\mu}_g^0 - \frac{V_g'''}{V_g''}\boldsymbol{\mu}_g' \cdot \boldsymbol{\mu}_g^0} \quad \frac{v_0^g}{v_0^e} \cdot (a_g \quad a_e)^3 \tag{5.6}$$

From table 5.2, it can be seen that the slope ratio is mostly governed by the factor containing the gas phase dipole moment terms: $\frac{v_e'''}{v_e''}\boldsymbol{\mu}_e' \cdot \boldsymbol{\mu}_e^0$, with $\boldsymbol{\mu}_i'' \cdot \boldsymbol{\mu}_i^0$ providing a significant correction term in both the ground and the excited state. In contrast, since the Onsager cavity size changes little upon excitation, $(a_g \;\; a_e)^3$ provides only a small correction term.

The experimental slope ratio for 1N is 1.08 ± 0.05, and 1.23 ± 0.05 for 2N, where the positive slope implies a frequency downshift. The calculated slope ratios are given in table 5.2 for the two rotamers. For 2N, the calculated slope ratio is practically the same for the *cis* and *trans* rotamers and is found to slightly overestimate the changes between the ground and the excited state. In the case of 1N, as the *cis* and *trans* slopes are greatly different, it is necessary to take into account the relative populations of the two rotamers. Given the large negative slope of the *cis*-rotamer, the calculated average slope ratio is 1.12 which is remarkably close to the experimental value.

5.1.3.3 Comparison between 1- and 2-naphthol

The ground-state frequency of the OH stretch of 1N is marginally more downshifted than that of 2N in a given solvent, concomitant with 1N's slightly higher acidity. In the excited-state, one instead finds that it is 2N which is at lower frequencies. In a particular solvent medium, the frequency shift ω_{ge} upon excitation is determined by the following:

$$v_0^g - v_s^g = S_g F_0 + B_g \tag{5.7}$$

$$v_0^e - v_s^e = S_e F_0 + B_e \tag{5.8}$$

from which we derive:

$$\omega_{ge} = v_s^g - v_s^e = (v_0^g - v_0^e) + (S_e - S_g)F_0 + (B_e - B_g) \tag{5.9}$$

Hence, ω_{ge} is determined by the frequency shift upon excitation in the gas phase $\nu_0^g - \nu_0^e$, the slope difference $S_e - S_g$ and the intercept difference $B_e - B_g$ of the frequency shifts between the electronic excited and ground states upon solvation. As the frequency shifts upon electronic excitation in the gas phase are due to charge rearrangement, one could initially conclude that the extent of charge transfer is larger in 2N. In order to properly characterize this effect, the electrostatic potential (ESP) charge difference due to the $S_0 \rightarrow {}^1L_b$ transition for the *cis*- and *trans*-rotamers of 1N and 2N was studied. ESP charges were calculated using the MP2/TZVP method for electronic ground states, and the TD-B3LYP/TZVP method for electronic excited states. The rationalization for choosing these *ab initio* methods was based on the fact that the calculated OH-stretching vibrational frequencies using these methods for the ground and excited states of 1N and 2N show good consistency with the experimental vibrational frequencies (Table 5.5).

Table 5.5: Charge flow induced by the $S_0 \rightarrow {}^1L_b$ excitation of 1N and 2N. The maximal negative change (i.e. increasing electron density) is represented in red, and the maximal positive change (i.e. decreasing electron density) is represented in blue. The range of charge change is from -0.1 to 0.1. The ground state ESP charge was obtained by the MP2/TZVP method, while the excited state ESP charge was obtained by the TD-B3LYP/TZVP method.

	1N	2N
cis		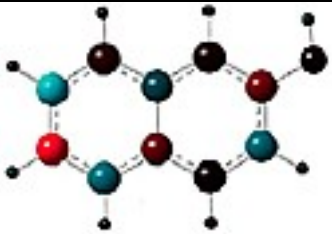
trans		

The calculations reveal that, contrary to the initial assumption, electronic excitation leads to a larger transfer of electron density from the OH-group to the naphthalene ring in 1N compared to 2N. While the extent of charge transfer is largest in *cis*-1N (+0.072 charge difference on the O-atom) which is the least abundant rotamer, the charge transfer in *trans*-1N (+0.032) is still larger than either rotamers of 2N (0.027 in *cis*-2N and 0.022 in *trans*-2N).

That the magnitude of the OH stretch frequency shift is not directly correlated with the extent of charge redistribution can be attributed to the fact that the first and second derivatives of the dipole moment are not directed along the OH bond vector (table 5.7). Consequently, despite the fact that the nature of the OH stretching vibration is largely that of a local mode, elongation along the OH stretching coordinate has a larger effect on the electronic charge distribution in a direction different from the OH bond vector.

Table 5.6: Calculated and experimental OH stretch vibrational frequencies.

		calcd frequency (cm^{-1}) [a]	scaled frequency (cm^{-1}) [b]	calcd ω_{ge} (cm^{-1}) $S_0 \rightarrow {}^1L_b$	exptl frequency (cm^{-1}) [c]	exptl ω_{ge} (cm^{-1}) $S_0 \rightarrow {}^1L_b$ [c]
***cis*-1N**	S_0	3850.6	3659	56	3661	35*
	^1L_b	3791.5	3603		3622*	
***trans*-1N**	S_0	3841.6	3650	37	3655	
	^1L_b	3802.0	3613		3622*	
***cis*-2N**	S_0	3840.4	3649	25	3653	48*
	^1L_b	3813.9	3624		3609*	
***trans*-2N**	S_0	3852.7	3661	32	3661	
	^1L_b	3818.8	3629		3609*	

[a]: S_0-state calculated using MP2/TZVP method, ^1L_b-state calculated with the TD-B3LYP/TZVP method. [b]: Scaling factor: 0.9502.[c]: Experimental values of 1N and 2N in the gas phase taken from references [73, 76, 223, 232]. "*"Average value for *cis*- and *trans*-conformers.

While quantifiable differences are observed between 1N and 2N, neither molecule undergoes large changes in charge on the oxygen upon excitation. This is in agreement with all the recent gas-phase calculations for 2N and cyanophenols [28, 29], where the lack of significant charge redistribution in the acid compared to the photobase has fueled a re-evaluation of the concept of photoacidity. Indeed, based on their calculations, it is now claimed that photoacidity is instead driven by changes in the conjugate base where large charge differences have been calculated and not the acid where only minor changes occur. Of course, this does not take into account the role of specific interactions with the solvent. Hydrogen-bonding in particular is likely central to the ESPT event.

5.2 2-naphthol complexed with acetonitrile

ESPT reactions proceed along the hydrogen-bonded coordinate between the photoacid and the solvent (or an accepting base). As such, looking at photoacids in non-polar solvents where no specific interactions are present is insufficient in order to unravel the molecular mechanism behind photoacidity. In order to further our understanding, the transient OH stretch of hydrogen-bonded complexes of 2N with acetonitrile (MeCN) in various non-polar solvents is measured. These results are compared with quantum calculations.

5.2.1 Ground-state vibrational spectra

The ground-state vibrational spectra of 2N:MeCN complexes in various non-polar solvents are given in figure 5.8. As expected from the presence of a HB donated from 2N to MeCN, the OH stretch frequency is red-shifted by over 100cm^{-1} compared to the uncomplexed case and the band is broadened (FWHM of 110-140cm^{-1} compared to 15-55cm^{-1}).

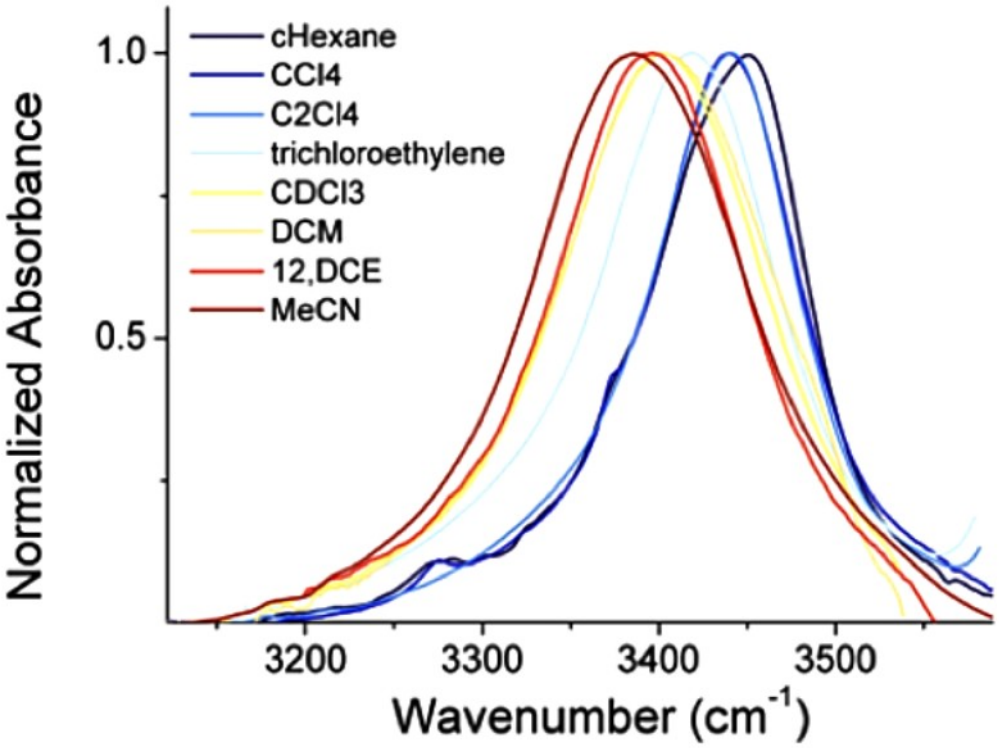

Figure 5.8: Steady-state IR spectra of the 2N:MeCN complex in various non-polar solvents. The higher frequency band due to residual uncomplexed 2N is not shown.

Similarly to what was found for phenol [224, 226], the ground-state anharmonicity is not much larger for 2N in MeCN compared to 2N in the uncomplexed, less polar solvents like C_2Cl_4: 106 for the first, versus 86 for the latter.

5.2.2 Excited-state vibrational spectra

The transient spectra of the OH stretch of 2N:MeCN complexes at 10ps are given in figure 5.9. The spectra are composed of a remaining fraction of uncomplexed 2N with corresponding bleach and excited-state bands located at higher frequencies. These bands are equivalent to the bands of 2N in the respective pure solvents (without MeCN) reported in figure 5.3. In addition, the complexed 2N:MeCN complex gives rise to red-shifted OH stretch bleach signals as well as excited state bands. Comparison of the solvent dependence frequency shift between the ground state and first excited state for the complex shows that the solvatochromic shift is noticeably larger in the excited state. Indeed, the slope of the vibrational OH frequency as a function of F_0 is 113 for S_0 and 194 for S_1 (figure 5.10). The frequencies were determined using a peak fit procedure with Voigt lineshapes in order to properly deconvolute the bands.

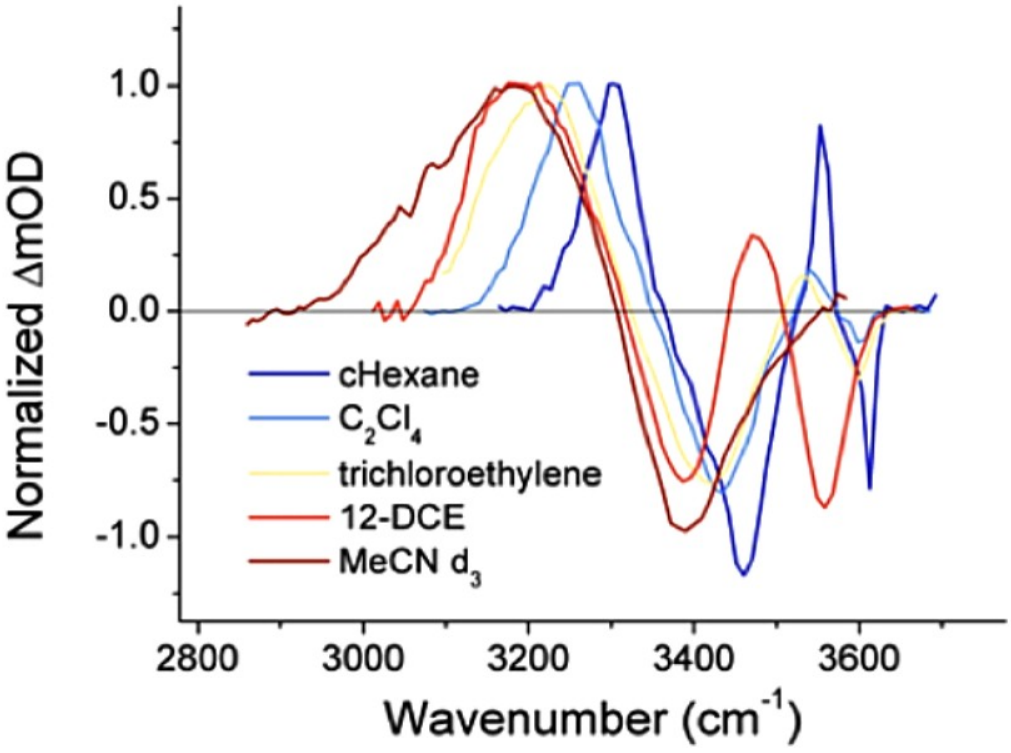

Figure 5.9: Transient IR spectra of the 2N:MeCN complex in various non-polar solvents at 10ps.

5.2.2.1 Calculated molecular parameters

The components and orientations of the dipole moment as well as its first and second derivative for the 2N:MeCN complex in the ground and excited-state are given in table 5.7. While the magnitude of the dipole moment for the complex is about 5 times larger than for 2N alone, the orientation is not much affected by complexation. The dipole moment is found to increase slightly upon excitation to the ^1L_b state for both cis and trans conformers: the dipole moment for cis-2N:MeCN increases from 6.71D to 7.05D, while the dipole moment of trans-2N:MeCN increases from 7.34D to 7.64D.

Table 5.7: Orientation and calculated values of $\boldsymbol{\mu_0}$, $\boldsymbol{\mu'}$ and $\boldsymbol{\mu''}$ for both cis and trans rotamers of the 2N acetonitrile complex.

	***cis*-2N:MeCN**	***trans*-2N:MeCN**
S_0, μ	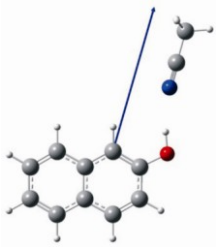	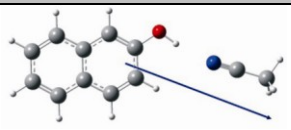
(D)	(6.0198, -2.9677, 0.0023)	(-6.9156, 2.4562, 0.0032)
S_0, μ′	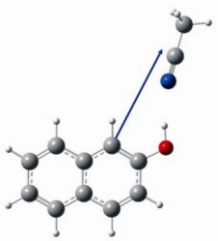	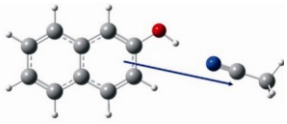
(D·A^{-1}·amu$^{-1/2}$)	(4.6797, -1.2094, 0.0000)	(-5.0939, 0.8068, 0.0000)
S_0, μ′′	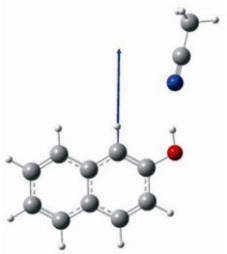	
(D·A^{-2}·amu^{-1})	(3.3934, -2.7939, -0.0218)	(-9.8194, 2.3498, -0.0010)

^1L_b, μ	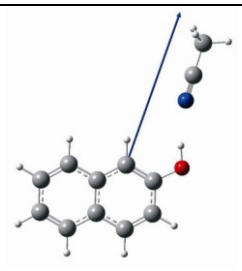	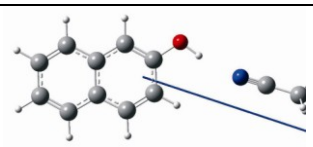
(D)	(6.4428, -2.8708, 0.0019)	(-7.3219, 2.1738, 0.0011)
^1L_b, μ′	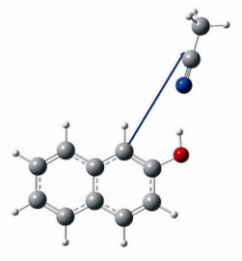	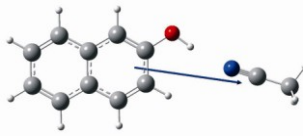
(D·A^{-1}·amu$^{-1/2}$)	(4.8918, -0.9894, -0.0005)	(-4.5959, 0.4872, -0.0038)
^1L_b, μ″	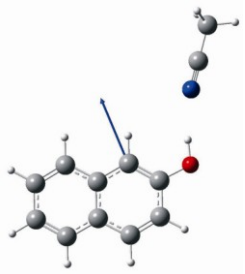	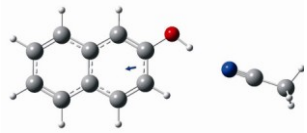
(D·A^{-2}·amu^{-1})	(1.2499, -2.5084, 0.0075)	(0.4325, 0.1023. -0.0033)

The molecular parameters necessary to calculate the slope of the OH vibrational frequency as a function of F_0 are given in table 5.8. The Onsager cavities of the complex are about 4 times larger than the uncomplexed 2N and increase slightly in the excited-state concomitant with the increase in dipole moment. The ratio of anharmonic force constant to harmonic force constant $\frac{V_i'''}{V_i''}$ also shows a small increase indicative of a larger anharmonic effect in the excited-state.

Table 5.8: Calculated parameter values for the 2N acetonitrile complex governing the solvent-induced vibrational frequency shifts.

Term	*cis*-2N:MeCN		*trans*-2N:MeCN	
	^1L_b	S_0	^1L_b	S_0
$\mu_i'' \cdot \mu_i^0$ ($D^2\ A^{-2}\ amu^{-1}$)	15.2539	28.7193	-2.9443	-73.6787
$\mu_i' \cdot \mu_i^0$ ($D^2\ A^{-1}\ amu^{-1/2}$)	34.3574	31.7578	34.7101	37.2088
$\frac{V_i'''}{V_i''}$($A^{-1}\ amu^{-1/2}$)	-7.4293	-7.3357	-7.3475	-7.3290
$\mu_i'' \cdot \mu_i^0 - \frac{V_i'''}{V_i''}\mu_i' \cdot \mu_i^0$	270.5050	261.6859	252.0875	346.3817
a_i(Å)	3.6578	3.6459	3.8454	3.8365
v_0^i (cm^{-1})	3358	3480	3358	3476
S_i(cm^{-1})	141.14	131.51	111.89	149.56
$\mu_i' \cdot \mu_i'$ [$D^2\ A^{-2}\ amu^{-1}$]	24.9889	23.3588	21.3601	26.5984
$\mu_i' \cdot \mu_i' + \mu_i^0 \cdot \mu_i''$	40.1628	52.0781	18.4157	100.2771
B_i [cm^{-1}]	8.3825	10.4691	3.2696	17.3188

5.2.2.2 Comparison between experiment and theory

Using the calculated molecular parameters, the ground-state slope of the OH vibrational frequency as a function of F_0 is found to be 131.52 for cis-2N:MeCN and 149.56 for trans-2N:MeCN. For the excited-state, a slope of 141 is found for cis-2N:MeCN and 112 for trans-2N:MeCN. Using a Boltzmann distribution of population for the cis and trans rotamers, this gives a ground-state slope of 137 and an excited-state slope of 132. The corresponding slope ratio is of 0.96 which is much smaller than the value of 1.72 obtained in the experiment. This can be better visualized by comparing the experimental OH stretch frequencies with those obtained using TD-DFT calculations and the Pullin model (figure 5.10).

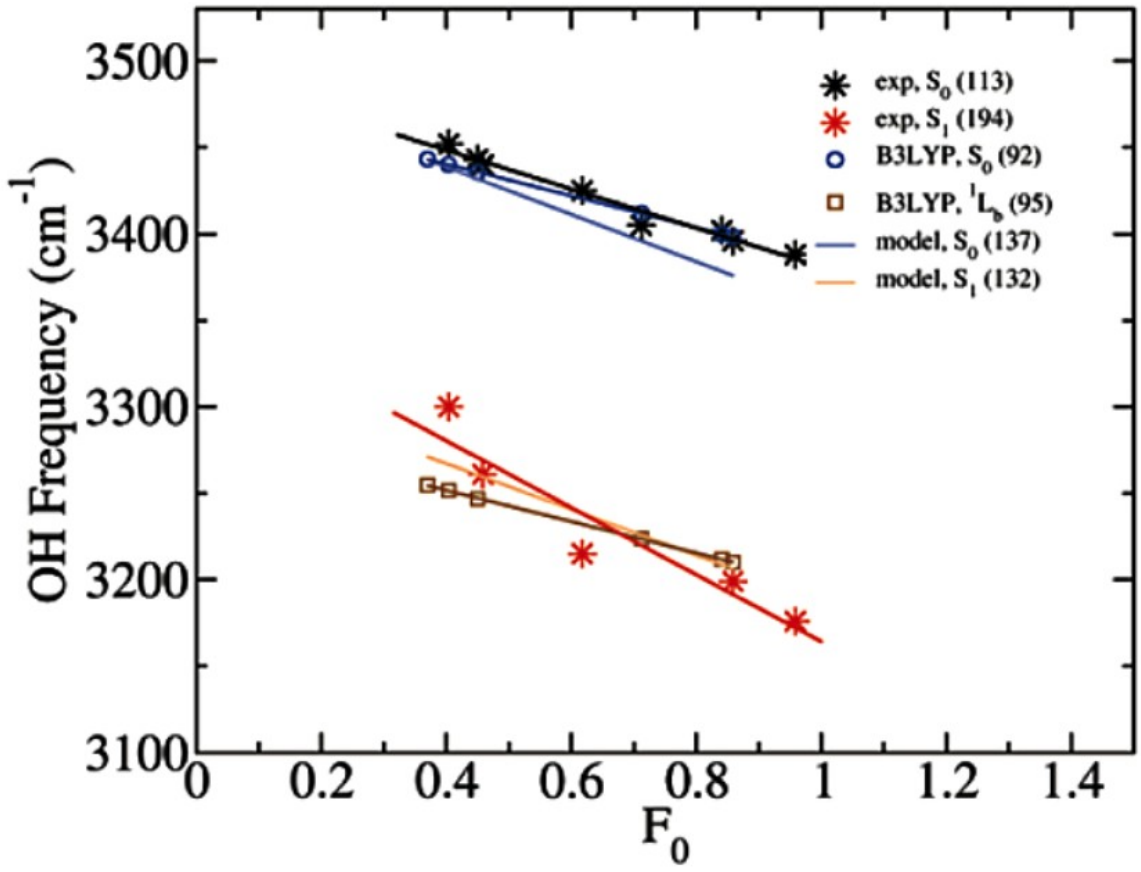

Figure 5.10: OH stretch frequencies as a function of F_0 for the 2N:MeCN complex obtained experimentally (exp), by ab initio calculations (B3LYP) and using the Pullin model (model). The DFT frequencies were scaled by a factor of 0.956, while the TD-DFT were scaled by a factor of 0.908. The intercepts were taken as the y-intercept of the experimental data.

It is evident from figure 5.10 that both the ab initio calculations and the Pullin model fail to reproduce the experimental trend whereby the solvent dependence is found to be much larger in the excited-state. Instead, it is calculated that the ground and excited-state properties should be similar. In order to understand the root of this discrepancy, several further calculations were attempted. In the first place, the M06-2x functional was used instead of the B3LYP as it gives a better performance for noncovalent interactions and main-group thermochemistry [233]. In this case, a slope of 135 was found for the ground-state and 126 for the excited-state. This again gives a slope ratio close to one such as was found using the B3LYP functional. Then, the discrete variable representation was used in order to investigate the effect of the anharmonicity. In this method, the vibrational quantum levels are solved using the OH potential well computed with B3LYP/TZVP. This enables the determination of the fundamental OH vibrational frequencies with the effect of the vibrational anharmonicity included implicitly. Once again, the calculations find similar slopes for the ground (122) and

excited-state (119). It can thus be concluded that the larger slope observed experimentally for the excited-state is not due to significant changes in anharmonicity upon excitation. However, at this time it is impossible to say why the calculational methods all fail to reproduce the experimental results. It was seen in section 5.1 that the correspondence between the experiment and theory for uncomplexed naphthols is quite good. Obviously, this is no longer the case upon formation of a hydrogen bonded complex, even a weak one such as that with MeCN. The very small charge redistribution observed in the gas-phase photoacids or in photoacids in low dielectric media with no specific interactions, might therefore not be the case when HB complexes are involved.

5.3 Summary

The vibrational solvatochromic effects in the ground and first excited state of 1N and 2N were explored by combining femtosecond MIR spectroscopy and a theoretical model based on the Pullin-van der Zwan-Hynes perturbative approach. For 1N and 2N in low dielectric solvents where specific interactions are absent, good agreement between experiment and theory was achieved. It was concluded that vibrational solvatochromic effects are dominated by the instantaneous dielectric response of the solvent, while time-dependent nuclear rearrangements are of minor importance. Additionally, in agreement with what was reported for gas-phase calculations of photoacids [28, 29], little charge redistribution from the oxygen into the ring was found in these systems. In contrast, for the 2N:acetonitrile hydrogen bonded complex in low dielectric solvents, the agreement between experiment and theory was poor. In the experiment, a marked difference in the solvatochromic properties of the complex in the ground and first excited state was measured. Indeed, the slope of the OH vibrational frequency as a function of the solvent dielectric function was almost twice as large in the first excited state (194) compared to the ground state (113). However, various calculations all predict similar slopes for the ground and excited state of the complex. Evidently, the calculations fail to properly account for changes occurring upon excitation. The coordinate for excited-state proton transfer reactions is the HB between the photoacid and the solvent or an accepting base. The discrepancy between experiment and theory for even a weak hydrogen bonded complex like 2N:acetonitrile thus needs to be further investigated in order to properly understand the photochemistry of photoacids.

6. Photoinduced charge transfer to halogenated solvents as a probe for electronic charge redistribution in naphthols

No charge redistribution was found to occur in photoacids upon electronic excitation in recent computational calculations [29, 66, 67]. This has raised considerable debate in the literature as to the relative importance of the acid in the excited-state proton transfer (ESPT) reaction. Indeed, it is now often claimed that it is the conjugate photobase which provides the driving force of the reaction. However, these gas-phase calculations do not take into account the influence of the hydrogen bond (HB) with the solvent along which coordinate the ESPT reaction occurs. Furthermore, it was seen in chapter 5 that, while current computational methods well reproduce experimental results in non-polar solvents where specific interactions such as HBs are absent, they fail to properly account for the behavior of hydrogen-bonded complexes in the excited-state. An experiment which can probe the electronic density of the aromatic ring thus appears necessary. To this aim, the quenching reaction of aromatic systems by haloalkanes is utilized. As quenching likely proceeds through a mechanism involving the aromatic ring instead of the OH functional group, it can provide direct experimental information about the extent of charge redistribution occurring upon electronic excitation.

For the naphthalene family of compounds, the first systematic study of the fluorescence quenching by halogenated alkanes was performed by Encinas *et al.* [38]. The quenching rate constants determined using Stern-Volmer plots is found to correlate with the ionization potential (IP) of the aromatic molecule and the electron affinity (EA) of the quencher. Since there is no overlap of the absorption spectra of the naphthols with the fluorescence spectra of the halogenoalkanes, the observed quenching is explained by the formation of a charge transfer complex, similar to what was proposed earlier for benzene and other aromatic compounds [39, 40, 41, 42]. As increasing the amount of quencher only leads to a progressive intensity decrease and not the appearance of new fluorescence bands [44, 45], the process is thought to occur by non-emissive exciplex formation. However, because the resulting exciplexes are non-emissive, fluorescent measurements must perforce rely on models. By looking instead at the transient IR spectra and monitoring the appearance of new IR peaks including characteristic bands of naphthol such as the OH stretch, it is possible to resolve the timescales of the charge transfer as well as attempt to better understand the mechanism. Furthermore, the good time resolution of our femtosecond setup allows for measurements using the acceptor as the solvent, thus avoiding complicated diffusion dynamics (see chapter

3.3), and instead isolating the actual charge transfer reaction. Comparison with fluorescence lifetimes as measured with time correlated single photon counting (TCSPC) should enable to establish the excited-state vibrations characteristic of the S_1 state, while molecular orbital analysis and quantum dynamics simulations can reveal the origin of the charge helping to draw a comprehensive picture of the event. Characterizing the quenching processes in different environments can provide information about differences between 1N and 2N as well quantifying the importance of a hydrogen bond and the solvent polarity towards the extent of charge redistribution.

6.1 Experimental results

6.1.1 Static absorbance and emission spectra

Fluorescence quenching of 1N and 2N occurs in solvents like carbon tetrachloride (CCl_4), tetrachloroethylene (C_2Cl_4) and chloroform ($CHCl_3$), while dichloromethane ($CHCl_2$) or 1,2-dichloroethane (CH_2ClCH_2Cl, 1,2-DCE) show no appreciable differences in quantum yield when compared to n-hexane. Static fluorescence can be observed for naphthalene in CCl_4, but in 1N and 2N whatever fluorescence may be present is below the experimental detection limit of steady-state fluorescent methods. The absorption and emission spectra of 1N and 2N are presented in figure 6.1.

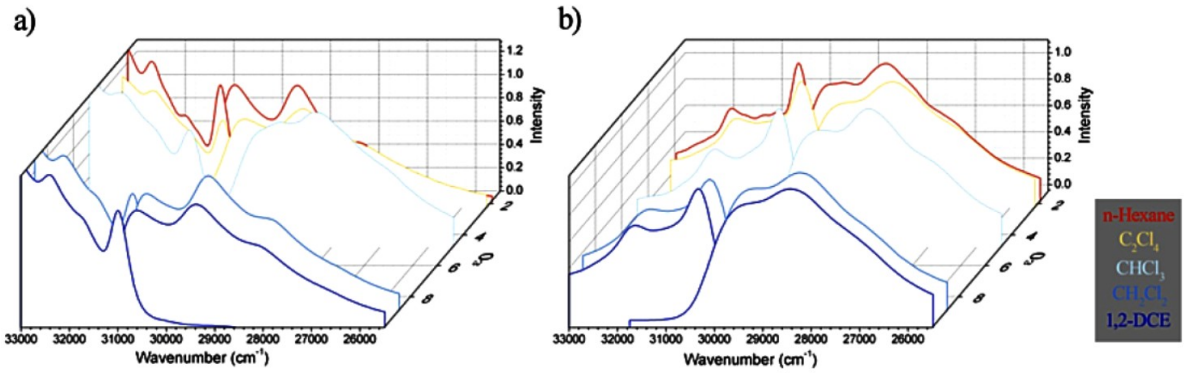

Figure 6.1: Normalized steady-state absorption and emission spectra of a) 1N and b) 2N.

6.1.2 Transient IR measurements

The transient IR spectra of 1N in C_2Cl_4 is presented in figure 6.2 for both the OH stretch and fingerprint region. It is immediately apparent that the initial state is rapidly quenched with about 40% bleach recovery (the recovery dynamics for the bleach at 1275cm^{-1} are obscured

by the decrease in the overlapped excited-state peak). The dynamics of the decay of the OH stretch at 3582cm^{-1} and the fingerprint band at 1271cm^{-1} given in figure 6.2c are characterized by a bi-exponential decay of 60ps (0.85) and 1ns (0.15). The bleach recovery plotted for the OH stretch at 3622cm^{-1} in figure 6.3d is characterized by the same timescales.

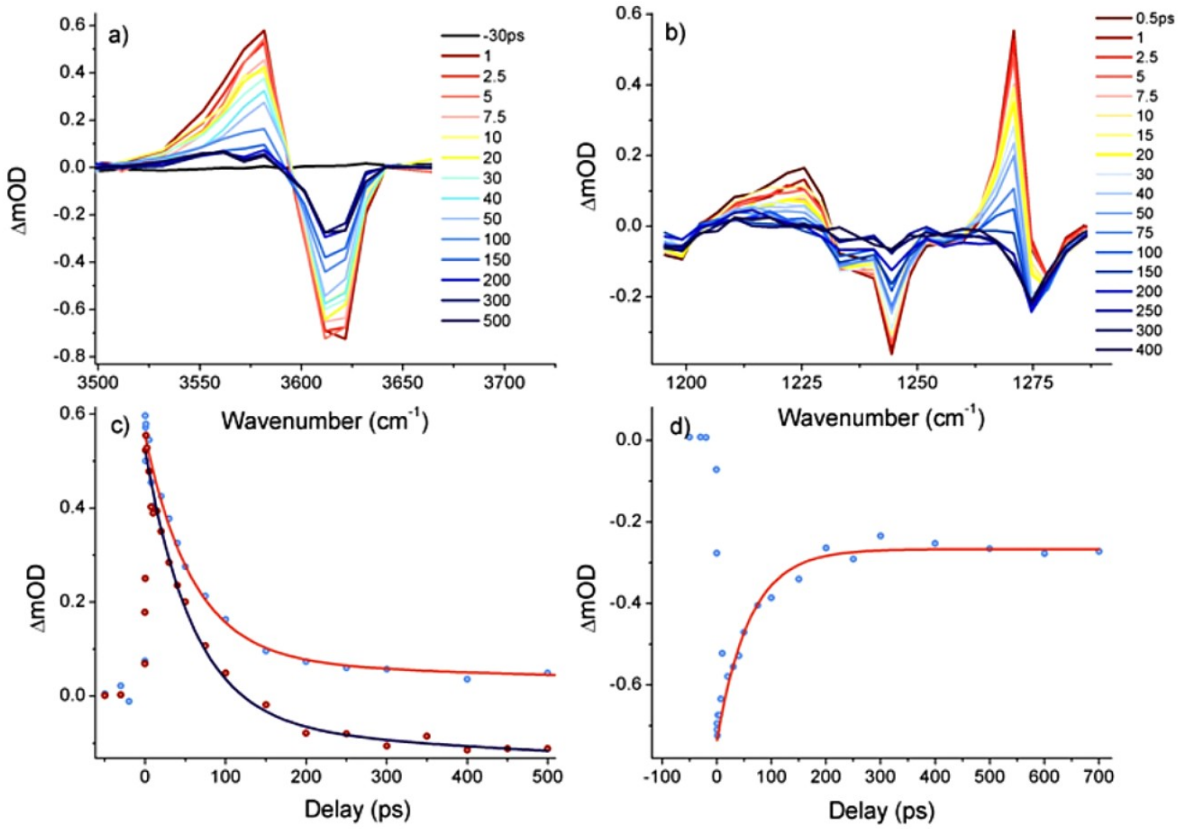

Figure 6.2: a) Transient spectra of the OH stretch of 1N in C_2Cl_4 b) transient fingerprint spectra of 1N in C_2Cl_4 c) dynamics for the decay of the excited-state OH stretch band at 3582cm^{-1} (light blue) and the fingerprint band at 1271cm^{-1} (dark red) d) dynamics for the partial bleach recovery of the OH stretch at 3622cm^{-1}. All dynamics are fit with a bi-exponential characterized by 60ps (0.85) and 1ns (0.15) time constants.

The time correlated single photon counting spectra for 1N in C_2Cl_4 is given in figure 6.3. Using an instrument response function of 60ps, it is found that the dynamics are characterized by 57ps (0.9) and 1ns (0.1) timescales which is in quite good agreement with the decay of the initial excited-state IR bands. It is thus possible to determine that the initial IR peaks are due to the uncomplexed S_1 state of 1N in C_2Cl_4 as the resulting exciplex is non-emissive.

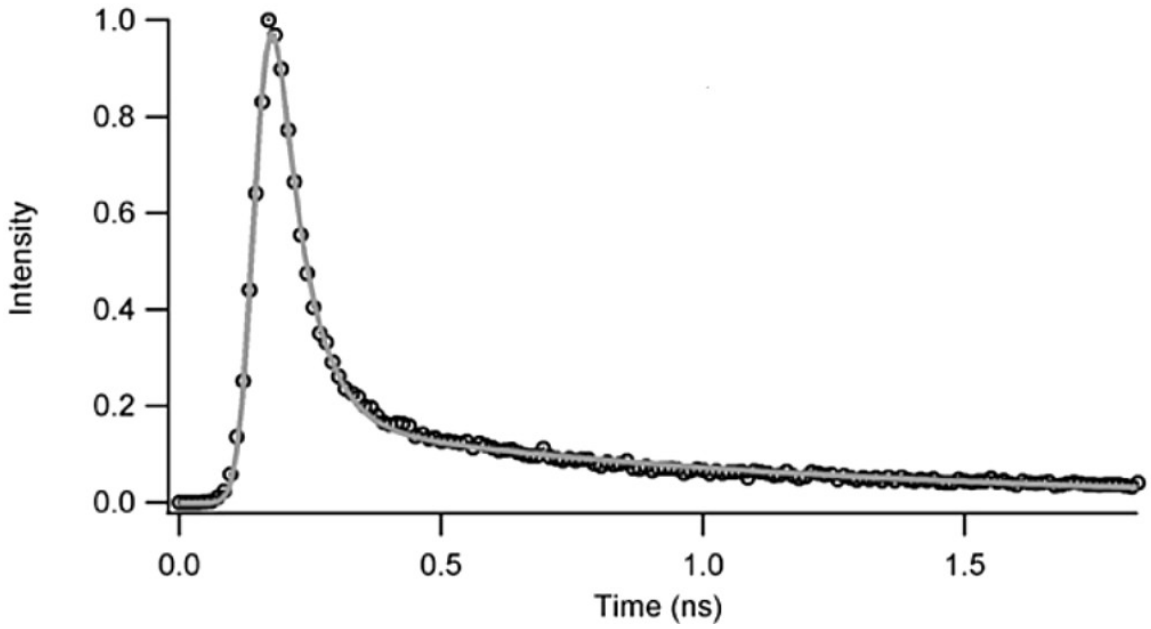

Figure 6.3: TCSPC spectra of 1N in C_2Cl_4 fit with a bi-exponential decay having 57ps (0.9) and 1ns (0.1) time constants and an instrument response function of 60ps.

Figure 6.4 shows the transient IR spectra of 1N in $CDCl_3$ for both the OH stretch and fingerprint region. Similar to what was found for 1N in C_2Cl_4, the initial bands show a rapid decrease. However, unlike C_2Cl_4, no bleach recovery is apparent, and new bands at 1296cm^{-1} and 1215cm^{-1} are rising on timescales corresponding to the decay of the initially excited-state bands. These dynamics are plotted in figure 6.5c for the decay of the OH stretch at 3558cm^{-1} and in figure 6.4d for the rise of the band corresponding to a new state at 1296cm^{-1}. In both cases the dynamics are characterized by a bi-exponential decay with 50ps (0.25) and 400ps (0.75) time constants.

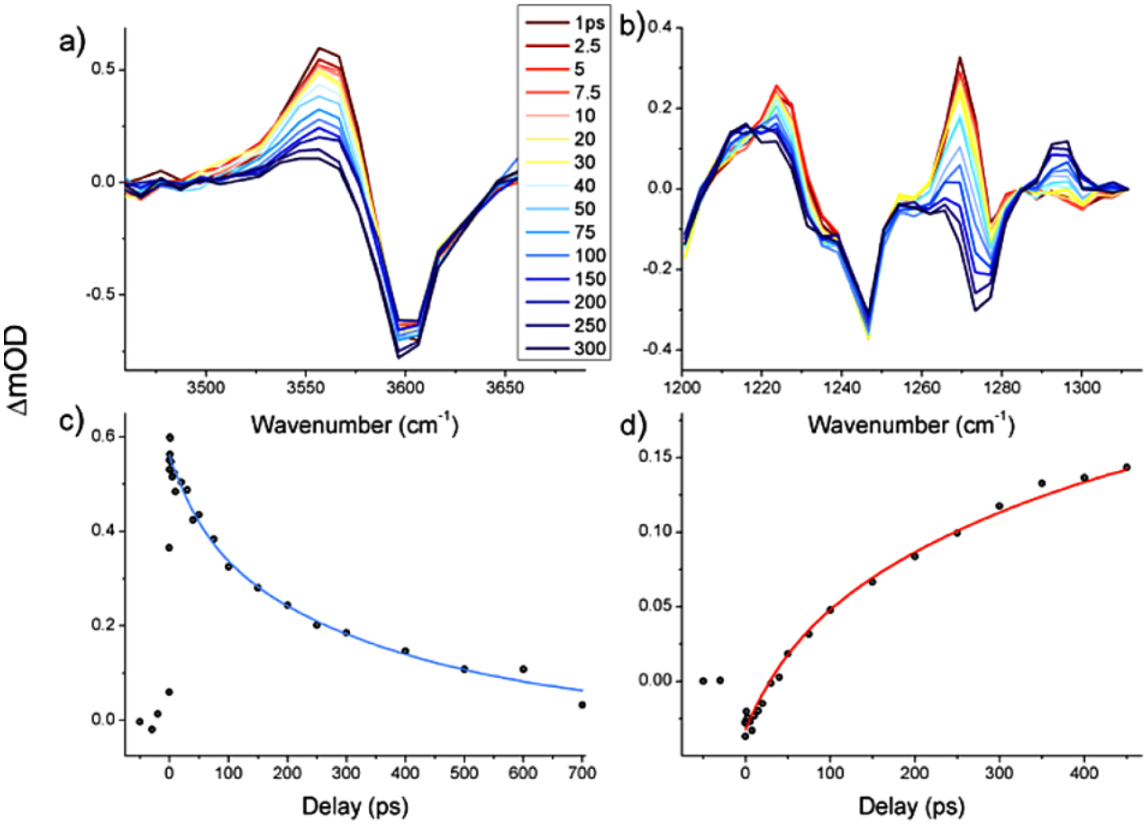

Figure 6.4: a) Transient spectra of the OH stretch of 1N in $CDCl_3$ b) transient fingerprint spectra of 1N in $CDCl_3$ c) dynamics for the decay of the excited-state OH stretch band at 3558cm^{-1} d) dynamics for the rise of the new fingerprint band at 1296cm^{-1}. All dynamics are fit with a bi-exponential characterized by 50ps (0.25) and 400ps (0.75) time constants.

The transient IR spectra of 1N in CCl_4 is presented in figure 6.5 where very rapid dynamics are observed with a behaviour similar to what was found for $CDCl_3$: the initial peaks are found to decrease with new peaks rising at 1290cm^{-1} and 1215cm^{-1}. Additionally, 50% bleach recovery is observed. The initial growing in and subsequent recovery of the bleach at 1275cm^{-1} is due to the overlapping excited-state band. A characteristic timescale of 1.4ps is found for the S_1 decrease, bleach recovery (figure 6.5c) and appearance of the new bands (figure 6.5d).

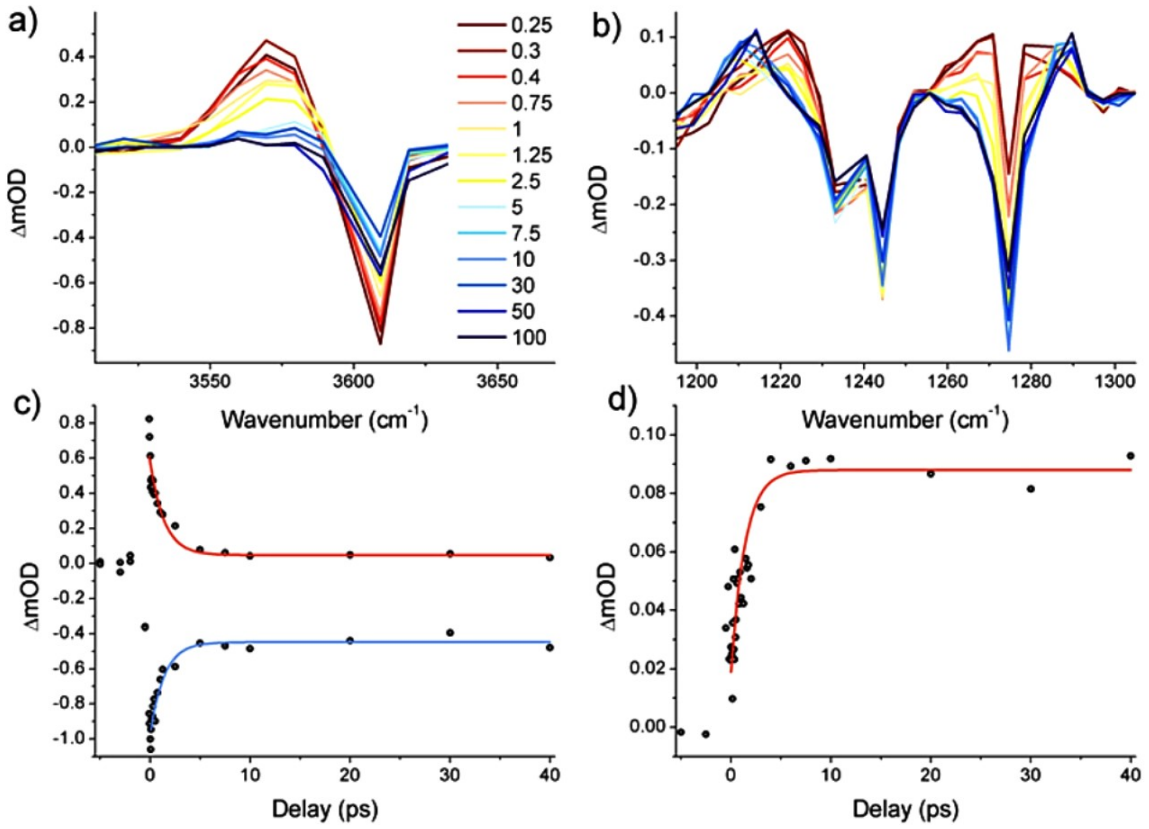

Figure 6.5: a) Transient spectra of the OH stretch of 1N in CCl_4 b) transient fingerprint spectra of 1N in CCl_4 c) dynamics for the decay of the excited-state OH stretch band at 3570cm^{-1} (red fit) and bleach recovery at 3608cm^{-1} (blue fit) d) dynamics for the rise of the new fingerprint band at 1296cm^{-1}. All dynamics are fit with a single exponential characterized by 1.4ps time constant.

In order to investigate the influence of hydrogen-bonds and solvent polarity on the quenching rates, 1N in pure C_2Cl_4 is compared to a hydrogen-bonded complex of 1N with acetonitrile (MeCN) in the same solvent, as well as 1N in MeCN to which 1M of C_2Cl_4 is added. In this way it is possible to isolate the effect of HB formation from that of general solvation in the more polar MeCN solvent (ε_{MeCN}=37.5 and ε_{C2Cl4}=2.5). A concentration of 1M of C_2Cl_4 was used in order to obtain significant ground-state complexation of 1N with C_2Cl_4 without altering the solvent properties. Indeed, sufficiently high concentrations are required since without ground-state complexes the reaction becomes diffusion limited, and as such does not offer a good comparison with the experiments done using the electron acceptor as solvent. It was found that the Stern-Volmer plots of the quenching of 1N by CCl_4 deviate from linearity at concentrations higher than 0.03M [45]. In order to account for the smaller complexation constant in C_2Cl_4, a much higher concentration of 1M was used instead. However, 1M is still a sufficiently low concentration so that the solvent properties of acetonitrile are not affected.

The transient IR spectra of the fingerprint region for the 1:1 complex of 1N with acetonitrile in C_2Cl_4 is given in figure 6.6a. The decay of the excited-state peak at 1294cm^{-1} (figure 6.6b) and that of the partial bleach recovery at 1258cm^{-1} (figure 6.6c) are characterized by a 5.6ps exponential, with the partial bleach recovery showing an additional timescale of 80ps. As the 5.6ps timescale found in this experiment is about ten times faster than the fastest timescale found for the uncomplexed 1N in C_2Cl_4 (60ps) the influence of the HB on the quenching mechanism is indubitable.

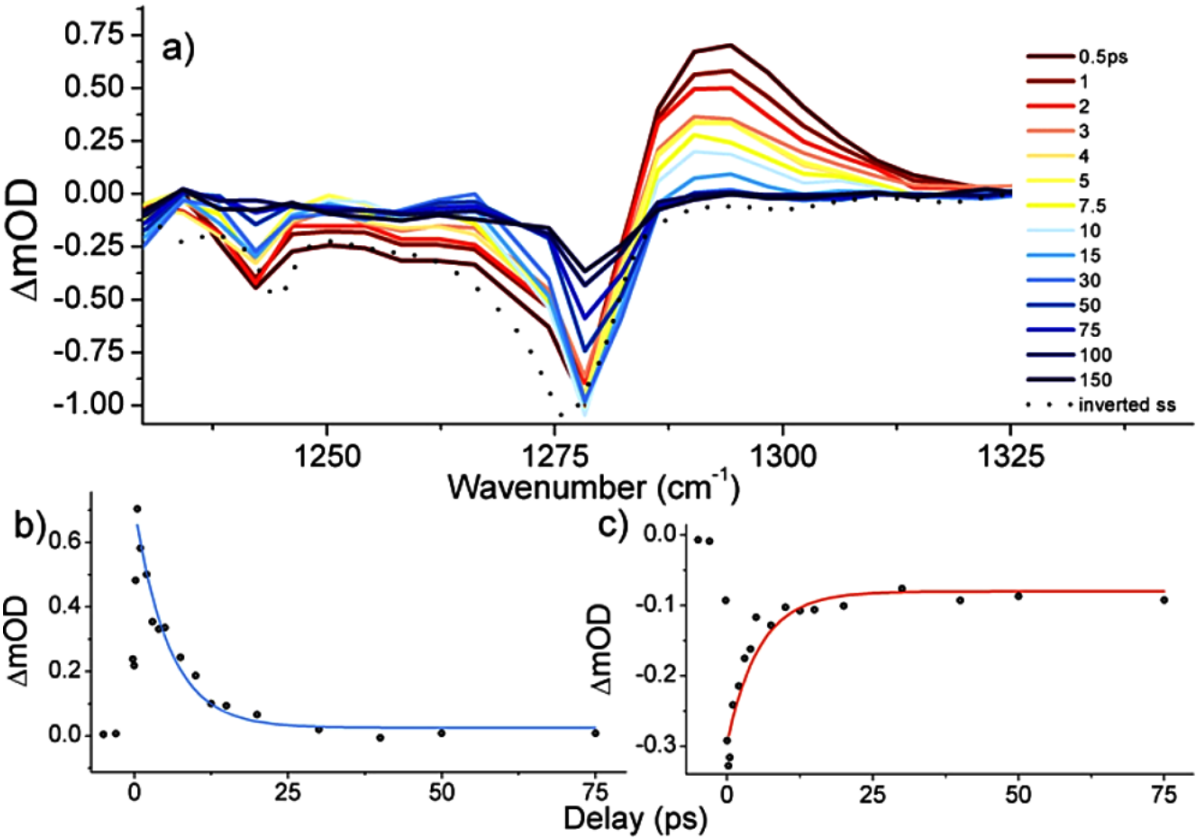

Figure 6.6: a) transient fingerprint spectra of a 1:1 complex of 1N with acetonitrile in C_2Cl_4 b) dynamics for the decay of the excited-state band at 1294cm^{-1} c) dynamics for the partial bleach recovery of the band at 1258cm^{-1}. All dynamics are fit with a single exponential characterized by a 5.4ps time constant.

The transient IR spectra of the fingerprint region for 1N in acetonitrile with 1M C_2Cl_4 is given in figure 6.7a. The dynamics of the bleach recovery at 1278cm^{-1} and those of the excited-state decay at 1295cm^{-1} are characterized by a fast initial decay with a 4ps timescale and then slower dynamics which can be fit with a 200ps exponential but are likely to be multiexponential. Indeed, it is expected in this case that the fast dynamics are due to charge transfer from the excitation of ground-state complexes, while slower dynamics will arise from electron transfer following the diffusion of the two reactive partners. The 4ps timescale is

only slightly faster than the 5.6ps dynamics obtained with the complex in pure C_2Cl_4 indicating that the effect of HBs on the rates is much more important than that of the solvent polarity. This will be discussed in more detail in section 6.2.7.

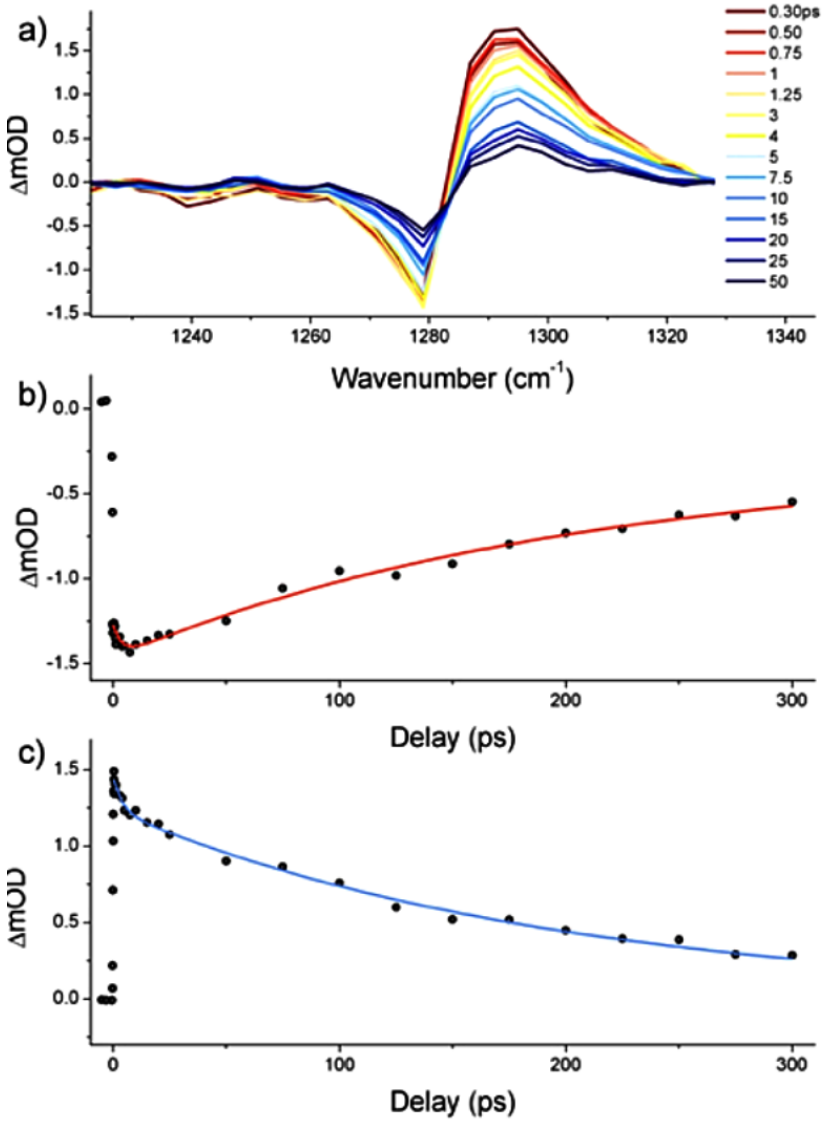

Figure 6.7: a) Transient fingerprint spectra of 1N in C_2Cl_4 with 1M acetonitrile b) dynamics for bleach recovery at 1278cm^{-1} d) dynamics for the decay of the excited-state band at 1295cm^{-1}. All dynamics are bi-exponential fits characterized by a 4ps and 200ps time constant.

The transient IR spectra for the OH stretch and fingerprint region of 2N in $CDCl_3$ are given in figures 6.8a and 6.8b respectively. Although the fluorescence quantum yield of this system is low and Stern-Volmer plots have revealed significant quenching of 2N by $CDCl_3$, no dynamics are apparent up to 50ps. An intensity decrease of the bands was seen at longer

delays, however, as our delay stage only permits for delays of up to about 800ps to be measured, the quenching dynamics in this system could not be properly characterized.

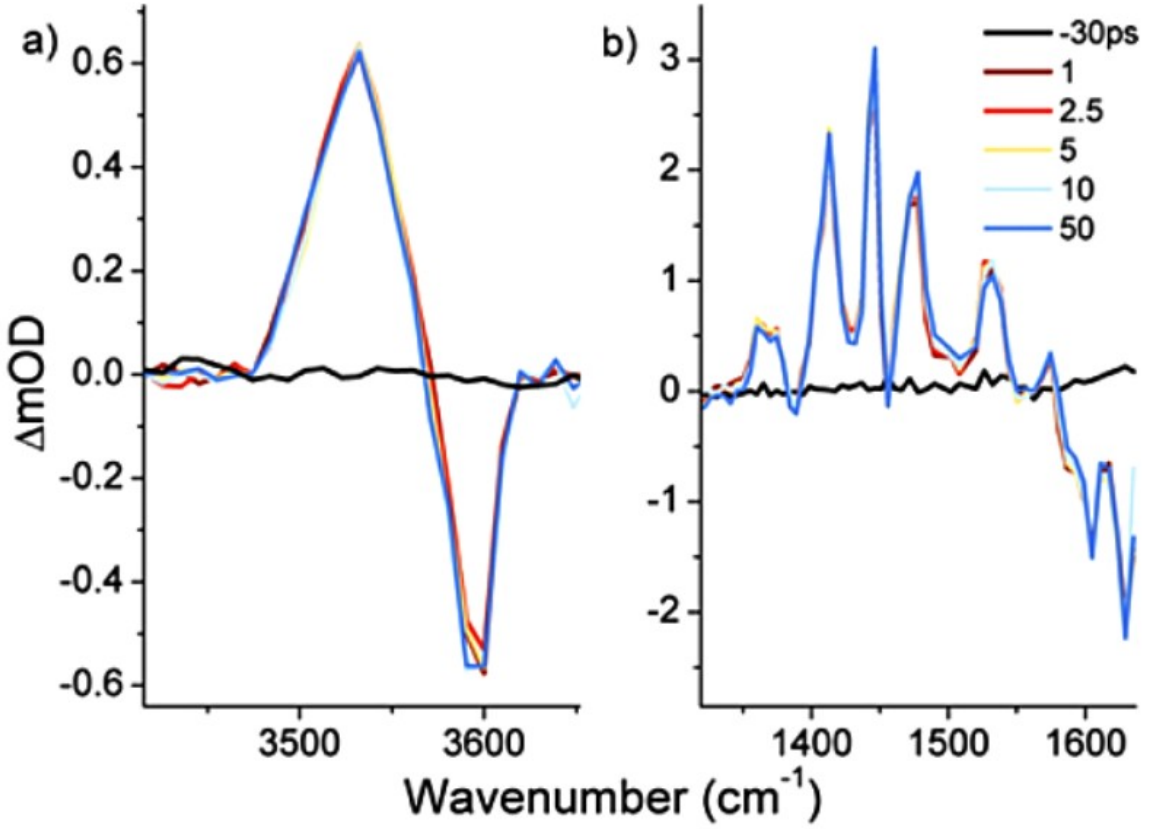

Figure 6.8: a) Transient IR spectra of the OH stretch of 2N in $CDCl_3$ b) transient IR spectra of the fingerprint region of 2N in $CDCl_3$.

The ground-state vibrational marker modes of 2N in various non-polar solvents are found to be nearly identical (figure 6.9a). As the excited-state mode pattern in dichloromethane (a non-quencher solvent) and $CDCl_3$ are also nearly identical (figure 6.9b), this is further confirmation that the initial excited-state peaks are due to the uncomplexed naphthols in the ^1L_b state also in the quenching solvents. The broader peaks observed in dichloromethane compared to $CDCl_3$ are mainly attributed to the use of a different grating with lower resolution.

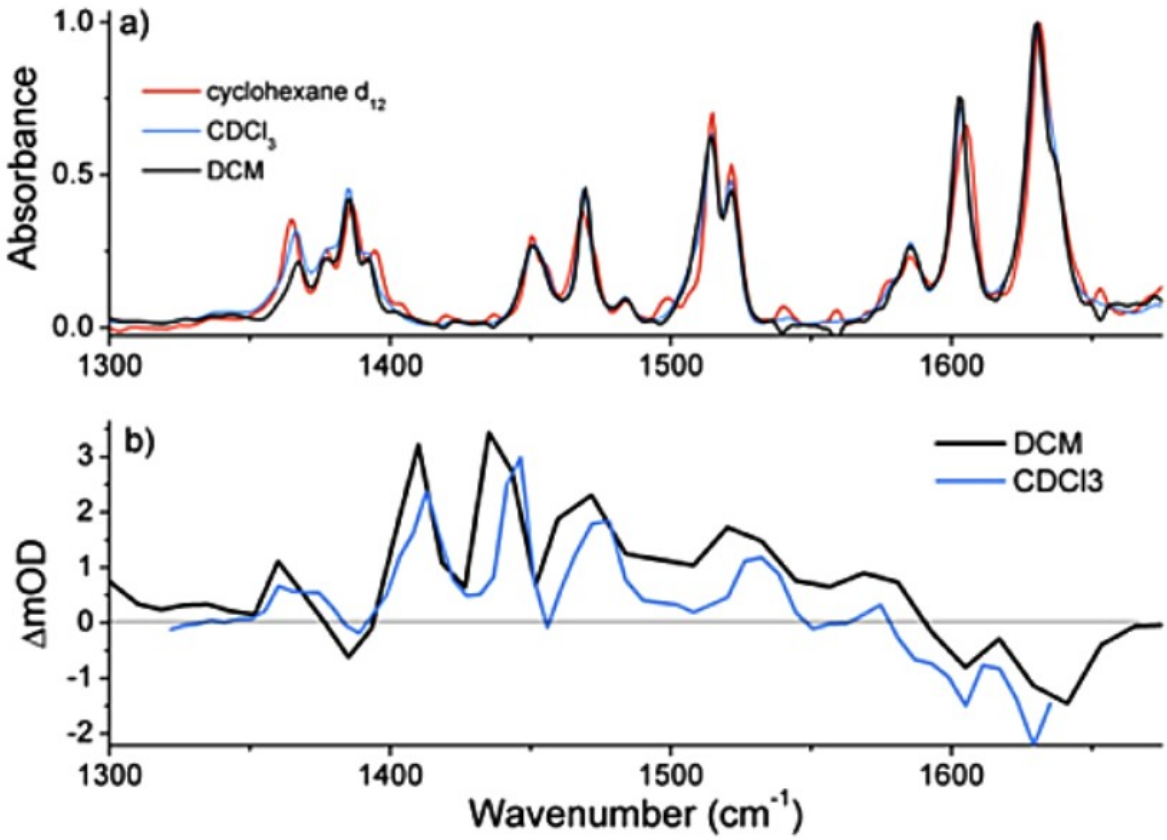

Figure 6.9: a) steady-state IR spectra of 2N in cyclohexane-d_{12}, $CDCl_3$ and dichloromethane (DCM) b) transient fingerprint spectra at 10ps of 2N in CDCl3 and DCM.

The transient IR spectra for the OH stretch of 2N in C_2Cl_4 is given in figure 6.10a. Similar to what was observed for 1N in the same solvent, the initial band is found to decrease with concomitant bleach recovery. However, in this case the dynamics characterized by 150ps (0.3) and 1ns (0.7) time constants are much slower than the dynamics in 1N where time constants of 60ps (0.85) and 1ns (0.15) were found.

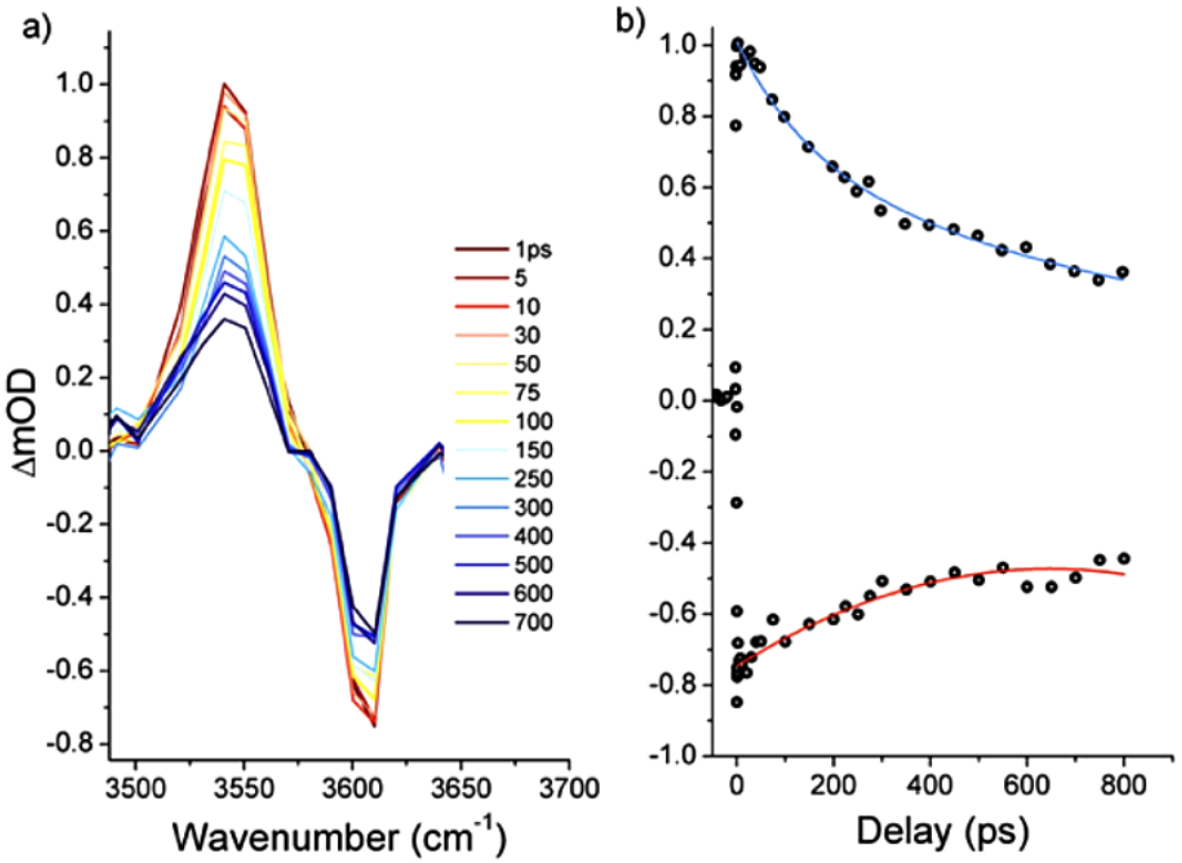

Figure 6.10: a) Transient spectra of the OH stretch of 2N in C_2Cl_4 b) dynamics for the decay of the excited-state OH stretch band at 3540cm^{-1} (blue fit) and the partial bleach recovery at 3610cm^{-1} (red fit). All dynamics are fit with a bi-exponential characterized by 150ps and 1ns time constants.

The transient IR spectra for 2N in CCl_4 is given in figure 6.11a with the dynamics of the excited-state decrease and bleach recovery given in figures 6.11b and 6.11c respectively. A partial bleach recovery of 50% is observed occurring with a 13ps timescale. This is the same timescale as that of the excited-state decrease and is once again about 10 times slower than what was observed for 1N.

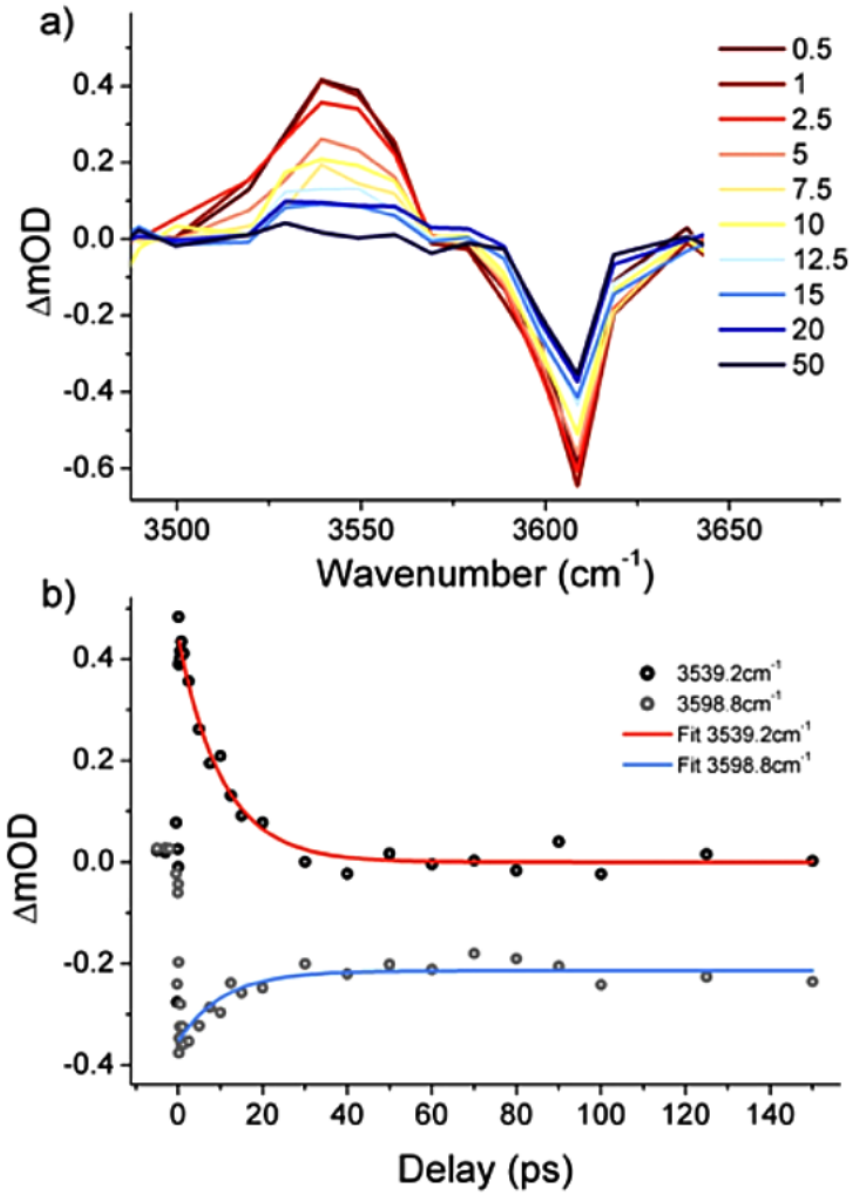

Figure 6.11: a) Transient spectra of the OH stretch of 2N in CCl_4 b) dynamics for the decay of the excited-state OH stretch band at 3539cm^{-1} (red fit) and the partial bleach recovery at 3599cm^{-1} (blue fit). All dynamics are fit with a single exponential characterized by a 14ps time constant.

6.2 Discussion

6.2.1 Provenance of the charge

1N and 2N possess two electron rich sites from whence the charge may originate: the π electron system, and the electron lone pairs on the oxygen of the OH group. In order for the reaction to serve as a probe of the electronic density of the aromatic ring, one must first establish that the charge is originating from the aromatic system and not instead from the lone

pairs on the oxygen. In the ground-state, recent gas-phase experiments and calculations found that the OH group and the aromatic system are protonated with equal probability [234, 235]. The comparable ground-state reactivity of the OH group and the π electronic system was further demonstrated in pulse radiolysis experiments with phenols and naphthols [236, 237]. In these experiments, free electron transfer from phenols or naphthols to radical cations of non-polar solvents such as n-butyl chloride, generated by pulse radiolysis, was shown to yield in equal amounts both the radical and radical cation of the corresponding aromatic molecule. Electron transfer from the oxygen is followed by rapid deprotonation to yield the radical, while electron transfer from the aromatic moiety gives the radical cation which is a relatively stable species, only undergoing deprotonation on timescales of a hundred nanoseconds. This is schematized in figure 6.12.

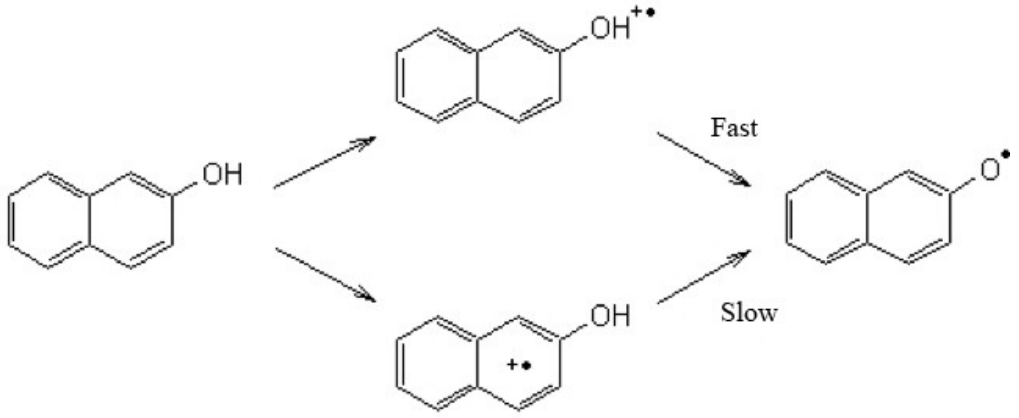

Figure 6.12: Schematic representation of the two pathways observed for electron transfer in phenol or naphthols with the formation of radical cations followed by deprotonation to generate the radical.

Conversely, in the excited-state, according to the traditional photoacidity Ansatz, one expects the electronic density of the aromatic ring to be enhanced at the expense of that of the OH group following charge redistribution. This view is supported by many recent studies which report efficient excited-state intramolecular proton transfer reactions for 1N and other related derivatives [47, 48, 50]. In these laser flash photolysis studies, the proton from the OH group is found to be added to the aromatic ring after photoexcitation evincing the greater excited-state basicity of the aromatic ring compared to the oxygen of the OH group. Furthermore, it is well established that electron transfer occurs in the parent aromatic systems without OH groups like naphthalene or anthracene, with these compounds constituting benchmark donor systems in the study of electron transfer reactions [173, 174, 238, 239, 240]. Additional experimental evidence of π charge is provided by comparing the transfer rates in the 1:1 1N:MeCN complex in C_2Cl_4 with the rates in the pure C_2Cl_4 solvent presented in figures 6.6

and 6.2 respectively. Indeed, it was found that the dynamics are ten times faster in the hydrogen-bonded complex with acetonitrile compared to the rate in pure tetrachloroethylene. As complexation does not significantly affect the $E_{0\text{-}0}$ transition energy, and as the solvent properties of C_2Cl_4 are not affected by the presence of 75mM acetonitrile, this means that the change in rate must be due to changes in the ionization potential of the 1N:MeCN complex (see the Rehm-Weller equation in chapter 3, equation 3.13). However, upon donation of a HB to MeCN, it was seen in chapter 5 that the electronic density on the oxygen is diminished, while that of the aromatic ring is augmented. As the transfer rate was found to increase, it can be deduced that the charge originates from the aromatic π system.

In order to substantiate the experimental evidence, quantum calculations and molecular dynamics simulations were performed. It was determined by TD-DFT calculations that the ^1L_b excited-state includes mainly the HOMO-1 (highest occupied molecular orbital-1) to the LUMO (lowest unoccupied molecular orbital) and HOMO to LUMO+1 transitions. The relevant molecular orbitals (MO) including specific solvent molecules are shown in table 6.1 for 1N and 2N in $CHCl_3$ and CCl_4. The HOMO and the HOMO-1 are found to be relatively unperturbed by the solvent which is in line with the formation of weak ground-state complexes with a small equilibrium constant. However, it is immediately apparent that significant delocalization of the MOs of naphthol to the surrounding solvent occurs in both the LUMO and LUMO+1. This provides an efficient channel for the electron to transfer from the solute molecule to the surrounding solvent. As expected from its higher electron affinity, the extent of delocalization is more pronounced in CCl_4 compared to $CHCl_3$. Furthermore, 1N shows considerably more delocalization than 2N.

Table 6.1: Relevant MOs of the $S_0 \rightarrow {}^1L_b$ transition for *trans*-1N and *trans*-2N in $CHCl_3$ and CCl_4.

	***Trans*-1N**		***Trans*-2N**	
	$CHCl_3$	CCl_4	$CHCl_3$	CCl_4
ψ^*_{L+1} **LUMO+1**	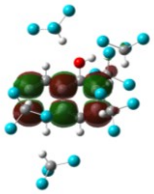	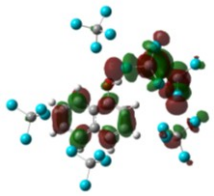	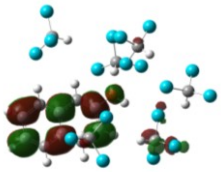	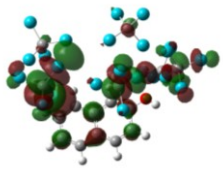
ψ^*_L **LUMO**	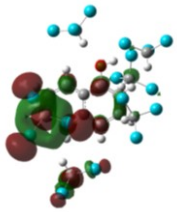	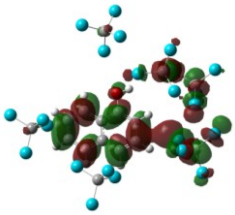	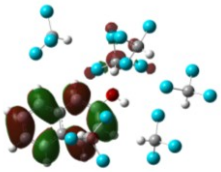	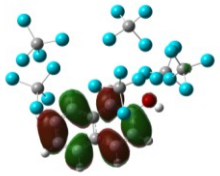
ψ_H **HOMO**	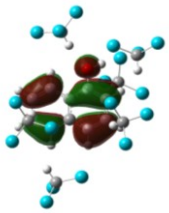	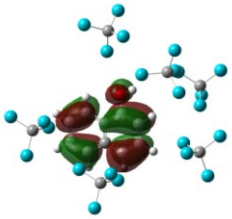	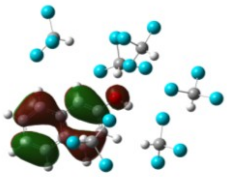	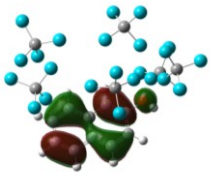
ψ_{H-1} **HOMO-1**	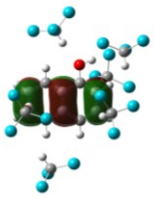	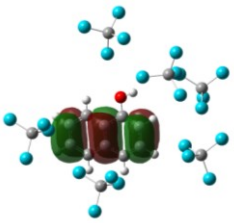	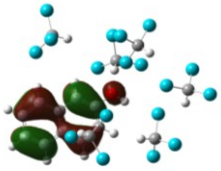	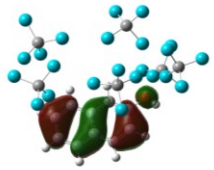

It can be seen in table 6.1 that the HOMO-1 to the LUMO and HOMO to LUMO+1 transitions have their electronic density centred primarily on the aromatic ring and not on the OH group. Additionally, the adiabatic evolution of the excited-state electron after excitation to the unoccupied LUMO and LUMO+1 orbitals is simulated using quantum dynamics at the level of the density functional theory with geometries optimized with the B3LYP/6-31g* method. As expected from the substantial delocalization of the unoccupied naphthol molecular orbitals to the surrounding solvent molecules (table 6.1), an electron is transferred following excitation. The screenshots of the molecular movie shown in figure 6.13 demonstrate that the electron is transferred from the π* orbital of naphthol to the d-orbitals of

solvent's chlorine atoms, further confirming the experimental evidence as to the provenance of the charge. While the calculations predict a full charge transfer, the experimental data can't establish the extent of the transfer. Further work would be necessary in order to detect the presence or absence of transiently formed radical cations and electrons.

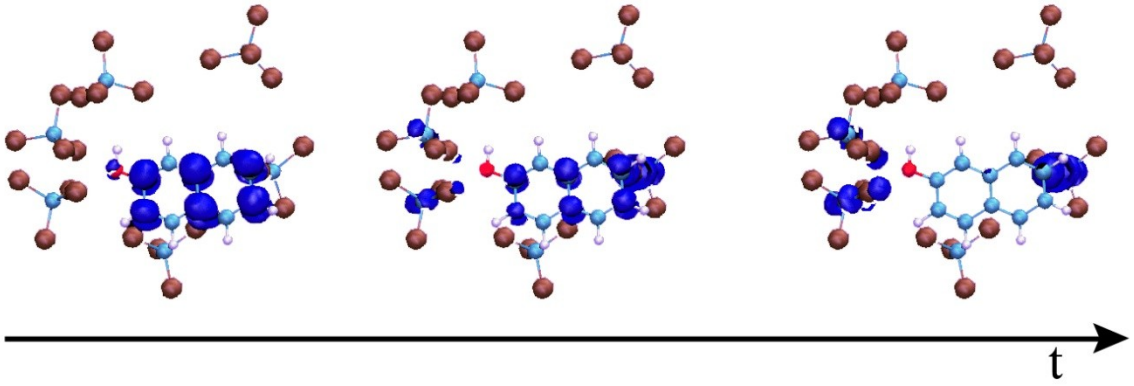

Figure 6.13: Molecular dynamics simulation for 2N in CCl_4.

6.2.2 Charge transfer reaction dynamics

It can be seen in figure 6.1 that the absorption and emission spectra in those solvents where quenching occurs are red-shifted compared to what would be expected from a simple dielectric picture. This is best visualized using the Lippert-Mataga theory for general solvation [159]. In this theory, the solute is considered to be a dipole in a continuum medium of uniform dielectric constant. The influence of the solvent on the energy separation between the ground and the excited state of the solute is characterized by the solvent dielectric constant and refractive index. The first accounts for the dynamic solvent response, while the latter accounts for the instantaneous response. The Lippert-Mataga equation is given by:

$$\nu_A - \nu_F = \frac{2}{hc}\ \frac{\varepsilon - 1}{2\varepsilon + 1} - \frac{n^2 - 1}{2n^2 + 1}\ \frac{(\mu_E - \mu_G)^2}{a^3} \tag{6.1}$$

$$\nu_A - \nu_F = \frac{2}{hc}\Delta f\,\frac{(\mu_E - \mu_G)^2}{a^3} \tag{6.2}$$

where ν_A is the absorption frequency of the solute (in wavenumbers), ν_F is the fluorescence frequency of the solute (in wavenumbers), h is Planck's constant, c is the speed of light, ε is the solvent's dielectric constant, n is the solvent's refractive index, μ_E is the dipole moment of

the excited-state, μ_G is the dipole moment of the ground-state, and a is the radius of the Onsager cavity. Thus, a plot of $(\nu_A - \nu_F)$ as a function of Δf should give a linear correlation with a slope proportional to $(\mu_E - \mu_G)^2$. Since no specific interactions between the solute and solvent are included in the theory, such interactions are revealed by deviations from linearity. The Lippert-Mataga plots for 1N and 2N are given in figure 6.14a and 6.14b respectively. While good linear correlations are found for the solvents in which quenching does not occur, significant deviation is found in both C_2Cl_4 and $CHCl_3$, indicative of the presence of specific interactions in these solvents.

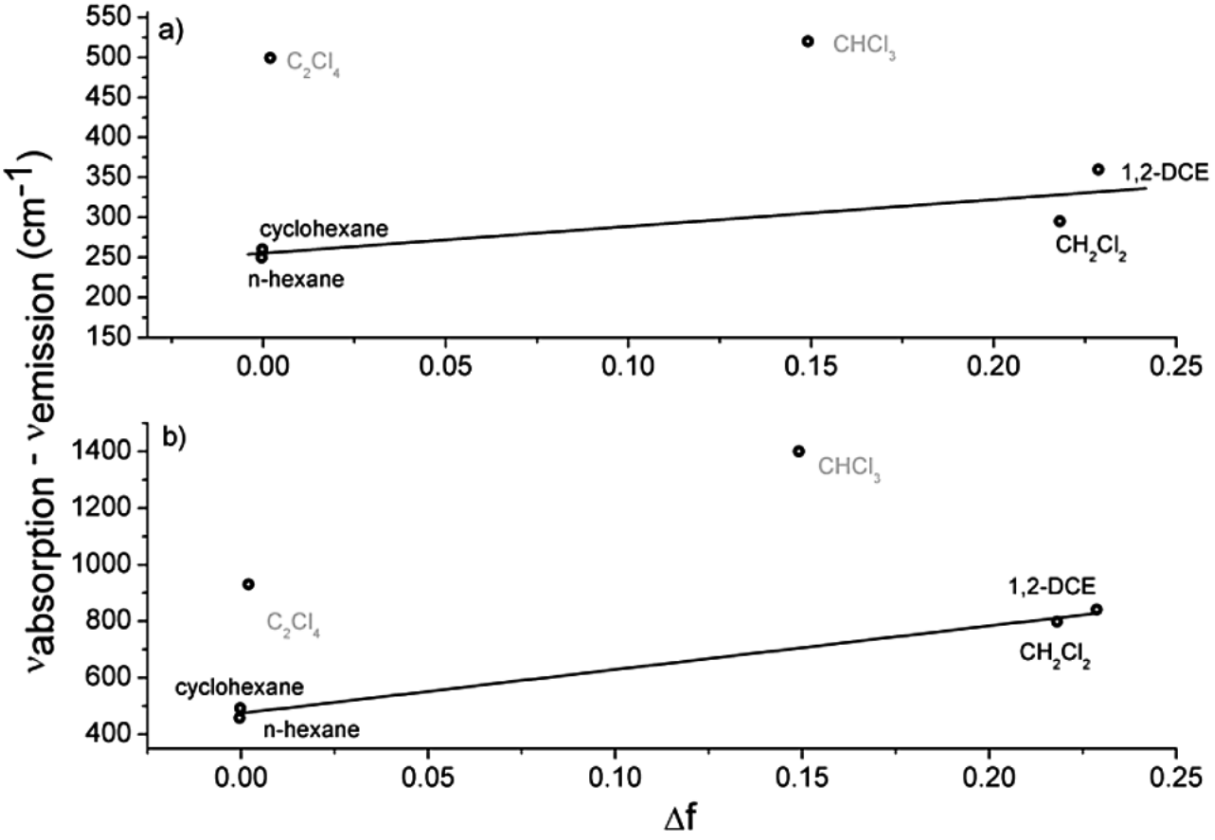

Figure 6.14: Lippert-Mataga plot of $(\boldsymbol{\nu_A - \nu_F})$ as a function of $\boldsymbol{\Delta f}$ for a) 1N and b) 2N in various solvents. The frequencies correspond to the lowest energy maxima of the respective absorption and emission spectra.

The quenching of anthracene by CCl_4 was found to be wavelength dependent. This was explained by the formation of a ground state complex which resulted in photoselection at wavelengths corresponding to its absorption spectra, where the main changes occur in the red-edge of the absorption spectra [41, 42]. This is similar to the changes in the absorption spectra of 1N and 2N in the pure quenching solvents, but unlike anthracene, these spectral differences are not apparent when using ternary systems. This indicates that while ground state complexes are present in the pure solvents, the complexation constant is smaller than for anthracene with

CCl_4, and therefore not sufficient to afford significant complexation in ternary systems such as those employed in the measurements of Encinas and coworkers [38]. The presence of ground-state complexes is further evidenced in a study by Mishra *et al.* who found evidence for static and dynamic components to the quenching rates when large quencher concentrations were used [43, 44].

Given the presence of ground-state complexes, both ground-state complexes as well as free naphthalene molecules are excited in the experiment. The free naphthalene molecules give rise to the vibrational bands characteristic of the S_1 state as confirmed by the correspondence with fluorescence lifetimes measured by TCSPC and by the vibrational mode pattern which is the same as the one measured in solvents where no charge transfer occurs. On the other hand, the excitation of ground-state complexes appears to give rise to very fast charge transfer occurring within our time resolution of 200fs. This reaction can be inferred by looking at the initial intensity of the excited-state fingerprint band of 1N at around 1280cm^{-1} in C_2Cl_4, $CDCl_3$ and CCl_4. It is immediately apparent that the initial intensity of this band in CCl_4 is much less than in C_2Cl_4 or $CDCl_3$, concomitant with the larger electron affinity of CCl_4 and its higher complexation constant: deviation from linear Stern-Volmer behaviour indicative of static quenching, ie complexation, was observed for concentrations of only 0.03M CCl_4, while deviations became apparent for $CDCl_3$ at concentrations higher than 1M [44].

Since the experiments are performed using the charge acceptor as solvent, the bi-exponential dynamics cannot be explained by diffusion processes. Instead, we propose that there are reactive and unreactive solvent configurations, where the reactive configuration is likely characterized by the adoption of a particular geometry between the chlorine of the solvent and the aromatic system. The bi-exponential behaviour can then be explained by the presence of an equilibrium between the reactive and unreactive solvent configurations, with the reactive configuration leading to charge transfer to form an exciplex.

6.2.3 Comparison between 1- and 2-naphthol

Electron transfer rates were found to be around ten times faster in 1N compared to 2N. This agrees with the calculated excited-state charges presented in chapter 5, where 1N was found to undergo more charge redistribution from the oxygen into the ring than 2N. While the ionization potentials of 1N (4.13eV) and 2N (4.18eV) are similar, it can be seen in figure 6.2 that the Stokes shift is at least 1.5 times larger for 2N than for 1N. According to the Rehm-

Weller equation presented in chapter 3 (equation 3.13), this serves to reduce the exergonicity of the reaction, and thus lower the electron transfer rate in the normal Marcus region.

6.2.3.1 Influence of a hydrogen bond and solvent polarity

Using binary mixtures to gradually change the solvent properties, Mishra *et al.* found that the charge transfer reaction of naphthols with CCl_4 are dependent on the viscosity of the solvent and not its polarity which points to a diffusion controlled reaction [43]. In chloroform however, the rates were found to be slower than diffusion controlled and as such, the influence of the solvent polarity was manifest with faster rates in more polar solvents capable of stabilizing the exciplex. This last observation is in accordance with our proposed model discussed in section 6.2.2, where the presence of reactive and unreactive solvent/quencher configuration illustrates the requirement of more than just diffusion to a certain contact distance for the charge transfer reaction to occur. In the case of transfer to CCl_4, as the equilibrium between the reactive and unreactive solvent configuration is highly displaced towards the reactive configuration, most diffusive approaches will result in successful electron transfer.

No clear trend of the quenching rates with the hydrogen bonding properties of the solvent were reported for the static experiments. However, these experiments only probe the dynamic quenching rates where the charge transfer rates are convoluted with the slow diffusion dynamics. In order to isolate the charge transfer dynamics, time resolved transient IR measurement were performed using the electron acceptor as solvent. The rates of 1N in C_2Cl_4, are compared to that of the 1:1 complex with MeCN in the same solvent, as well as the dynamics of 1N in MeCN to which 1M of C_2Cl_4 is added. By comparing the rate in C_2Cl_4 to that of the 1:1 complex where the solvent properties of C_2Cl_4 are not altered, it is possible to isolate the effect of a hydrogen-bond on the charge transfer reaction. The relative importance of the solvent polarity and specific hydrogen bond interactions can then be inferred by comparison of the rate in the 1:1 complex with that in acetonitrile to which 1M of C_2Cl_4 is added: in the first case only the presence of a hydrogen-bond differs from the experiment in pure C_2Cl_4, while in the second, both specific (HB) and non-specific (polarity) solvent effects are present. We find that the transfer rate is ten times faster in the hydrogen-bonded complex (5.6ps versus 60ps) while it is only 1.4 times faster due to the effect of the solvent polarity (4ps versus 5.6ps). Given that the charge was shown to originate from the aromatic system,

these results constitute convincing evidence of the importance of a hydrogen-bond on the extent of charge transfer.

6.3 Summary

The excited state charge transfer reaction from 1N and 2N to halogenated solvent acceptors like chloroform or carbon tetrachloride was investigated with transient IR spectroscopy of both the OH stretch vibration and the fingerprint region. By using the charge acceptor as solvent, it was possible to directly investigate the charge transfer without complication from diffusion dynamics. The presence of ground state complexes was established by looking at the absorption spectra, where the charge transfer dynamics are characterized by an equilibrium between reactive (complexed) and unreactive solvent configurations. Using theoretical calculations, it was possible to confirm that the charge originates from the aromatic π orbitals of the naphthols and not the oxygen lone pair. As such, the reaction can be utilized to probe the changes in electronic density occurring in the aromatic ring upon excitation. In this way, the influence of a hydrogen bond on the extent of charge redistribution was evidenced. Indeed, charge transfer from hydrogen bonded complexes of 1N with acetonitrile were found to have transfer rates ten times faster than for the non hydrogen bonded case in the same solvent. Comparison with the charge transfer rates using pure acetonitrile as the solvent with 1M electron acceptor further enabled us to determine that the effect of solvent polarity is much smaller than that of specific HB interactions. The current experimental evidence, as well as the fact that the theory was unable to correctly reproduce the larger solvatochromism of the 2N:acetonitrile complex in the excited state compared to the ground state (chapter 5), constitute mounting evidence that the small charge redistribution calculated for photoacids in the gas phase or in low polarity solvents is limited to those systems where no hydrogen bonds are present.

7. Level dynamics and the relative acidity of 1- and 2-naphthol

1-Naphthol (1N) and 2-Naphthol (2N) are two structurally similar molecules with significantly different spectral properties. As discussed in chapter 2, these differences are attributed to the influence of the OH functional group on the two perpendicular transition dipole moments of the parent naphthalene molecule. Of particular interest to the field of photoacid research is the thousand-fold higher excited-state acidity of 1N. Excited-state level crossing occurring dynamically upon excitation due to the differential solvation of the ^1L_a and ^1L_b states has commonly been postulated to explain why these two geometrical isomers with comparable ground-state acidities (pK_a 1N=9.4 and 2N=9.6) show such marked differences in the excited-state [243] (figure 7.1).

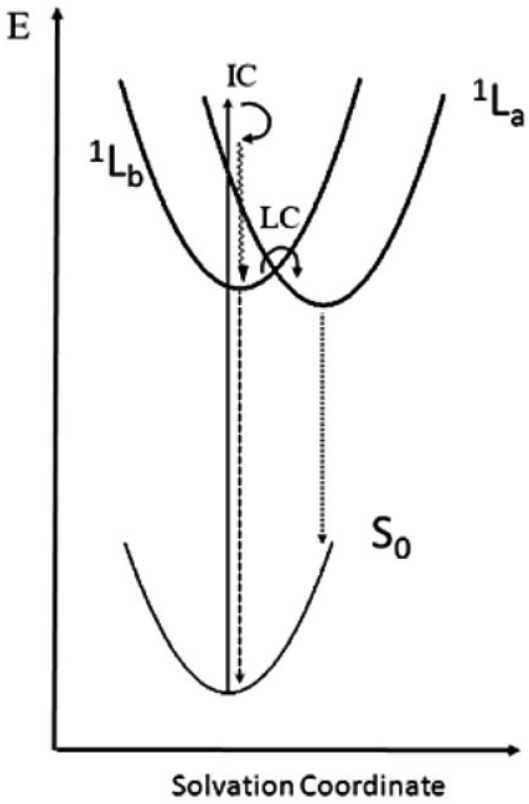

Figure 7.1: Level scheme for the proposed dynamical level crossing occurring in 1N where rapid internal conversion (IC) first leads to the ^1L_b state followed by solvation driven level crossing (LC) to the more polar ^1L_a state.

Although 1N and 2N are commonly regarded as the two prototype photoacids, they have not yet been investigated with femtosecond techniques. This is likely due to the fact that they

absorb in the ultraviolet with low cross-sections, they are only slightly soluble in water, and they are not very photostable. Thus, although it is generally agreed upon that level crossing (LC) occurs in 1N based on the shape, polarization and solvent or temperature dependence of the steady-state spectra [30, 31, 32, 33, 34, 35], no measurements with sufficient time-resolution have been performed in order to determine the dynamics or characteristics of the LC event. It is therefore impossible to say if this LC happens on timescales characteristic of solvent relaxation, or if it instead occurs on timescales comparable to the ESPT event where internal conversion to the more charge transferred ^1L_a state would then serve as a trigger for the ESPT reaction. Coupled molecular dynamics/quantum simulations of gas-phase 1N-water clusters performed by Knochenmuss *et al.* point to the last mechanism: basing themselves on their experimental results where they found signatures of vibronic state mixing in the fluorescence spectra, they found that when the 1N:H_2O cluster was distorted along the vibronic mixing coordinate, level inversion occured. According to their simulation, the polarity of the excited-state is increased by the vibronic coupling with the more polar ^1L_a state which leads to a water-naphthol feedback cycle ultimately resulting in LC. The ESPT event itself was not modeled but, as the ^1L_a state is found to quickly revert back to the ^1L_b state, it is thought that level inversion must lead directly to ESPT. On the other hand, an extended study of the solvent dependent fluorescence of 1N by Magnes *et al.*, found that LC in solution occurs in polar solvents such as DMSO where ESPT does not occur [35]. This is in accordance with an earlier study by Tramer *el al.* [30]. As such it was concluded that the proton transfer rate is not controlled by LC and is instead determined by the overall solvent stabilization of the photoacid, photobase and proton.

Given the experimental difficulties associated with measuring the naphthols, most research has focused on pyrene derivatives, especially 1-hydroxypyrene-3,6,8-trisulfonate (HPTS). This last possesses all the spectral advantages lacking in the naphthols, namely: it absorbs at 400nm, it is very soluble in water due to its three sulfonate groups, it is a fluorescent dye with a large cross-section and it is photostable. Femtosecond fluorescence up-conversion studies coupled with transient absorption measurements performed by Tran-Thi *et al.*, identified two fast dynamics occurring well before the signature ESPT to water which is characterized by a 88ps time constant: a 300fs dynamics attributed to solvation and a 2.5ps dynamics assigned to level inversion occurring in the acid before the ESPT event [66, 114]. This last was found to be accompanied by a 1400cm^{-1} red-shift and a 40% decrease in integrated intensity. On the other hand, the fluorescence up-conversion (UC) spectra of HPTS in ethanol only showed a slight red-shift of 100cm^{-1} characterized by a 2ps timescale. Interestingly, direct excitation of

the HPTS anion in basic media gave rise to a very moderate shift of 350cm^{-1} with a 400fs characteristic time constant. It was thus deduced that no level inversion occurs in the conjugate photobase. However, according to the thermodynamic considerations brought forth to justify a product-side driven ESPT reaction, level crossing in 1N which effectively lowers the energy of the acid should instead inhibit ESPT unless it is compensated by an even larger stabilization occurring in the conjugate photobase [28]. Indeed it is claimed that any stabilization occurring in the acid makes dissociation to the photobase more uphill. As it is evidently the case for HPTS that solvation is instead more important in the acid, it seems apparent that the simple thermodynamical picture is insufficient to characterize the nature of photoacidity.

Tran-Thi *et al.* support their level crossing hypothesis mainly by the fact that a 40% decrease in oscillator strength was observed which is inconsistent with pure solvation processes [114]. However, it is quite surprising that the LC from the ^1L_b to the ^1L_a state which has a larger charge transfer character should be accompanied by a *decrease* in intensity as that would imply a lower transition dipole moment for the ^1L_a state. Furthermore, LC only makes sense in the case that the locally excited state is the ^1L_b state. For HPTS, several conflicting assignments exist in the literature but recent magnetic circular dichroism and polarization measurements on HPTS have established that while the ^1L_b and ^1L_a states are heavily mixed, have nearly parallel transition dipoles and are relatively close in energy, the lowest state in both the protonated and the deprotonated form has primarily ^1L_a character [244, 245]. In addition, they were able to fully attribute the solvent dependence of the vibronic structure of HPTS to solvent induced vibrational dephasing using a Brownian oscillator model without needing to invoke any solvent dependent level inversion. In light of these results, it is problematic to assign the dynamics which were observed in water but not in ethanol to excited-state level crossing. A further argument against the LC hypothesis is the fact that no dynamics on similar timescales were observed in the transient spectra of the MIR fingerprint region of HPTS [246]. If it is supposed that the molecule changes electronic state, at least some modification of the fingerprint band pattern is expected.

The Fayer group has expanded on the measurements of Tran-Thi *et al.* by measuring HPTS and other pyrene derivative photoacids in various solvents with transient absorption spectroscopy [247, 248, 249]. They also observe picosecond dynamics in the more polar solvents which they ascribe to slow charge redistribution which primes the molecule for ESPT, even though it is decoupled from the main proton transfer dynamics. As the fast

dynamics were not observed in the methoxy derivative, they concluded that this redistribution is determined by specific rearrangements of the hydrogen bond between the hydroxyl and the accepting base molecules which occurs relatively slowly given the magnitude of the charge transfer in such strong photoacids as well as the need to attain a special geometrical configuration.

However, this interpretation is at odds with the fact that only a small Stokes shift was measured by Tran-Thi *et al.* in ethanol which is a stronger hydrogen bond acceptor than water. In addition, while photoacids like HPTS and 8-Hydroxy-N,N,N′,N′,N″,N″-hexamethylpyrene-1,3,6-trisulfonamide (HPTA) measured by the Fayer group are often touted as strong photoacids, they are actually not so as one must distinguish between the value of the pK_a* which determines the rates of the ESPT, and the ΔpK_a ($\Delta pK_a = pK_a - pK_a$*) which characterizes the *change* in acidity. Adding electron withdrawing groups like sulfonates (HPTS) or sulfonamides (HPTA) on the aromatic ring capable of pulling away electronic density increases the charge transfer away from the oxygen. However, this also affects the ground state electronic distribution, thereby also reducing the ground state pK_a. Indeed, the ground state pK_a of the parent molecule, 1-hydroxypyrene, is 8.7 while that of HPTS is 7.7 and HPTA is 5.6. The change in pK_a for these two molecules is larger than for 1-hydroxypyrene which is concomitant with the greater intramolecular charge transfer in the excited state ansatz leading to a larger effect of the electron withdrawing groups. However, their ΔpKa are nonetheless even a bit lower than that of 2N which is not considered a strong photoacid (see table 1.1 for values). This is supported by the change in dipole moments for these molecules. While HPTS and HPTA have larger dipole moments than 2N, the actual changes upon electronic excitation are comparable [250].

Solvent relaxation due to specific interactions such as hydrogen bonding (HB) is generally found to proceed on tens to hundreds of femtoseconds [211, 251](Pines, Pines [227]). Postulating that this could extend to several picoseconds in the case of strong photoacids where it is thought that large changes in charge redistribution occurs only makes sense when the timescale and magnitude of the accompanying spectral shifts are directly correlated to the HB accepting capabilities of the solvent and the changes upon excitation of the HB donating capabilities of the photoacid. As the existing data does not seem to support this hypothesis, another explanation appears to be necessary.

Given the uncertainty and dissent facing the interpretation of HPTS's steady state data, it is not surprising that attaining a proper understanding of the femtosecond results is challenging. The aim was therefore to look at the much simpler, albeit harder to measure, naphthols with well agreed upon steady-state properties. As the two prototype photoacids, comparison of their spectral behavior can hopefully highlight the changes occurring in 1N which result in the thousand fold increase in photoacidity when compared to 2N. This should also help to better understand the molecular mechanism and important processes for photoacidity. First the fluorescence UC data of 1N and 2N will be presented. Then, given the near perpendicularity of the two states involved in 1N, fluorescence ansisotropy measurements will be given where LC should give rise to changes in anisotropy on timescales characteristic of the LC event. Finally, transient infra-red (TrIR) measurements are shown which should reveal changes in the highly specific fingerprint region in the occurrence of LC. Discussion of the possible mechanisms giving rise to the observed behavior and parallels with the existing data on other photoacids such as HPTS will then be attempted. Lastly, the origin of the important decrease in fluorescence integrated intensity observed in several systems will be discussed.

7.1 Experimental results

7.1.1 Fluorescence up-conversion results

7.1.1.1 2-naphthol

As we are ultimately interested in the relaxation processes and nature of the excited state, fluorescence up-conversion (UC) spectroscopy is indicated. The fluorescence UC data of 2N in both DMSO and H_2O are measured in order to provide a basis for comparison with subsequent 1N measurements. Indeed, according to steady-state studies, no level crossing should occur. Furthermore, although partial ESPT of 2N occurs in water, this happens on a timescale of several nanoseconds which is much longer than those probed by the current femtosecond experiments [252, 253].

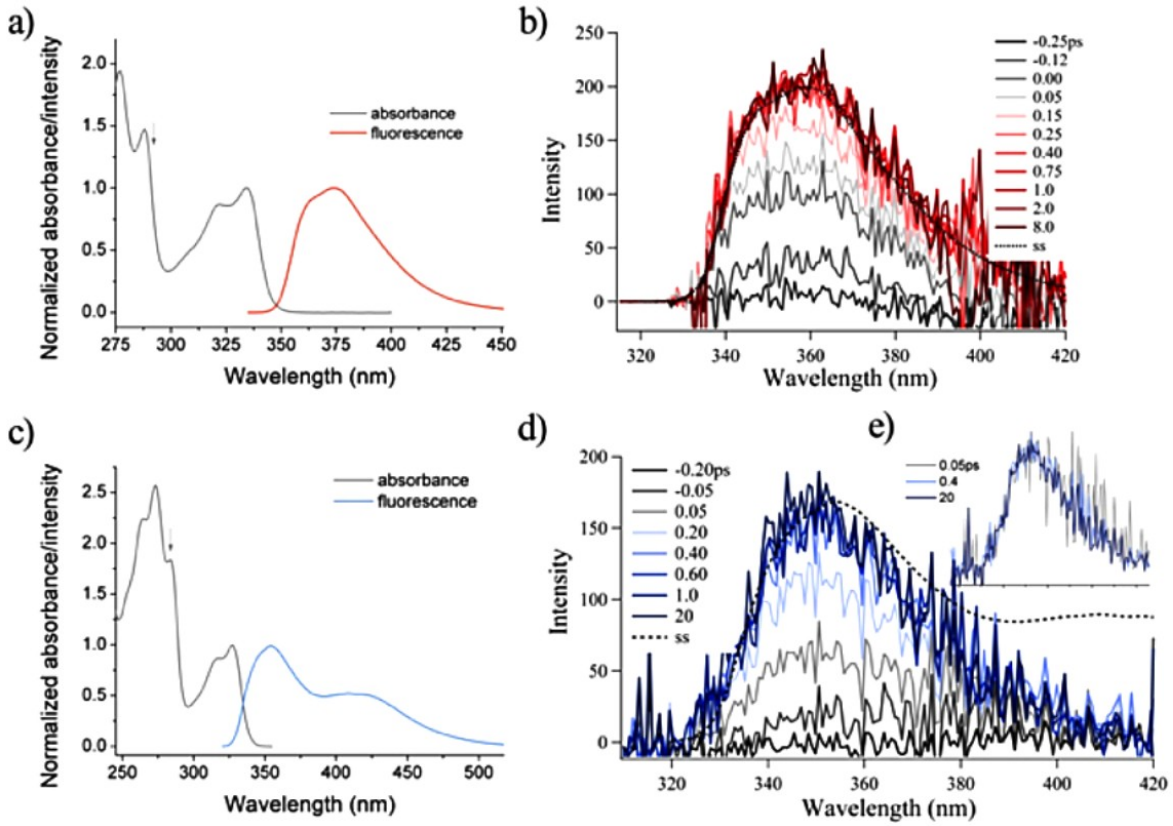

Figure 7.2: a) Absorbance and fluorescence spectra of 2N in DMSO where the arrow indicates the excitation wavelength for the b) fluorescence up-conversion spectra at various delays. c) Absorbance and fluorescence spectra of 2N in H_2O where the arrow indicates the excitation wavelength for the d) fluorescence up-conversion spectra at various delays. Note that the steady-state spectra in water contains emission from the conjugate photobase created from the ESPT event, however this happens on much longer timescales than those probed here. e) Normalized fluorescence up-conversion spectra of 2N in H_2O for pulse delays of 50fs, 400fs and 20ps.

As can be seen in the fluorescence up-conversion data presented in figure 7.2, no significant dynamics beyond the rise of the signal within our time resolution of 150fs are seen in either system. In order to better visualize this, spectra for 2N in water at various times have been normalized and are shown in Figure 7.2e. Given the high polarity of the solvent and the small increase in dipole moment, a Stokes shift is expected which is not observed. However, this is in line with previous results on the triply negatively charged HPTS photoacid where a Stokes shift of only 100 cm^{-1}, i.e. a few nanometers, was observed in ethanol [66]. The inferior signal-to-noise ratio of the current experiment given the much smaller fluorescence cross-sections of the naphthols does not allow us to discount the possibility of such minute shifts due to solvation effects. We estimate that our signal-to-noise ratio would allow us to observe any shifts larger than 150cm^{-1} in DMSO and 250cm^{-1} in H_2O.

Excitation with excess energy is unavoidable in order to probe the blue edges of fluorescence bands. However, even though we excite at 290nm which corresponds to the ^1L_a transition (see

arrows in figure 7.2), relaxation to the lower-lying ^1L_b state is exceedingly fast, occurring within the pulse duration. Fast internal conversion (IC) on 10-50fs timescales are commonly found for aromatic molecules. For example, IC from the excited ^1L_a state (S_2) to the ^1L_b state (S_1) in gas-phase naphthalene occurs in 30fs [254]. No fluorescence dynamics indicative of vibrational cooling were observed and a test transient IR experiment exciting with 3000cm^{-1} excess energy showed no signature for vibrational cooling in the fingerprint region of 2N in DMSO.

7.1.1.2 1-naphthol in dimethylsulfoxide

Steady-state studies have revealed the lack of mirror symmetry between the absorbance and fluorescence spectra of 1N in DMSO (figure 7.3a). This has commonly been attributed to solvent assisted level crossing from the ^1L_b to the ^1L_a state, with the more polar ^1L_a state further stabilized in high dielectric solvents. However, unlike in water, there is no ESPT event occurring within the excited state lifetime. This should make it possible to isolate level crossing dynamics from those of the ESPT. The fluorescence UC data of 1N in DMSO is shown in Figure 7.3b.

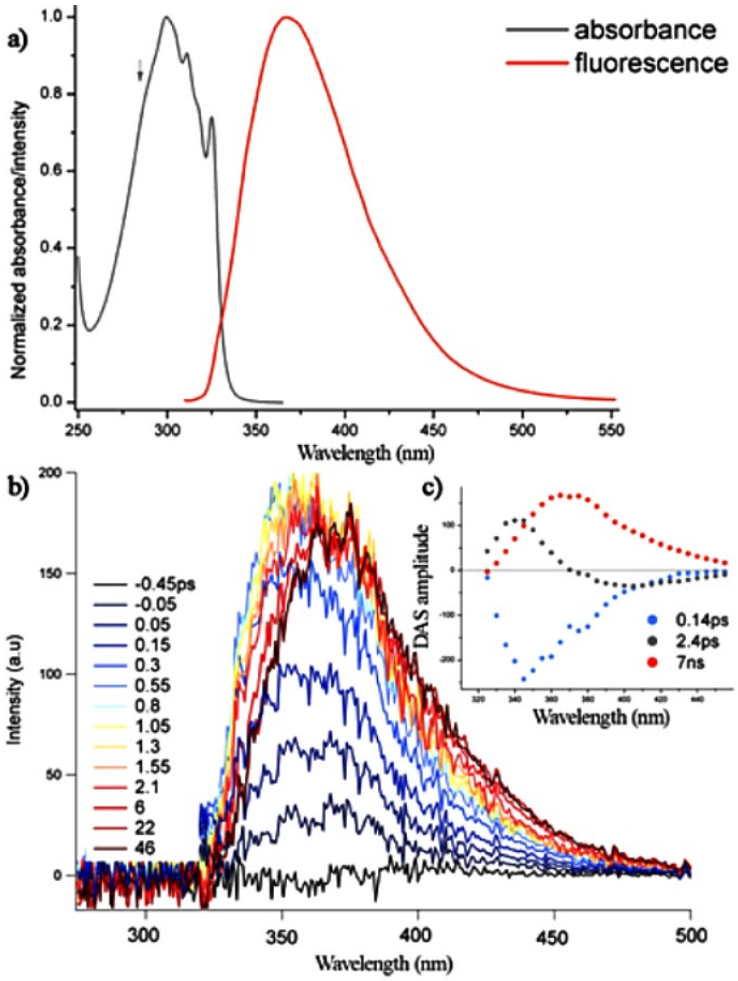

Figure 7.3: a) Absorbance and fluorescence spectra of 1N in DMSO with the arrow indicating the excitation wavelength b) Fluorescence up-conversion spectra of 1N in DMSO for selected pulse delays b) Decay associated spectra (DAS). The global fit was only performed for the first 20ps of dynamics in order to give better results at early times with the lifetime fixed to 7ns according to TCSPC measurements.

Significant dynamics are readily apparent which were characterized by means of a global fit procedure with kinetic traces averaged over 5nm. Global analysis serves to improve the resolution of correlated parameters by the simultaneous analysis of multiple intensity decay curves. In this case, the time constants have been assumed to be independent of emission wavelength. Three characteristic times were needed: one to fit the lifetime of the 1N emission and two to fit the early time dynamics (τ_1, τ_2 and τ_3). The related amplitudes (A_1, A_2 and A_3) are recovered for each wavelength according to:

$$I = \sum_{i=1}^{3} A_i \cdot e^{-t/\tau_i} \otimes exp\left(-\frac{t - t_0}{\Delta_{IRF}/(2\sqrt{ln2})}\right)^2 \quad (7.1)$$

The Gaussian term describes the convolution with the instrument response function with a full width half maxima of Δ_{IRF} and time zero, t_0. The instrument response function was estimated using the dynamics of the Raman line of water. The resulting decay associated spectra are shown in Figure 8.2c. In order to better reproduce the early dynamics, delays up to only 20ps were used in the global fit and the lifetime was fixed to 7ns as determined by previous time correlated single photon counting (TCSPC) experiments [253]. Interestingly, one finds a delayed rise of the fluorescence with a 140fs time constant followed by a 2.4ps Stokes shift.

A spectral moment analysis was also performed to better characterize the observed behavior whereby:

$$M_0\ t\ = \int_{v_1}^{v_2} I(v,t)\cdot dv \tag{7.2}$$

$$M_1\ t\ = \frac{1}{M_0}\int_{v_1}^{v_2} v\cdot I(v,t)\cdot dv \tag{7.3}$$

$$M_2\ t\ = \frac{1}{M_0}\int_{v_1}^{v_2} v^2\cdot I(v,t)\cdot dv\ - M_1^2 \tag{7.4}$$

where v is the frequency and $I(v,t)$ is the intensity. Thus, the zeroth moment ($M_0\ t\ $) gives the integrated intensity, the first spectral moment ($M_1\ t\ $) gives the average spectral position and the second spectral moment ($M_2\ t\ $) gives the spectral variance.

The dynamics of M_0 clearly show the delayed rise of the signal which is well modeled by the 140fs time constant found in the global analysis, and a subsequent 15% decrease of the band intensity with a 2.4ps timescale (figure 7.4a and 7.4b). This last behavior is unexpected as regular solvation processes are not usually found to affect the integrated band intensity. Furthermore, under the premise that the observed dynamics are related to level crossing to a state with a higher dipole moment, one would also expect a higher transition dipole moment which would instead lead to an increase in the integrated intensity. This peculiar behavior will be discussed in more detail in section 7.4. The 1050cm^{-1} Stokes shift dynamics was also found to have the same characteristic 2.4ps timescale (figure 7.4c).

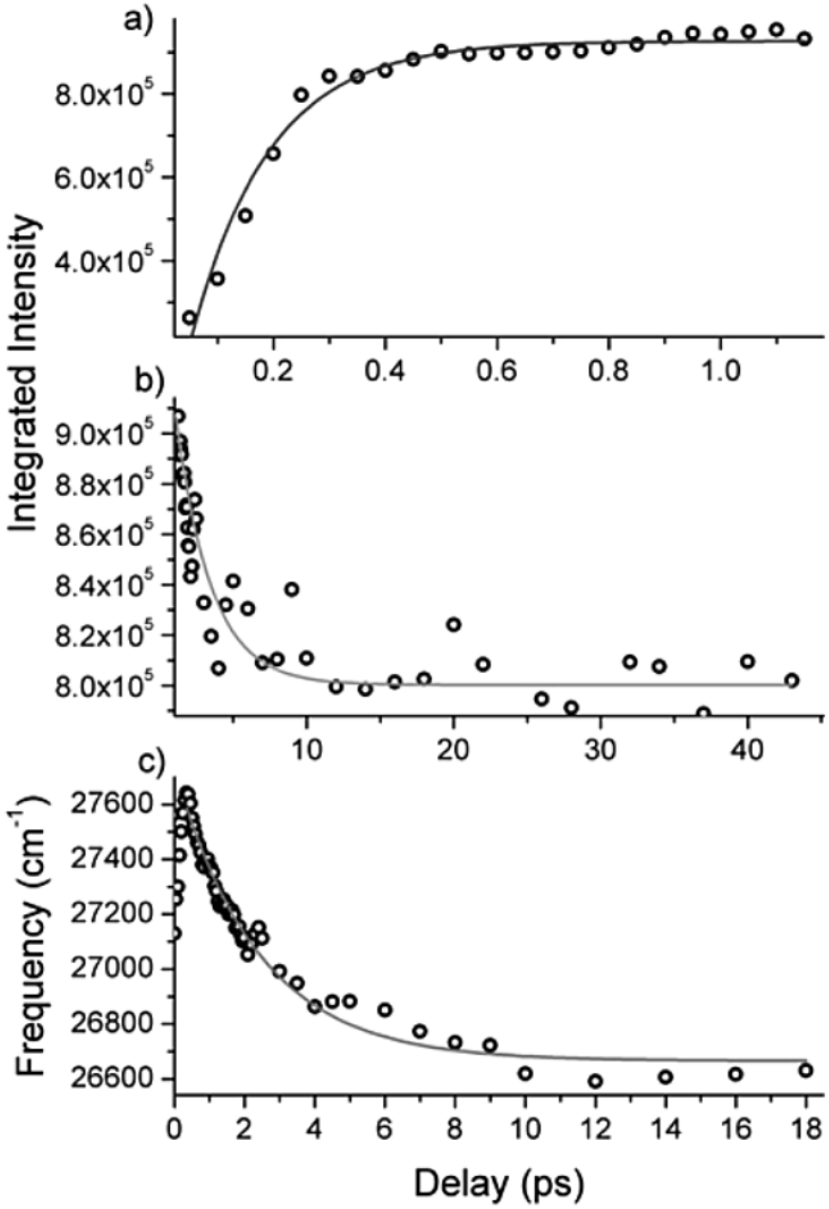

Figure 7.4: a) Dynamics of M_0 at early times with a 140fs fit. b) Dynamics of M_0 at longer times with a 15% decrease characterized by a 2.4ps time constant. c) Dynamics of M_1 corresponding to a 1050cm^{-1} red-shift with a 2.4ps time constant.

Similar to what was found for 2N, transient UV pump IR probe measurements performed with 3000cm^{-1} excess energy was identical to the measurement performed exciting the maxima of the lowest energy absorption band. As such, it is possible to discount vibrational cooling as being responsible for the observed dynamics.

7.1.1.3 1-naphthol in H_2O

It is purported that 1N in H_2O undergoes level crossing before ESPT, the latter occurring in around 35ps as measured with the rise of the conjugate base by TCSPC [253, 255].

Fluorescence UC spectra at various representative delays are given in figure 7.5a. The decay of the initial blue fluorescence correlated with the rise of the red emission from the anion represents the ESPT reaction. Furthermore, substantial dynamics are occurring in the acid on timescales much faster than that of the proton transfer. In order to characterize the observed dynamics, a global fit procedure was applied. Initially, three exponentials were used for the fit: one for the initial acid shift, another for the ESPT and lastly one for the lifetime of the base. However, similarly to what was found in DMSO, two exponentials were necessary to model the kinetics of the acid band at early times. A fourth exponential was therefore added to the fit with the resulting decay associated spectra given in figure 7.5b, where the lifetime of the anion was fixed to the value of 7.5ns found by TCSPC measurements [255]. In this TCSPC study it was found that the lifetime recovered from kinetic traces varied from 7 to 7.8ns depending on the fitted time range. However, modifying the anion lifetime in our fit from 7 to 8ns did not have any appreciable effect.

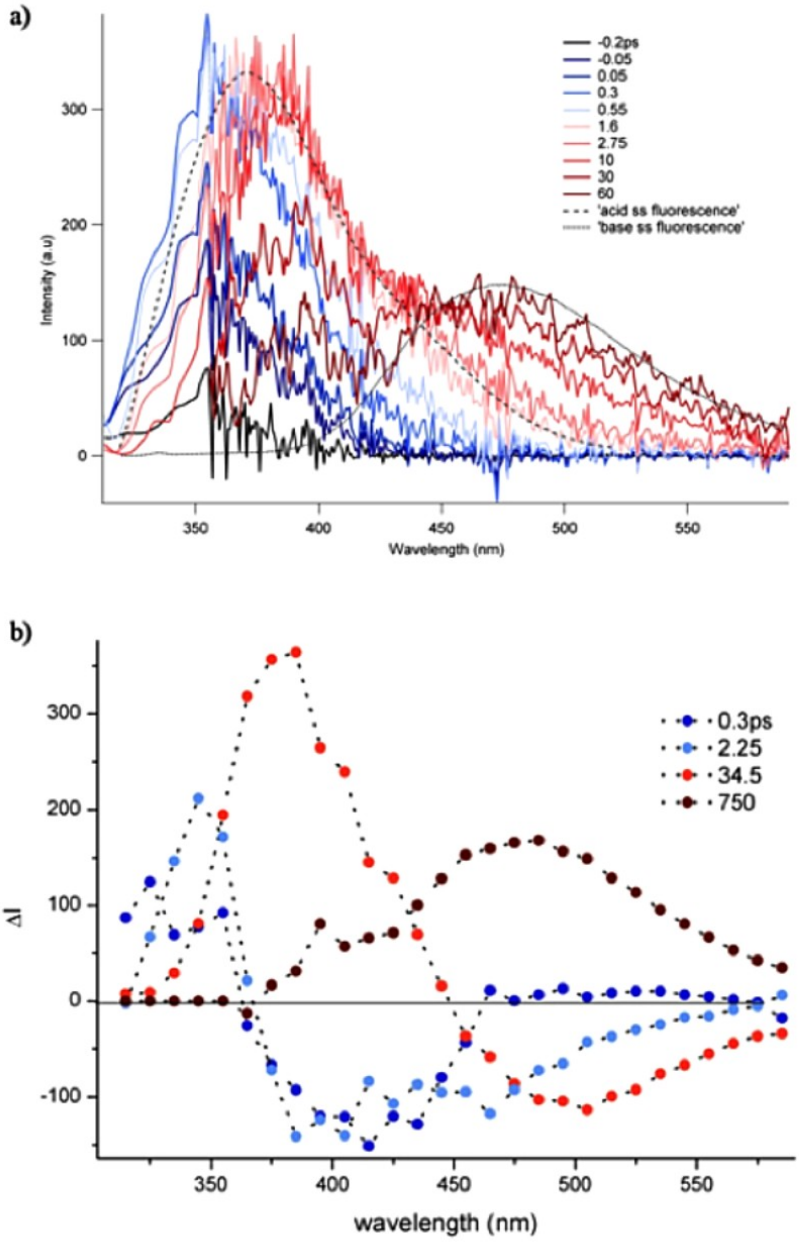

Figure 7.5: Fluorescence up-conversion spectra of 1N in H_2O pH=7. The steady-state fluorescence spectra of the acid and the base are shown for comparison. Note that the steady-state acid spectrum was obtained after base subtraction in acid media. Unfortunately, as the low signal in the blue-most spectral region precluded 2D measurements, spectra were instead interpolated from kinetic traces taken every 5nm. This accounts for the lack of noise in this region. b) Decay associated spectra from the fluorescence up-conversion measurement of 1N in H_2O with a four-exponential fit characterized by 300fs, 2.25ps, 34.5ps and 7500ps time scales, where the last time constant was fixed.

Similar to what was observed in DMSO, the first 300fs timescale represents a delayed rise, while the second 2.25ps timescale is accompanied by a 3025cm^{-1} shift and a decrease in integrated intensity.

The much smaller apparent cross-section of the signal attributable to 1-naphtholate emission at 480nm and the fact that after around 60ps, even though the acid signal is still decreasing, no concomitant rise of the base fluorescence is observed, is indicative of significant quenching processes occurring in the conjugate photobase. This will be discussed in more detail in section 7.2.

7.1.1.4 1-naphtholate in H_2O (pH=12)

Since the ESPT in neutral water occurs in 34.5ps, any rapid dynamics occurring in the base will therefore be convoluted with this time constant and not identifiable. In order to derive a complete picture of the solvation relaxations for the whole photocycle, the fluorescence UC spectra of the directly excited base was measured. This is shown in figure 7.6 where a very important Stokes shift is immediately apparent.

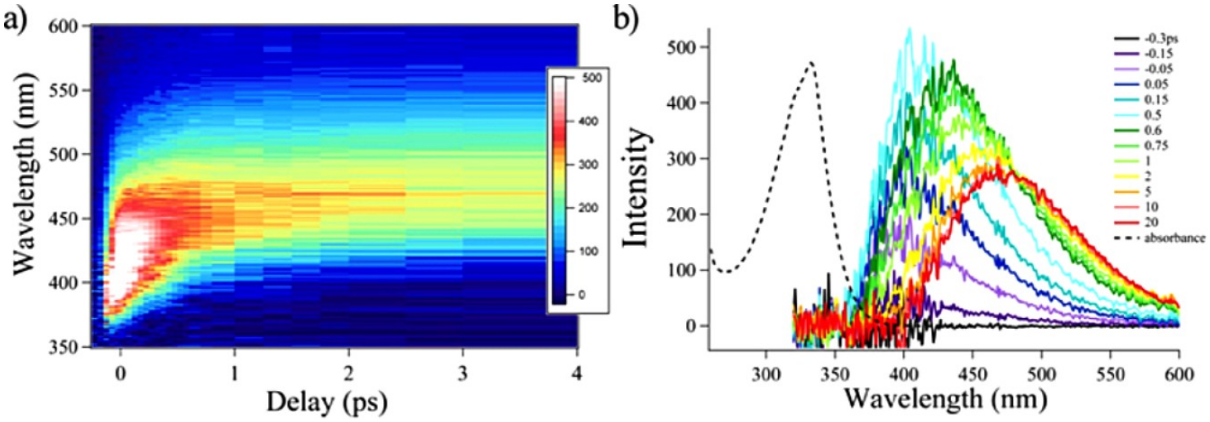

Figure 7.6: a) 2D figure of the fluorescence up-conversion spectra of 1N in H_2O at pH 12 i.e. the directly excited anion. b) Spectra at various delays with the steady-state absorbance spectra shown for comparison.

The global fit procedure revealed four characteristic time constants of: 120fs, 450fs, 1.9ps and a lifetime of 7.5ns, which was once again fixed to the value found in earlier TCSPC measurements (figure 7.7a).

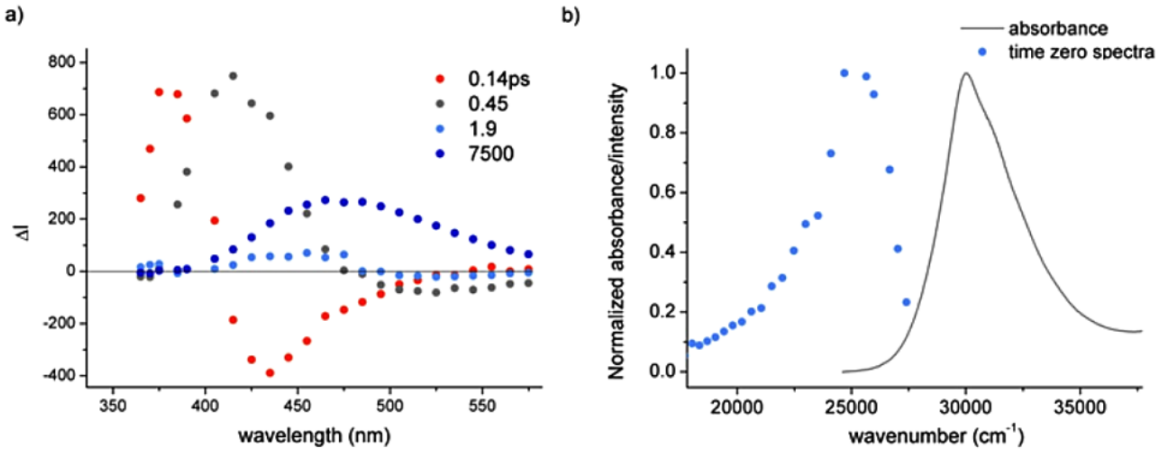

Figure 7.7: a) Decay associated spectra showing the three components with characteristic timescales of 120fs, 450fs and 7.5ns. b) Reconstructed "time-zero" spectrum shown with the absorbance spectra.

Reconstruction of the "time-zero" spectrum from the decay associated spectra gives a spectra which is a mirror image of the absorbance spectra (figure 7.7b). Subsequently, there is a rapid red-shift followed by a slower shift which is accompanied by significant reduction in the integrated intensity. According to a moment analysis we find that the spectra is shifted by 3200cm^{-1} and undergoes 60% loss in integrated intensity. A very efficient quenching mechanism is evidently present.

7.1.2 Fluorescence anisotropy results

The time resolved fluorescence anisotropy data for 1N, 2N and 1-naphtholate (1Nate) in DMSO is presented in figure 7.8. In order to excite only one band, it was decided to excite the ^1L_a transition as it is not possible to selectively excite the ^1L_b state in 1N. Thus 266nm excitation was used which also affords a much better time resolution of 100fs compared to the 200-250fs obtained in the broadband fluorescence measurements obtained using the doubled output of an optical parametric amplifier. However, for 1Nate in DMSO, 266nm excitation corresponds instead to the $^1B_{3u}^-$ transition which has a transition dipole moment perpendicular to that of the ^1L_a transition in 1N [105].

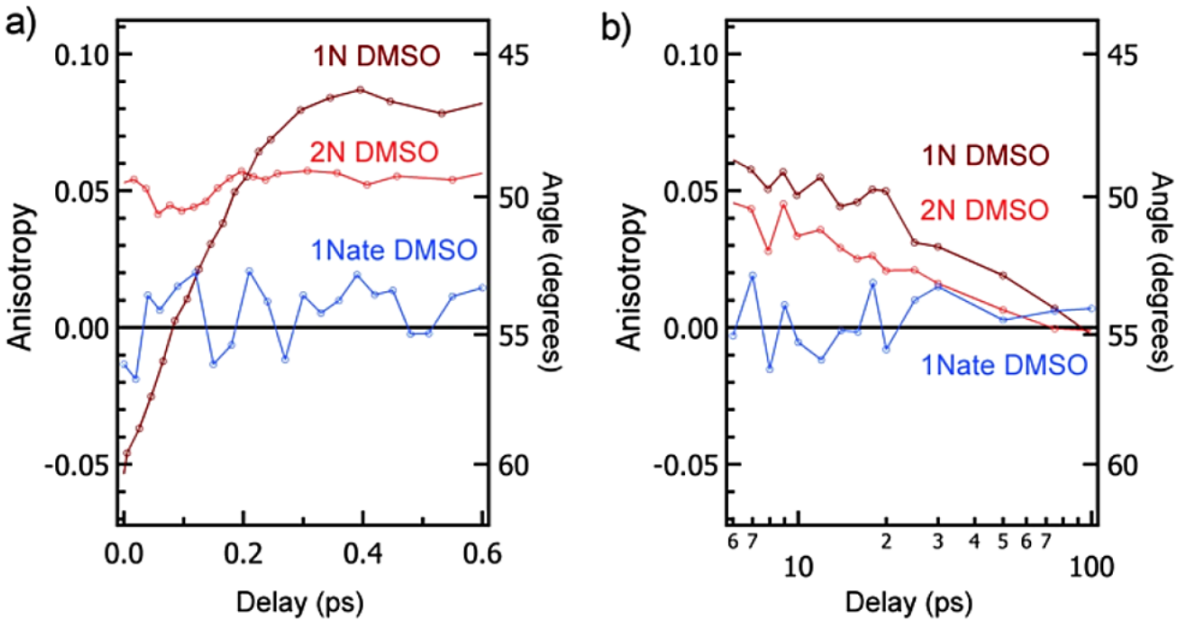

Figure 7.8: a) Time resolved fluorescence anisotropy of 1N, 2N, 1Nate in DMSO at early times. b) Anisotropy decay at longer times due to rotational diffusion.

It is immediately apparent for 2N in DMSO that, with the exception of an anisotropy decay through rotational diffusion happening on longer timescales, no dynamics are occurring. This is also the case for 1Nate in DMSO where even the initial anisotropy is zero. On the other hand, a significant increase in anisotropy for 1N in DMSO is happening on very fast timescales which peaks at a value of $r \approx 0.1$. No further changes are then found to occur apart from the decay back to zero with a 28ps timescale on the same order of magnitude as the 21ps decay found for 2N in DMSO.

7.1.3 Transient IR results

The fingerprint mid infra-red spectra of the naphthols are composed of a multitude of bands due to various ring vibrations as well as combination modes with the C-O-H bend and out-of-phase C-C-O stretch vibration (see chapter 2.3). Since the mode pattern is highly specific, it is expected that level crossing should be accompanied by the disappearance of the initial bands of the ^1L_b state and the appearance of new bands characteristic of the ^1L_a state.

7.1.3.1 2-naphthol

The steady-state fingerprint spectra of 2N in both dichloromethane (DCM) and DMSO are presented in figure 7.9a. The influence of hydrogen bonding and the polarity of the solvent

leads to important differences in the respective spectra. The next panel (figure 7.9b) shows the transient spectra in DCM and DMSO where bleach signals corresponding to the IR in the S_0 state as well as new bands arising from vibrations in the S_1 state are observed. Like all other molecules previously measured by transient IR spectroscopy, it is found that the fingerprint pattern changes considerably upon electronic excitation and that the vibrational mode pattern is also quite dependent upon the nature of the solvent.

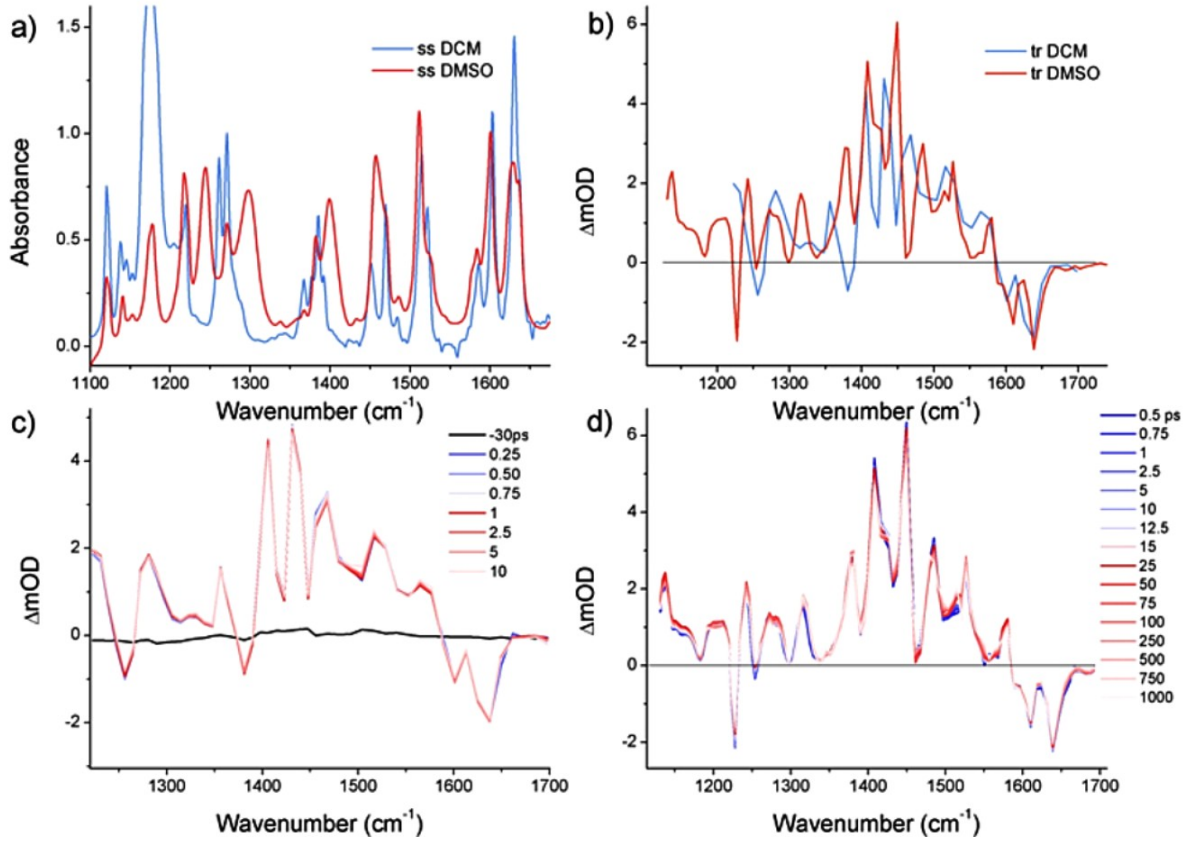

Figure 7.9: a) Steady-state spectra of 2N in dichloromethane and dimethylsulfoxide-d_6. b) Transient spectra of 2N in DCM and DMSO-d_6. Dynamics of the transient spectra of 2N in c) DCM and d)DMSO-d_6.

The spectra of 2N in DCM and DMSO at several time delays are given in figures 7.9c and 7.9d. It can be seen that no substantial dynamics are occurring in either case. The slow decay in DMSO is due to lifetime recovery.

7.1.3.2 1-naphthol

The transient spectra of the fingerprint region of 1N in DMSO-d_6 is presented in figure 7.10a.

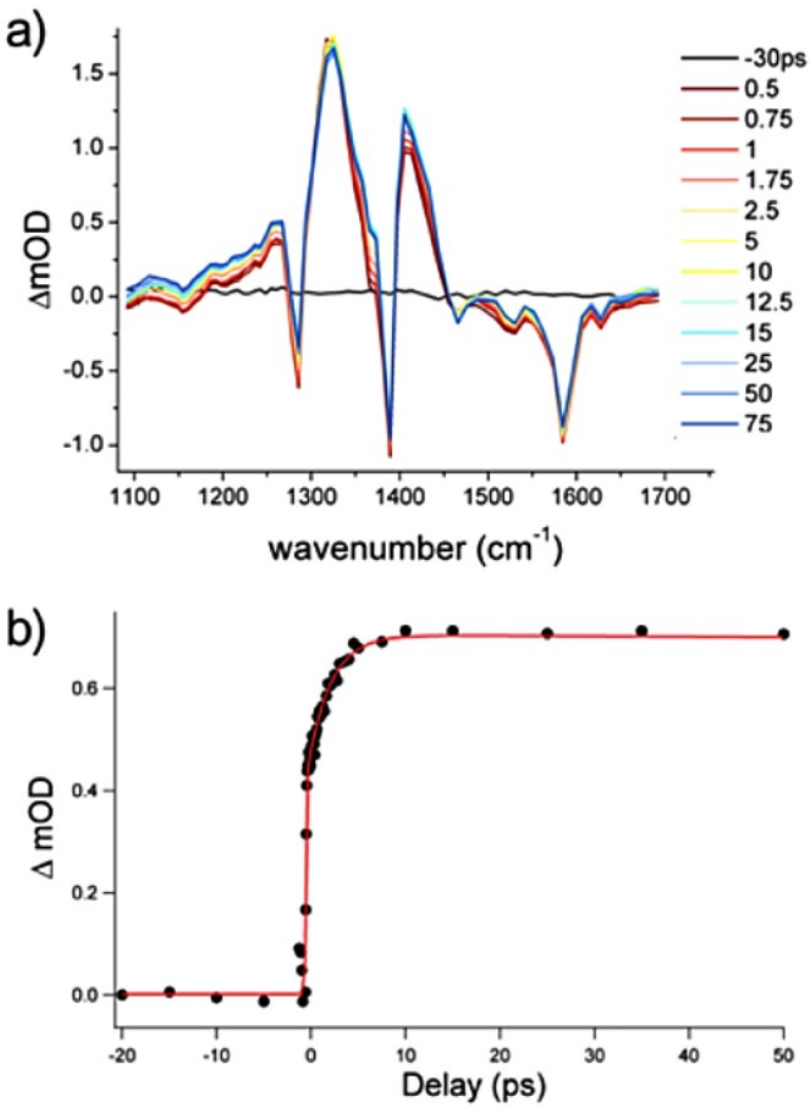

Figure 7.10: a) Transient spectra of 1N in DMSO-d_6. b) Dynamics of the spectral changes in the transient spectra with a characteristic 2.4ps timescales and an instrument response function of 200fs.

No distinct bands appear to be decreasing and there also does not appear to be any new bands. However, unlike what was observed in 2N, there are definitely significant changes occurring in the contour of the transient IR spectra on timescales matching those found by fluorescence up-conversion. The origin of these spectral changes will be discussed in conjunction with the fluorescence UC data in section 7.2.

7.1.3.3 1-naphtholate

The transient IR spectra of 1Nate was measured in order to better understand the nature of the important quenching reaction and the origin of the large Stokes shift which was observed in the fluorescence UC measurement.

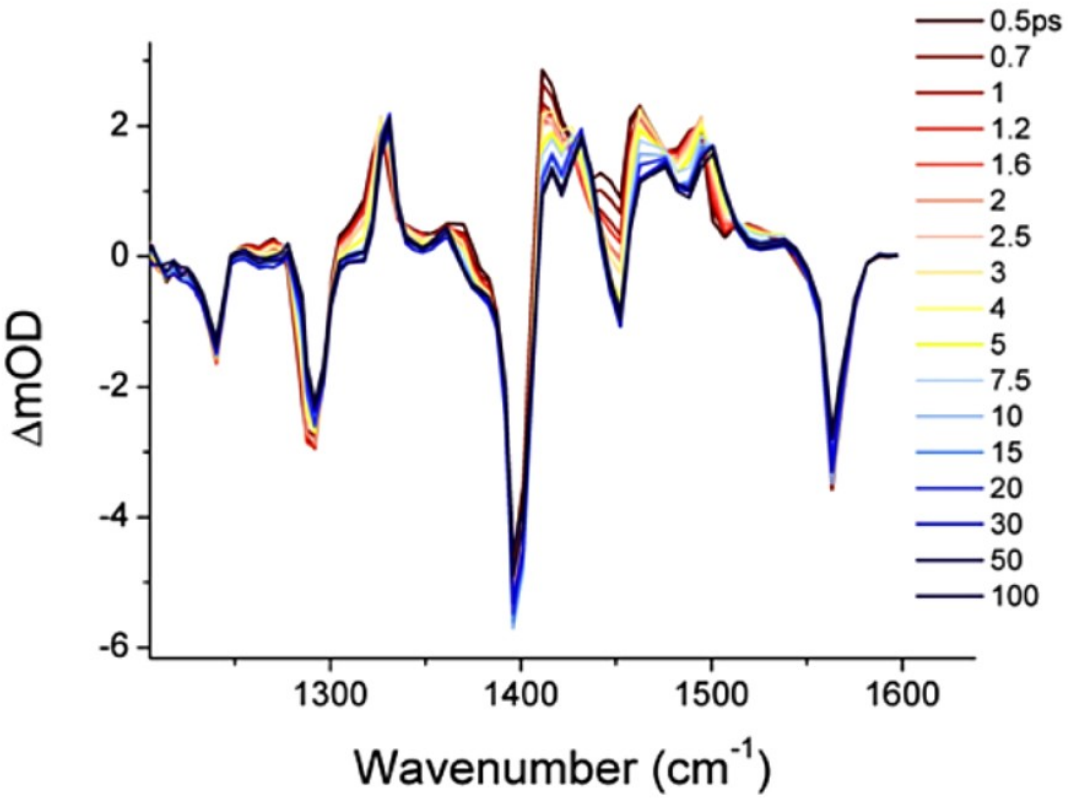

Figure 7.11: a) Transient spectra of 1Nate in MeOD-d_4.

Concomitant with the observed quenching of the S_1 fluorescence, the initial IR vibrations decrease in intensity but do not entirely disappear, while other bands grow in. This is accompanied by a very small bleach recovery of around 20%. Furthermore, as the new bands are both to the red and the blue of the initial vibrations, it is possible to discount solvation as the mechanism behind the observed dynamics. The decay of the initial peaks and rise of the new bands are characterized by a 10.3ps timescale in MeOD-d_4 and 2.4ps in both H_2O and D_2O. Given the absence of an isotope effect, it is likely that the quenching does not involve the HB donated to 1Nate by the solvent. A fitting procedure was applied to the band at 1410cm^{-1} in order to estimate the percentage decrease of the initial state. A value of 50% was found which is on the same order of magnitude as that found in the fluorescence UC measurements.

7.1.3.4 2-naphtholate

The transient IR spectra of 2-naphtholate (2Nate) in MeOD-d_4 is shown in figure 7.12a. Like what was observed for 1Nate, the initial bands decrease in intensity and new peaks appear including a very intense peak at 1350cm^{-1}. The dynamics are characterized by a 6.8ps timescale (figure 7.12b). Using the band at 1240cm^{-1} which does not appear to be overlapped with other vibrations, it is possible to estimate that the decrease in intensity is on the order of 25%.

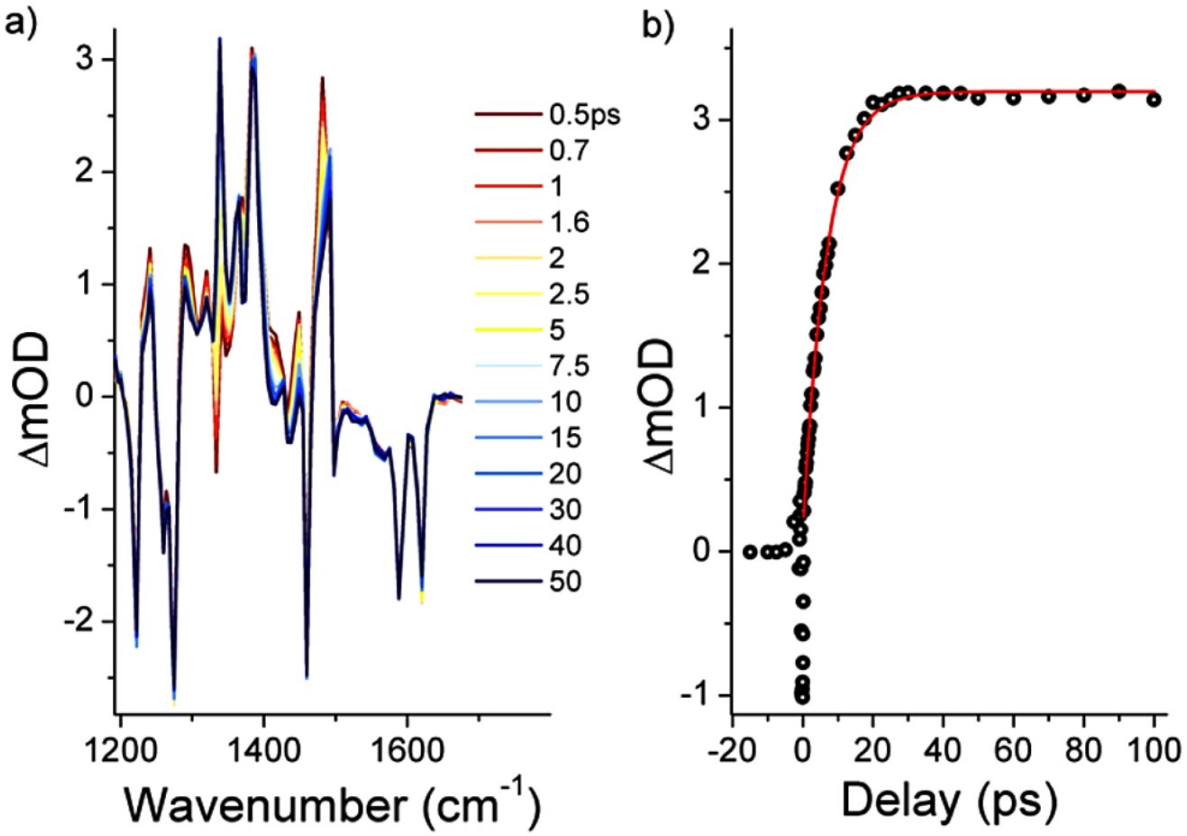

Figure 7.12: a) Transient spectra of 2Nate in MeOD-d_4. b) Dynamics of the spectral changes in the transient spectra.

7.2 Discussion

7.2.1 Nature of the dynamics

As expected from steady-state studies, 2N did not display any appreciable dynamics even in polar solvents like DMSO or H_2O, while dynamics were readily apparent for 1N in systems presenting large Stokes shifts thought to be indicative of level crossing (LC). With the aid of

the time resolved fluorescence UC, anisotropy and TrIR presented, it is now possible to better quantify and discuss the nature of the observed dynamics.

7.2.1.1 Fluorescence up-conversion

Since the ^1L_a transition was excited in the fluorescence UC measurements for both 1N and 2N, it is therefore expected that rapid internal conversion will lead to the ^1L_b state as this is the one with the lowest energy in the Franck Condon state. Following this, LC to the ^1L_a state should occur for 1N in DMSO and H_2O, likely resulting in changes in solvation due to the accompanying increase in the magnitude of the transition dipole moment (TDM). In addition, for 1N in water, ESPT ultimately occurs with a 35ps timescale resulting in the formation of the conjugate photobase.

The occurrence of a very fast internal conversion in 2N is evidenced by the lack of dynamics resolvable with the 250fs time resolution of the experiment as well as the negligible solvation of the non-polar ^1L_b state. This is in line with the sub 50fs internal conversion measured for gas-phase naphthalene [82]. On the other hand, in 1N significant spectral shifts are occurring in 2.4ps in DMSO and 0.3 and 2.25ps in H_2O. Furthermore, a delayed rise of the fluorescence signal is evident which was not present in 2N. Specifically, there is an intensity increase within the first picosecond of 10% in DMSO (due to the large and rapid Stokes shift it is much harder to characterize this delayed rise in H_2O). This is interpreted as evidence of an increase in the ^1L_a character of the emitting state. Indeed, the fluorescence UC is proportional to the radiative emission rate which is itself proportional to the TDM.

7.2.1.2 Fluorescence anisotropy

Given the near perpendicularity of the ^1L_a and ^1L_b TDMs in 1N, the occurrence of an ultra-fast LC followed by solvation can be confirmed with time-resolved fluorescence anisotropy, where the angle $\varphi(t)$ between the TDM of the initially excited-state and that of the emitting state is measured. For 2N in DMSO, a time-independent anisotropy of r=0.05 was found which corresponds to a 50±2° angle between the TDMs of ^1L_a and ^1L_b (see equation 4.11). This is in good agreement with the 140° calculated angle using time-dependent density functional theory calculations presented in chapter 2 as φ and π− φ correspond to the same r value. Thus, the measured anisotropy corresponds to an emitting state which is essentially of ^1L_b character: ^1L_a excitation at 266 nm is followed by ultrafast IC down to the lower-lying ^1L_b

state, which remains the emitting state at all successive times with no further level dynamics. The initial internal conversion dynamics which result in a decrease of *r* from the initial expected value of 0.4 [159] to 0.05 occur too quickly to be resolved with the current experiment, further confirming the sub-50fs timescale of the event.

The situation is markedly different for the anisotropy of 1N in DMSO where the initial anisotropy of -0.05 is seen to rise within the first few hundreds of femtoseconds to a value approaching 0.01 (figure 7.7). The initial anisotropy of -0.05 corresponding to an angle of 60° between the TDMs, is again indicative of an ultrafast internal conversion which populates the ^1L_b state after the initial ^1L_a excitation. However, the calculated angle between the TDM of the ^1L_a and ^1L_b transitions is of 88° which should lead to an initial anisotropy of essentially -0.2 after internal conversion.

In contrast to the LC hypothesis which is commonly postulated in the literature, the anisotropy does not rise above 0.1, where pure ^1L_a emission would lead instead to an anisotropy of 0.4. By fitting the anisotropy data taking into account our instrument response function as well as the effect of rotational diffusion occurring with a 28 ps timescale it is possible to see that the observed rise in anisotropy is characterized by a (60±10)fs timescale. Unlike the fluorescence UC dynamics, no 2.5ps component is present which is further evidence that the picosecond dynamics are purely due to solvation of the more polar state.

7.2.1.3 Transient IR

Further confirmation that the level dynamics are complete on sub-200fs timescales (in DMSO), with the later picosecond dynamics arising from solvent shell rearrangements is provided by transient infrared (TrIR) measurements. As the fingerprint region of the IR spectra is constituted of a multitude of highly characteristic vibrations, a change in the nature of the electronic state gives rise to significant changes in the mode pattern, such as that regularly observed between the ground-state and the first excited-state [131, 256]. It can be seen in figure 7.9a that, unlike 2N where no dynamics are evident (figure 7.8d), 1N shows dynamics with the same characteristic timescale of 2.4ps as observed in the fluorescence UC measurement. However, these dynamics do not reflect a change in the mode pattern. Instead, the baseline absorption rises and the peak at around 1375cm^{-1}, which dominates the excited-state spectra, is found to slightly blue-shift.

It is expected that the charge transfer from the hydroxyl group to the aromatic ring is enhanced in the ^1L_a state. This should then have large effects on the OH stretch vibration whose frequency and width are incredibly sensitive to HB interactions and general solvent effects [152]. Unfortunately, given the inherent broadness of such a signal, reliable measurements were impossible. However, the broad peak around 1375cm^{-1} shows a blue-shift on timescales found for the solvation of the ^1L_a state. In order to understand this behavior, it was first necessary to determine if this band could be attributed to a particular vibration as fingerprint modes are often highly non-local.

The C-O stretch vibration of alcohols is generally located at frequencies of 1000-1275cm^{-1} with primary alcohols at the redmost frequencies and aromatic alcohols the bluemost frequencies. This can be easily rationalized by the inductive effect of secondary and tertiary alchols as well as the resonance structures of aromatic alcohols where the C-O bond has a bond order higher than one due to conjugation with the ring. Indeed, x-ray diffraction studies of phenol show a C-O bond distance of 1.364Å which is significantly shorter than 1.43 found in regular C-O bonds [37]. However, there is a veritable dearth of information in the literature regarding the effect of hydrogen bonding on the C-O stretch vibration of aromatic alcohols which is surprising as changes in electronic density lead to changes of the resonance structures and thus the bond order of the C-O bond. Of course, unlike O-H stretch or C=O stretch vibrations, the C-O stretch is rarely a purely local vibration given its low frequency which entails significant mixing with other vibrational modes. Despite this fact, it is common to be able to identify a band in the aforementioned frequency range with mainly C-O stretch character. For phenol in non-polar solvents like C_2Cl_4 it is situated at 1261cm^{-1} and calculations show a potential energy distribution with 52% ν(C-O) (the other main contribution is 20% from ν(C-C)) [37]. When a hydrogen bond with an accepting base is formed, significant electronic redistribution is expected which should affect the C-O bond in a revealing manner.

In 1N, DFT calculations find that it is the band at 1276cm^{-1} which has a ν(C-O) stretch character. The behavior of this band in C_2Cl_4 with progressive addition of DMSO-d_6 is shown in figure 7.14a. The O-H stretch region is also shown in order to properly characterize the formation of HB complexes (figure 7.14b). As expected, addition of DMSO leads to the progressive disappearance of the free OH band at 3606cm^{-1} coupled to the appearance of the hydrogen-bonded OH stretch at 3210cm^{-1}. The much higher polarity of DMSO compared to C_2Cl_4 also leads to a slight red-shift of the hydrogen-bonded band with increasing DMSO

concentration. Looking at the band calculated to have predominantly C-O stretch character, formation of hydrogen bonded complexes results in the appearance of a broadened band at a higher frequency. An isobestic point between the C-O stretch band of uncomplexed 1N at 1276cm^{-1} and the C-O stretch of the hydrogen-bonded complex at 1288cm^{-1} is seen at 1277cm^{-1}. The isobestic point is slightly smeared out due to the effect of the increasing solvent polarity. The frequency upshift of the C-O stretch in the hydrogen-bonded complexes can easily be explained with the larger electronic redistribution of the electron lone pair of the oxygen into the aromatic ring. Consequently, the C-O bond will adopt a higher bond order, displacing the vibration to a higher frequency.

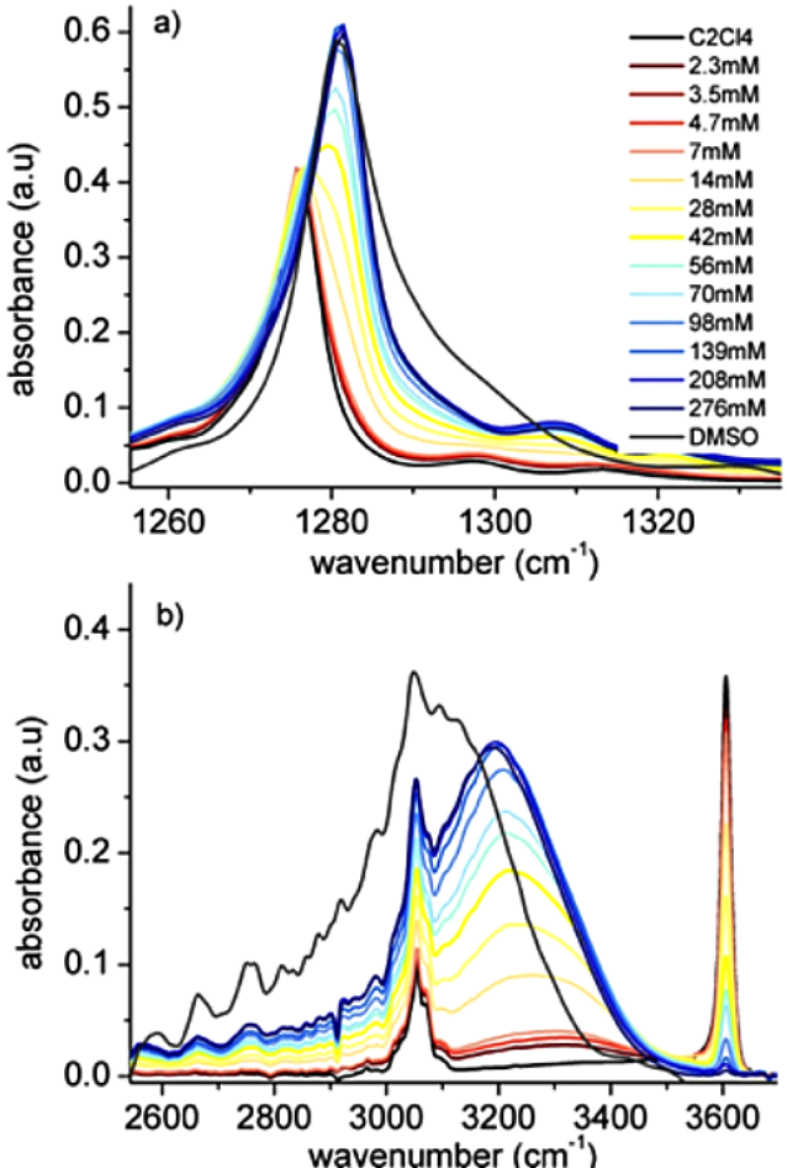

Figure 7.13: 88mM solution of 1N in C_2Cl_4 with progressive addition of DMSO-d_6 for a) the C-O stretch region and b) the OH stretch region.

Remarkably, a linear correlation was found between the C-O stretch vibration and the O-H stretch frequency for a number of 1N acceptor complexes (figure 7.14c). This indicates that, although the C-O stretch vibration only constitutes about 50% of the potential energy distribution of the band at 1276cm^{-1}, the band still behaves like a local C-O stretch vibration. This is likely due to the fact that the other normal modes are much less sensitive to specific solvent effects.

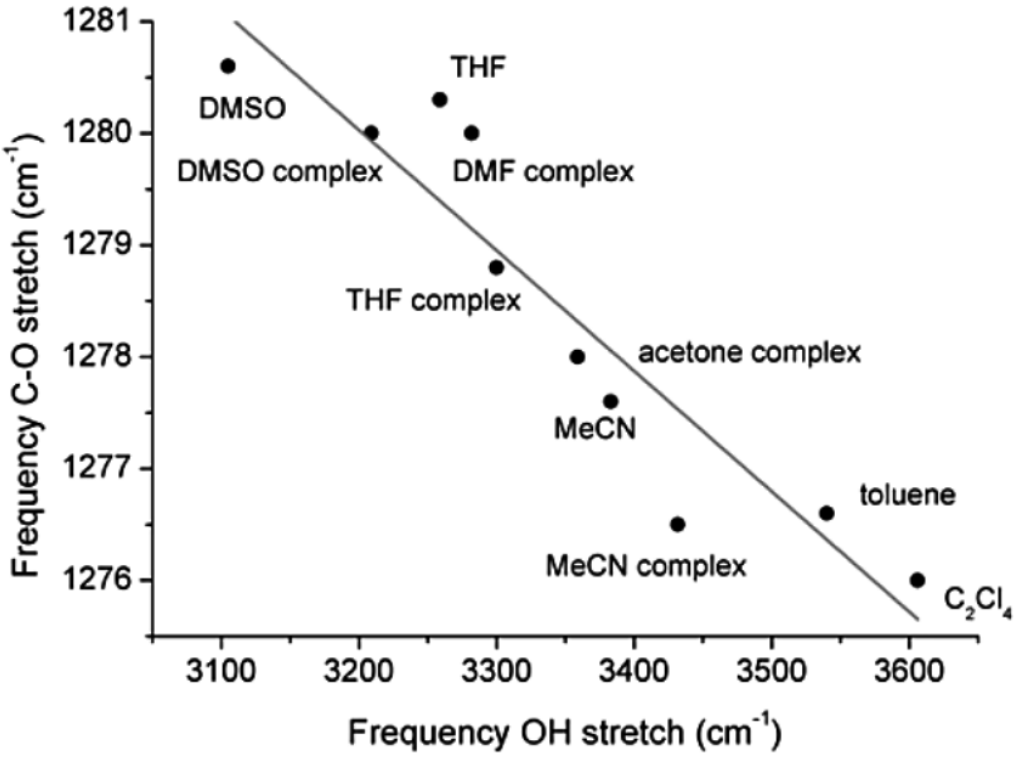

Figure 7.14: Correlation between the OH stretch and C-O stretch frequencies for 1N in a number of solvents.

For the excited-state, comparison of the transient spectra in different solvents reveals a clear blue-shift and broadening of the peak at 1276cm^{-1} which comes to largely dominate the spectral shape in DMSO (figure 7.16a). By analogy with the ground-state, this band is attributed to the excited-state C-O stretch vibration. The increasing blue-shift compared to the ground-state peak is concomitant with the photoacidity ansatz whereby the excited-state is characterized by further charge transfer from the oxygen into the ring. The transient blue-shift observed in DMSO is then attributed to HB rearrangements occurring upon solvation of the ^1L_a state.

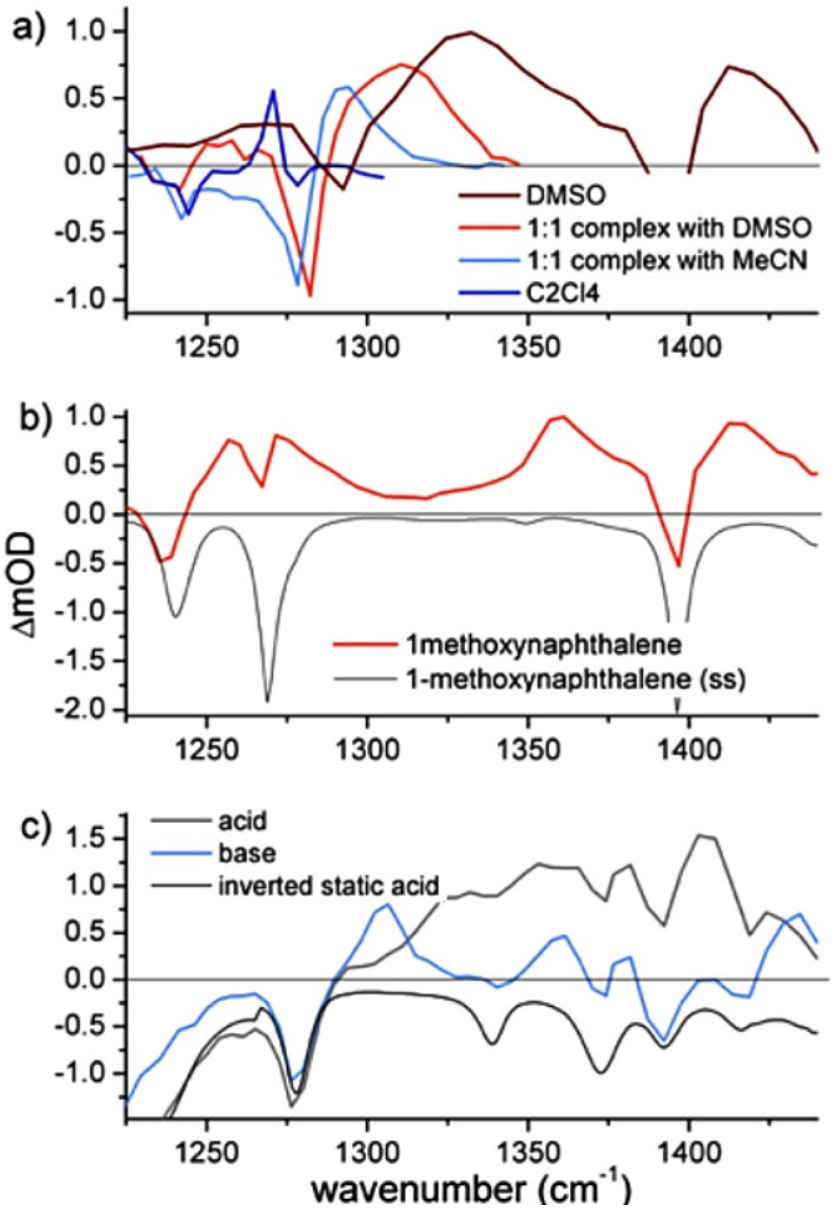

Figure 7.15: a) Transient IR spectra of 1N in various solvents where the 1:1 complexes were measured in C_2Cl_4 b) Transient IR spectra of 1-methoxynaphthalene in DMSO-d_6 at 10ps with the inverted steady-state spectra shown for reference. c) Transient IR spectra of 1N-3,6-disulfonate in D_2O at 1ps (acid) and 75ps (base) with the inverted steady-state spectra shown for reference.

Further evidence that the broad excited-state peak around 1315cm^{-1} is due to the C-O stretch vibration is obtained by comparison with the 1-methoxynaphthalene derivative where no HB is donated to the solvent given the replacement of the alcohol function by a methoxy group. As can be seen in figure 7.16b, the spectra is characterized by a multitude of sharp peaks with no broad signal. On the other hand, looking at the spectra of the 1N derivative, 1-naphthol-3,6-disulfonate in water, the spectrum is similarly dominated by a broad peak in the same spectral region as for 1N in DMSO (1N in water also shows such a broad spectral signature,

but due to the low solubility, the obtained spectra are quite noisy). Furthermore, after the ESPT event which occurs in 5.9ps, the broad peak is absent in the spectra of the conjugate base.

While OH stretch vibrations are routinely found to exhibit full width half maxima of several hundreds of wavenumbers due to the large polarizability of the bond upon formation of a HB [257, 258], this has not been found to be the case for C-O vibrations. As such, this phenomena requires further investigation. One aspect that bears elucidation is whether this broad C-O stretch is a phenomena characteristic to all photoacids? For 2N, as there is no band which behaves with C-O stretch character, this effect would not be apparent. It would thus be instructive to see if hydrogen-bonded complexes of phenol, where there is also a characteristic C-O band, behaves in the same way as 1N and its derivatives.

7.2.1.4 Level crossing versus level mixing

Level crossing in 1N, whereby the ^1L_a state is further stabilized in the excited-state by polar solvents effectively bringing its energy lower than that of the ^1L_b state, is postulated in previous studies in order to account for the static spectra. However, the time resolved measurements presented here point instead to significant level mixing (LM). For 1N in DMSO, the rise in anisotropy corresponds to a rotation of the TDM back 15° towards the direction of the initially excited ^1L_a transition and occurs in 60fs. In a LC scenario, the subsequent solvation, where the energy of the ^1L_a state is lowered by 900cm^{-1} ($>>kT$), would lead to a further population transfer from the ^1L_b state and a concomitant rise in anisotropy on this timescale. As no such rise in anisotropy was measured, LC cannot serve to explain the current experimental results. On the other hand, in a LM scenario, non-diagonal coupling due to the perturbative effect of the solvent leads to two new states: A' and B' which are linear combinations of the initial ^1L_a and ^1L_b states. The lower energy combination, A', then undergoes solvation on a 2.5ps timescale.

It is generally held that it is the polarity of the solvent which is responsible for the level dynamics in 1N. This is supported by the fact that no level dynamics occur in hydrogen bonded complexes in non-polar solvents. Also, LM is evident in acetonitrile (ε=37.5) but not tetrahydrofuran (ε=7.58), even though tetrahydrofuran is a much better HB acceptor than acetonitrile [111]. However, the 60fs timescale for LM measured in the transient anisotropy experiment is faster than any previously reported solvation dynamics in DMSO, ie 200fs

[259]. It thus runs counter to the expected polarity driven mechanism. On the other hand, HB dynamics are reported to occur on sub 100fs timescales [13, 227]. The apparent discrepancy between the spectral behavior observed in the static spectra and the ultrafast timescale for LM can be explained if we consider that a high solvent polarity is needed in order to bring the energy of the ^1L_a state sufficiently near to that of the ^1L_b, where HB dynamics can then trigger LM. Indeed, it was seen in chapter 2 that since the solvent polarity causes a greater red-shift of the ^1L_a state compared to the ^1L_b state, this effectively serves to diminish their energy separation.

7.2.2 Quenching mechanism

Several of the transient fluorescence spectra showed significant quenching occurring on fast timescales similar to what was observed for HPTS in H_2O [114]. In 1N, steady-state measurements performed by systematically lowering the pH saw an initial increase in the quantum yield (QY) of acid emission followed by a decrease at low pHs [260, 261, 262]. The initial increase is readily rationalized with the additional protons shifting the acid-base reaction towards the acid side, thereby increasing the acid fluorescence at the expense of the base fluorescence. The following decrease in very acidic media was then explained by diabatic proton quenching. As the fluorescence UC measurements were performed at neutral pH where very few protons are available, this quenching mechanism is not of particular concern. However, it was also found that protons quench the fluorescence through addition at positions 5 and 8 of the naphthalene ring [253]. The proposed mechanism and resultant structure for quenching at position 5 is shown in figure 7.17. This quenching mechanism was established by using acidic deuteurated solutions which produced the tautomers 5D-1-naphthalenone and 8D-1-naphthalenone as monitored by NMR spectroscopy. Even though no emission from either enones has been observed, quenching in this case could still be adiabatic as enone emission is rarely observed in room temperature solutions. It was advanced by Pines and Flemming that this proton addition could explain the low QYs observed for the anion. Indeed, while the equilibrated concentration in protons remains very low, as the ESPT reaction generates a contact ion-pair this means that there is a proton present in close proximity to a quenching site [255]. Measuring the TCSPC signal of 1-naphtholate as generated from ESPT in the neutral solution and that generated directly at basic pH, they found that the former had a much lower QY: the ratio of QYs between the indirect and direct path was found to be 0.64. Furthermore, addition of a proton scavenger like acetate led to an increase of the indirect pathway's quantum yield. Competing with the quenching mechanism

is geminate recombination of the proton with 1Nate as well as diffusion of the ion pair away from each other. The long time behavior of the TCSPC signal also revealed the diffusion controlled geminate recombination of the proton and 1Nate, but these occur on much longer timescales than what was probed in the fluorescence UC measurements.

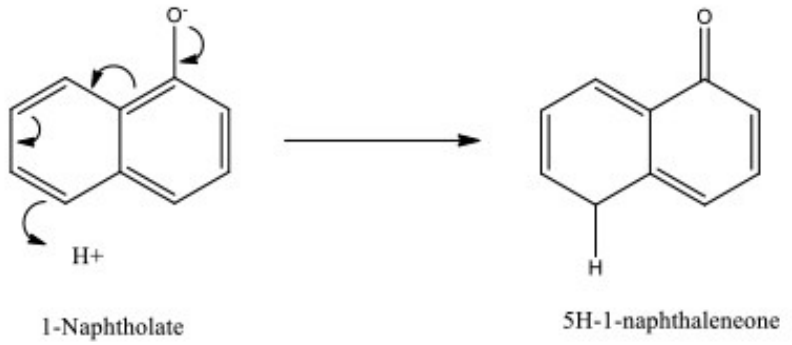

Figure 7.16: Quenching mechanism of 1-naphtholate by protons.

However, when looking at the 1N-5,8-dicyano derivative, Tolbert found that the anion fluorescence was still significantly quenched even though there were two cyano groups at the ring positions where a proton is thought to be added [1]. They proposed that the proton should then add to the cyano group. Yet, further measurements using bulky alkyl substituents to protect the 5 and 8 ring positions revealed that quenching was still occurring (Pines, unpublished data). Furthermore, proton addition cannot account for the quenching which was observed for 1N in DMSO where no ESPT occurs, nor the dramatic quenching in the directly excited anions in water. It thus appears evident that another mechanism must be invoked to fully explain the observed quenching.

Phenols, naphthols and to a greater extent their respective anions, have been shown to yield solvated electrons following single photon excitation [51, 52, 53, 54, 55, 56, 57, 58, 59, 60, 61]. Earlier studies employing triplet quenchers showed that the electron is generated from the singlet state [51]. What is more, a recent femtosecond transient absorption study of the photoionization of phenolate has shown that the electrons are generated via two channels: the first being the locally excited state and the second the relaxed S_1 state, where this last slower ejection channel accounts for 64% of the electrons ([62]). Given the delayed nature of the ionization process in the anion, it is quite likely that electron ejection could be operative upon indirect generation of the anion through ESPT.

A further argument to support the hypothesis of ionization in the anion after ESPT is the fact that for 2N the total quantum yield (acid+base) is constant throughout the pH range [3]. As ionization has conclusively been shown to occur in the directly excited base at high pH [53, 56], for the total quantum yield to remain constant, it should also occur to the same extent at lower pH in the indirectly excited anion.

The ionization quenching channel will be favored in the systems where the electronic density on the aromatic ring is the highest. This explains why the fluorescence intensity was found to decrease by 15% for 1N in DMSO after the LM event which enhanced the charge transfer from the oxygen lone pair into the ring. The generation of electrons also accounts for the baseline rise that was observed in the TrIR spectra. Indeed, electrons have been shown to absorb throughout the IR [263, 264]. This then accounts for the flat and featureless nature of the observed signal and provides further justification for attributing the observed decrease in the fluorescence emission to ionization. Similarly, the emissive QY of several indole derivatives in non-polar solvents were found to be higher than in polar solvents where LC to the ^1L_a state was evidenced. This discrepancy was also attributed to electron transfer based on the demonstrated ionization of indole [265].

In line with the amount of fluorescence quenching being proportional to the amount of charge transfer of the emitting state, no quenching was observed in 2N, while 1Nate fluorescence in water was quenched by 50%. Quenching of the indirectly generated 1Nate following ESPT from 1N was also evident. This substantial quenching is understood by the fact that in 1Nate the ^1L_a state is already the lowest energy state [31] and by the fact that 1Nate has a full negative charge. Indeed, quenching also occurs in 2Nate even though emission is from the less polar ^1L_b state. Given the importance of the ionization channel in the naphtholates to generate the corresponding radicals, this mechanism should also be evidenced in the TrIR spectra. It was seen that the bands corresponding to the S_1 state substantially decrease on fast timescales with the concomitant rise of new IR peaks. As expected from an ionization process, no isotope effect on the rate constant was observed.

7.2.3 Comparison with HPTS

As discussed in the introduction, substantial dynamics were observed in both time resolved fluorescence and absorption measurements for HPTS but not in the corresponding TrIR measurement. This discrepancy can now be understood by the occurrence of sub 100fs level dynamics which were not resolved in the TrIR measurements. The dynamics seen in the

electronic spectra are then due to solvation to which the TrIR measurement is much less sensitive. As was found for 2N, no vibrational band in the IR spectra of HPTS is found to exhibit ν(C-O) character. The effects of possible HB rearrangements which were seen for 1N are thus not identifiable.

7.3 Summary

The two lowest energy levels of aromatic compounds (^1L_b and ^1L_a) are energetically close in bicyclic molecules. Due to the small energy separation in these systems, the photophysical properties are highly influenced by the nature of the solvent which can modulate the relative energy of the two levels. Thus, for several indole derivatives like tryptophan, ground state solvation is sufficient to cause a static level inversion between the two levels compared to their respective gas-phase energies [265, 266, 267]. For naphthols, solvent assisted level crossing was postulated to occur in 1N but not in 2N. It is now possible to confirm the lack of level dynamics in 2N, however, the situation in 1N is different from what has commonly been postulated. Indeed, using time resolved anisotropy measurements, it was established that the level dynamics of 1N in DMSO occur on timescales (60fs) faster than those of solvation. Thus, instead of a polarity driven mechanism due to the preferential stabilization of the more charge transferred ^1L_a state, hydrogen bonding is likely responsible for the observed dynamics. The role of solvent polarity is then necessary in order to bring the two energy levels sufficiently close in energy for the hydrogen bond coordinate to couple the two states. The fast level dynamics were further confirmed by the presence of a delayed rise in the fluorescence up conversion spectrum as well as the absence of mode pattern changes in the transient fingerprint IR occurring on longer timescales. Furthermore, due to the absence of anisotropy changes on solvation timescales, pure level crossing population dynamics can be discounted and the presence of level mixing inferred.

Important fluorescence quenching was observed in several systems, with the magnitude of the quenching correlated to the charge transfer character of the emitting state. This quenching is attributed to electron ejection from the excited state and corresponding decrease in the S_1 fingerprint bands was observed with the appearance of new marker modes.

8. Conclusion and outlook

1-naphthol (1N) and 2-naphthol (2N) were investigated as the two prototype photoacids in order to characterize the influence of solute-solvent interactions on their photophysical properties. First, the OH stretch vibration in both the ground and first excited state was measured in order to understand the intrinsic electronic charge redistribution occurring upon excitation and the nature and magnitude of solute-solvent couplings. A theoretical model based on the Pullin-van der Zwan-Hynes perturbative approach was found to give a good correspondence with the experimental results. It was thus possible to quantify the observed frequency shifts in terms of molecular parameters such as the molecular dipole moments and its first and second derivatives, or the degree of anharmonicity of the OH stretching vibration. The vibrational solvatochromic effects are seen to be largely dominated by the instantaneous solvent dielectric response with little time-dependent nuclear rearrangements. In addition, very little charge redistribution was evidenced which is in contrast to the traditional view of photoacidity whereby the increase in acidity is due to charge redistribution from the oxygen into the ring upon excitation.

As the excited-state proton transfer reactions proceed along the hydrogen bond formed between the photoacid and the solvent or an accepting base, the influence of a hydrogen bond cannot be discounted. For this purpose, 2-naphthol complexed with acetonitrile in non-polar to weakly polar solvents was measured. In this case, the agreement between experiment and theory was poor. In the experiment, the first excited state was characterized by a solvatochromic response that was almost twice as large as in the ground state, while the calculations find no significant differences between the two states. This may be an indication that modeling the solvent-induced OH-stretching frequency shifts for stronger hydrogen-bonded complexes where anharmonicities of the OH-stretching potential are more pronounced necessitates a sophistication of the description of these complexes extending to states involving conjugate photobase-conjugate acid configurations.

Since the theory was unable to correctly reproduce the experimental trends for the OH frequency shifts of hydrogen bonded complexes, it was decided to utilize the excited state charge transfer reaction of 1-naphthol and 2-naphthol to halogenated solvents as a probe for the electronic density of the aromatic ring. Using the electron acceptor as the solvent enabled us to avoid complicated diffusion dynamics and isolate the charge transfer reaction in order to determine the importance of specific hydrogen bond interactions. After establishing that the

charge originates from the π orbitals and not the lone pair of the oxygen, it was found that the transfer rate in a hydrogen bonded complex with acetonitrile is ten times faster than in the free molecule. This constitutes strong experimental evidence that, while the photoacid state may be characterized by little charge transfer in the gas phase or in non-polar solvents, the situation is markedly different when specific hydrogen bond interactions are present. Since such hydrogen bond interactions are central to the excited state proton transfer event, the role of the photoacid cannot be so easily discounted. Indeed, these results suggest that the molecular mechanism behind photoacidity is unlikely to be provided solely by changes occurring in the conjugate photobase as has been claimed in recent years. It appears that further refinements to computational methods are necessary in order to properly characterize the relative role of the photoacid and its conjugate photobase.

The thousand times higher excited state acidity of 1-naphthol compared to 2-naphthol has typically been ascribed to solvent driven dynamical level crossing to the more charge transferred ^1L_a state thought to occur in 1N but not in 2N. By combining time resolved anisotropy, fluorescence up conversion, and transient infrared measurements of 1-naphthol and 2-naphthol in dimethylsulfoxide, it was possible to determine that the level dynamics in 1N are not due to the solvent polarity but are instead likely due to changes in hydrogen bond interactions. In addition, the very fast (60fs) anisotropy dynamics, with no further dynamics occurring on the picosecond timescales characteristic of solvation, makes it possible to discount population level crossing as the operative mechanism. Indeed, in this scenario solvation should lead to further population changes. The presence of level mixing is thus inferred. The substantial quenching observed was attributed to the ionization of the naphthols/naphtholates and its importance was found to correlate with the amount of charge transfer of the emitting state.

In order to understand the molecular mechanism behind photoacidity we are ultimately interested in finding out about the charge flow during the excited-state proton transfer from photoacids. X-ray absorption spectroscopy therefore constitutes an attractive complement to IR methods with the current progress in picosecond and even femtoslicing methods in many synchrotrons.

Acknowledgements

First and foremost I would like to thank Bob, my wonderful laser, without whom this thesis would not have been possible. I am indebted to Professor Thomas Elsässer who gave me the opportunity to conduct my PhD thesis at the Max Born Institut, and who provided me with helpful guidance. I am grateful to Dr. Erik Nibbering who introduced me to the mysterious world of the naphthols and who was always there to listen about new strange occurrences. My thanks to Dr. Katrin Adamczyk who showed me the ropes when I arrived at the Institute and with whom many great hours were spent in the lab. Often overnight.

Many people at the Max Born Institute helped make my stay enjoyable through insightful and helpful discussions. For their company I would like to thank Dr. Lukasz Szyc, Dr. Ming Yang, Rene Costard, Dr. Henk Fidder, Christian Greve, Dr. Benjamin Koeppe, Dr. Ismael Hesler, Dr. Cynthia Aku-Leh, Benjamin Freyer, Dr. Uwe Griebner, Dr. Rüdiger Grunwald, Dr. Jens Dreyer and Dr. Peter Tolstoy. I also would like to thank the wonderful Regina Lendt who measured countless fluorescence spectra of the “Liebe Naphtholen”, the always smiling Brigitte Steinert, Regina Goleschny with all her stories, the ever helpful Peter Scholze, Helmut Walz with the magical hands that would can repare electronic appliances without needing to do anything, Marina Friedrich for her computer help and the two secretaries: Alexandra Wettstein and Margarett Lehmann.

I would like to thank Professor Majed Chergui for the wonderful opportunity to be able to go back and perform some measurements at the EPFL, as well as Dr. Fabrizio Messina and Dr. Olivier Braem who made those measurements possible (and enjoyable!).

For all the skype chats Wednesdays at 16h30, I would like to thank our collaborators at Yale University Professor Victor Batista and Dr. Dequan Xiao. I would also like to thank our collaborators Professor Ehud Pines and Dr. Dina Pines at the Ben Gurion University. For their help and company during the long measuring periods at BESSY, I would like to thank Dr. Philippe Wernet, Simon Schreck, Christian Weniger and Dr. Gianina Gavrila.

Lastly, my sincere thanks to all my friends and family who stood by my side during these years.

Bibliography

1. Tolbert, L.M. and J.E. Haubrich, *Enhanced Photoacidities of Cyanonaphthols.* Journal of the American Chemical Society, 1990. **112**(22): p. 8163-8165.

2. Weber, K., *The close relationship of fluorescence obliteration to the inhibition of photochemical reactions.* Zeitschrift Fur Physikalische Chemie-Abteilung B-Chemie Der Elementarprozesse Aufbau Der Materie, 1931. **15**(1): p. 18-44.

3. Forster, T., **Die Ph-Abhangigkeit Der Fluoreszenz Von Naphthalinderivaten.* Zeitschrift Fur Elektrochemie, 1950. **54**(7): p. 531-535.

4. Forster, T., *Fluoreszenzspektrum Und Wasserstoffionenkonzentration.* Naturwissenschaften, 1949. **36**(6): p. 186-187.

5. Weller, A., *Fast Reactions of Excited Molecules.* Progress in Reaction Kinetics and Mechanism, 1961. **1**: p. 187-&.

6. Weller, A., *Quantitative Untersuchungen Der Fluoreszenzumwandlung Bei Naphtholen.* Zeitschrift Fur Elektrochemie, 1952. **56**(7): p. 662-668.

7. Pines, E., et al., *Real-Time Observation of Carbonic Acid Formation in Aqueous Solution.* Science, 2009. **326**(5960): p. 1690-1694.

8. Bakker, H.J., et al., *Distance-Dependent Proton Transfer along Water Wires Connecting Acid-Base Pairs.* Journal of Physical Chemistry A, 2009. **113**(24): p. 6599-6606.

9. Pines, E., et al., *Aqueous bimolecular proton transfer in acid-base neutralization.* Chemical Physics, 2007. **341**(1-3): p. 240-257.

10. Pines, E., et al., *Direct measurement of intrinsic proton transfer rates in diffusion-controlled reactions.* Chemical Physics Letters, 1997. **281**(4-6): p. 413-420.

11. Mohammed, O.F., et al., *Base-induced solvent switches in acid-base reactions.* Angewandte Chemie-International Edition, 2007. **46**(9): p. 1458-1461.

12. Rini, M., et al., *Real-time observation of bimodal proton transfer in acid-base pairs in water.* Science, 2003. **301**(5631): p. 349-352.

13. Nibbering, E.T.J., H. Fidder, and E. Pines, *Ultrafast chemistry: Using time-resolved vibrational spectroscopy for interrogation of structural dynamics.* Annual Review of Physical Chemistry, 2005. **56**: p. 337-367.

14. Agmon, N., E. Pines, and D. Huppert, *Geminate Recombination in Proton-Transfer Reactions .2. Comparison of Diffusional and Kinetic Schemes.* Journal of Chemical Physics, 1988. **88**(9): p. 5631-5638.

15. Pines, E., D. Huppert, and N. Agmon, *Geminate Recombination in Excited-State Proton-Transfer Reactions - Numerical-Solution of the Debye-Smoluchowski Equation*

with Backreaction and Comparison with Experimental Results. Journal of Chemical Physics, 1988. **88**(9): p. 5620-5630.

16. Pines, E. and D. Huppert, *Geminate Recombination Proton-Transfer Reactions.* Chemical Physics Letters, 1986. **126**(1): p. 88-91.

17. Pines, E. and D. Huppert, *Observation of Geminate Recombination in Excited-State Proton-Transfer.* Journal of Chemical Physics, 1986. **84**(6): p. 3576-3577.

18. Gutman, M., D. Huppert, and E. Pines, *The Ph Jump - a Rapid Modulation of Ph of Aqueous-Solutions by a Laser-Pulse.* Journal of the American Chemical Society, 1981. **103**(13): p. 3709-3713.

19. Gutman, M. and D. Huppert, *Rapid Ph and Delta-Mu-H+ Jump by Short Laser-Pulse.* Journal of Biochemical and Biophysical Methods, 1979. **1**(1): p. 9-19.

20. Nunes, R.M.D., M. Pineiro, and L.G. Arnaut, *Photoacid for Extremely Long-Lived and Reversible pH-Jumps.* Journal of the American Chemical Society, 2009. **131**(26): p. 9456-9462.

21. Gutman, M., E. Nachliel, and D. Huppert, *Direct Measurement of Proton-Transfer as a Probing Reaction for the Micro-Environment of the Apomyoglobin Heme-Binding Site.* European Journal of Biochemistry, 1982. **125**(1): p. 175-181.

22. Gutman, M., D. Huppert, and E. Nachliel, *Kinetic-Studies of Proton-Transfer in the Micro-Environment of a Binding-Site.* European Journal of Biochemistry, 1982. **121**(3): p. 637-642.

23. Gutman, M., *The Ph Jump - Probing of Macromolecules and Solutions by a Laser-Induced, Ultrashort Proton Pulse - Theory and Applications in Biochemistry.* Methods of Biochemical Analysis, 1984. **30**: p. 1-103.

24. Loken, M.R., et al., *Excited-State Proton-Transfer as a Biological Probe - Determination of Rate Constants by Means of Nanosecond Fluorometry.* Biochemistry, 1972. **11**(25): p. 4779-&.

25. Barth, A. and J.E.T. Corrie, *Characterization of a new caged proton capable of inducing large pH jumps.* Biophysical Journal, 2002. **83**(5): p. 2864-2871.

26. Mansueto, E.S. and C.A. Wight, *Excited-state proton-transfer polymerization of amorphous formaldehyde.* Journal of the American Chemical Society, 1989. **111**(5): p. 1900-1901.

27. Conrad, P.G., et al., *p-hydroxyphenacyl phototriggers: The reactive excited state of phosphate photorelease.* Journal of the American Chemical Society, 2000. **122**(38): p. 9346-9347.

28. Agmon, N., *Elementary steps in excited-state proton transfer.* Journal of Physical Chemistry A, 2005. **109**(1): p. 13-35.

29. Granucci, G., et al., *A theoretical investigation of excited-state acidity of phenol and cyanophenols.* Journal of the American Chemical Society, 2000. **122**(49): p. 12243-12253.

30. Tramer, A. and M. Zaborowska, *Hydrogen Bond and Level Reversal in Excited 1-Naphthol.* Acta Physica Polonica, 1968. **5**.

31. Schulman, S.G., *Correspondence of Fluorescing States of Naphthols and Naphtholate Anions and Its Effect on Calculation of Pka] from Spectral Shifts.* Spectroscopy Letters, 1973. **6**(3): p. 197-202.

32. Suzuki, S., K. Sato, and T. Fujii, *Temperature Dependence of Fluorescence and Polarization Spectra of 1-Naphthol.* Bulletin of the Chemical Society of Japan, 1972. **45**(6): p. 1937-&.

33. Suzuki, S., et al., *Fluorescent Level Inversion of Dual Fluorescences and Motional Relaxation of Excited-State Molecules in Solutions.* Journal of Physical Chemistry, 1977. **81**(16): p. 1592-1598.

34. Suzuki, S. and H. Baba, *Polarization Study of Fluorescent State of Hydrogen Bonded Alpha-Naphthol.* Bulletin of the Chemical Society of Japan, 1967. **40**(9): p. 2199-&.

35. Magnes, B.Z., N.V. Strashnikova, and E. Pines, *Evidence for L-1(a), L-1(b) dual state emission in 1-naphthol and 1-methoxynaphthalene fluorescence in liquid solutions.* Israel Journal of Chemistry, 1999. **39**(3-4): p. 361-373.

36. Milosavljevic, B.H. and J.K. Thomas, *The photophysics of 1-hydroxypyrene, the acidity of its singlet excited state, and the nature of its photoionization process in polar media.* Photochemical & Photobiological Sciences, 2002. **1**(2): p. 100-104.

37. Rappoport, Z., *The chemistry of phenols*. The chemistry of functional groups. 2003, Hoboken, NJ: Wiley.

38. Encinas, M.V., M.A. Rubio, and E.A. Lissi, *Quenching and Photobleaching of Excited Polycyclic Aromatic-Hydrocarbons by Carbon-Tetrachloride.* Journal of Photochemistry, 1982. **18**(2): p. 137-150.

39. Saperstein, D. and E. Levin, *Fluorescence Quenching of Ultraviolet Excited Aromatic Solutions by Chloroform and Several Related Chlorinated Methanes.* Journal of Chemical Physics, 1975. **62**(9): p. 3560-3567.

40. Loutfy, R.O. and A.C. Somersall, *Exciplex Mechanism for Quenching of Singlet Excited-States of Aliphatic-Ketones by Carbon-Tetrachloride.* Canadian Journal of Chemistry-Revue Canadienne De Chimie, 1976. **54**(5): p. 760-764.

41. Lewis, C. and W.R. Ware, *Wavelength Effects in Fluorescence Quenching - Anthracene-Carbon Tetrachloride System.* Chemical Physics Letters, 1972. **15**(2): p. 290-&.

42. Ware, W.R. and C. Lewis, *Wavelength Effects in Fluorescence Quenching - Aromatic-Hydrocarbons Quenched by Carbon Tetrachloride.* Journal of Chemical Physics, 1972. **57**(8): p. 3546-&.

43. Behera, P.K. and A.K. Mishra, *Static and Dynamic-Model for 1-Naphthol Fluorescence Quenching by Carbon-Tetrachloride in Dioxane Acetonitrile Mixtures.* Journal of Photochemistry and Photobiology a-Chemistry, 1993. **71**(2): p. 115-118.

44. Behera, P.K., T. Mukherjee, and A.K. Mishra, *Simultaneous Presence of Static and Dynamic Component in the Fluorescence Quenching for Substituted Naphthalene-Ccl4 System.* Journal of Luminescence, 1995. **65**(3): p. 131-136.

45. Behera, P.K., T. Mukherjee, and A.K. Mishra, *Quenching of Substituted Naphthalenes Fluorescence by Chloromethanes.* Journal of Luminescence, 1995. **65**(3): p. 137-142.

46. Sujatha, J. and A.K. Mishra, *Fluorescence quenching of naphthalene and its substitutions by chloroethanes and -ethylenes.* Journal of Luminescence, 1997. **75**(2): p. 135-141.

47. Brahmia, O. and C. Richard, *Photochemical transformation of 1-naphthol in aerated aqueous solution.* Photochemical & Photobiological Sciences, 2005. **4**(6): p. 454-458.

48. Lukeman, M., et al., *Photogeneration of 1,5-naphthoquinone methides via excited-state (formal) intramolecular proton transfer (ESIPT) and photodehydration of 1-naphthol derivatives in aqueous solution.* Canadian Journal of Chemistry-Revue Canadienne De Chimie, 2004. **82**(2): p. 240-253.

49. Seiler, P. and J. Wirz, *Structure and Photochemical Reactivity - Photohydrolysis of Trifluoromethyl Substituted Phenols and Naphthols.* Helvetica Chimica Acta, 1972. **55**(8): p. 2693-&.

50. Lukeman, M., M.D. Burns, and P. Wan, *Excited state intramolecular proton transfer in 1-hydroxypyrene.* Canadian Journal of Chemistry-Revue Canadienne De Chimie, 2011. **89**(3): p. 433-440.

51. Zechner, J., et al., *Excitation-Energy Dependence of Quantum Yields of Fluorescence and Electron Formation from Aqueous Phenol by Means of Heavy-Atom Effect.* Chemical Physics Letters, 1976. **37**(2): p. 297-300.

52. Legros, B., P. Vandereecken, and J.P. Soumillion, *Electron-Transfer Photoinduced from Naphtholate Anions - Anion Oxidation Potentials and Use of Marcus Free-Energy Relationships.* Journal of Physical Chemistry, 1991. **95**(12): p. 4752-4761.

53. Feitelso.J and G. Stein, *Wavelength and Temperature Dependent Effects on Hydrated Electron Formation and Fluorescence of Beta-Naphtholate.* Journal of Chemical Physics, 1972. **57**(12): p. 5378-&.

54. Mialocq, J.C., J. Sutton, and P. Goujon, *Picosecond Study of Electron Ejection in Aqueous Phenol and Phenolate Solutions.* Journal of Chemical Physics, 1980. **72**(12): p. 6338-6345.

55. Matsuzaki, A., T. Kobayashi, and S. Nagakura, *Picosecond Time-Resolved Spectroscopic Study of Solvated Electron Formation from Photoexcited Beta-Naphtholate Ion.* Journal of Physical Chemistry, 1978. **82**(10): p. 1201-1202.

56. Goldschmidt, C.R. and G. Stein, *Fast formation of the hydrated electron by dissociation of excited beta-naphtholate.* Chemical Physics Letters, 1970. **6**(4): p. 299-303.

57. Ottolenghi, M., *Electron Ejection and Fluorescence in Aqueous Beta-Naphthol Solutions.* Journal of the American Chemical Society, 1963. **85**(22): p. 3557-&.

58. Kohler, G., G. Kittel, and N. Getoff, *Decay Processes of Singlet Excited Phenol in Solution.* Journal of Photochemistry, 1982. **18**(1): p. 19-27.

59. Getoff, N., *A Review of the Relationship between Qe-Aq(-) and Qf of Excited Compounds in Aqueous-Solution.* Radiation Physics and Chemistry, 1989. **34**(4): p. 711-719.

60. Bussandri, A. and H. van Willigen, *FT-EPR study of the wavelength dependence of the photochemistry of phenols.* Journal of Physical Chemistry A, 2002. **106**(8): p. 1524-1532.

61. Grabner, G., et al., *Temperature-Dependence of Photoprocesses in Aqueous Phenol.* Journal of Physical Chemistry, 1980. **84**(23): p. 3000-3004.

62. Chen, X.Y., et al., *Broadband Spectral Probing Revealing Ultrafast Photochemical Branching after Ultraviolet Excitation of the Aqueous Phenolate Anion.* Journal of Physical Chemistry A, 2011. **115**(16): p. 3807-3819.

63. Bronsted, J.N., *Acid and Basic Catalysis.* Chemical Reviews, 1928. **5**(3): p. 231-338.

64. Ireland, J.F. and P.A.H. Wyatt, Adv. Phys. Org. Chem, 1976. **12**.

65. Barroso, M., L.G. Arnaut, and S.J. Formosinho, *Intersecting-state model calculations on fast and ultrafast excited-state proton transfers in naphthols and substituted naphthols.* Journal of Photochemistry and Photobiology A: Chemistry, 2002. **154**(1): p. 13-21.

66. Hynes, J.T., T.-H. Tran-Thi, and G. Granucci, *Intermolecular photochemical proton transfer in solution: new insights and perspectives.* Journal of Photochemistry and Photobiology A: Chemistry, 2002. **154**(1): p. 3-11.

67. Agmon, N., W. Rettig, and C. Groth, *Electronic determinants of photoacidity in cyanonaphthols.* Journal of the American Chemical Society, 2002. **124**(6): p. 1089-1096.

68. Pino, G.A., et al., *Intracluster hydrogen transfer followed by dissociation in the phenol-(NH3)(3) excited state: PhOH(S-1)-(NH3)(3)-> PhO center dot+(NH4)(NH3)(2).* Journal of Chemical Physics, 1999. **111**(24): p. 10747-10749.

69. Pino, G., et al., *A forgotten channel in the excited state dynamics of phenol-(ammonia)(n) clusters: hydrogen transfer.* Physical Chemistry Chemical Physics, 2000. **2**(4): p. 893-900.

70. Sobolewski, A.L. and W. Domcke, *Photoinduced electron and proton transfer in phenol and its clusters with water and ammonia.* Journal of Physical Chemistry A, 2001. **105**(40): p. 9275-9283.

71. David, O., C. Dedonder-Lardeux, and C. Jouvet, *Is there an excited state proton transfer in phenol (or 1-naphthol)-ammonia clusters? Hydrogen detachment and transfer to solvent: a key for non-radiative processes in clusters.* International Reviews in Physical Chemistry, 2002. **21**(3): p. 499-523.

72. Tolbert, L.M. and K.M. Solntsev, *Excited-state proton transfer: From constrained systems to "super" photoacids to superfast proton transfer.* Accounts of Chemical Research, 2002. **35**(1): p. 19-27.

73. Matsumoto, Y., T. Ebata, and N. Mikami, *Photofragment-detected IR spectroscopy (PFDIRS) for the OH stretching vibration of the hydrogen-bonded clusters in the S-1 state - Application to 2-naphthol-B (B = H2O and CH3OH) clusters.* Journal of Physical Chemistry A, 2001. **105**(24): p. 5727-5730.

74. Burgi, T., T. Droz, and S. Leutwyler, *Accurate Hydrogen-Bonding Energies between 1-Naphthol and Water, Methanol and Ammonia.* Chemical Physics Letters, 1995. **246**(3): p. 291-299.

75. Kouyama, K., et al., *IR laser manipulation of cis <-> trans isomerization of 2-naphthol and its hydrogen-bonded clusters.* Journal of Chemical Physics, 2006. **124**(5).

76. Matsumoto, Y., T. Ebata, and N. Mikami, *Structures and vibrations of 2-naphthol-(NH3)(n) (n=1-3) hydrogen-bonded clusters investigated by IR-UV double-resonance spectroscopy.* Journal of Molecular Structure, 2000. **552**: p. 257-271.

77. Klevens, H.B. and J.R. Platt, *Spectral Resemblances of Cata-Condensed Hydrocarbons.* Journal of Chemical Physics, 1949. **17**(5): p. 470-481.

78. Platt, J.R., *Classification of Spectra of Cata-Condensed Hydrocarbons.* Journal of Chemical Physics, 1949. **17**(5): p. 484-495.

79. George, G.A. and G.C. Morris, *Intensity of Absorption of Naphthalene from 30 000 Cm-1 to 53 000 Cm-1.* Journal of Molecular Spectroscopy, 1968. **26**(1): p. 67-&.

80. Hollas, J.M. and S.N. Thakur, *Rotational Band Contour Analysis in 3120 a System of Naphthalene.* Molecular Physics, 1971. **22**(2): p. 203-&.

81. Wild, U.P., H. Kanzig, and U.B. Ranalder, *Triplet-Triplet Absorption-Spectra of Aromatic-Hydrocarbons .1. Naphthalene.* Helvetica Chimica Acta, 1972. **55**(8): p. 2724-&.

82. Montero, R., et al., *A time resolved study of S-1/S-2 electronic coupling in naphthalene.* Chemical Physics Letters, 2009. **468**(4-6): p. 134-137.

83. Dilthey, W., F. Quint, and H. Stephen, *Die Wirkung der Auxochrome in m- und p-Stellung bei Dehydreniumfarbstoffen. [Dehydrenium, III. Mitteilung]. [Pyreniumsalze, XXXIII]*. Journal für Praktische Chemie, 1939. **152**(3-6): p. 99-113.

84. Hercules, D.M. and L.B. Rogers, *Spectrofluorometric Studies on Some Mono-Hydroxy and Di-Hydroxy Naphthalenes.* Spectrochimica Acta, 1958. **12**(4): p. 385-385.

85. Daglish, C., *The Ultraviolet Absorption Spectra of Some Hydroxynaphthalenes.* Journal of the American Chemical Society, 1950. **72**(11): p. 4859-4864.

86. Baba, H. and S. Suzuki, *Electronic Spectra of Substituted Aromatic Hydrocarbons .2. Naphthols and Naphthylamines.* Bulletin of the Chemical Society of Japan, 1961. **34**(1): p. 82-88.

87. Suzuki, S., T. Fujii, and H. Baba, *Interpretation of Electronic-Spectra by Configuration Analysis - Absorption-Spectra of Monosubstituted Naphthalenes.* Journal of Molecular Spectroscopy, 1973. **47**(2): p. 243-251.

88. Nishimot.K and L.S. Forster, *Scfmo Calculations of Heteroatomic Systems with Variable-Beta Approximation .3. Electronic Spectra of Anions of Hydroxyaromatics.* Journal of Physical Chemistry, 1968. **72**(3): p. 914-&.

89. Nishimoto, K. and R. Fujishiro, *Nature of the π-Electronic Spectra of Aromatic Compounds I. Aromatic Hydrocarbons and Their Hydroxyl Derivatives.* Bulletin of the Chemical Society of Japan, 1964. **37**(11): p. 1660-1669.

90. Schüürmann, G. and M. Klessinger, *Interpretation of the electronic spectra of substituted naphthalenes.* Chemical Physics, 1987. **113**(2): p. 241-249.

91. Suzuki, S., T. Fujii, and T. Ishikawa, *Interpretation of electronic spectra by configuration analysis: Absorption spectra of monosubstituted naphthalenes with an electron-accepting group.* Journal of Molecular Spectroscopy, 1975. **57**(3): p. 490-499.

92. Nishimoto, K., *Electronic Spectra and Structure of Alpha- and Beta-Naphthol.* Journal of Physical Chemistry, 1963. **67**(7): p. 1443-&.

93. Forster, L.S. and Nishimot.K, *Self-Consistent Field Calculations of Alpha- and Beta-Naphthol.* Journal of the American Chemical Society, 1965. **87**(7): p. 1459-&.

94. Singh, R.A. and S.N. Thakur, *Electronic-Transition Moments in the Spectra of Substituted Naphthalenes.* Journal of Crystal and Molecular Structure, 1981. **11**(5-6): p. 197-201.

95. Vasak, M., M.R. Whipple, and J. Michl, *Magnetic circular dichroism of cyclic .pi.-electron systems. 7. Aza analogs of naphthalene.* Journal of the American Chemical Society, 1978. **100**(22): p. 6838-6843.

96. Michl, J., *Magnetic circular dichroism of aromatic molecules.* Tetrahedron, 1984. **40**(19): p. 3845-3934.

97. Lyle, S.M. and E.C. Lim, *Polarization of singlet-singlet electronic transitions in substituted naphtahlenes.* Chemical Physics Letters, 1972. **17**(3): p. 367-369.

98. Fleisher, A.J., P.J. Morgan, and D.W. Pratt, *Charge transfer by electronic excitation: Direct measurement by high resolution spectroscopy in the gas phase.* Journal of Chemical Physics, 2009. **131**(21).

99. Johnson, J.R., et al., *High-Resolution S1[-S0 Fluorescence Excitation-Spectra of the 1-Hydroxynaphthalene and 2-Hydroxynaphthalene - Distinguishing the Cis and Trans Rotamers.* Journal of Chemical Physics, 1990. **93**(4): p. 2258-2273.

100. Hollas, J.M. and S.N. Thakur, *Rotational Band Contour Analysis in A1a'-X1a' Electronic Systems of Substituted Naphthalenes .2. 1-Fluoro, 1-Hydroxy and 1-Aminonaphthalene.* Molecular Physics, 1974. **27**(4): p. 1001-1011.

101. Hollas, J.M. and M.Z. Binhussein, *Evidence for 2 Rotational Isomers of 1-Naphthol and 2-Naphthol from Their Gas-Phase Electronic Absorption-Spectra.* Journal of Molecular Spectroscopy, 1988. **127**(2): p. 497-508.

102. Oikawa, A., et al., *Rotational Isomers of Meta-Substituted Phenols and Beta-Naphthol Studied by Electronic-Spectra in Supersonic Free Jets.* Journal of Physical Chemistry, 1984. **88**(22): p. 5180-5186.

103. Johnson, J.R., et al., *High-resolution S1-S0 fluorescence excitation-spectra of the 1-hydroxynaphthalene and 2-hydroxynaphthalene - Distinguishing the cis and trans isomers.* Journal of Chemical Physics, 1990. **93**(4): p. 2258-2273.

104. Fleisher, A.J., P.J. Morgan, and D.W. Pratt, *Charge transfer by electronic excitation: Direct measurement by high resolution spectroscopy in the gas phase.* Journal of Chemical Physics, 2009. **131**(21): p. 211101.

105. Baba, H. and S. Suzuki, *Electronic Spectra and Hydrogen Bonding .1. Phenol and Naphthols.* Journal of Chemical Physics, 1961. **35**(3): p. 1118-&.

106. Nagakura, S. and M. Gouterman, *Effect of Hydrogen Bonding on the near Ultraviolet Absorption of Naphthol.* Journal of Chemical Physics, 1957. **26**(4): p. 881-886.

107. Gramstad, T., *Studies of Hydrogen Bonding .8. Hydrogen-Bond Association between Phenol and Sulphoxides and Nitroso Compounds.* Spectrochimica Acta, 1963. **19**(5): p. 829-834.

108. Drago, R.S., B. Wayland, and R.L. Carlson, *Donor Properties of Sulfoxides, Alkyl Sulfites, and Sulfones.* Journal of the American Chemical Society, 1963. **85**(20): p. 3125-&.

109. Reichardt, C., *Solvents and solvent effects in organic chemistry*. 4th ed. 2011, New York: Wiley. 718 p.

110. Abraham, M.H., *Scales of Solute Hydrogen-Bonding - Their Construction and Application to Physicochemical and Biochemical Processes.* Chemical Society Reviews, 1993. **22**(2): p. 73-83.

111. Kamlet, M.J., et al., *Linear Solvation Energy Relationships .23. A Comprehensive Collection of the Solvatochromic Parameters, Pi-Star, Alpha and Beta, and Some Methods for Simplifying the Generalized Solvatochromic Equation.* Journal of Organic Chemistry, 1983. **48**(17): p. 2877-2887.

112. Marcus, Y., *The Properties of Organic Liquids That Are Relevant to Their Use as Solvating Solvents.* Chemical Society Reviews, 1993. **22**(6): p. 409-416.

113. Pimentel, G.C., *Hydrogen Bonding and Electronic Transitions - the Role of the Franck-Condon Principle.* Journal of the American Chemical Society, 1957. **79**(13): p. 3323-3326.

114. Tran-Thi, T.H., et al., *Substituent and solvent effects on the nature of the transitions of pyrenol and pyranine. Identification of an intermediate in the excited-state proton-transfer reaction.* Journal of Physical Chemistry A, 2002. **106**(10): p. 2244-2255.

115. Solntsev, K.M., D. Huppert, and N. Agmon, *Solvatochromism of beta-naphthol.* Journal of Physical Chemistry A, 1998. **102**(47): p. 9599-9606.

116. Magnes, B.Z., et al., *Hydrogen-bonding interactions of photoacids: correlation of optical solvatochromism with IR absorption spectra.* Solid State Ionics, 2004. **168**(3-4): p. 225-233.

117. Soumillion, J.P., et al., *Photophysical Analysis of Ion-Pairing of Beta-Naphtholate in Medium Polarity Solvents - Mixtures of Contact and Solvent-Separated Ion-Pairs.* Journal of the American Chemical Society, 1989. **111**(6): p. 2217-2225.

118. Solntsev, K.M., D. Huppert, and N. Agmon, *Photochemistry of "Super"-Photoacids. Solvent effects.* Journal of Physical Chemistry A, 1999. **103**(35): p. 6984-6997.

119. Solntsev, K.M., et al., *Solvatochromic shifts of "super" photoacids.* Journal of the American Chemical Society, 1998. **120**(31): p. 7981-7982.

120. Carsey, T.P., G.L. Findley, and S.P. Mcglynn, *Systematics in the Electronic-Spectra of Polar-Molecules .1. Para-Disubstituted Benzenes.* Journal of the American Chemical Society, 1979. **101**(16): p. 4502-4510.

121. Findley, G.L., T.P. Carsey, and S.P. Mcglynn, *Systematics in the Electronic-Spectra of Polar-Molecules .2. Ortho-Disubstituted and Meta-Disubstituted Benzenes.* Journal of the American Chemical Society, 1979. **101**(16): p. 4511-4517.

122. Scalmani, G., et al., *Geometries and properties of excited states in the gas phase and in solution: Theory and application of a time-dependent density functional theory polarizable continuum model.* Journal of Chemical Physics, 2006. **124**(9).

123. Catalan, J. and C. Diaz, *First reported evidence that solvent polarity induces an L-1(b)<-> L-1(a) inversion in the indole chromophore.* Chemical Physics Letters, 2003. **368**(5-6): p. 717-723.

124. Knochenmuss, R., O. Cheshnovsky, and S. Leutwyler, *Proton-Transfer Reactions in Neutral Gas-Phase Clusters - 1-Naphthol with H2o, D2o, Ch3oh, Nh3 and Piperidine.* Chemical Physics Letters, 1988. **144**(4): p. 317-323.

125. Knochenmuss, R. and S. Leutwyler, *Proton-Transfer from 1-Naphthol to Water - Small Clusters to the Bulk.* Journal of Chemical Physics, 1989. **91**(2): p. 1268-1278.

126. Knochenmuss, R., P.L. Muino, and C. Wickleder, *Vibronic coupling and microscopic solvation of 1-naphthol.* Journal of Physical Chemistry, 1996. **100**(27): p. 11218-11227.

127. Knochenmuss, R. and P.L. Muno, *Vibronic Coupling and Solvent Relaxation in the Excited-State Proton-Transfer Reaction of 1-Naphthol to Water.* Abstracts of Papers of the American Chemical Society, 1995. **210**: p. 114-PHYS.

128. Knochenmuss, R.D. and D.E. Smith, *Time and Internal Energy-Dependent Fluorescence-Spectra of Naphthol-Center-Dot-Water Clusters.* Journal of Chemical Physics, 1994. **101**(9): p. 7327-7336.

129. Humphrey, S.J. and D.W. Pratt, *Evidence for S-1/S-2 electronic state mixing in the S-1 <- S-0 fluorescence excitation spectrum of 1-naphthol.* Chemical Physics Letters, 1996. **257**(1-2): p. 169-174.

130. Spectroscopy, T.o.t.T.C.f., Journal of the Optical Society of America, 1962. **52**(4).

131. Adamczyk, K., et al., *Real-Time Observation of Carbonic Acid Formation in Aqueous Solution.* Science, 2009. **326**(5960): p. 1690-1694.

132. Cox, M.J., et al., *Distance-Dependent Proton Transfer along Water Wires Connecting Acid-Base Pairs.* Journal of Physical Chemistry A, 2009. **113**(24): p. 6599-6606.

133. Varasanyi, G., *Vibrational Spectra of Benzene Derivatives*. 1969, New York: Academic Press.

134. Lin-Vien, D., et al., *The Handbook of Infrared and Raman Characteristic Frequencies of Organic Molecules*. 1991, London: Academic Press.

135. Nguyen, M.T., E.S. Kryachko, and L.G. Vanquickenborne, *General and theoretical aspects of phenols*, in *The Chemistry of Phenols*, Z. Rappoport, Editor. 2003, John Wiley & Sons Ltd: Chishester.

136. Tishchenko, O., E.S. Kryachko, and M.T. Nguyen, *Theoretical vibrational analysis of monohalogenated phenols.* Spectrochimica Acta Part a-Molecular and Biomolecular Spectroscopy, 2002. **58**(9): p. 1951-1969.

137. Salman, S.R., *Conformational preference of substituted naphthalenes. 2—proton–proton coupling constants of hydroxy derivatives of naphthalene.* Organic Magnetic Resonance, 1984. **22**(6): p. 385-387.

138. West, W. and R.T. Edwards, *The infrared absorption spectrum of hydrogen chloride in solution.* Journal of Chemical Physics, 1937. **5**: p. 14-22.

139. Onsager, L., *Electric moments of molecules in liquids.* Journal of the American Chemical Society, 1936. **58**: p. 1486-1493.

140. Bauer, E. and M. Magat, *Regarding the deformation of molecules in a condensed phase, and the "hydrogen bond".* Journal De Physique Et Le Radium, 1938. **9**: p. 319-330.

141. Buckingham, A.D., *A Theory of Frequency, Intensity and Band-Width Changes Due to Solvents in Infra-Red Spectroscopy.* Proceedings of the Royal Society of London Series a-Mathematical and Physical Sciences, 1960. **255**(1280): p. 32-39.

142. Buckingham, A.D., *Solvent Effects in Vibrational Spectroscopy.* Transactions of the Faraday Society, 1960. **56**(6): p. 753-760.

143. Buckingham, A.D., *Solvent Effects in Infra-Red Spectroscopy.* Proceedings of the Royal Society of London Series a-Mathematical and Physical Sciences, 1958. **248**(1253): p. 169-182.

144. Lutskii, A.E., et al., *Spectroscopy of Intermolecular Field Interaction in Solutions.* Uspekhi Khimii, 1982. **51**(8): p. 1398-1423.

145. Pullin, A.D.E., *Solution Frequency Shift and Solvent Refractive Index.* Spectrochimica Acta, 1960. **16**(1-2): p. 12-24.

146. Pullin, A.D.E., *A Theory of Solvent Effects in Infra-Red Spectra.* Proceedings of the Royal Society of London Series a-Mathematical and Physical Sciences, 1960. **255**(1280): p. 39-43.

147. Pullin, A.D.E., *The Variation of Infra-Red Vibration Frequencies with Solvent.* Spectrochimica Acta, 1958. **13**(1-2): p. 125-138.

148. Bayliss, N.S. and E.G. Mcrae, *Solvent Effects in Organic Spectra - Dipole Forces and the Franck-Condon Principle.* Journal of Physical Chemistry, 1954. **58**(11): p. 1002-1006.

149. Bayliss, N.S., *The Effect of the Electrostatic Polarization of the Solvent on Electronic Absorption Spectra in Solution.* Journal of Chemical Physics, 1950. **18**(3): p. 292-296.

150. Stratt, R.M. and M. Maroncelli, *Nonreactive dynamics in solution: The emerging molecular view of solvation dynamics and vibrational relaxation.* Journal of Physical Chemistry, 1996. **100**(31): p. 12981-12996.

151. Maroncelli, M., *The Dynamics of Solvation in Polar Liquids.* Journal of Molecular Liquids, 1993. **57**: p. 1-37.

152. Nibbering, E.T.J. and T. Elsaesser, *Ultrafast vibrational dynamics of hydrogen bonds in the condensed phase.* Chemical Reviews, 2004. **104**(4): p. 1887-1914.

153. Dreyer, J., *Density functional theory simulations of two-dimensional infrared spectra for hydrogen-bonded acetic acid dimers.* International Journal of Quantum Chemistry, 2005. **104**(5): p. 782-793.

154. Dreyer, J., *Hydrogen-bonded acetic acid dimers: Anharmonic coupling and linear infrared spectra studied with density-functional theory.* Journal of Chemical Physics, 2005. **122**(18).

155. Dreyer, J., *Unraveling the structure of hydrogen bond stretching mode infrared absorption bands: An anharmonic density functional theory study on 7-azaindole dimers.* Journal of Chemical Physics, 2007. **127**(5).

156. Dreyer, J., V. Kozich, and W. Werncke, *Tuning intramolecular anharmonic vibrational coupling in 4-nitroaniline by solvent-solute interaction.* Journal of Chemical Physics, 2007. **127**(23).

157. Huse, N., et al., *Anharmonic couplings underlying the ultrafast vibrational dynamics of hydrogen bonds in liquids.* Physical Review Letters, 2005. **95**(14).

158. Riddick, J.A., W.B. Bunger, and T.K. Sakano, *Organic Solvents: Physical Properties and Methods of Purification*. 1986, New York: John Wiley & Sons.

159. Lakowicz, J.R., *Principles of fluorescence spectroscopy*. 3rd ed. 2006, New York: Springer. xxvi, 954 p.

160. Vanderzwan, G. and J.T. Hynes, *Time-Dependent Fluorescence Solvent Shifts, Dielectric Friction, and Nonequilibrium Solvation in Polar-Solvents.* Journal of Physical Chemistry, 1985. **89**(20): p. 4181-4188.

161. Bratos, S., et al., *Infra-Red Spectra of Hydrogen Bonded Systems: Theory and Experiment*, in *Ultrafast Hydrogen Bonding Dynamics and Proton Transfer Processes in the Condensed Phase*, T. Elsaesser and H.J. Bakker, Editors. 2002, Kluwer Academic Publishers: Dordrecht.

162. Bratos, S., *Profiles of Hydrogen Stretching Ir Bands of Molecules with Hydrogen-Bonds - Stochastic Theory .1. Weak and Medium Strength Hydrogen-Bonds.* Journal of Chemical Physics, 1975. **63**(8): p. 3499-3509.

163. Bratos, S. and H. Ratajczak, *Profiles of Hydrogen Stretching Ir Bands of Molecules with Hydrogen-Bonds - a Stochastic-Theory .2. Strong Hydrogen-Bonds.* Journal of Chemical Physics, 1982. **76**(1): p. 77-85.

164. Monroe, B.M. and G.C. Weed, *Photoinitiators for Free-Radical-Initiated Photoimaging Systems.* Chemical Reviews, 1993. **93**(1): p. 435-448.

165. Gratzel, M., *Recent Advances in Sensitized Mesoscopic Solar Cells.* Accounts of Chemical Research, 2009. **42**(11): p. 1788-1798.

166. Marcus, R.A., *Theory of Oxidation-Reduction Reactions Involving Electron Transfer .5. Comparison and Properties of Electrochemical and Chemical Rate Constants.* Journal of Physical Chemistry, 1963. **67**(4): p. 853-&.

167. Marcus, R.A., *Theory of Oxidation-Reduction Reactions Involving Electron Transfer .2. Applications to Data on the Rates of Isotopic Exchange Reactions.* Journal of Chemical Physics, 1957. **26**(4): p. 867-871.

168. Marcus, R.A., *Theory of Oxidation-Reduction Reactions Involving Electron Transfer .3. Applications to Data on the Rates of Organic Redox Reactions.* Journal of Chemical Physics, 1957. **26**(4): p. 872-877.

169. Marcus, R.A., *On the Theory of Oxidation-Reduction Reactions Involving Electron Transfer .1.* Journal of Chemical Physics, 1956. **24**(5): p. 966-978.

170. Hush, N.S., *Adiabatic Rate Processes at Electrodes .1. Energy-Charge Relationships.* Journal of Chemical Physics, 1958. **28**(5): p. 962-972.

171. Levich, V.G. and R.R. Dogonadze, *Theory of Non-Radiation Electron Transitions from Ion to Ion in Solutions.* Doklady Akademii Nauk Sssr, 1959. **124**(1): p. 123-126.

172. Weller, A., *Photoinduced Electron Transfer in Solution: Exciplex and Radical Ion Pair Formation Free Enthalpies and their Solvent Dependence.* Zeitschrift Fur Physikalische Chemie, 1982. **133**: p. 93.

173. Rehm, D. and A. Weller, *Kinetics of Fluorescence Quenching by Electron and Hydrogen Atom Transfer.* Israel Journal of Chemistry, 1970. **8**.

174. Rehm, D. and A. Weller, *Kinetics and Mechanism of Electron Transfer in Fluorescence Quenching in Acetonitrile.* Berichte Der Bunsen-Gesellschaft-Physical Chemistry Chemical Physics, 1969. **73**.

175. Yoshihara, K., *Ultrafast intermolecular electron transfer in solution.* Electron Transfer-from Isolated Molecules to Biomolecules, Pt 2, 1999. **107**: p. 371-402.

176. Siders, P. and R.A. Marcus, *Quantum Effects for Electron-Transfer Reactions in the Inverted Region.* Journal of the American Chemical Society, 1981. **103**(4): p. 748-752.

177. Siders, P. and R.A. Marcus, *Quantum Effects in Electron-Transfer Reactions.* Journal of the American Chemical Society, 1981. **103**(4): p. 741-747.

178. Efrima, S. and M. Bixon, *Vibrational Effects in Outer-Sphere Electron-Transfer Reactions in Polar Media.* Chemical Physics, 1976. **13**(4): p. 447-460.

179. Efrima, S. and M. Bixon, *Role of Vibrational-Excitation in Electron-Transfer Reactions with Large Negative Free-Energies.* Chemical Physics Letters, 1974. **25**(1): p. 34-37.

180. Vanduyne, R.P. and S.F. Fischer, *Nonadiabatic Description of Electron-Transfer Reactions Involving Large Free-Energy Changes.* Chemical Physics, 1974. **5**(2): p. 183-197.

181. Jortner, J. and M. Bixon, *Intramolecular Vibrational Excitations Accompanying Solvent-Controlled Electron-Transfer Reactions.* Journal of Chemical Physics, 1988. **88**(1): p. 167-170.

182. Bagchi, B. and N. Gayathri, *Interplay between ultrafast polar solvation and vibrational dynamics in electron transfer reactions: Role of high-frequency vibrational modes.* Electron Transfer-from Isolated Molecules to Biomolecules, Pt 2, 1999. **107**: p. 1-80.

183. Collins, F.C. and G.E. Kimball, *Diffusion-Controlled Reaction Rates.* Journal of Colloid Science, 1949. **4**(4): p. 425-437.

184. Collins, F.C. and G.E. Kimball, *Diffusion-Controlled Reactions in Liquid Solutions.* Industrial and Engineering Chemistry, 1949. **41**(11): p. 2551-2553.

185. Eads, D.D., B.G. Dismer, and G.R. Fleming, *A Subpicosecond, Subnanosecond and Steady-State Study of Diffusion-Influenced Fluorescence Quenching.* Journal of Chemical Physics, 1990. **93**(2): p. 1136-1148.

186. Pages, S., B. Lang, and E. Vauthey, *Ultrafast spectroscopic investigation of the charge recombination dynamics of ion pairs formed upon highly exergonic bimolecular electron-transfer quenching: Looking for the normal region.* Journal of Physical Chemistry A, 2004. **108**(4): p. 549-555.

187. Gould, I.R. and S. Farid, *Dynamics of bimolecular photoinduced electron-transfer reactions.* Accounts of Chemical Research, 1996. **29**(11): p. 522-528.

188. Mohammed, O.F., et al., *Direct Femtosecond Observation of Tight and Loose Ion Pairs upon Photoinduced Bimolecular Electron Transfer.* Angewandte Chemie-International Edition, 2008. **47**(47): p. 9044-9048.

189. Vauthey, E., *Investigations of bimolecular photoinduced electron transfer reactions in polar solvents using ultrafast spectroscopy.* Journal of Photochemistry and Photobiology a-Chemistry, 2006. **179**(1-2): p. 1-12.

190. Mataga, N., H. Chosrowjan, and S. Taniguchi, *Ultrafast charge transfer in excited electronic states and investigations into fundamental problems of exciplex chemistry: Our early studies and recent developments.* Journal of Photochemistry and Photobiology C-Photochemistry Reviews, 2005. **6**(1): p. 37-79.

191. Einstein, A., *Zur Quanthentheorie der Strahlung.* Physikalische Zeitschrift, 1917. **18**.

192. Moulton, P.F., *Spectroscopic and Laser Characteristics of Ti-Al2o3.* Journal of the Optical Society of America B-Optical Physics, 1986. **3**(1): p. 125-133.

193. Franken, P.A., et al., *Generation of Optical Harmonics.* Physical Review Letters, 1961. **7**(4): p. 118-&.

194. Shen, Y.R., *The principles of nonlinear optics*. Wiley classics library ed. Wiley classics library. 2003, Hoboken, N.J.: Wiley-Interscience. xii, 563 p.

195. Fortier, T.M., et al., *Generation of ultrastable microwaves via optical frequency division.* Nature Photonics, 2011. **5**(7): p. 425-429.

196. Korn, G., et al., *Ultrashort 1-kHz laser plasma hard x-ray source.* Optics Letters, 2002. **27**(10): p. 866-868.

197. Richmond, G.L., *Molecular bonding and interactions at aqueous surfaces as probed by vibrational sum frequency spectroscopy.* Chemical Reviews, 2002. **102**(8): p. 2693-2724.

198. Yan, Y.J., L.E. Fried, and S. Mukamel, *Ultrafast Pump-Probe Spectroscopy - Femtosecond Dynamics in Liouville Space.* Journal of Physical Chemistry, 1989. **93**(25): p. 8149-8162.

199. Pollard, W.T. and R.A. Mathies, *Analysis of Femtosecond Dynamic Absorption-Spectra of Nonstationary States.* Annual Review of Physical Chemistry, 1992. **43**: p. 497-523.

200. Mukamel, S., *Principles of nonlinear optical spectroscopy*. Oxford series in optical and imaging sciences. 1995, New York: Oxford University Press. xviii, 543 p.

201. Feynman, R.P., *Space-Time Approach to Quantum Electrodynamics.* Physical Review, 1949. **76**(6): p. 769-789.

202. Hamm, P., *Principles of Nonlinear Optical Spectroscopy: A Practical Approach*, L.o.V.E.U.o. Lasers, Editor 2005.

203. Fleming, G.R., *Chemical applications of ultrafast spectroscopy*. The International series of monographs on chemistry. 1986, New York, Oxford Oxfordshire: Oxford University Press ; Clarendon Press. ix, 262 p.

204. Kaindl, R.A., et al., *Generation, shaping, and characterization of intense femtosecond pulses tunable from 3 to 20 mu m.* Journal of the Optical Society of America B-Optical Physics, 2000. **17**(12): p. 2086-2094.

205. Bollinger, L. and G.E. Thomas, *Measurement of Time Dependence of Scintillation Intensity by a Delayed-Coincidence Method.* Review of Scientific Instruments, 1961. **32**(9): p. 1044-&.

206. Pimentel, G.C. and Mcclella.Al, *Hydrogen Bonding.* Annual Review of Physical Chemistry, 1971. **22**: p. 347-&.

207. Barbara, P.F. and W. Jarzeba, *Ultrafast Photochemical Intramolecular Charge and Excited State Solvation*, in *Advances in Photochemistry*. 2007, John Wiley & Sons, Inc. p. 1-68.

208. Castner Jr, E.W. and M. Maroncelli, *Solvent dynamics derived from optical Kerr effect, dielectric dispersion, and time-resolved stokes shift measurements: an empirical comparison.* Journal of Molecular Liquids, 1998. **77**(1–3): p. 1-36.

209. Bagchi, B. and B. Jana, *Solvation dynamics in dipolar liquids.* Chemical Society Reviews, 2010. **39**(6): p. 1936-1954.

210. Chudoba, C., E.T.J. Nibbering, and T. Elsaesser, *Site-specific excited-state solute-solvent interactions probed by femtosecond vibrational spectroscopy.* Physical Review Letters, 1998. **81**(14): p. 3010-3013.

211. Nibbering, E.T.J., C. Chudoba, and T. Elsaesser, *Hydrogen-bond dynamics and solvation of electronically excited states as determined by femtosecond vibrational spectroscopy.* Israel Journal of Chemistry, 1999. **39**(3-4): p. 333-346.

212. Asbury, J.B., Y.Q. Wang, and T.Q. Lian, *Time-dependent vibration Stokes shift during solvation: Experiment and theory.* Bulletin of the Chemical Society of Japan, 2002. **75**(5): p. 973-983.

213. Novak, A., *Hydrogen bonding in solids correlation of spectroscopic and crystallographic data Large Molecules*. 1974, Springer Berlin / Heidelberg. p. 177-216.

214. Rey, R., K.B. Møller, and J.T. Hynes, *Hydrogen Bond Dynamics in Water and Ultrafast Infrared Spectroscopy.* The Journal of Physical Chemistry A, 2002. **106**(50): p. 11993-11996.

215. Badger, R.M. and S.H. Bauer, *Spectroscopic studies of the hydrogen bond. II. The shift of the O-H vibrational frequency in the formation of the hydrogen bond.* Journal of Chemical Physics, 1937. **5**(11): p. 839-851.

216. Schuster, P., G. Zundel, and C. Sandorfy, *The Hydrogen bond : recent developments in theory and experiments*. 1976, Amsterdam, New York: North-Holland Pub. Co. ; distributor, American Elsevier Pub. Co.

217. Arnett, E.M. and E.J. Mitchell, *Hydrogen Bonding .6. Dramatic Difference between Proton Transfer and Hydrogen Bonding.* Journal of the American Chemical Society, 1971. **93**(16): p. 4052-&.

218. Bakker, H.J. and J.L. Skinner, *Vibrational Spectroscopy as a Probe of Structure and Dynamics in Liquid Water.* Chemical Reviews, 2010. **110**(3): p. 1498-1517.

219. Fayer, M.D., et al., *Water Dynamics in Salt Solutions Studied with Ultrafast Two-Dimensional Infrared (2D IR) Vibrational Echo Spectroscopy.* Accounts of Chemical Research, 2009. **42**(9): p. 1210-1219.

220. Josien, M.-L., *Étude par Spectroscopie Infrarouge des Actions Intermoléculaires dans les Liquides.* Pure and Applied Chemistry, 1962. **4**(1).

221. Cole, A.R.H., L.H. Little, and A.J. Michell, *Solvent Effects in Infra-Red Spectra . O-H and S-H Stretching Vibrations.* Spectrochimica Acta, 1965. **21**(7): p. 1169-&.

222. Yoshino, R., et al., *Structure of 1-Naphthol−Water Clusters Studied by IR Dip Spectroscopy and Ab Initio Molecular Orbital Calculations.* The Journal of Physical Chemistry A, 1998. **102**(31): p. 6227-6233.

223. Matsumoto, Y., T. Ebata, and N. Mikami, *Characterizations of the hydrogen-bond structures of 2-naphthol-(H2O)(n), (n = 0-3 and 5) clusters by infrared-ultraviolet double-resonance spectroscopy.* Journal of Chemical Physics, 1998. **109**(15): p. 6303-6311.

224. Durocher, G. and C. Sandorfy, *A Study of Effects of Solvent on Overtone Frequencies.* Journal of Molecular Spectroscopy, 1967. **22**(3): p. 347-&.

225. Rospenk, M., B. Czarnik-Matusewicz, and T. Zeegers-Huyskens, *Near infrared spectra (4000-10 500 cm(-1)) of phenol-OH and phenol-OD in carbon tetrachloride.* Spectrochimica Acta Part a-Molecular and Biomolecular Spectroscopy, 2001. **57**(1): p. 185-195.

226. Couzi, M. and P.V. Houng, *Effect of Molecular Interactions on Anharmonicity of Phenol-Oh Vibrators.* Spectrochimica Acta Part a-Molecular Spectroscopy, 1970. **A 26**(1): p. 49-&.

227. Pines, E., et al., *Femtosecond pump-probe measurements of solvation by hydrogen-bonding interactions.* Chemphyschem, 2004. **5**(9): p. 1315-1327.

228. Frisch, M.J., et al., *Gaussian 09, Revision A.1*. 2009, Wallingford CT: Gaussian, Inc.

229. Plusquellic, D.F., X.-Q. Tan, and D.W. Pratt, *ACID-BASE CHEMISTRY IN THE GAS-PHASE - THE CIS-2-NAPHTHOL.NH3 AND TRANS-2-NAPHTHOL.NH3 COMPLEXES IN THEIR S0 AND S1 STATES.* Journal of Chemical Physics, 1992. **96**(11): p. 8026-8036.

230. Grimme, S. and M. Parac, *Substantial errors from time-dependent density functional theory for the calculation of excited states of large pi systems.* ChemPhysChem, 2003. **3**: p. 292-295.

231. Hamm, P., S.M. Ohline, and W. Zinth, *Vibrational cooling after ultrafast photoisomerization of azobenzene measured by femtosecond infrared spectroscopy.* Journal of Chemical Physics, 1997. **106**(2): p. 519-529.

232. Yoshino, R., et al., *Structure of 1-naphthol-water clusters studied by IR dip spectroscopy and ab initio molecular orbital calculations.* Journal of Physical Chemistry A, 1998. **102**(31): p. 6227-6233.

233. Zhao, Y. and D.G. Truhlar, *Density functionals with broad applicability in chemistry.* Accounts of Chemical Research, 2008. **41**(2): p. 157-167.

234. Solca, N. and O. Dopfer, *Protonation of aromatic molecules: competition between ring and oxygen protonation of phenol (Ph) revealed by IR spectra of PhH+-Ar-n.* Chemical Physics Letters, 2001. **342**(1-2): p. 191-199.

235. Tishchenko, O., et al., *Protonation of gaseous halogenated phenols and anisoles and its interpretation using DFT-based local reactivity indices.* Journal of Physical Chemistry A, 2001. **105**(38): p. 8709-8717.

236. Ganapathi, M.R., et al., *Free electron transfer from several phenols to radical cations of non-polar solvents.* Physical Chemistry Chemical Physics, 2000. **2**(21): p. 4947-4955.

237. Mohan, H., et al., *Two channels of electron transfer observed for the reaction of n-butyl chloride parent radical cations with naphthols and hydroxybiphenyls.* Journal of Physical Chemistry A, 1998. **102**(29): p. 5754-5762.

238. Miller, J.R., L.T. Calcaterra, and G.L. Closs, *Intramolecular Long-Distance Electron-Transfer in Radical-Anions - the Effects of Free-Energy and Solvent on the Reaction-Rates.* Journal of the American Chemical Society, 1984. **106**(10): p. 3047-3049.

239. Hino, T., et al., *Ionic Photodissociation of Excited Electron Donor-Acceptor Systems .2. Importance of Chemical Property of Donor-Acceptor Pairs.* Journal of Physical Chemistry, 1976. **80**(1): p. 33-37.

240. Hino, T., H. Masuhara, and N. Mataga, *Formation and Dissociation of Solvated Ion-Pair in Excited Pyrene-Dicyanobenzene System.* Bulletin of the Chemical Society of Japan, 1976. **49**(2): p. 394-396.

241. Peon, J., et al., *Ultrafast photoionization dynamics of indole in water.* Journal of Physical Chemistry A, 1999. **103**(14): p. 2460-2466.

242. Shimamori, H. and H. Musasa, *Contact-ion-pair formation in photolyzed aniline and N,N-dimethylaniline in the presence of CCl4.* Journal of Physical Chemistry, 1996. **100**(13): p. 5343-5348.

243. Pines, E., *UV-visible spectra and photoacidity of phenols, naphthols and pyrenols*, in *The Chemistry of Phenols*, Z. Rappoport, Editor. 2003, John Wiley & Sons Ltd: Chichester.

244. Spry, D.B., et al., *Identification and properties of the L-1(a) and L-1(b) states of pyranine.* Journal of Chemical Physics, 2006. **125**(14).

245. Spry, D.B., *Ultrafast Excited State Proton Transfer in the Condensed Phase and Nanoconfinement*, in *Department of Chemistry*, M.D. Fayer, Editor 2009, Standford University.

246. Mohammed, O.F., et al., *Solvent-dependent photoacidity state of pyranine monitored by transient mid-infrared spectroscopy.* Chemphyschem, 2005. **6**(4): p. 625-636.

247. Fayer, M.D., D.B. Spry, and A. Goun, *Deprotonation dynamics and stokes shift of pyranine (HPTS).* Journal of Physical Chemistry A, 2007. **111**(2): p. 230-237.

248. Spry, D.B. and M.D. Fayer, *Observation of slow charge redistribution preceding excited-state proton transfer.* Journal of Chemical Physics, 2007. **127**(20).

249. Spry, D.B. and M.D. Fayer, *Charge redistribution and photoacidity: Neutral versus cationic photoacids.* Journal of Chemical Physics, 2008. **128**(8).

250. Fayer, M.D., et al., *Charge Transfer in Photoacids Observed by Stark Spectroscopy.* Journal of Physical Chemistry A, 2008. **112**(41): p. 10244-10249.

251. Chudoba, C., E.T.J. Nibbering, and T. Elsaesser, *Ultrafast Structural Response of Hydrogen Bonded Complexes to Electronic Excitation in the Liquid Phase.* The Journal of Physical Chemistry A, 1999. **103**(29): p. 5625-5628.

252. Laws, W.R. and L. Brand, *Analysis of 2-State Excited-State Reactions - Fluorescence Decay of 2-Naphthol.* Journal of Physical Chemistry, 1979. **83**(7): p. 795-802.

253. Lee, J., et al., *Hydration Dynamics of Protons from Photon Initiated Acids.* Journal of the American Chemical Society, 1986. **108**(21): p. 6538-6542.

254. Castano, F., et al., *A time resolved study of S(1)/S(2) electronic coupling in naphthalene.* Chemical Physics Letters, 2009. **468**(4-6): p. 134-137.

255. Pines, E. and G.R. Fleming, *Self-Quenching of 1-Naphthol - Connection between Time-Resolved and Steady-State Measurements.* Chemical Physics, 1994. **183**(2-3): p. 393-402.

256. Mohammed, O.F., et al., *Sequential proton transfer through water bridges in acid-base reactions.* Science, 2005. **310**(5745): p. 83-86.

257. Brzezinski, B., et al., *Proton Potential as a Function of the Pka of Phenol in Intermolecular Phenol Trimethylamine N-Oxide Hydrogen-Bonds.* Journal of Physical Chemistry, 1991. **95**(22): p. 8598-8600.

258. Janosche.R, et al., *Extremely High Polarizability of Hydrogen-Bonds.* Journal of the American Chemical Society, 1972. **94**(7): p. 2387-&.

259. Horng, M.L., et al., *Subpicosecond Measurements of Polar Solvation Dynamics: Coumarin 153 Revisited.* The Journal of Physical Chemistry, 1995. **99**(48): p. 17311-17337.

260. Shizuka, H., *Excited-State Proton-Transfer Reactions and Proton-Induced Quenching of Aromatic-Compounds.* Accounts of Chemical Research, 1985. **18**(5): p. 141-147.

261. Harris, C.M. and B.K. Selinger, *Acid-Base Properties of 1-Naphthol - Proton-Induced Fluorescence Quenching.* Journal of Physical Chemistry, 1980. **84**(11): p. 1366-1371.

262. Harris, C.M. and B.K. Selinger, *Proton-Induced Fluorescence Quenching of 2-Naphthol.* Journal of Physical Chemistry, 1980. **84**(8): p. 891-898.

263. Alfano, J.C., et al., *Ultrafast Transient Absorption-Spectroscopy of the Aqueous Solvated Electron.* Abstracts of Papers of the American Chemical Society, 1993. **206**: p. 66-Phys.

264. Anderson, N.A., et al., *Ultrafast mid-IR detection of the direct precursor to the presolvated electron following electron ejection from ferrocyanide.* Chemical Physics Letters, 2000. **329**(5-6): p. 386-392.

265. Lami, H. and N. Glasser, *Indole Solvatochromism Revisited.* Journal of Chemical Physics, 1986. **84**(2): p. 597-604.

266. Callis, P.R., *L-1(a) and L-1(b) transitions of tryptophan: Applications of theory and experimental observations to fluorescence of proteins.* Fluorescence Spectroscopy, 1997. **278**: p. 113-150.

267. Bram, O., et al., *Relaxation Dynamics of Tryptophan in Water: A UV Fluorescence Up-Conversion and Molecular Dynamics Study.* Journal of Physical Chemistry A, 2010. **114**(34): p. 9034-9042.

Selbständigkeiterklärung

Hiermit erkläre ich, die Dissertation selbständig und nur unter Verwendung der angegebenen Hilfen und Hilfsmittel angefertigt zu haben.

Ich habe mich anderwärts nicht um einen Doktorgrad beworben und besitze einen entsprechenden Doktorgrad nicht.

Ich habe die dem Verfahren zugrunde liegenden Promotionsordnung der Mathematisch-Naturwissenschaftlichen Fakultät I der Humboldt-Universität zu Berlin zur Kenntnis genommen.

Berlin, den 25.01.2013 Mirabelle Prémont-Schwarz